Bifunctional catalysts for the direct production of liquid fuels from syngas

Sina Sartipi

Author: Sina Sartipi

PhD Thesis, Delft University of Technology

The Netherlands, March 2014

Cover design: Im3diA communication/Jorge Gascon

Bifunctional catalysts for the direct production of liquid fuels from syngas

Proefschrift

ter verkrijging van de graad van doctor
aan de Technische Universiteit Delft,
op gezag van de Rector Magnificus prof. ir. K.C.A.M. Luyben,
voorzitter van het College voor Promoties,
in het openbaar te verdedigen op maandag 31 maart 2014 om 12.30 uur

door Sina SARTIPI

Master of Science in Chemical Engineering, University of Tehran, Iran
geboren te Teheran, Iran

Dit proefschrift is goedgekeurd door de promotor:

Prof.dr. F. Kapteijn

Dr. J. Gascon, copromotor

Samenstelling promotiecommissie:

Rector Magnificus,	voorzitter
Prof.dr. F. Kapteijn	Technische Universiteit Delft, promotor
Dr. J. Gascon	Technische Universiteit Delft, copromotor
Prof.dr.ir. M. Makkee	Politecnico di Torino/Technische Universiteit Delft
Prof. Y. Wang	Xiamen University
Prof.dr. J. Pérez-Ramírez	ETH Zürich
Prof.dr.ir. K.P. de Jong	Universiteit Utrecht
Dr. H.P.C.E. Kuipers	Shell Global Solutions International B.V.
Prof.dr.ir. H. van Bekkum	Technische Universiteit Delft, reservelid

The research reported in this thesis was conducted in the Catalysis Engineering section of the Chemical Engineering department, Faculty of Applied Sciences (TNW) of the Delft University of Technology.
This research has been performed within the framework of the CatchBio program (project 053.70.005). The author gratefully acknowledges the support of the Smart Mix Program of the Netherlands Ministry of Economic Affairs and the Netherlands Ministry of Education, Culture and Science.

Proefschrift, Technische Universiteit Delft
Met samenvatting in het Nederlands

ISBN/EAN 978-94-6203-554-6

Printed by CPI - WÖHRMANN PRINT SERVICE B.V.

Content

To the stars of my life

keep shining…

Scope of the thesis

Depletion of fossil resources over the last few decades, the increasing price of crude oil, the rapid increase of identified methane reserves, and environmental concerns have spurred a world-wide interest in practical applications of Fischer-Tropsch synthesis (FTS)-related technologies. Different types of fossil- and renewable-based feedstocks can be converted into industrially relevant chemicals such as lower olefins and alcohols as well as ultra clean liquid fuels through the FTS reaction. The latter case is already commercialized *via* the so-called low-temperature Fischer-Tropsch and high-temperature Fischer-Tropsch processes, using syngas (mixture of CO and H_2) as feed. However, these technologies are economically feasible only at very large scales and therefore, process intensification is needed in applications with limited (and scattered) availability of feedstock (*e.g.*, biomass) and/or space (*e.g.*, offshore associated petroleum gas).

In the state of the art gas-to-liquid process, FTS reactors are followed by separate product upgrading units for hydrocracking and/or isomerization of FTS hydrocarbons. As a way to attain the above-mentioned process intensification, design and development of catalyst formulations that maximize the direct production of liquid fuels (desired products) by combining FTS, hydrocarbon cracking, and isomerization into one single catalyst particle (bifunctional FTS catalyst) are investigated in this thesis, through eight chapters:

In **Chapter 1**, the aim and approaches of this research area are introduced in more detail. Challenges are described and recent advances, as reported in open literature, are critically reviewed.

In **Chapter 2** design and operation of a 'six-flow' lab-scale equipment that was constructed (as part of this PhD project) for FTS experimentation is demonstrated.

To proceed with the research objective, combination of cobalt FTS active phase and acid functionality of H-ZSM-5 zeolite is explored in **Chapter 3**, *via* two different catalyst configurations: (*i*) H-ZSM-5 as catalytic coating on Co and (*ii*) H-ZSM-5 as catalytic support for Co. The latter is studied comprehensively in Chapters 4 to 7.

Mesoporous H-ZSM-5 is introduced as carrier for Co-based FTS catalysts in **Chapter 4**. Synthesis optimization of this catalyst support for applications in bifunctional FTS is described extensively in **Chapter 5**. A large number of prepared reference samples are characterized thoroughly by advanced techniques and their catalytic performance is assessed in detail in Chapters 5 and 6, where a relationship is drawn between structural characteristics of Co (when supported on the zeolite) and its

FTS activity and selectivity. Moreover, promotion of zeolite-supported Co-catalysts by noble and non-noble materials is studied in **Chapter 6**.

Application of alternative hierarchical zeolite topologies, in the context of bifunctionality, is explored in **Chapter 7** where the effect of zeolite structure and acidity on the performance of the bifunctional catalysts is studied. Finally, the overall conclusions and outlook of this thesis work are summarized in **Chapter 8**.

Since all the Chapters (except 'Summary and outlook') are adapted from published articles, some duplication is unavoidable. The Chapters can therefore be read independently. Supplementary information accompanying Chapters 2–7 is presented in Appendix A–F.

Chapter 1

Introduction: Catalysis Engineering of bifunctional solids for the direct production of liquid fuels from syngas

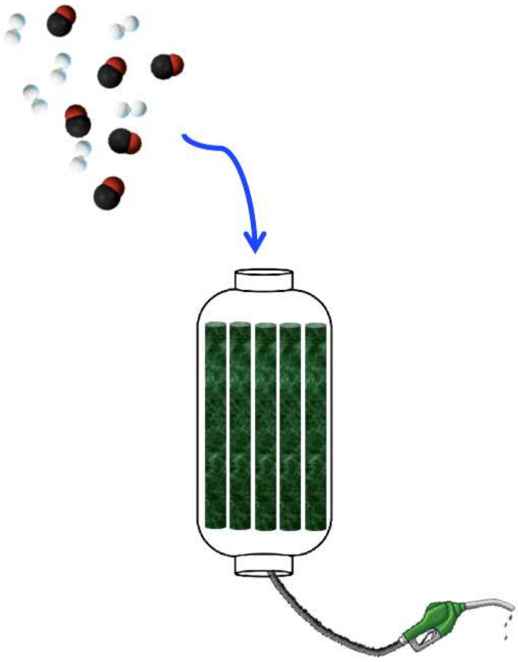

This Chapter is based on the following publication:

S. Sartipi, M. Makkee, F. Kapteijn, J. Gascon, Catal. Sci. Technol. (**2014**) In Press. DOI: 10.1039/c3cy01021j

Abstract: The combination of acidic zeolites and Fischer-Tropsch synthesis (FTS) catalysts for one-step production of liquid fuels from syngas is critically reviewed. Bifunctional systems are classified by the proximity between FTS and acid functionalities on three levels: reactor, catalyst particle, and active phase. A thorough analysis of the published literature on this topic reveals that efficiency in the production of liquid fuels correlates well with the proximity of FTS and acid sites.

Moreover, possible side reactions over the FTS metal, including direct CO hydrogenation and hydrocarbon hydrogenolysis, are addressed. The contribution of these side reactions should carefully be considered and separated from that of the zeolite function when evaluating the performance and product spectrum of zeolite-containing catalysts.

1.1. Introduction

Due to their high volumetric and reasonable mass energy densities and low cost/price, gasoline and diesel are the preferred transportation fuels. To date, these liquid fuels are being mainly produced in conventional refineries from crude oil. Depletion of petroleum and environmental concerns have driven a worldwide research on alternative processes for the production of energy carriers. Among the various possibilities and chemical conversion routes, syngas (a mixture of CO and H_2) production followed by Fischer-Tropsch synthesis (FTS) holds promises for extensive implementation in the near future. This is due to the maturity of both technologies in addition to abundance of alternative resources such as natural gas, coal, and biomass. Furthermore, the dependency on centralized fossil-based reservoirs may be relaxed if globally dispersed raw materials can be utilized as feedstock.

When producing liquid fuels by the state of the art gas-to-liquid (GTL) processes, low-temperature Fischer-Tropsch (LTFT) reactors are operated at high chain growth probability conditions at which heavy paraffinic hydrocarbons (wax) are produced with high selectivities. Waxes are subsequently fed to hydrocrackers and converted to the desired cut of the barrel [1]. Lower hydrocarbon chain growths are expected in processes based on high-temperature Fischer-Tropsch (HTFT) for gasoline production [2]. Nevertheless, hydrocarbon conversion reactions, including hydroisomerization, are required to upgrade the octane number of the FTS-based gasoline.

Practical feasibility of the conventional GTL should benefit from the so-called ‘economy of scale’ [3]. However, process intensification is essential to make use of feedstocks with limited and scattered availability (*e.g.*, renewables) or associated petroleum gas on offshore platforms. The current importance of intensified GTL technologies is illustrated by the number of academic research groups and companies such as CompactGTL [4], Velocys [5], and Chevron [6], currently involved in this research. Yet, it should be stressed that efforts to develop intensified GTL processes do not necessarily aim to substitute the state of the art, already optimized for large scale applications, but are responses to the availability of alternative feedstocks.

From the catalysis engineering prospect, running several reactions by coupling two or more functionalities in a single catalyst particle is a well-known and attractive approach, such as in hydroisomerization. First examples describing the incorporation of additional functionalities in FTS, including water-gas-shift (WGS) and acidity, have been reported more than two decades ago [7-9]. The former is intrinsically present in Fe-based FTS catalysts or alternatively can be introduced by addition of a dedicated component such as Cu-based WGS catalysts [9]. If H_2/CO ratio is smaller than the reaction stoichiometry (*i.e.*, $H_2/CO = 2$), a high CO conversion may only be achieved in combination with a reasonable extent of *in situ* WGS. On the other hand, intraparticle H_2/CO ratios stay closer to the optimal stoichiometric value by feeding H_2 deficient syngas, due to the higher diffusivity of H_2 [10]. Therefore, WGS functionality is of high importance, especially when coal or biomass are used as syngas sources with H_2/CO ratios around unity [11].

Other active sites have been introduced to add acid functionality to the catalyst. This aims to couple FTS to either etherification [12] or acid-catalyzed hydrocarbon upgrading (*via* (hydro)cracking, (hydro)isomerization, *etc.*). The latter is the subject of this report. While almost a century of literature is available on FTS catalysts, still new reviews update the recent advances and findings on this topic [11, 13-20]. This contribution is confined to the recent open literature on zeolite-based bifunctional catalyst systems. The possible acid-catalyzed reactions that are likely to occur under FTS conditions are discussed first and their feasibility is assessed (Section 1.2). Following, the possible side reactions at the metal sites, resulting from their interaction with the zeolite, are addressed. These side reactions are consequences of the combination of functionalities, which may affect or alter the product distribution (Section 1.3). On these grounds, the combination of FTS and acid functionalities and their cooperative catalytic performances are discussed in detail as a function of the proximity between both phases, namely on the reactor, catalyst particle, and active phase levels (Section 1.4).

1.2. Relevant acid/zeolite catalyzed reactions

The idea behind the combination of FTS and acid functionalities is the direct production of liquid hydrocarbons from syngas *via* consecutive CO polymerization and hydrocracking. In this Section, the feasibility of hydrocracking and other acid-catalyzed reactions, likely to occur over bifunctional catalysts, under FTS conditions is discussed.

1.2.1. Hydrocracking

Hydrocracking, catalytic cracking, and thermal cracking are the most important types of cracking. The former two proceed in the presence of a solid catalyst and their main difference is H_2 co-feed in the case of hydrocracking. Fluidized catalytic cracking or FCC is a well-known cracking process where no H_2 is co-fed to the reactor, operated at 753–823 K. One of the most important components of FCC catalysts is an acidic zeolite. Hydrocrackers on the other hand, are operated in the temperature range of 623–713 K [2]. At such lower temperatures, incorporation of a (de)hydrogenation function into the catalyst formulation, besides the acidity, is the key to enhance catalyst activity and stability. Conventionally, the (de)hydrogenation function is introduced by a metal, supported on the solid acid catalyst (Table 1).

Hydrocracking catalysts are similar as those of hydroisomerization in the sense that they both contain (de)hydrogenation and acid functionalities. This is due to the fact that reaction intermediates are similar in both reactions: the formation of cracked products is preceded by an isomerization step.

Table 1 Various (de)hydrogenation and acid functions of hydrocracking catalysts. Reproduced from reference [21].

	Hydrogenation function (metal)	Acid function (support)	
	Ni/Mo	Al_2O_3	
Increasing hydrogenation ↓	Ni/W	Al_2O_3/halogen	Increasing acidity ↓
	Pt/Pd	SiO_2/Al_2O_3	
		Zeolites	
	low sulfur conditions		

The hydrocracking reaction mechanism is schematically illustrated in Figure 1 for a representative hydrocarbon. The reaction is initiated by formation of a carbocation. In case of olefins, the carbocation can readily be formed *via* addition of a proton, supplied by Brønsted acid sites. Otherwise, in the case of saturated hydrocarbons, a dehydrogenation step should precede. Alternatively the olefin may form by abstraction of a hydride ion from the hydrocarbon. The hydride ion can be accepted by the acid catalyst and be combined with a proton to form molecular H_2 [22].

Before C–C scission, the carbocation undergoes skeletal isomerization to form an iso-carbocation. This proceeds through a secondary carbocation rearrangement, most probably *via* a protonated dialkylcyclopropane (Figure 1) for hydrocarbons containing five or more carbon atoms. For C4 hydrocarbons, formation of protonated dialkylcyclopropane is energetically unfavorable since it would call for a primary carbocation as intermediate [23].

The next mechanistic step of hydrocracking is scission of the C–C bond at the β position of the positively charged carbon atom (β-scission) to form a lighter alkene and a lighter carbocation. The

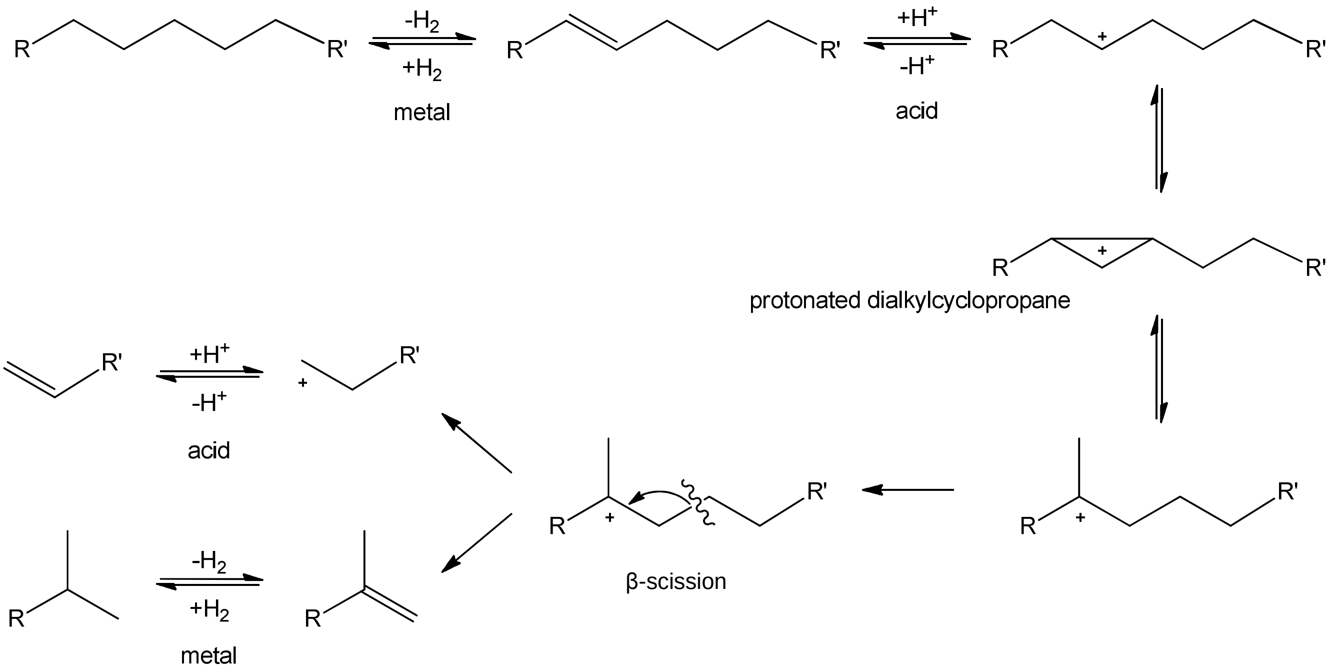

Figure 1. Hydrocracking reaction mechanism for a representative hydrocarbon.

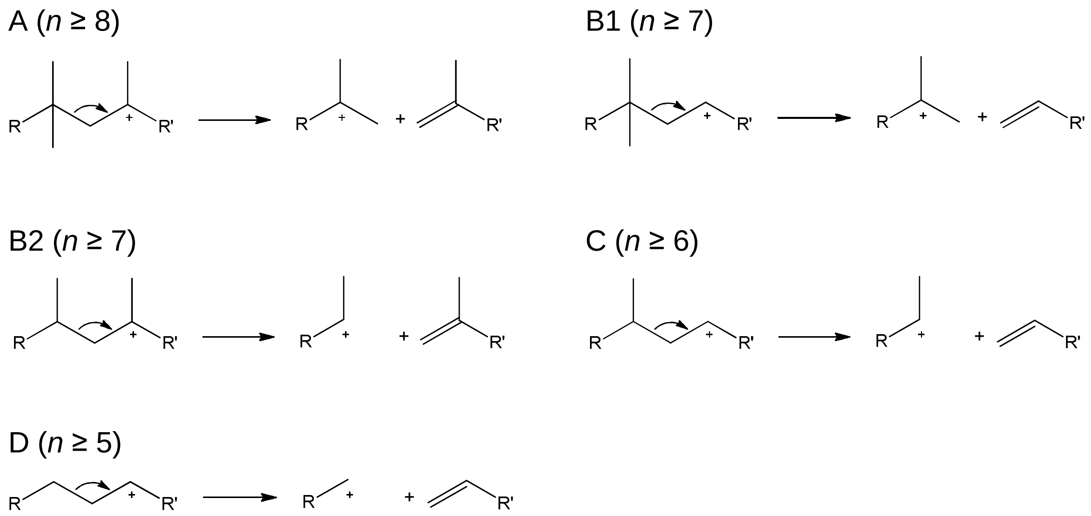

Figure 2. Examples of different types of β-scission, imposed to different carbocation intermediates. *n*: carbon number.

latter may go through a further sequence of reactions as described above or it may be converted to an alkene upon proton abstraction by the acid catalyst. Finally, the olefinic products may adsorb on a metal site and become hydrogenated.

Five types of β-scission can be distinguished with respect to the stability of the carbocations involved (Figure 2) for which the relative reaction rates obey the following order: A >> B1 ≈ B2 > C >>> D [24]. A ‘fast’ hydrocracking occurs once the hydrocarbon has been hydroisomerized and subsequent branching in the chain leads to fastest hydrocracking. Among the different acid supports employed in hydrocracking catalysts (Table 1), zeolites offer a high stability as well as shape selectivity. Inside shape selective zeolites such as ZSM-5, the branched reaction intermediates are blocked where they undergo successive isomerization steps and rapid cracking [25].

The above-mentioned reaction steps for hydrocracking are based on a monomolecular mechanism. In the so-called bimolecular mechanism [26-28], an alkene is protonated by the Brønsted acid and forms a dimer with another olefinic hydrocarbon (Figure 3). This oligomerization process may continue and depending on the position of the double bond and the positively charged carbon on the chain, branched carbocations may be produced. The carbocations may further return a proton to the acid catalyst to form an olefin (which is larger than the starting molecules) or they may crack. The bimolecular mechanism seems more feasible than the protonated cyclopropane formation for hydroisomerization and/or hydrocracking of small hydrocarbons (such as C4) that would require

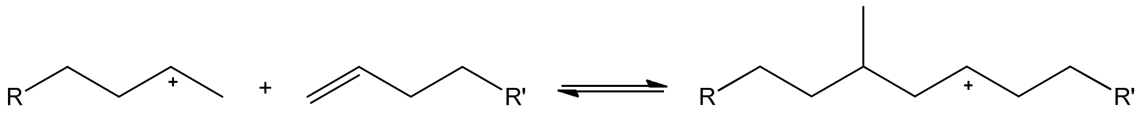

Figure 3. Dimerization of a carbenium ion and an alkene.

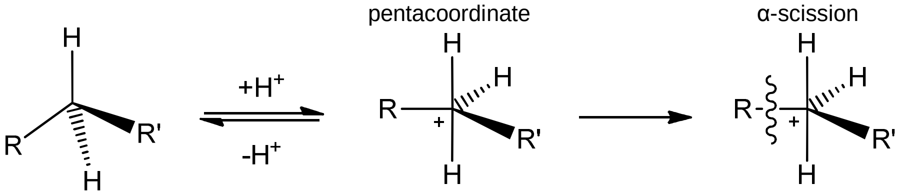

Figure 4. Catalytic cracking by protonation of an alkane to form a pentacoordinated carbocation followed by α-scission (protolysis). Reproduced from reference [2].

primary carbocation intermediates through the latter route [29, 30].

In the absence of a (de)hydrogenation functionality (such as in FCC catalysts), hydrogen is transferred from the hydrocarbon feed to the catalyst surface and distributed over the adsorbed hydrocarbon species. This enriches the H/C ratio of a fraction of components (usually the lighter ones) while reducing that of the others (usually the heavier ones) and thus carbon is rejected in the form of coke on the catalyst surface [31]. In this case, pentacoordinated structures (Figure 4) are formed by direct protonation of the paraffins which can crack in α position of the positively charged carbon (α-scission, protolysis). Once significant concentrations of alkenes are created, cracking through the aforementioned mechanism(s) and β-scission may follow. Products of α-scission include those that require primary carbocation intermediates if to be formed *via* β-scission [32].

Technology selection for FTS product upgrading *via* cracking is based on the following considerations: FTS hydrocarbons are in principle hydrogen rich. Therefore, a carbon rejection strategy such as that in FCC is not essential, although applicable [33, 34]. In addition, the absence of contaminants like sulfur in FTS wax allows cracking under mild conditions and high partial pressures of hydrogen are not necessary (see below), thus hydrogen addition to the process would not become costly. On these grounds, hydrocrackers are the standard units for conversion of LTFT heavy hydrocarbons to liquid fuels [1]. Both process and catalysts involved are designed as such to be selective to the target hydrocarbon range (conventionally to middle distillates) and minimize over-cracking of the desired products. Further, they are optimized for production of branched hydrocarbons to improve the cold flow properties in case of diesel or octane number for gasoline-range hydrocarbons [35].

As compared with the refinery hydrocrackers, these units are operated at much milder conditions in terms of temperature, pressure, and H_2/feed ratio in the case of FTS wax hydrocracking. This is due to the high reactivity of heavy paraffinic molecules in hydrocracking, plus the absence of strong catalyst poisons, such as sulfur and nitrogen containing compounds, in FTS wax. The involved catalysts are typically less acidic as well [36].

A bifunctional FTS catalyst should be capable of catalyzing hydrocracking along with FTS at the process conditions of the latter. Although this is limited to speculation in many related reports, there

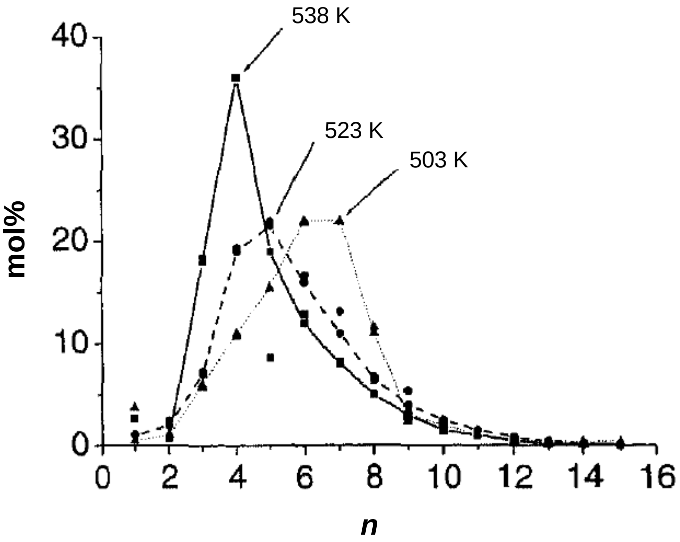

Figure 5. Product distribution of *n*-hexadecane hydrocracking over Pt containing H-ZSM-5 (Si/Al ≈ 16) extrudates (including Al_2O_3 as binder) at different temperatures. In addition to *n*-C16 ($SV_{n\text{-C16}}$ = 0.08–0.1 h^{-1}), the feed included H_2O (SV_{H2O} = 0.25–0.3 h^{-1}) and syngas with the composition N_2:H_2:CO = 50:33:16 ($GHSV_{gas}$ = 3600–3800 l l^{-1}_{cat} h^{-1}). *n*-C16 conversion is 33%, 83%, and 100% at 503 K, 523 K, and 538 K, respectively. [37]

are crystal clear indications that H-ZSM-5 satisfies this objective for the cracking functionality [37-44] (see Figure 5).

In model reactions, Martínez *et al.* [38] showed that *n*-hexadecane conversion drops rapidly from 80% to zero over H-ZSM-5 (Si/Al = 15) in 1 h, regardless of co-feeding H_2. However, a stable conversion level of 80% was measured once the same H-ZSM-5 was physically mixed with equal mass of Co/SiO_2. Since hardly any C1 was found in the reaction products, this stability improvement was attributed to the (de)hydrogenation activity of Co. In fact, reduced (non-sulfided) Co-containing catalysts have been explored for FTS wax hydrocracking elsewhere [45].

A challenge that the hydrocracking component has to deal with under FTS reaction conditions is the presence of CO and H_2O. While the former may disturb the (de)hydrogenation functionality, H_2O affects the acid-catalyzed reactions. Although stable, *n*-C16 conversion over H-ZSM-5 halved upon H_2O addition to the feed stream [38]. The negative effect of CO and H_2O addition on *n*-dodecane hydroconversion was demonstrated over Ni/H-ZSM-5 (Si/Al = 66) extrudates (including Al_2O_3 as binder) [41]. The choice of Ni as the (de)hydrogenation function was on the basis that it is less sensitive than Pt to the presence of CO. An almost 80% *n*-C12 conversion drops to *ca.* 5% at 493 K after CO and H_2O are co-fed in order to simulate an FTS environment. However, the conversion level can be increased to *ca.* 80% by raising the reaction temperature to 533 K. This *n*-C12 conversion was reasonably stable up to 70 h on-stream.

Since unsaturated hydrocarbons (mainly α-olefins) are FTS primary products, they can be protonated directly by the acid catalyst even in absence of a (de)hydrogenation function. This is

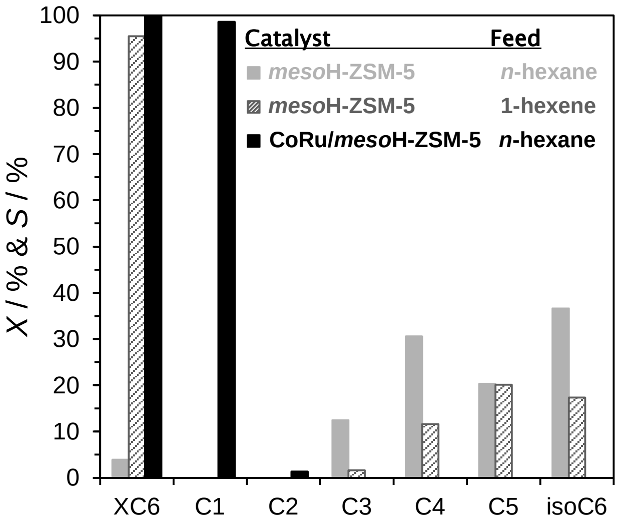

Figure 6. Conversion and product selectivities in C6 hydroconversion over a mesoporous H-ZSM-5 (*meso*H-ZSM-5) and 20 wt% Co-0.3 wt% Ru/*meso*H-ZSM-5. Data were collected after 20 h on-stream at 513 K, 15 bar total pressure, H_2/C6 = 9.0, N_2/H_2 = 2.0, and *SV* = 13 $\text{mol}_{C6}\ \text{kg}^{-1}_{cat}\ \text{h}^{-1}$. Either *n*-hexane or 1-hexene was used, as indicated in the legend. [46] Note that hydrocarbons larger than C6 were also formed over *meso*H-ZSM-5 which were not specified.

confirmed by results obtained in bifunctional reaction systems consisting of a catalyst bed of acid zeolite downstream that of an FTS catalyst bed (see Section 1.4.1). Sartipi *et al.* [47] observed C7–C9 hydrocarbon formation along with C3–C5 during C6 hydroconversion over a mesoporous H-ZSM-5 catalyst at FTS process conditions. This observation points at the importance of the bimolecular mechanism during bifunctional FTS, as also suggested by others [8]. C6 conversion considerably increases from 4 to 96% over mesoporous H-ZSM-5 (Si/Al ≈ 40) by switching the reactant from *n*-hexane to 1-hexene (Figure 6) [46]. Addition of a hydrogenation metal to the acid component in this case enhances the formations of isoparaffins [40, 48, 49].

It is noteworthy that no C1 was observed in the product spectrum of mono-functional H-ZSM-5 catalysts. This result excludes the protolysis mechanism (α-scission) and rules out the acid-catalyzed reactions as origin of methane production during bifunctional FTS. A Co-containing catalyst may produce significant amounts of C1 through hydrocarbon hydrogenolysis (see Figure 6 and Section 1.3.2) while the selectivity to this product is low over Pt-containing hydrocracking catalysts (see Figure 5).

Among zeolites H-ZSM-5 (Si/Al ≈ 16), H-Beta (Si/Al ≈ 13), and H-Y (Si/Al ≈ 3), the first one shows the highest activity in *n*-C6 cracking followed by H-Beta and H-Y. The latter displayed the highest selectivity to C6 isomers [37]. A more recent work [43] demonstrates that only strong acid sites, active for hydrocracking at the operating temperature window of cobalt-based FTS catalysts, give rise to deviations from a conventional ASF product distribution (see also Section 1.4.2).

1.2.2. Other acid-catalyzed reactions of importance under FTS conditions

Besides hydrocracking, an acidic zeolite may catalyze other reactions, including (but not limited to) hydroisomerization, oligomerization, aromatization, alcohol dehydration, *etc.* As explained in Section 1.2.1, hydroisomerization and oligomerization intermediates are already involved in the hydrocracking mechanism. Thus, products of both reactions are expected during bifunctional FTS. Hydrocarbons up to C13 are formed through oligomerization reactions from a mixture of ethene and propene over Pt/H-ZSM-5 and Pt/H-Beta, regardless of syngas addition. The major products are mono-branched hydrocarbons in C5–C9 range while Pt/H-ZSM-5 is more active than Pt/H-Beta [40]. The significant oligomerization activity of H-ZSM-5 reduces the production of lower olefins when this zeolite is added to the FTS catalyst, whereas this effect is less for H-Beta and H-MOR [50] and is not observed for mixtures containing MCM-22, ITQ-2, and ITQ-22 [51]. The C2–C4 range olefin to paraffin ratio decreases with a decrease in Si/Al ratio of H-ZSM-5, when physically mixed with a Fe-based FTS catalyst [52], which further highlights the occurrence of olefin oligomerization over this zeolite in bifunctional FTS.

In principle, zeolites having more acid sites of medium strength show higher isomerization activity, whereas stronger acid sites catalyze cracking [2]. In line with this general statement, mesoporous H-ZSM-5 (Si/Al ≈ 40) was compared with H-ITQ-2 (Si/Al ≈ 40) and mesoporous H-USY (Si/Al ≈ 40) for the effect of their acid strength and density on catalytic performance [43]. While the former shows activity in *n*-C6 hydrocracking, H-ITQ-2, having even a higher density of weaker acid sites, catalyzes only the isomerization reaction and mesoporous H-USY was inactive under the applied process conditions. Both mesoporous H-ZSM-5 and H-ITQ-2 supported Co-catalysts yield a similar ratio of *iso*- to *n*-C4 in FTS, but the former is considerably more selective to the C5–C11 fraction due to cracking of large FTS hydrocarbons, resulting in a non-ASF product distribution (Figure 7). Further comparing the product slate of Co supported on the three above-mentioned zeolites, revealed that hydrocarbon isomerization alone is not enough to lead to non-ASF catalytic behavior [43]. It was concluded that an outstanding isomerization activity might only decrease the chain growth probability (Figure 7), since branched hydrocarbons may not participate in chain propagation as effectively as linear ones.

At low temperatures, hydrocracking catalysts effectively catalyze the hydroisomerization reaction. The extent of hydrocracking relative to hydroisomerization can be tuned by adapting the process conditions, acid strength, and the ratio between metal and acid sites in a catalyst. At temperatures below 523 K, hydroisomerization of 1-octene over Pt/H-ZSM-5 (Si/Al = 32) dominates over hydrocracking in the presence of CO. The contrary holds at higher temperatures and/or in absence of CO [40]. Process temperatures of LTFT favor hydroisomerization and oligomerization rather than

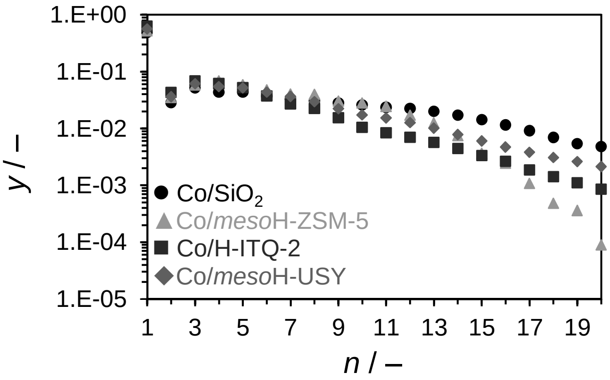

Figure 7. Molar fractional distribution of FTS products after 140 h on-stream at 513 K, 15 bar total pressure, feed composition H_2/CO = 1, and *GHSV* = 12 m^3_{STP} kg^{-1}_{cat} h^{-1}. Co/*meso*H-ZSM-5: mesoporous H-ZSM-5-supported Co; Co/*meso*H-USY: mesoporous H-USY-supported Co. Co loadings are about 20 wt%. [43]

hydrocracking over H-ZSM-5 catalysts. Oligomerization of lower olefins followed by the limited growth of branched hydrocarbons (that are produced by hydroisomerization, oligomerization, and hydrocracking) effectively stops the chain propagation at around C10 while the large hydrocarbons are very reactive to hydrocracking [53]. This may explain why most of the reported bifunctional catalysts, operated at LTFT conditions, are selective towards gasoline-range hydrocarbons rather than the diesel range (which is the desired product of the conventional two-steps LTFT and hydrocracking process).

On the other hand, HTFT conditions are typically associated with low chain growth probabilities and targets gasoline-range hydrocarbons, lower olefins, and oxygenates. Consistent results show that FTS oxygenates are dehydrated by zeolites in bifunctional systems [54-56]. As long as liquid fuels are targeted, HTFT is followed by isomerization and reforming units to improve the octane number of the produced gasoline. Bifunctional catalysts that contain zeolites are reported to produce notable amounts of aromatic compounds [51, 57-59] and olefins, which essentially can improve the octane number. However, a high production of aromatics may result in severe deactivation of the acid catalyst (see Section 1.5). Formation of aromatics may become smaller at lower operating temperatures [46].

1.3. Side reactions at the metal sites

The main function of metal sites with respect to the present application is FTS, *i.e.*, chain propagation (*e.g.*, *via* CO insertion) and hydrogenation. In the current context, FTS performance in combination with acid functionality is included in Section 1.4, while two important side reactions are described in this part.

1.3.1. Hydrogenation

Co^0 is the FTS active phase in Co-based catalysts whereas carbides form over Fe^0 in an early stage of the FTS reaction or during the catalyst activation by means of CO. These carbon containing species are believed to effectively catalyze FTS rather than metallic Fe [60]. In parallel, hydrogenation is anticipated over both Co- and Fe-based catalysts. In addition to saturation of olefinic hydrocarbons, this reaction directly converts CO into methane. Figure 8 shows that, as compared with a Fe-catalyst and in spite of a lower reaction temperature, the methane level is higher than what is anticipated by extrapolating the ASF distribution to $n = 1$ over a Co-catalyst. This is due to the higher hydrogenation activity of Co in comparison with Fe, which makes this side reaction more important over the former. Therefore, Co FTS catalysts are known to be more sensitive than Fe-based catalysts to changes in H_2 concentration and/or process temperature [61, 62].

De Jong *et al.* [63] showed that methane selectivity through CO hydrogenation sharply increases as Co particle size becomes smaller than 6–10 nm, while for larger sizes the reaction is not structure sensitive. The density of lower index surface crystallographic planes or steps and corners increases as particle size decreases [64]. The higher methane selectivity of small particles is mainly brought about by their higher hydrogen coverage [65] and the high activity of low coordination sites, residing at corners and edges [66].

As compared with conventional catalysts, more heterogeneous Co sites are found when supported on a zeolite *via* impregnation [44, 46]. For example, infrared (IR) spectra of pre-adsorbed CO (Figure 9) shows that low frequency bands at 1988–2020 cm^{-1} are clearly detected over an H-ZSM-5-suppored

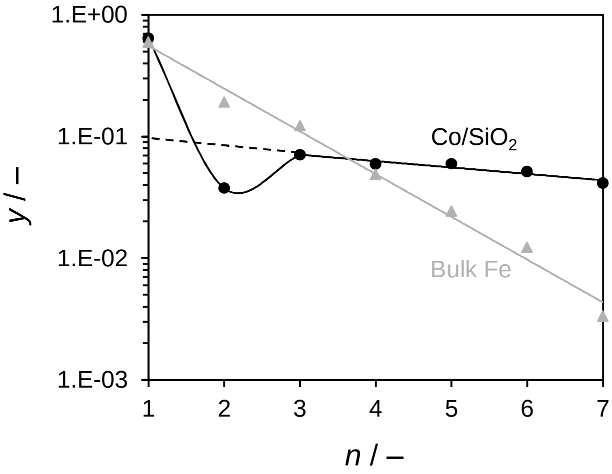

Figure 8. Molar fractional distribution of FTS products over 20 wt% Co/SiO_2 and a bulk Fe-catalyst after 5 h on-stream. Experiments were performed at 15 bar total pressure, feed composition $H_2/CO = 1$, 513 K and 523 K for Co/SiO_2 and bulk Fe, respectively, $GHSV$ / m^3_{STP} kg^{-1}_{cat} h^{-1} = 12 and 24 for Co/SiO_2 and bulk Fe, respectively.

Co while these bands are less pronounced over Co/SiO_2. Such IR bands are assigned to linearly adsorbed CO on Co^0 centers of lower coordination that are more located on open low-index surface crystallographic planes or steps and corners [67-69]. Therefore, direct CO hydrogenation ($CO + 3H_2 \rightarrow CH_4 + H_2O$) partly explains the relatively high methane production over zeolite-supported Co-catalysts (even in absence of Brønsted acidity) and can be rationalized on the basis of the strong metal-support interaction on the structured aluminosilicate [44, 46].

Due to their lower intrinsic activity, relatively high reaction temperatures are employed for Fe-base catalysts even in LTFT applications. Higher reaction temperatures will lead to a decrease in FTS chain growth probability and thus higher production of methane through FTS. In spite of this, the C1 selectivity is almost similar over both SiO_2 and zeolite-supported Fe-catalysts [70]. In some occasions,

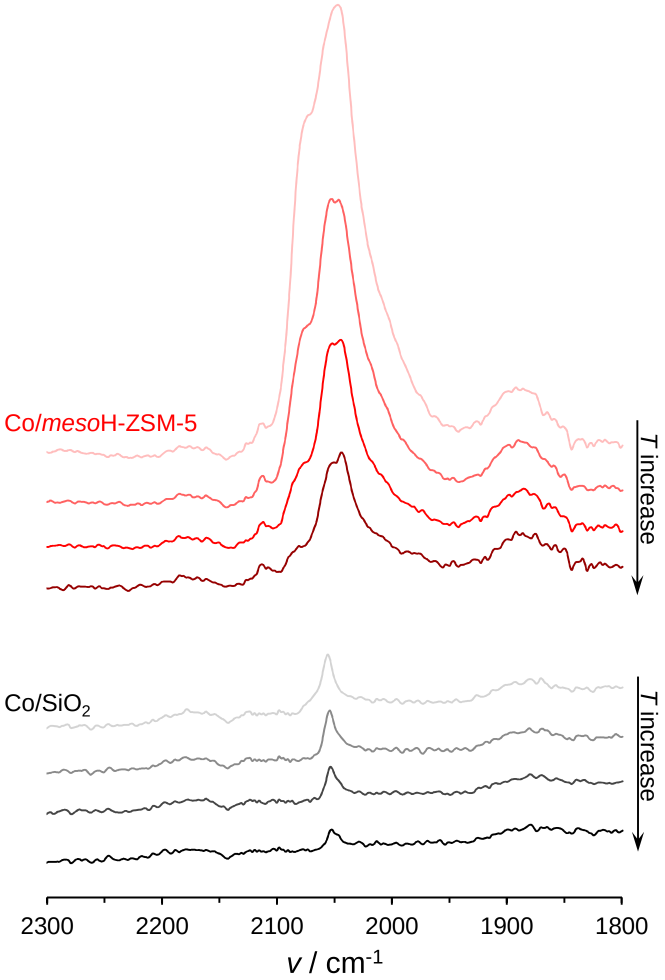

Figure 9. IR spectra of pre-adsorbed CO on Co/SiO_2 (bottom data set) and mesoporous H-ZSM-5-supported Co (Co/*meso*H-ZSM-5, top data set). In each data set, the temperature is increased in a DRIFTS cell to 373, 423, 473, and 513 K, respectively, according to the arrows. Co loadings are about 10 wt%.

it is claimed that H-ZSM-5 would even enhance the formation of the active carbide phase and improve the catalyst performance [71].

1.3.2. Hydrogenolysis

Other than hydrogenation, a hydrocarbon may undergo many types of reactions over metals, namely hydrogenolysis, isomerization, dehydrocyclization, and aromatization [72]. Except for hydrogenolysis, most of these reactions do not occur in the FTS reaction environment as evidenced by negligible presence of branched, cyclic, and aromatic hydrocarbons in conventional FTS products. It should be noted that in bifunctional catalysts, some of the above-mentioned reactions become important over acid sites, as already discussed in Section 1.2.

Hydrogenolysis is an exothermal reaction, catalyzed by group VIII metals (including Ru, Co, Fe, and Ni). This reaction proceeds *via* formation of adsorbed hydrocarbon radicals as reaction intermediates followed by C–C scission. In contrast to hydrocracking, the adsorbed radical intermediate mechanism results in low isomerization activity and therefore unbranched products [45].

Different mechanisms have been proposed for hydrogenolysis of saturated hydrocarbons. In all cases the reaction is initiated by dehydrogenative chemisorption of the hydrocarbon [73, 74]. As first example, ethane hydrogenolysis proceeds *via* 1,2-adsorbed intermediates followed by a series of elementary steps that lead to formation of hydrogen deficient surface species [75].

$$C_2H_6 \rightleftarrows C_2H_5(ads) + H(ads) \rightleftarrows C_2H_x(ads) + a\ H_2\ (a = (6 - x) / 2) \tag{1}$$

$$C_2H_x(ads) + H_2 \longrightarrow \text{adsorbed C1 fragments} \xrightarrow{H_2} CH_4 \tag{2}$$

C–C scission results from the reaction between the adsorbed intermediate and H_2, being the rate determining step [73]. As the ratio of dehydrogenation-to-hydrogenolysis activity of a metal increases, lower x values (reaction (1)) are expected. Thus, values of 4 and 2 are reported for Co and Ni, respectively [76]. It is noteworthy that H_2 pressure has a strong inverse effect on the reaction rates over most group VIII metals except for Fe and Re. This has been explained by a decrease in the concentration of C_2H_x(ads) with increasing H_2 pressure [73]. The specific activity of group VIII metals for ethane hydrogenolysis follows the following order [77]: Os > **Ru** > **Ni** > Rh > Ir > Re > **Co** > **Fe** > Cu > Pt ≈ Pd, while for propane Co shows a higher activity than Ni [78].

The rate of hydrogenolysis increases with the carbon number of alkanes which is attributed to lower average dissociation energies of C–C bonds in larger molecules [79]. As an example, *n*-heptane hydrogenolysis is several orders of magnitude faster than that of ethane at 478 K [76].

Alternatively, Anderson and Avery proposed 1,3-adsorbed intermediates for isomerization and hydrogenolysis of simple aliphatic hydrocarbons larger than C2. In this scheme, one carbon atom is doubly bonded to a surface metal atom (Figure 10) [80]. If the C–metal double bond is located

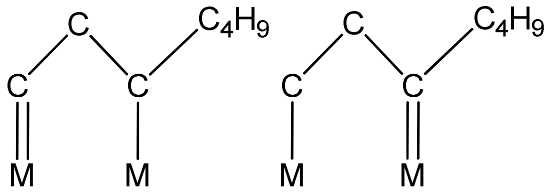

Figure 10. Structure of adsorbed *n*-heptane intermediates formed on metals. [79]

primarily at the terminal C atom, and assuming that the C–C bond adjacent to the C–metal double bond cracks preferentially, then methane will be the main product of hydrogenolysis.

The distribution of primary hydrogenolysis products depends on the metal. On Ni, the reaction scheme involves successive demethylation at terminal C–C bonds of the hydrocarbon chain which lead to formation of C1 fragments that are hydrogenated to form methane [45, 81]. This scheme also applies reasonably well to Co, but not to Fe [81]. This explains the significant amounts of C1 and C2, reported over hydrocracking catalysts that contain Ni or Co as the (de)hydrogenation function [35].

In contrast, a nonselective rupture of different C–C bonds is reported over Pt-containing catalysts. For *n*-heptane, hydrogenolysis was the predominant reaction on all the metals of group VIII except Pt, on which extensive isomerization and dehydrocyclization were also observed [82]. The lower hydrogenolysis activity of noble metals, as compared with very active hydrogenation metals such as Ni, makes them the preferred choice for (de)hydrogenation functionality when employed in hydrocracking and hydroisomerization catalysts.

Some reports speculate that hydrogenolysis may add to methane production over bifunctional FTS catalysts [8, 44, 77]. Related literature on this aspect is not clear and even controversial in some occasions. *n*-hexadecane hardly showed any conversion over Co/SiO_2 at 523 K (H_2/*n*-C16 = 2.9, N_2/*n*-C16 = 4.4) [38]. In another work however, *ca.* 25% *n*-hexane conversion is reported over Co/SiO_2 at 493 K where C1 was dominantly produced (H_2/*n*-C6 = 9.0, N_2/*n*-C6 = 2.0) [44]. Under similar conditions, Co/H-ZSM-5 was more than 50% selective towards methane while no C1 was detected over H-ZSM-5. The *n*-C6 conversion over Co/H-ZSM-5 and H-ZSM-5 was 94 and 13%, respectively [44]. Accordingly, zeolite-supported Co-catalysts that contain a large fraction of coordinatively unsaturated Co sites are more active than Co/SiO_2 in *n*-C6 hydrogenolysis [44, 46]. This reaction is known to be structure sensitive and *TOF*s often vary with particle size. Nevertheless, there is no consistency in literature on the type of such dependence [83]. In any case due to competitive CO adsorption under FTS reaction conditions, hydrogenolysis is not expected to occur to such an extent as in absence of CO. Including propane in a syngas feed did not significantly change the methane selectivity, and ethylene and propylene addition even reduced this value [77], probably due to reinsertion and scavenging of C1 surface species. Further investigations, *e.g.*, *via* labeling the reactant molecules, are required in order to (completely) unveil the extent of hydrocarbon hydrogenolysis as side reaction during FTS.

1.4. Zeolite-containing FTS systems

From the perspective of Catalysis Engineering [84], three different process levels can be distinguished in bifunctional FTS catalysts based on the state and extent of the contact between the acidic and FTS function: the reactor level, the catalyst particle level and the catalyst active phase level. These three levels are thoroughly discussed in this Section.

1.4.1. Reactor level

Two different configurations can be distinguished in literature for combination of zeolites and FTS metals (Co and Fe) at the reactor level: separate or dual layer beds, containing the zeolite downstream of the FTS catalyst (denoted as ‘2BED’), and single mixed beds containing a homogeneous physical mixture of the two catalysts (denoted as ‘1BED’) (Figure 11). Both catalyst beds can be operated at a similar temperature, which is in the limit of either LTFT or HTFT conditions. Applications with a higher temperature at the zeolite bed region, closer to that of hydrocrackers, or even dual reactor systems have also been reported [85, 86]. Such layouts resemble the two steps processes (such as in the Shell SMDS [1]) and are not discussed in this context. 1BED systems may be considered as at the border between the reactor and catalyst particle levels and their related discussions are divided between Sections 1.4.1 and 1.4.2.

Both Fe- and Co-based FTS have been studied in the two above-mentioned configurations (2BED and 1BED). Severe alkali migration from the alkali-promoted Fe-containing catalysts to H-ZSM-5 is reported for 1BED during the course of reaction [57, 59]. As the result, a decline in FTS activity [59] and a considerable selectivity shift towards lower value light paraffins (including C1) [57] make the 1BED configuration less attractive than the 2BED. In contrast, higher CO conversions and C5–C11 selectivity were obtained in 1BED when a La-promoted Fe was studied [55].

The improved performance of 1BED over 2BED systems in terms of increased selectivities to gasoline-range hydrocarbons is in line with results reported for Co-based catalysts [40, 41, 54]. Schaub *et al.* [40, 41] reveal that under the applied process conditions, the C10–C20 molar fraction may be larger in the 2BED configuration than in the 1BED, while both systems represent similar fractions of liquid hydrocarbons (C5–C20) [40]. In any case, the 1BED operation leads to more branched hydrocarbons [40, 41, 54], pointing to an enhanced contribution of acid-catalyzed reactions in the latter.

Many reports indicate that the C1 selectivity increases as the bed configuration changes from 2BED

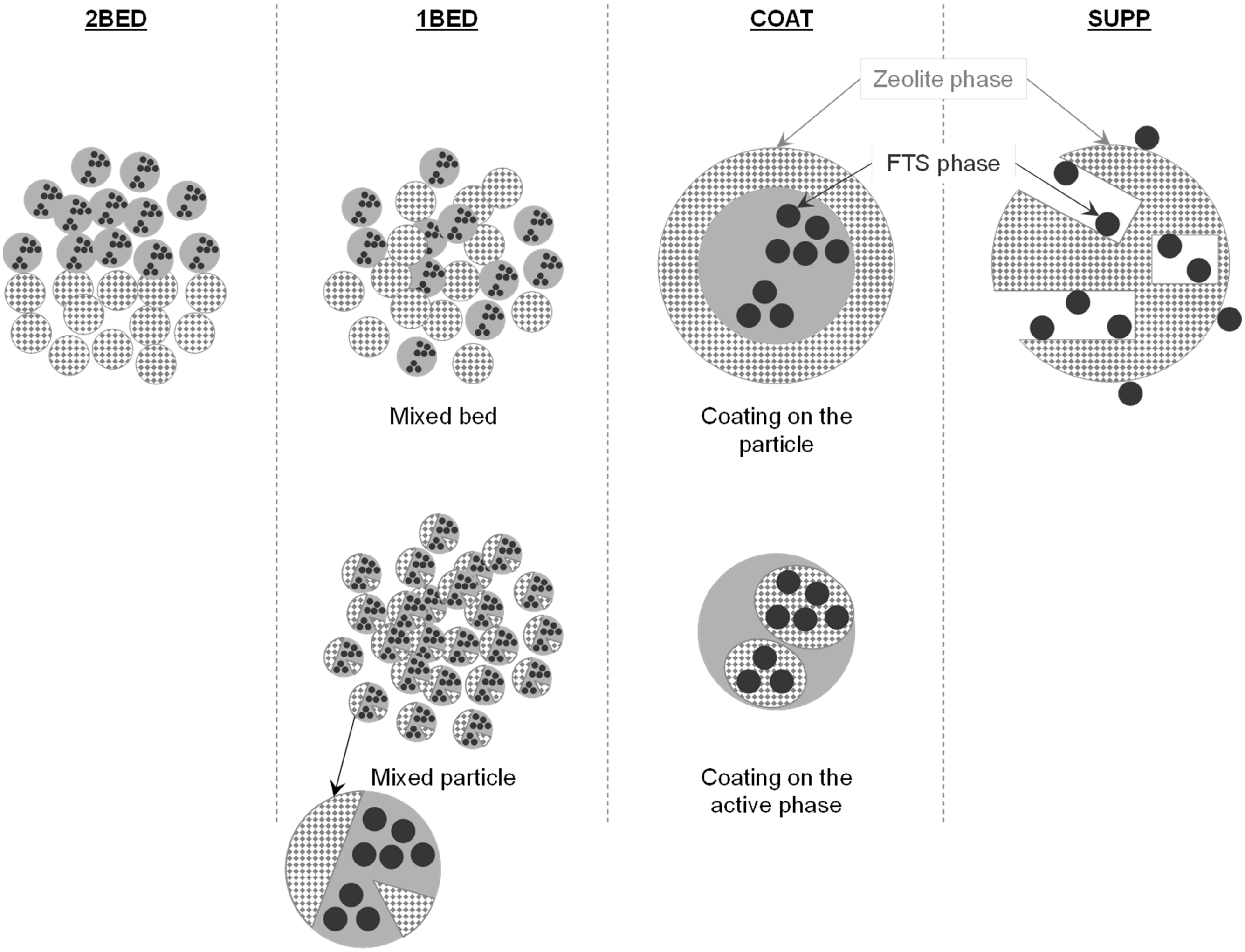

Figure 11. Schematic representation of different configurations that zeolite and FTS phases may have with respect to one another in bifunctional systems. From left to right: separate or dual layer beds, containing the zeolite downstream the FTS catalyst (2BED), single mixed bed containing a homogeneous physical mixture of the zeolite and FTS catalyst particles (1BED), coating layer of the zeolite over FTS catalyst (COAT), and FTS active phase supported on the zeolite (SUPP).

to 1BED [8, 40, 41, 55, 77] and various reasons, including acid cracking, hydrocarbon hydrogenolysis, heat effects, *etc.* are hypothesized as possible origins. FTS is highly exothermic and heat effects are typically eliminated by diluting the catalyst bed with an inert and/or recycle of liquid product. However, some acid zeolite catalyzed reactions, including hydrocracking, as well as possible hydrocarbon hydrogenolysis over metal sites are also exothermic and may add to the produced heat. The C1 selectivity was reduced by half upon adding an inert solid to a physical mixture of Co/SiO_2 and H-ZSM-5 while it did not change in absence of the zeolite. Furthermore, less aromatics were detected in the liquid products after dilution [77]. These results indicate that heat effects are even more important in bifunctional systems, especially in 1BED configuration. In more recent works, zeolites H-USY, H-Beta, H-MOR, and H-ZSM-5 that were mixed with Co/SiO_2 and diluted with SiC in a 1BED configuration, did not lead to additional C1 at all [38, 87]. This observation suggests that reactions over the acid zeolites do not produce additional methane.

1.4.2. Catalyst particle and active phase levels

1BED systems may also consist of catalyst particles that are homogeneous mixtures of zeolite and FTS phases (Figure 11). A closer contact (than that in the 1BED configuration) between the FTS and zeolite functionalities is possible if a coating layer of the latter is put over the FTS active phase [88-90] (denoted as 'COAT'). As schematically shown in Figure 11, the zeolite layer may coat the catalyst particle (*i.e.*, coating of µm sized particles) or the FTS metal agglomerates (*i.e.*, coating of nm sized particles). The contact can be further maximized by dispersing the FTS metal particles in a zeolitic support [42, 47, 89, 91] (denoted as 'SUPP').

For Fe-based catalysts it is shown that SUPP [92] and COAT [71, 93] systems are more selective than 1BED to the C5–C11 fraction. Accordingly, an intimate contact between the two components is a key to the bifunctional performance of these hybrid catalysts. A systematic study on Co-catalysts revealed that upon changing the system configuration from 1BED to COAT and further to SUPP (Figure 11), deviations from a classical ASF product distribution become more pronounced (Figure 12) [89]. This practical observation is an evidence of the above statement about the necessity of the close proximity of the two types of active sites.

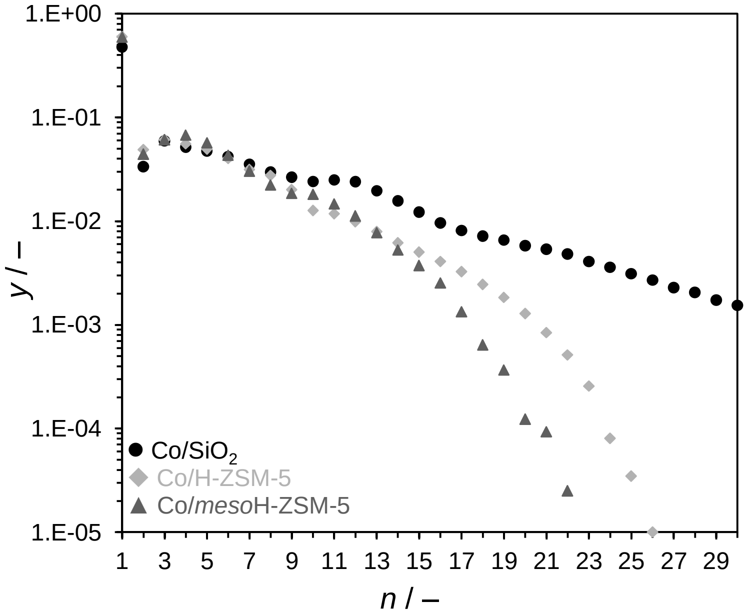

Figure 12. Fractional molar distribution of FTS products after 20 h on-stream at 513 K, 15 bar total pressure, feed composition $H_2/CO = 2$, and *GHSV* = 2.4 $m^3_{STP}\ kg^{-1}_{cat}\ h^{-1}$. Co/*meso*H-ZSM-5: mesoporous H-ZSM-5-supported Co. Co loadings are about 10 wt%. [89]

The COAT configuration concept may be termed 'core-shell' as described by Tsubaki *et al.* [94, 95] for FTS reaction in analogy to earlier works for other reactions [96, 97]. In an ideal core-shell scenario, a defect free reactive zeolite membrane should cover a core of FTS catalyst. A critical review of the relatively large number of reports on this topic [49, 71, 88, 90, 93-95, 98-110], points to the challenge of making and characterizing such catalytic membrane reactor on the level of catalyst particles (*i.e.*, coating of µm sized particles) *via* the hydrothermal synthesis approach [89]: Exposing a Co/SiO_2 core to a hydrothermal environment in the presence of zeolite structure directing agent, brings about partial transformation of the SiO_2 into zeolite where Co agglomerates are enwrapped (*i.e.*, coating of nm sized particles). In other words, the supported Co-catalyst functions as a synthesis precursor during the hydrothermal approach rather than as an ideal catalyst core [88]. Regardless of the necessity for in depth characterization, good selectivity data to gasoline-range hydrocarbons and/or isoparaffins are reported for both Fe- and Co-based COAT systems [71, 98, 105] along with too high C1 selectivity. At the same time, Co-based coated catalysts exhibit lower CO conversion levels than the conventional base catalysts [88, 89, 94, 95, 98-110] due to mass transport limitations [89]. Unfortunately, the majority of the FTS reactions catalyzed by coated catalysts are reported at very high conversion levels of the limiting reactants (*e.g.*, > 90% CO conversion at H_2/CO ratio of 2 [49, 90, 93]) which is not desired for activity evaluations [111]. Since FTS catalysts in general are not highly productive, a loss in activity should be considered as a significant obstacle for practical applications. One report claims that an intimate contact with H-ZSM-5 promotes the formation of an active carbide phase in Fe-containing catalysts and hence, enhances the catalyst activity [71]: The authors report a 90% CO conversion for H-ZSM-5-coated Fe-catalyst after *ca.* 150 h on-stream which is *ca.* 30% higher than that over the uncoated sample. However, since this reaction was performed at H_2/CO ratio of 1 (which is half of the stoichiometric value of 2), products associated with *ca.* 15% of the converted CO are not clearly stated (olefin/paraffin ratio of 0.9 and 17% carbon selectivity to CO_2 are reported).

Alternatively, the cooperative action of FTS and acid sites can be enhanced by employing the acidic zeolite as FTS catalyst support (SUPP, Figure 11). However, such an application is restricted by the limited external surface area of zeolites. Dispersion of metals in the zeolite micropores reduces their FTS activity and selectivity for the following reasons: (*i*) due to stronger metal-support interactions, metal reducibility decreases considerably inside the zeolite structure [46, 112], (*ii*) even on inert carriers, it is well-known that Co particles smaller than 6–10 nm in size are not optimal for FTS (Section 1.3.1) [63, 65], and (*iii*) mass transport limitations in the very narrow zeolite micropores may severely alter the local H_2/CO ratio with respect to that in the bulk and also lead to over-exposure of the hydrocarbon products to acid sites [42, 47]. To address these drawbacks mesopores were created in crystallites of different zeolites *via* desilication [113] and the resulting hierarchical zeolites were employed as support for Co [43, 44, 46, 47, 89] and Ru [42, 91]. For 3 wt% Ru-catalysts supported on ZSM-5 and Beta, product selectivity correlates with the extent of support mesoporosity: Upon increasing the NaOH concentration (employed desilicating agent) and thus creating more mesoporosity, the selectivity to methane decreases (over the prospect catalyst) while that to gasoline-range hydrocarbons increases [42, 91]. This has been attributed to reduced diffusion limitations, which eliminate the over-exposure of the FTS hydrocarbons to strong acid sites and keep the local H_2/CO ratio inside the catalyst particle closer to bulk conditions [42, 47]. Nevertheless, very high concentrations of NaOH results in excessive zeolite amorphization and lowers the C5–C11 selectivity by reducing the acid-catalyzed reaction. Therefore, synthesis optimization of mesoporous zeolites should be realized specifically for FTS catalyst applications. In a series of reports by Sartipi *et al.* [43, 44, 46, 47, 89], synthesis optimization of mesoporous H-ZSM-5 (denoted as '*meso*H-ZSM-5') involved demetalation *via* subsequent base and acid treatments. NaOH (alkaline) and tetrapropylammonium hydroxide (TPAOH, organic) bases were employed as desilicating agents. Under similar treatment conditions, NaOH results in a more severe desilication than TPAOH [47], creating mesostructures with pore sizes and volumes very similar to the amorphous SiO_2 reference support [44, 47]. A more controlled desilication with TPAOH gives rise to more mesoporosity suggesting a higher degree of hierarchy with large cavities communicated with smaller mesopores [46, 47]. Further, TPAOH is preferred over NaOH, since Na^+ is a well-known poison for Co-based FTS catalysts and trace amounts results in a lower FTS activity as compared with the organic treated samples [47].

The consecutive acid treatment (with HNO_3) removes the produced extraframework aluminum, caused by zeolite desilication, and boosts the FTS activity. Moreover, the acid treatment increases the Brønsted acidity of *meso*H-ZSM-5 [44].

The large mesopore surface area of *meso*H-ZSM-5 improves the metal dispersion at elevated Co loadings. The Co/*meso*H-ZSM-5 catalyst is much more active than Co/H-ZSM-5 and the conventional Co/SiO_2 [44, 89]. Moreover, the time-on-stream stability of Co/*meso*H-ZSM-5 and Co/SiO_2 is comparable, in terms of CO conversion, during 140 h [43, 46] (insert in Figure 13a). The high selectivity to liquid hydrocarbons over H-ZSM-5-supported catalysts is visible as a cutoff in the molar distribution above C11 in terms of the ASF distribution of conventional catalysts (*e.g.*, Co/SiO_2, Figure 7 and 12). Measurements after 140 h on-stream shows that Co/*meso*H-ZSM-5 is *ca.* three times more selective than Co/SiO_2 towards C5–C11 cut, producing a large fraction of unsaturated hydrocarbons, other than α-olefins. Moreover, wax production is considerably suppressed over the zeolite-containing catalyst [46] (Figure 13).

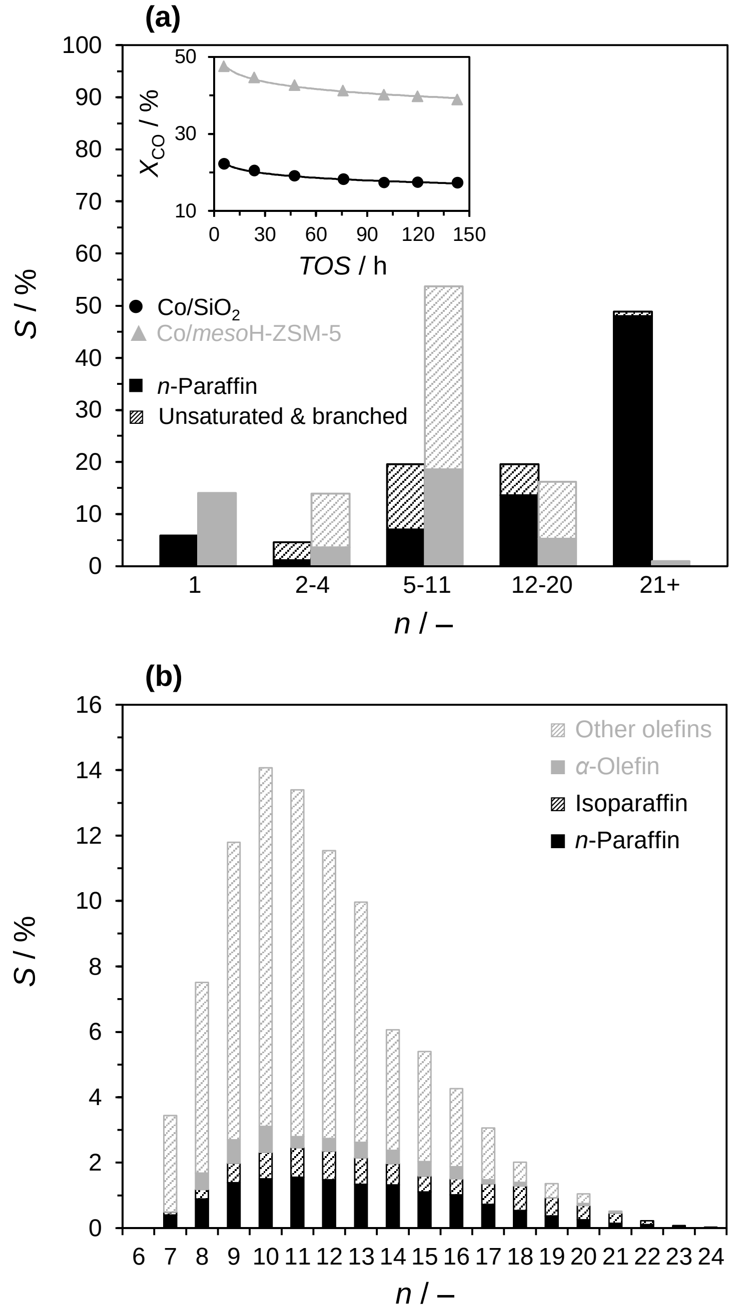

Figure 13. (a) Carbon selectivity of FTS products after 140 h on-stream. In each carbon number group from left to right: Co/SiO$_2$ and Co/*meso*H-ZSM-5. ■: *n*-paraffins; ▨: sum of isoparaffins and olefins. Insert shows the time-on-stream (*TOS*) evolution of the CO conversion. (b) Selectivity distribution of liquid hydrocarbons, produced over Co/*meso*H-ZSM-5 as collected after 140 h on-stream. FTS experiments were performed at 513 K, 15 bar total pressure, feed composition H_2/CO = 1, and *GHSV* = 12 m^3_{STP} kg^{-1}_{cat} h^{-1}. Co loadings are about 20 wt%. [46]

1.5. Stability of zeolites in view of bifunctional FTS applications

One of the major concerns regarding industrial applications of zeolite-containing bifunctional catalysts is the stability and lifetime of the acid component with respect to that of the FTS. In this view, coke formation is a main parameter, since deposition of coke would eventually deactivate the acid functionality and, consequently, alter the product selectivity [38]. This parameter correlates with the extent of aromatic formation in the course of reaction. Botes *et al.* [57, 58] compared two H-ZSM-5 zeolites with different Si/Al ratios (15 and 140) when combined with Fe-based catalysts in 1BED and 2BED configurations. Although initially higher, the aromatic fraction produced over the high-acidity zeolite sharply decreased and dropped below that produced over the low-acidity one. Therefore, the low-acidity zeolite showed a more stable behavior and produced a higher fraction of aromatics after 150 h *TOS*. This conclusion on H-ZSM-5 is confirmed by others as well [52, 92]. In general H-ZSM-5 is fairly resistant towards coke formation due to its narrow channel type structure and well distributed acid sites. FTS reaction results confirm that H-ZSM-5-containg 1BED systems are more stable and selective to branched hydrocarbons than mixed catalysts containing other zeolite topologies including MCM-22, ITQ-2, ITQ-22, IM-5, USY, H-Beta, and H-MOR [38, 51, 87]. The lifetime can considerably be improved by decreasing the zeolite crystallite size, allowing a better utilization of the zeolite microporosity, due to shorter diffusion distances. Another approach frequently reported is adding Pd as a (de)hydrogenation function [51, 52, 92].

Up to 250 h on-stream at 553 K, the isomer selectivity drops by less than 25% of its corresponding value at 50 h *TOS* over H-ZSM-5 (Si/Al = 140) [92]. However, the decrease in production of C4 isomers is more than 50% of its initial value after *ca.* 200 h on-stream at 573 K (H-ZSM-5, Si/Al = 25) [56]. FTS rate was relatively stable over the Fe component under these conditions. Reactivation at 573 K in an O_2 containing environment is not sufficient to regenerate the H-ZSM-5 zeolite (Si/Al =14) while the Fe component is totally reactivated after reduction [114]. As expected, coke formation is amplified over the zeolite at HTFT conditions, where the reaction temperatures are higher than 573 K. One the other hand, many reports suggest a more stable performance of the acid function at LTFT conditions [6, 41, 46, 98, 103, 107]. Recently, a 7.5 wt% Co-0.2 wt% Ru-catalyst, supported on alumina bound ZSM-5, is reported to show a stable performance and high selectivity to C5–C20 up to 1500 h on-stream at 493 K [6]. After 140 h on-stream at 513 K, reactivation of Co/*meso*H-ZSM-5 by H_2 at 773 K results in the recovery of the initial *iso-* to *n*-C4 product ratio over this catalyst along with its initial FTS activity [46]. This suggests that H-ZSM-5 framework does not collapse under LTFT conditions, although lowered intensity of MFI diffraction patterns are reported for spent catalysts as compared with the fresh ones [50].

1.6. Conclusions

The combination of zeolites with an active FTS phase increases the product selectivity towards liquid hydrocarbons. This approach offers a great potential for intensified and direct production of synthetic fuels from syngas. Among different zeolite topologies, the most promising results are obtained with H-ZSM-5. The main advantages of the use of this zeolite in combination with FTS functionalities are: (*i*) it is one of the few zeolites industrially produced and applied for acid-catalyzed hydrocarbon conversion reactions, (*ii*) it has a (relatively) stable catalytic performance, especially at LTFT process conditions, and (*iii*) besides acid-catalyzed cracking, it has a fair isomerization and oligomerization activity at low temperatures. The latter oligomerization initiates the hydrocracking reaction *via* a bimolecular mechanism, since olefins are primary FTS products.

Although HTFT conditions are, in principle, more compatible with hydrocracking and other acid-catalyzed reactions than LTFT conditions, acid sites deactivate relatively fast due to coke formation during HTFT. Therefore, such an integration of different functions seems to be more feasible at LTFT conditions, making Co the desired FTS phase.

In most literature examples, the combination of Co based FTS catalyst and zeolitic acidity results in high selectivities towards gasoline range hydrocarbons. This is mostly due to the type and mechanisms of acid-catalyzed reactions over zeolites in bifunctional systems (Fig. 14). While oligomerization decreases the amount of lower olefins, cracking of the reactive large hydrocarbons breaks the conventional ASF product selectivity at higher carbon numbers. Both reactions will produce branched hydrocarbons. Small branched hydrocarbons do not participate in the FTS chain propagation effectively and, at the same time, larger hydrocarbons will be get trapped in the narrow zeolite channels (such as those of H-ZSM-5) where they undergo excessive isomerization and cracking. In this sense, the use of larger pore zeolites, acidic enough as to display cracking activity under FTS conditions, would be ideal for the production of longer hydrocarbons, in the diesel fuel range.

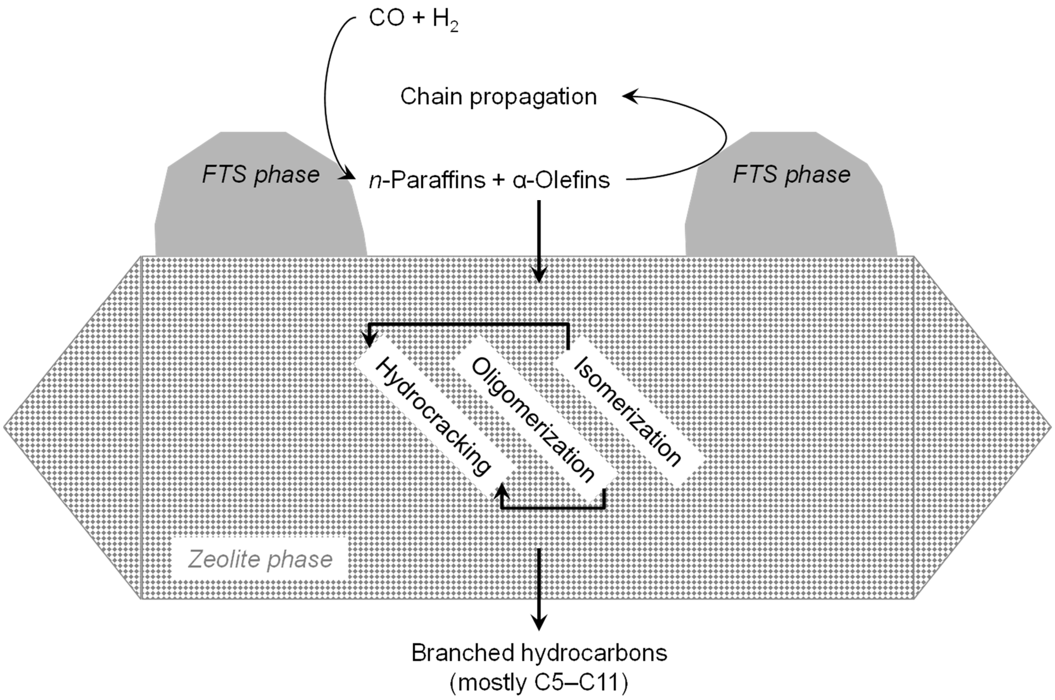

Figure 14. Schematic representation of reactions involved in zeolite-containing FTS catalysts.

A crucial factor affecting the product selectivity of bifunctional catalysts is the proximity between acid and FTS components. The closer the sites the more olefinic products reach acid sites before undergoing hydrogenation. This fact makes zeolite-supported Co-catalysts the best performing ones among the different options in terms of active site proximity. However, in spite of these advantages, a number of drawbacks need to be addressed in order to make the direct synthesis of liquid hydrocarbons from syngas more attractive, namely:

- The high selectivity towards methane derived from the strong interactions between the FTS phase and the zeolite. This is a great catalyst synthesis challenge related to the state of the FTS metal particles, since reducibility, size, interactions with the zeolite, coordination of metal atoms, *etc.* directly affects the FTS chain growth. In many occasions, approaches including hydrothermal synthesis to form a zeolite coating around the metal (agglomerates) or impregnation of the FTS functionality with zeolitic supports, led to lower chain growth probabilities and/or promotion of side reactions (*e.g.*, CO hydrogenation and hydrocarbon hydrogenolysis).

The long-term stability of these catalysts has been largely unexplored. Future works should certainly address this point and demonstrate that the lifetime of the zeolite containing catalysts is comparable to that of other FTS catalysts.

References

[1] S.T. Sie, M.M.G. Senden, H.M.H. Van Wechem, Catal. Today 8 (1991) 371-394.
[2] A. de Klerk, E. Furimsky, Catalysis in the Refining of Fischer-Tropsch Syncrude, RSCPublishing, Cambridge, UK, 2010.
[3] M.J.A. Tijmensen, A.P.C. Faaij, C.N. Hamelinck, M.R.M. Van Hardeveld, Biomass Bioenerg. 23 (2002) 129-152.
[4] http://www.compactgtl.com/.
[5] http://www.velocys.com/.
[6] C. Kibby, K. Jothimurugesan, T. Das, H.S. Lacheen, T. Rea, R.J. Saxton, Catal. Today 215 (2013) 131-141.
[7] V.U.S. Rao, R.J. Gormley, A. Shamsi, T.R. Petrick, J.M. Stencel, R.R. Schehl, R.D.H. Chi, R.T. Obermyer, J. Mol. Catal. 29 (1985) 271-283.
[8] V. Udaya, S. Rao, R.J. Gormley, Catal. Today 6 (1990) 207-234.
[9] C.A. Chanenchuk, I.C. Yates, C.N. Satterfield, Energy Fuels 5 (1991) 847-855.
[10] D. Vervloet, F. Kapteijn, J. Nijenhuis, J.R. van Ommen, Catal. Sci. Technol. 2 (2012) 1221-1233.
[11] O.O. James, A.M. Mesubi, T.C. Ako, S. Maity, Fuel Process. Technol. 91 (2010) 136-144.
[12] C. Zeng, J. Sun, G. Yang, I. Ooki, K. Hayashi, Y. Yoneyama, A. Taguchi, T. Abe, N. Tsubaki, Fuel 112 (2013) 140-144.
[13] M.E. Dry, Catal. Today 71 (2002) 227-241.
[14] A.Y. Khodakov, W. Chu, P. Fongarland, Chem. Rev. 107 (2007) 1692-1744.
[15] A. Martínez, G. Prieto, Top. Catal. 52 (2009) 75-90.
[16] Q. Zhang, J. Kang, Y. Wang, ChemCatChem 2 (2010) 1030-1058.
[17] S. Abelló, D. Montané, ChemSusChem 4 (2011) 1538-1556.

[18] E.F. Sousa-Aguiar, F.B. Noronha, A. Faro, Catal. Sci. Technol. 1 (2011) 698-713.

[19] B. Sun, M. Qiao, K. Fan, J. Ulrich, F.F. Tao, ChemCatChem 3 (2011) 542-550.

[20] Q. Zhang, K. Cheng, J. Kang, W. Deng, Y. Wang, ChemSusChem, In Press (2014).

[21] M. Rigutto, Cracking and Hydrocracking, in: J. Čejka, A. Corma, S. Zones (Eds.) Zeolites and Catalysis: Synthesis, Reactions and Applications, WILEY-VCH Verlag GmbH & Co. KGaA, Weinheim, 2010, pp. 547-584.

[22] J.D. Roberts, C.C. Lee, W.H. Saunders Jr, J. Am. Chem. Soc. 76 (1954) 4501-4510.

[23] S.T. Sie, Ind. Eng. Chem. Res. 31 (1992) 1881-1889.

[24] J. Weitkamp, P.A. Jacobs, J.A. Martens, Appl. Catal. 8 (1983) 123-141.

[25] A. Soualah, J.L. Lemberton, L. Pinard, M. Chater, P. Magnoux, K. Moljord, Appl. Catal. A-Gen. 336 (2008) 23-28.

[26] M.J.G. Janssen, W.J. Mortier, C.W.M. van Oorschot, M. Makkee, Process for catalytic conversion of olefins, 1991, WO 91/18851.

[27] G.D. Pirngruber, O.P.E. Zinck-Stagno, K. Seshan, J.A. Lercher, J. Catal. 190 (2000) 374-386.

[28] F. Bauer, E. Bilz, W.H. Chen, A. Freyer, V. Sauerland, S.B. Liu, Stud. Surf. Sci. Catal. 170 (2007) 1096-1103.

[29] M. Guisnet, P. Andy, N.S. Gnep, E. Benazzi, C. Travers, J. Catal. 158 (1996) 551-560.

[30] P. Meriaudeau, R. Bacaud, L. Ngoc Hung, A.T. Vu, J. Mol. Catal. A-Chem. 110 (1996) L177-L179.

[31] K.A. Cumming, B.W. Wojciechowski, Catal. Rev.-Sci. Eng. 38 (1996) 101-157.

[32] A. Corma, J. Planelles, J. Sánchez-Marín, F. Tomás, J. Catal. 93 (1985) 30-37.

[33] X. Dupain, R.A. Krul, C.J. Schaverien, M. Makkee, J.A. Moulijn, Appl. Catal. B-Environ. 63 (2006) 277-295.

[34] T.V. Malleswara Rao, X. Dupain, M. Makkee, Microporous Mesoporous Mat. 164 (2012) 148-163.

[35] C. Bouchy, G. Hastoy, E. Guillon, J.A. Martens, Oil Gas Sci. Technol. 64 (2009) 91-112.

[36] D. Leckel, Energy Fuels 21 (2007) 1425-1431.

[37] A.V. Abramova, A.A. Panin, G.A. Kliger, E.A. Kulikova, E.V. Slivinsky, Stud. Surf. Sci. Catal. 158 B (2005) 1709-1716.

[38] A. Martínez, J. Rollán, M.A. Arribas, H.S. Cerqueira, A.F. Costa, E.F. S.-Aguiar, J. Catal. 249 (2007) 162-173.

[39] A. Mena Subiranas, G. Schaub, Int. J. Chem. React. Eng. 5 (2007) Article A78.

[40] A. Mena Subiranas, G. Schaub, Int. J. Chem. React. Eng. 7 (2009) Article A31.

[41] A. Freitez, K. Pabst, B. Kraushaar-Czarnetzki, G. Schaub, Ind. Eng. Chem. Res. 50 (2011) 13732-13741.

[42] J. Kang, K. Cheng, L. Zhang, Q. Zhang, J. Ding, W. Hua, Y. Lou, Q. Zhai, Y. Wang, Angew. Chem.-Int. Edit. 50 (2011) 5200-5203.

[43] S. Sartipi, M. Alberts, M.J. Meijerink, T.C. Keller, J. Pérez-Ramírez, J. Gascon, F. Kapteijn, ChemSusChem 6 (2013) 1646-1650.

[44] S. Sartipi, K. Parashar, M.J. Valero-Romero, V.P. Santos, B. van der Linden, M. Makkee, F. Kapteijn, J. Gascon, J. Catal. 305 (2013) 179-190.

[45] W. Böhringer, A. Kotsiopoulos, M. de Boer, C. Knottenbelt, J.C.Q. Fletcher, Stud. Surf. Sci. Catal. 163 (2007) 345-365.

[46] S. Sartipi, M. Alberts, V.P. Santos, M. Nasalevich, J. Gascon, F. Kapteijn, ChemCatChem 6 (2014) 142-151.

[47] S. Sartipi, K. Parashar, M. Makkee, J. Gascon, F. Kapteijn, Catal. Sci. Technol. 3 (2013) 572-575.

[48] N. Tsubaki, Y. Yoneyama, K. Michiki, K. Fujimoto, Catal. Commun. 4 (2003) 108-111.

[49] Y. Jin, R. Yang, Y. Mori, J. Sun, A. Taguchi, Y. Yoneyama, T. Abe, N. Tsubaki, Appl. Catal. A-Gen. 456 (2013) 75-81.

[50] S.H. Kang, J.W. Bae, P.S.S. Prasad, K.W. Jun, Catal. Lett. 125 (2008) 264-270.

[51] A. Martínez, C. López, E. Peris, A. Corma, Stud. Surf. Sci. Catal. 158 B (2005) 1327-1334.

[52] A. Martínez, C. López, Appl. Catal. A-Gen. 294 (2005) 251-259.

[53] J. Wei, Ind. Eng. Chem. Res. 33 (1994) 2467-2472.

[54] K. Jothimurugesan, S.K. Gangwal, Ind. Eng. Chem. Res. 37 (1998) 1181-1188.

[55] A.N. Pour, M. Zare, S.M. Kamali Shahri, Y. Zamani, M.R. Alaei, J. Nat. Gas Sci. Eng. 1 (2009) 183-189.

[56] A.V. Karre, A. Kababji, E.L. Kugler, D.B. Dadyburjor, Catal. Today 214 (2013) 82-89.

[57] F.G. Botes, W. Böhringer, Appl. Catal. A-Gen. 267 (2004) 217-225.

[58] F.G. Botes, Appl. Catal. A-Gen. 284 (2005) 21-29.

[59] A.V. Karre, A. Kababji, E.L. Kugler, D.B. Dadyburjor, Catal. Today 198 (2012) 280-288.

[60] H.M.T. Galvis, J.H. Bitter, C.B. Khare, M. Ruitenbeek, A.I. Dugulan, K.P. de Jong, Science 335 (2012) 835-838.

[61] I.C. Yates, C.N. Satterfield, Energy Fuels 6 (1992) 308-314.

[62] H. Schulz, Stud. Surf. Sci. Catal. 163 (2007) 177-199.

[63] G.L. Bezemer, J.H. Bitter, H.P.C.E. Kuipers, H. Oosterbeek, J.E. Holewijn, X. Xu, F. Kapteijn, A.J. van Dillen, K.P. De Jong, J. Am. Chem. Soc. 128 (2006) 3956-3964.

[64] R. Van Hardeveld, F. Hartog, Surf. Sci. 15 (1969) 189-230.

[65] J.P. Den Breejen, P.B. Radstake, G.L. Bezemer, J.H. Bitter, V. Frøseth, A. Holmen, K.P. De Jong, J. Am. Chem. Soc. 131 (2009) 7197-7203.

[66] H.M. Torres Galvis, J.H. Bitter, T. Davidian, M. Ruitenbeek, A.I. Dugulan, K.P. De Jong, J. Am. Chem. Soc. 134 (2012) 16207-16215.

[67] G. Blyholder, J. Phys. Chem. 68 (1964) 2772-2778.

[68] G. Blyholder, L.D. Neff, J. Phys. Chem. 73 (1969) 3494-3496.

[69] L.E.S. Rygh, C.J. Nielsen, J. Catal. 194 (2000) 401-409.

[70] P. Wang, J. Kang, Q. Zhang, Y. Wang, Catal. Lett. 114 (2007) 178-184.

[71] B. Sun, G. Yu, J. Lin, K. Xu, Y. Pei, S. Yan, M. Qiao, K. Fan, X. Zhang, B. Zong, Catal. Sci. Technol. 2 (2012) 1625-1629.

[72] G. Maire, F. Garin, J. Mol. Catal. 48 (1988) 99-116.

[73] A. Cimino, M. Boudart, H. Taylor, J. Phys. Chem. 58 (1954) 796-800.

[74] J.H. Sinfelt, Catal. Rev.-Sci. Eng. 3 (1970) 175-205.

[75] J.H. Sinfelt, Catal. Lett. 9 (1991) 159-171.

[76] J.H. Sinfelt, Adv. Catal. 23 (1973) 91-119.

[77] R.J. Gormley, V.U.S. Rao, R.R. Anderson, R.R. Schehl, R.D.H. Chi, J. Catal. 113 (1988) 193-205.

[78] C.J. Machiels, R.B. Anderson, J. Catal. 58 (1979) 253-259.

[79] J.L. Carter, J.A. Cusumano, J.H. Sinfelt, J. Catal. 20 (1971) 223-229.

[80] J.R. Anderson, N.R. Avery, J. Catal. 7 (1967) 315-323.

[81] H. Matsumoto, Y. Saito, Y. Yoneda, J. Catal. 19 (1970) 101-112.

[82] Y. Barron, G. Maire, J.M. Muller, F.G. Gault, J. Catal. 5 (1966) 428-445.

[83] V. Ponec, G.C. Bond, Stud. Surf. Sci. Catal. Volume 95 (1995) 247-297.

[84] J.A. Moulijn, J. Perez-Ramirez, A. van Diepen, M.T. Kreutzer, F. Kapteijn, Int. J. Chem. React. Eng. 1 (2003) Review R4.

[85] T.S. Zhao, J. Chang, Y. Yoneyama, N. Tsubaki, Ind. Eng. Chem. Res. 44 (2005) 769-775.

[86] I. Nam, K.M. Cho, J.G. Seo, S. Hwang, K.W. Jun, I.K. Song, Catal. Lett. 130 (2009) 192-197.

[87] A. Martínez, S. Valencia, R. Murciano, H.S. Cerqueira, A.F. Costa, E.F. S.-Aguiar, Appl. Catal. A-Gen. 346 (2008) 117-125.

[88] J.Y. Liu, J.F. Chen, Y. Zhang, Catal. Sci. Technol. 3 (2013) 2559-2564.

[89] S. Sartipi, J. van Dijk, J. Gascon, F. Kapteijn, Appl. Catal. A-Gen. 456 (2013) 11-22.

[90] G. Yang, C. Xing, W. Hirohama, Y. Jin, C. Zeng, Y. Suehiro, T. Wang, Y. Yoneyama, N. Tsubaki, Catal. Today 215 (2013) 29-35.

[91] K. Cheng, J. Kang, S. Huang, Z. You, Q. Zhang, J. Ding, W. Hua, Y. Lou, W. Deng, Y. Wang, ACS Catal. 2 (2012) 441-449.

[92] M. Baranak, B. Gürünlü, A. Sarioğlan, Ö. Ataç, H. Atakül, Catal. Today 207 (2013) 57-64.
[93] J. Bao, G. Yang, C. Okada, Y. Yoneyama, N. Tsubaki, Appl. Catal. A-Gen. 394 (2011) 195-200.
[94] J. He, B. Xu, Y. Yoneyama, N. Nishiyama, N. Tsubaki, Chem. Lett. 34 (2005) 148-149.
[95] J. He, Y. Yoneyama, B. Xu, N. Nishiyama, N. Tsubaki, Langmuir 21 (2005) 1699-1702.
[96] N. Nishiyama, K. Ichioka, D.H. Park, Y. Egashira, K. Ueyama, L. Gora, W. Zhu, F. Kapteijn, J.A. Moulijn, Ind. Eng. Chem. Res. 43 (2004) 1211-1215.
[97] N. Nishiyama, K. Ichioka, M. Miyamoto, Y. Egashira, K. Ueyama, L. Gora, W. Zhu, F. Kapteijn, J.A. Moulijn, Microporous Mesoporous Mat. 83 (2005) 244-250.
[98] J. He, Z. Liu, Y. Yoneyama, N. Nishiyama, N. Tsubaki, Chem.-Eur. J. 12 (2006) 8296-8304.
[99] G. Yang, J. He, Y. Yoneyama, Y. Tan, Y. Han, N. Tsubaki, Appl. Catal. A-Gen. 329 (2007) 99-105.
[100] G. Yang, J. He, Y. Yoneyama, N. Tsubaki, Stud. Surf. Sci. Catal. 167 (2007) 73-78.
[101] J. Bao, J. He, Y. Zhang, Y. Yoneyama, N. Tsubaki, Angew. Chem.-Int. Edit. 47 (2008) 353-356.
[102] G. Yang, J. He, Y. Yoneyama, Y. Tan, Y. Han, N. Tsubaki, Res. Chem. Intermed. 34 (2008) 771-779.
[103] G. Yang, J. He, Y. Zhang, Y. Yoneyama, Y. Tan, Y. Han, T. Vitidsant, N. Tsubaki, Energy Fuels 22 (2008) 1463-1468.
[104] G. Yang, Y. Tan, Y. Han, J. Qiu, N. Tsubaki, Catal. Commun. 9 (2008) 2520-2524.
[105] X. Li, J. He, M. Meng, Y. Yoneyama, N. Tsubaki, J. Catal. 265 (2009) 26-34.
[106] M. Thongkam, G. Yang, T. Vitidsant, N. Tsubaki, J. Jpn. Pet. Inst 52 (2009) 216-217.
[107] X. Huang, B. Hou, J. Wang, D. Li, L. Jia, J. Chen, Y. Sun, Appl. Catal. A-Gen. 408 (2011) 38-46.
[108] N. Jiang, G. Yang, X. Zhang, L. Wang, C. Shi, N. Tsubaki, Catal. Commun. 12 (2011) 951-954.
[109] S.H. Kang, J.H. Ryu, J.H. Kim, I.H. Jang, A.R. Kim, G.Y. Han, J.W. Bae, K.S. Ha, Energy Fuels 26 (2012) 6061-6069.
[110] C. Li, H. Xu, Y. Kido, Y. Yoneyama, Y. Suehiro, N. Tsubaki, ChemSusChem 5 (2012) 862-866.
[111] F. Kapteijn, J.A. Moulijn, Laboratory Catalytic Reactors: Aspects of Catalyst Testing, in: Handbook of Heterogeneous Catalysis, Wiley-VCH Verlag GmbH & Co. KGaA, 2008.
[112] C. Ngamcharussrivichai, A. Imyim, X. Li, K. Fujimoto, Ind. Eng. Chem. Res. 46 (2007) 6883-6890.
[113] S. Mitchell, N.L. Michels, K. Kunze, J. Pérez-Ramírez, Nat. Chem. 4 (2012) 825-831.
[114] A. Nakhaei Pour, M.R. Housaindokht, J. Nat. Gas Sci. Eng. 14 (2013) 49-54.

Chapter 2

Six-flow operations for catalyst development in Fischer-Tropsch synthesis: Bridging the gap between high-throughput experimentation and extensive product evaluation

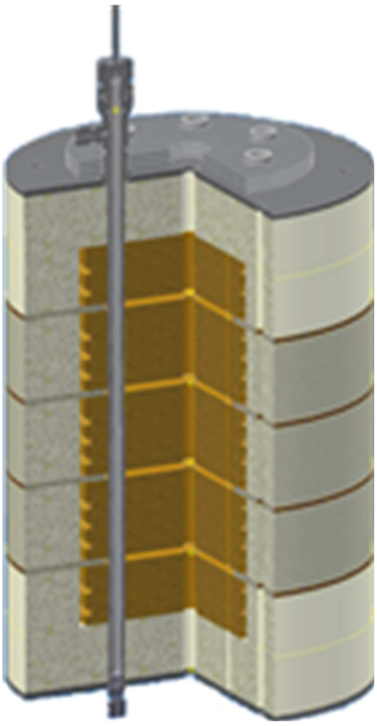

This Chapter is based on the following publication:

S. Sartipi, H. Jansma, D. Bosma, B. Boshuizen, M. Makkee, J. Gascon, F. Kapteijn, Rev. Sci. Instrum. 84 (**2013**) 124101.

Abstract: Design and operation of a ‘six-flow fixed-bed microreactor’ setup for Fischer-Tropsch synthesis (FTS) is described. The unit consists of feed and mixing, flow division, reaction, separation, and analysis sections. The reactor system is made of five heating blocks with individual temperature controllers, assuring an identical isothermal zone of at least 10 cm along six fixed-bed microreactor inserts (4 mm inner diameter). Such a lab-scale setup allows running six experiments in parallel, under equal feed composition, reaction temperature, and conditions of separation and analysis equipment. It permits separate collection of wax and liquid samples (from each flow line), allowing operation with high productivities of C5+ hydrocarbons. The latter is crucial for a complete quantification of FTS product compositions and will represent an advantage over high-throughput setups with more than ten flows where such instrumental considerations lead to elevated equipment volume, cost, and operation complexity. The identical performance (of the six flows) under similar reaction conditions was assured by testing a same catalyst batch, loaded in all microreactors.

2.1. Introduction

The key principle of high-throughput experimentation is parallelization [1-3], an approach to run several tests simultaneously rather than carrying them out one after another [4]. This is a valuable tool to conduct cost efficient research and development. While parallelization of experiments increases the research load without subsequently increasing the development time, small scale testing results in a reduction of materials and feed, ultimately decreasing the total cost per experiment [5].

When it comes to catalyst development, much care has to be taken when parallelizing kinetic experiments to avoid missing valuable information. Increasing catalyst screening throughput may lead to partial or even wrong conclusions, especially in case of complex reactions such as Fischer-Tropsch synthesis (FTS).

FTS is an alternative process for the sustainable production of key chemical building blocks from non-petroleum-based resources such as natural gas, coal, or biomass. The scientific community has devoted a great deal of efforts to FTS-related technologies during the last few decades due to the increasing price of crude oil, the rapid increase of natural gas reserves, and environmental concerns [6].

When liquid fuels such as diesel are aimed, FTS process conditions and catalysts are designed to maximize the so-called chain growth probability (α), *i.e.*, to increase the production of liquid (C5–C20) and wax (C21+) fractions. Long chain hydrocarbons are further hydrocracked to narrow the product distribution to the desired hydrocarbon cut [7, 8].

Since its discovery (almost one century ago), many studies dealing with FTS catalyst development have been published. Nevertheless, hazardous nature of the reactants (H_2 and CO) and on the other hand, complexity of the products (hydrocarbons in a wide range of boiling points, oxygenates, *etc.*) has been an obstacle for relevant catalyst performance evaluations in many occasions. In this respect, advances in laboratory instrumentation, operation atomization, data acquisition and treatment, *etc.* in the last couple of decades have allowed meeting the high demand for accurate and efficient catalyst performance evaluation methods.

In an early course of FTS reaction, the initial chemical and structural properties of a freshly activated catalyst change, resulting in evolution of activity and product selectivity as the reaction proceeds. Catalyst stabilization under reaction conditions may take more than 100 h [9]. On the other hand, long chain hydrocarbons formed over the FTS active phase have to fill the catalyst porosity and liquid reactor effluents will wet the internal surface of the equipment. Depending on the setup volume, its stabilization period might be shorter than that of the catalyst. Yet, sufficient time is required in order to substitute (wash off) the products of a preceding reaction from the tubing and equipment's internal volume by the new effluents. Consequently, experiments related to FTS catalyst evaluation are

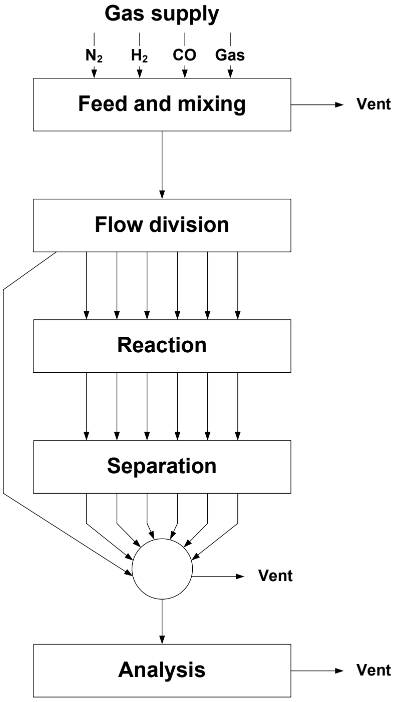

Figure 1. Overall process flow scheme of the six-flow fixed-bed microreactor FTS setup.

time demanding and thus reaction parallelization is highly advantageous. We were among the first research groups that proposed the concept of such high-throughput experimentation, under realistic FTS process conditions [2, 10-12]. To date high-throughput FTS setups with up to 64 parallel reactors are reported and marketed [13].

Although high-throughput experimental setups are very suitable for exploratory screening of catalysts, they are often limited to analysis of the gas phase products [14-16]. Bringing the higher hydrocarbons to the gas phase is to some extent possible by diluting the reactor effluents. However, the separation of such mixture by an online GC will become demanding due to significant differences in the hydrocarbons boiling points. In this contribution, the 'six-flow fixed-bed microreactor Fischer-Tropsch synthesis' setup concept is introduced for lab scale catalyst performance assessments. The detailed equipment design and configuration is reported and linked to operation modes which lead to performing six parallel reactions with an extensive evaluation of the product spectrum. Furthermore, the accuracy of obtained data is assessed and discussed by screening the same catalyst batch in the six reactors (flows).

2.2. Setup configuration

The overall design of the lab-scale unit for FTS reaction is shown in Figure 1. This setup consists of the following sections: (1) feed and mixing, (2) flow division, (3) reaction, (4) separation, and (5) analysis. The detailed process flow scheme with respect to the above-mentioned five sections is

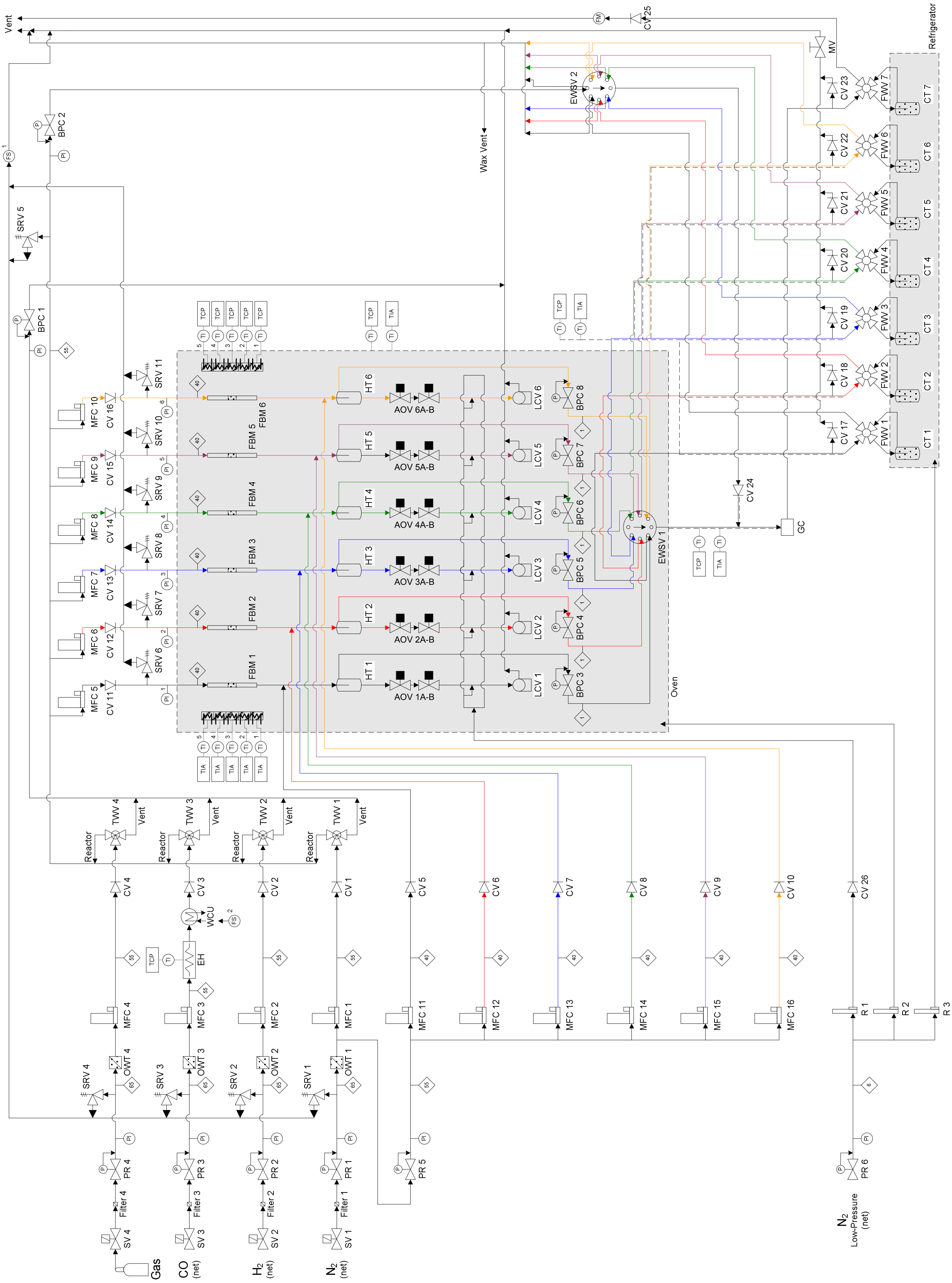

Figure 2. Detailed process flow scheme of the six-flow fixed-bed microreactor FTS setup. Description of used symbols and acronyms is included in Figure 3 and Table A1/Appendix A.

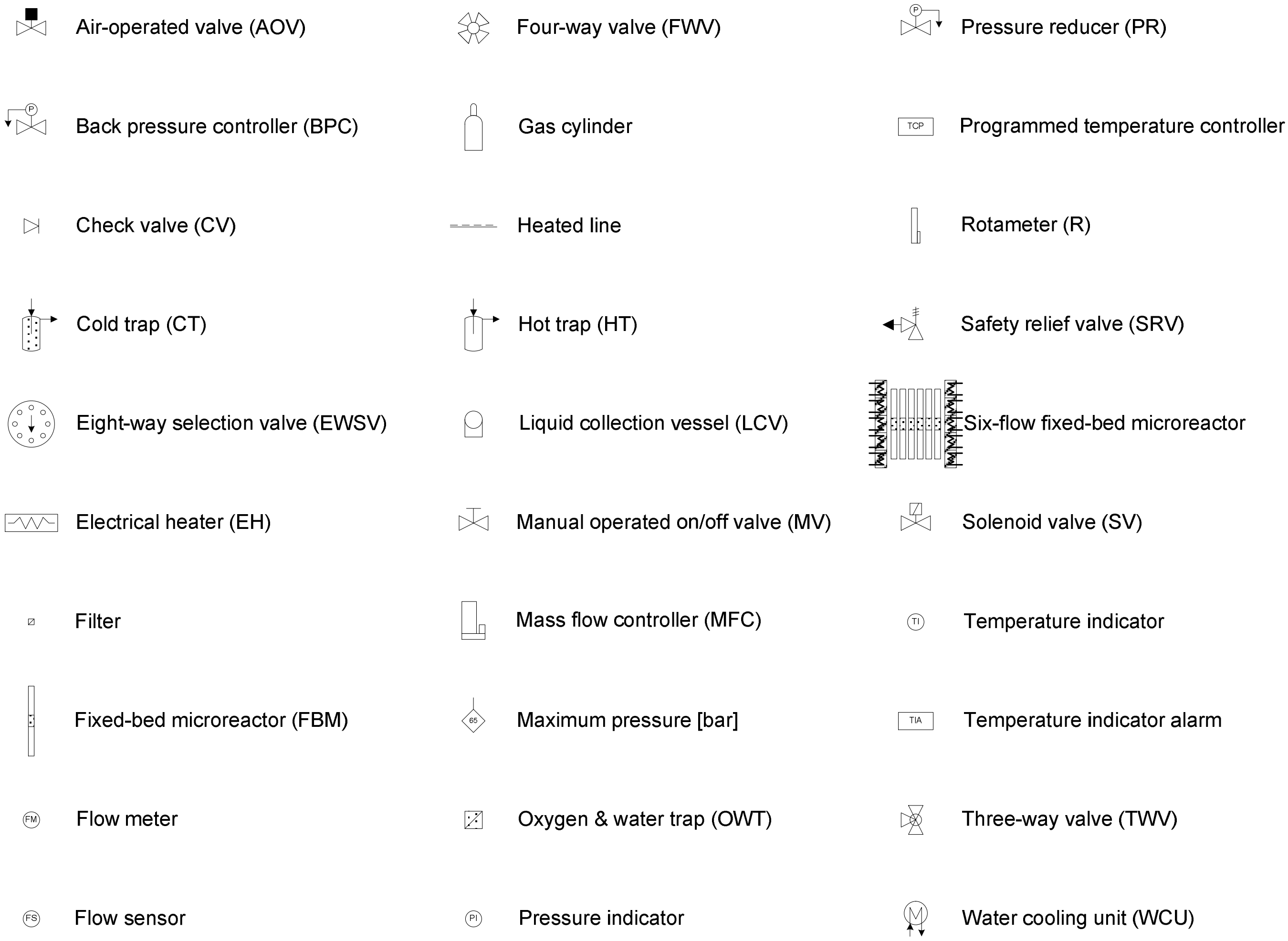

Figure 3. Description of the symbols and acronyms used in Figure 2 (see Table A1/Appendix A for equipment models and more details).

presented in Figure 2.

2.2.1. Feed and mixing/flow division

In the feed and mixing section, flows of pure N_2, H_2, and CO are set by individual mass flow controllers (MFC 1, 2, and 3, respectively, Figure 2) after they are purified from possible traces of particular matter, H_2O, and O_2 by a set of filters (1–3) and traps (OWT 1–3). Moreover, an additional supply line is implemented in this section. ‘A fourth gas’ may be introduced to the setup by MFC 4 *via* this extra line for different purposes (*e.g.*, an already prepared (model) mixture as feed, He for leak detection, *etc.*). CO can react with metals such as Fe, Ni, and Cr at a high pressure to form highly toxic metal carbonyls. Therefore, the tubing material is either fused silica coated SS 304 or titanium where it is in contact with CO (at high pressures and/or temperatures). Furthermore, an electrical heater (EH), operated at 473 K, followed by a water cooling unit (WCU) is placed downstream of the CO mass flow controller to decompose the carbonyls that were possibly formed in the gas network.

By means of a set of three-way valves (TWV 1–3), flows of pure gases can be switched to a ‘reactor manifold’ and thus mixed to produce the desired feed composition. In the flow division part, six flows are tapped from the reactor manifold, each connected to an individual mass flow controller (MFC 5–10, Figure 2). The excess flow mixture leaves the manifold *via* the backpressure controller BPC 2 and maintains a constant feed pressure for these mass flow controllers.

2.2.2. Reaction

The reaction section is surrounded by a large heating box (oven) which is shown in Figure 4a (marked with △) and 4b. The temperature of this oven is set at 448 K in order to prevent solidification of FTS products in tubing and other equipment. A ‘six-flow fixed-bed microreactor’ (marked with □ in Figure 4b) is located inside the oven with equal distances from the oven walls where heating elements are mounted. The reactor system consists of five heating sections (Figure 5a) with individual temperature controllers (Figure A1/Appendix A). Six tubes fit in this reactor system, each including a glass-lined insert (4 mm inner diameter), where catalyst particles can be loaded (Figure 5b). The isothermal zone along the six fixed-bed microreactors (FBM 1–6) is identical and at least of 10 cm (Figure 5c).

As mentioned in Section 2.2.1, the feed flow rate to each FBM is set by an independent MFC. Additionally, a flow of N_2 is introduced to the top-side part of each FBM (Figure 5b) by separate MFCs (11–16, Figure 2). The N_2 stream flushes the gap between the outer and insert tubes and mixes with the reactors effluents downstream of the FBMs (Figure 2). In this way N_2 will not dilute the reaction environment. The pressure of the FBMs is set by separate back pressure controllers (BPC 3–8, Figure 2) which are located inside the oven and controlled from outside. A continuous flow of gas, assured by N_2, results in a stable process pressure at high conversion levels and α values where most of the syngas feed is converted into liquid products. The N_2 inert can also be used as an internal standard for the online gas analysis (see Section 2.3.1).

2.2.3. Separation/analysis

Due to differences in boiling points, FTS products may be in the form of either gas, liquid, or solid at ambient conditions. Separation of these fractions is of importance since: (*i*) heavy components may solidify in tubing and equipment at (possible) cold spots, and (*ii*) revealing the product composition asks for analysis strategies which may vary for different hydrocarbon ranges. FTS wax which is mostly in the liquid phase at 448 K and typical reaction pressures (≥10 bar) [11] is collected by gas/liquid separators (‘hot traps’) located in the oven (HT 1–6, Figure 2 and 4b). HTs are regularly drained into liquid collection vessels (LCV 1–6) by assistance of two sets of air-operated on/off valves (AOV 1–6,

Figure 4. Photographs of the six-flow fixed-bed microreactor FTS setup (a), the oven (△) where the five heated zones six-flow fixed-bed microreactor (□) is located at the center and hot traps beside the wall (as illustrated by the white oval) (b), and the cold traps with a collection vial (○) inside (c).

set A and B). The system pressure allows discharging the wax, first from HTs into a piece of tube (that connects AOVs A to B) and, consequently, in LCVs through a subsequent sequence of opening and closure of the two sets of valves (see Figure A2/Appendix A for complete description). An inert

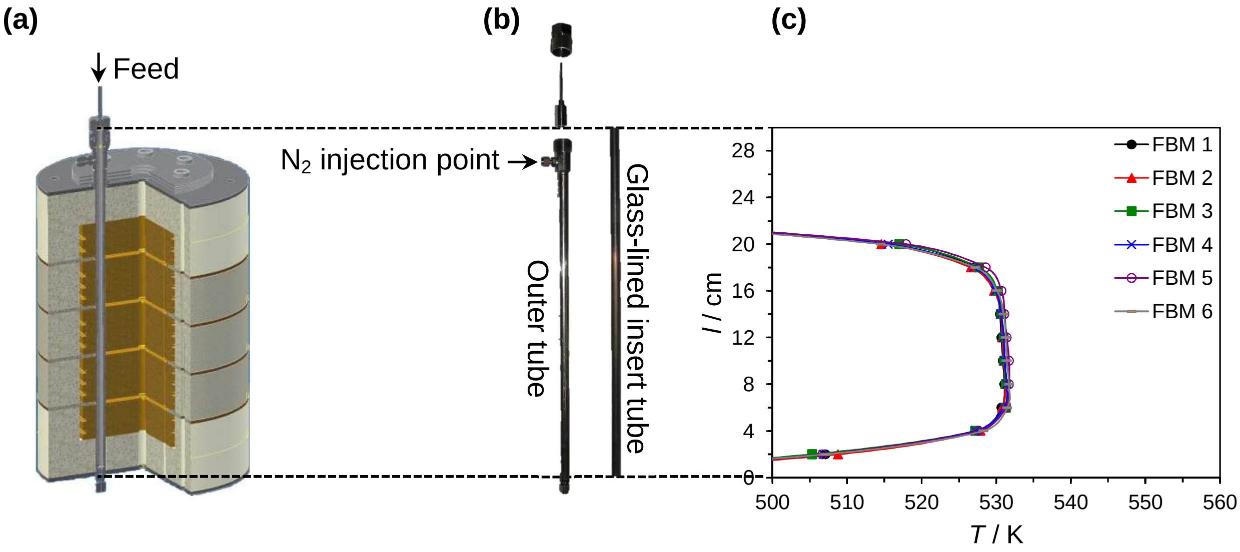

Figure 5. Schematic figure of the five heated zones fixed-bed microreactor (a), and reactor insert and outer tubes (b). Temperature profiles of the six fixed-bed microreactors (FBM 1–6) at 533 K (c).

environment is kept inside LCVs by *ca.* 100 cm^3 min^{-1} flow of N_2 at atmospheric pressure.

After expansion to atmospheric pressure (by BPC 3–8), the products flow out from the oven *via* heated lines to a refrigerator where ‘cold traps’ are located (CT 1–7, Figure 2 and 4c). Water and lighter hydrocarbons are separated from unreacted feed, gas phase hydrocarbons, and internal standard in CTs at *ca.* 278 K. To collect the liquids, a vial (marked with ○ in Figure 4c) can be inserted in CTs while they are bypassed by a set of four-way valves (FWV 1–6). (*Note that precautions must be considered while removing the HTs and CTs since they may contain hazardous gases.*)

Samples collected in LCVs and CTs may be analyzed offline, while the gas phase is analyzed by an online gas chromatograph (GC) (see Section 2.3). By means of two eight-way selection valves (EWSV), one located upstream of the CTs (in the oven, EWSV 1) and the other at their downstream (EWSV 2), two different analysis modes can be followed: (mode *i*) C1–C20 can be analyzed online, when the targeted flow (*i.e.*, effluents of FBM 1–6) is selected by EWSV 1, before separation of the liquid fractions. This mode is preferred at low conversion levels and/or low *α* values, when a low production of liquid hydrocarbons is expected. (mode *ii*) Once separated from the liquids, gas phase hydrocarbons can be analyzed online upon flow selection by EWSV 2. This mode is preferred at high conversion levels and high *α* values when a high concentration of heavy hydrocarbons and H_2O may damage the GC columns. If a thorough product analysis is aimed for in the latter case, the online analysis should be supplemented by offline measurements of the collected samples (see Section 2.3.2).

A volumetric gas flow meter (FM) is installed downstream of the GC (sample loop) which can be used occasionally to calibrate the MFCs or measure the gas flows (Figure 2). Most of the setup equipment is computer controlled through a dedicated LabVIEW code. Instrument models are reported

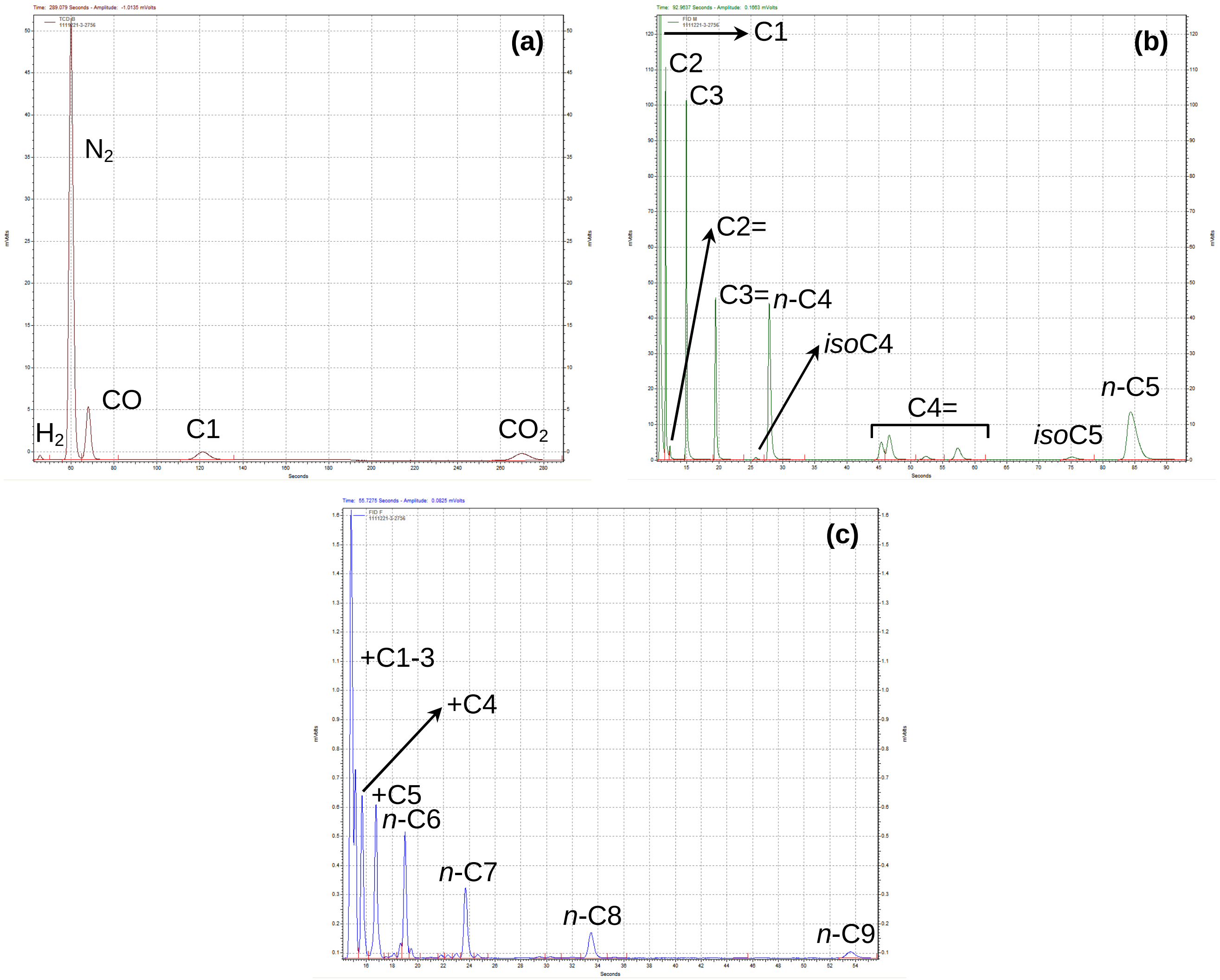

Figure 6. Compact GC chromatograms of reactor effluents in the gas phase, analyzed online after 20 h on-stream over 10 wt% Co/SiO$_2$ at 533 K, 10 bar total pressure, feed composition H$_2$/CO = 2, and *GHSV* = 2.4 m^3_{STP} kg^{-1}_{cat} h^{-1}. TCD signal (a) and FID signals (b and c). C2=: ethylene, C3=: propylene, *iso*C4: isobutane, *iso*C5: isopentane, +C1-3: all C1–C3 hydrocarbons, +C4: all C4 hydrocarbons, and +C5: all C5 hydrocarbons.

in Table A1/Appendix A.

2.3. Product analysis and quantification

2.3.1. Online analysis of gas phase reactor effluents

The gas phase, containing light FTS hydrocarbons and unreacted feed, is analyzed online by a Compact GC from Interscience. The GC is equipped with three columns and detectors in parallel, using He as carrier gas. In the first column (Carboxen 1010, 10 m × 0.32 mm), H$_2$, N$_2$, CO, CH$_4$, and CO$_2$ are separated at 333 K and analyzed by TCD (Figure 6a). In the second column (Al$_2$O$_3$/KCl, 10 m × 0.32 mm) and FID detection, separation between all C1–C4 components is achieved at 434 K (Figure 6b). In the third column (RTx-1 0.5 lm, 15 m × 0.32 mm), C5–C10 hydrocarbons are separated at 353 K and detected by FID (Figure 6c). The analysis duration for each sample is less than 5 min.

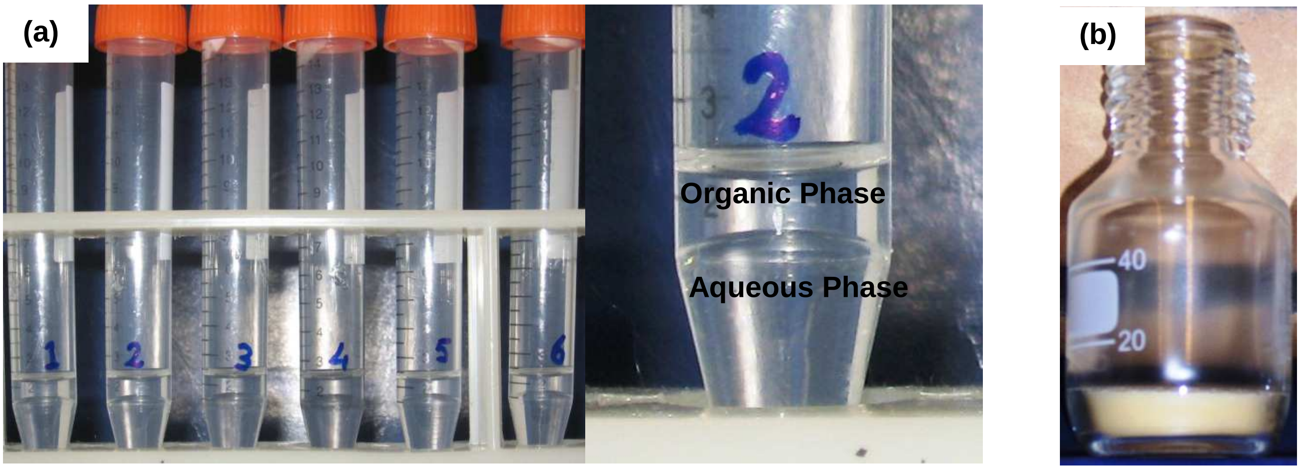

Figure 7. Liquid FTS products (*i.e.*, a biphasic mixture containing an organic phase over an aqueous phase), collected in the cold traps after 20 h on-stream at 533 K, 10 bar total pressure, feed composition $H_2/CO = 2$, and $GHSV = 2.4\ m^3_{STP}\ kg^{-1}_{cat}\ h^{-1}$ (a). FBM 1–6 were loaded with the same catalyst batch of 10 wt% Co/SiO_2. FTS wax, separated in a hot trap and collected by the corresponding liquid collection vessel (b).

Total flow rate of the reactor effluents in gas phase ($\nu_{T,gas}$, not including N_2) can be calculated from Eq. (1) if the N_2 molar fraction ($y_{N2,loop}$) is measured.

$$y_{N2,loop} = \frac{\nu_{N2}}{\nu_{N2} + \nu_{T,gas}} \tag{1}$$

It should be noted that $\nu_{T,gas}$ is not necessarily equal to the total flow rate out of the corresponding FBM, due to (partial) separation of reaction products in HTs and CTs. On the other hand, since N_2 is an inert gas, its flow rate is equal to what was fed downstream of the reactors (ν_{N2}, see Section 2.2.2).

Response factors of the analysis equipment for the different components are obtained upon calibration with a mixture that contains H_2, N_2, CO, CH_4, and CO_2 (detected by TCD, Figure 6a) as well as all the hydrocarbons shown in Figure 6b (detected by FID). For higher hydrocarbons, response factors (*rf*) of all hydrocarbons with *n* carbon number (C*n*) may be assumed to be equal and calculated from Eq. (2) [17]:

$$rf_{Cn} = \frac{n-1}{n} rf_{Cn-1} \tag{2}$$

Therefore, Eq. (3) will provide the flow rate of component i in gas phase reactor effluents ($\nu_{i,gas}$):

$$\nu_{i,gas} = y_{i,gas}\nu_{T,gas} = y_{i,loop}\left(\nu_{T,gas} + \nu_{N2}\right) \tag{3}$$

where $y_{i,loop}$ is the molar fraction of component i in the N_2 diluted gas phase and is directly obtained from the GC analysis. $\nu_{i,gas}$ can be converted into molar flow rate, assuming the ideal gas behavior.

2.3.2. Offline analysis of the collected samples

After separation from the aqueous phase, liquid hydrocarbons (collected in CTs, Figure 7a) as well

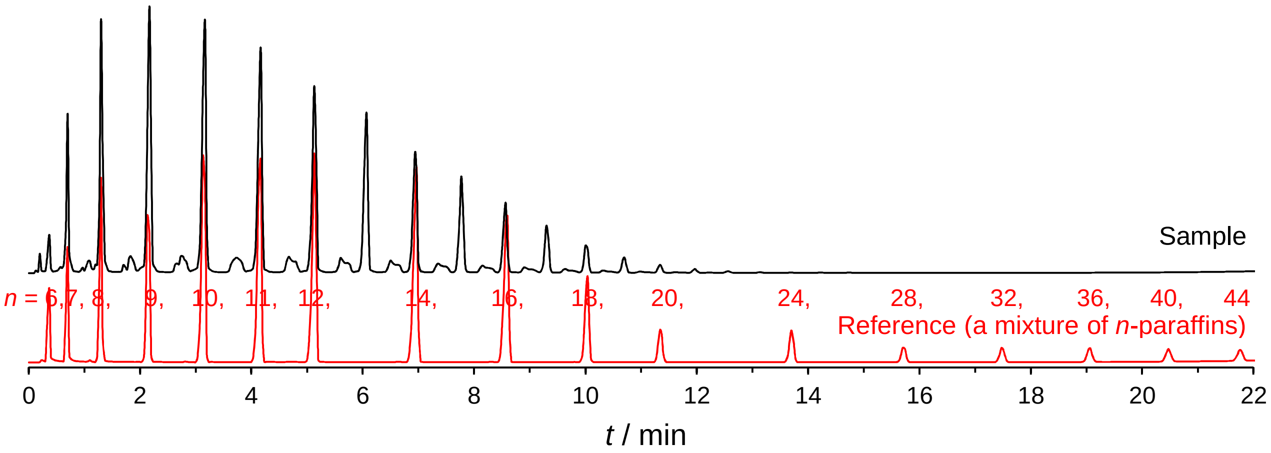

Figure 8. SimDis GC chromatogram of liquid FTS hydrocarbons, collected after 20 h on-stream over 10 wt% Co/SiO_2 at 533 K, 10 bar total pressure, feed composition $H_2/CO = 2$, and *GHSV* = 2.4 $m^3_{STP}\ kg^{-1}_{cat}\ h^{-1}$. *n*: carbon number.

as the wax (collected in HTs, Figure 7b) can be weighted and analyzed offline to identify the overall product spectrum. Certainly, various analytical methods may be applied in this case such as simulated distillation (SimDis) chromatography, PIONA analysis, two-dimensional chromatography, *etc.* In this report, a SimDis GC (Hewlett Packard 5890, Series II) is employed which is equipped with an FID and HP-1 column (7.5 m × 0.53 mm, film thickness 2.65 µm), using He as carrier gas. During the analysis, the oven temperature is ramped from 308 to 623 K (14 K min^{-1}) and kept at the final temperature for 5 min. Before injection, samples are diluted with CS_2.

A representative chromatogram of the organic phase (as indicated in Figure 7a) shows that it contains C5–C20 hydrocarbons (Figure 8). Comparison between Figure 6c and 8 reveals that some C5+ hydrocarbons are noticeably present in both gas and liquid phases. Therefore, offline measurements are necessary for analysis of C5+, when flow selection is done by EWSV 2 (operation mode (*ii*), see Section 2.2.3). At the same time, such integration of offline and online data may lead to overestimation (or underestimation) of the fractional molar distributions for hydrocarbons that are present in both gas and liquid phases. This is due to temperature fluctuations of the refrigerator (Figure 2 and 4c), which may result in a lower (or higher) average temperature of CTs during the collection period, as compared with their temperature at the instant of the online analysis. So to demonstrate, a flash separation of FTS product mixture (at $\alpha = 0.9$) was simulated by Aspen Plus, employing the Peng-Robinson thermodynamic model. The simulation integrated the gas phase composition at different flash separation temperatures with that of the liquid phase for a flash separation at 273 K. Figure 9 shows that such temperature variations lead to artifacts in the form of a ‘bump’ in fractional molar distribution of FTS hydrocarbons above C5.

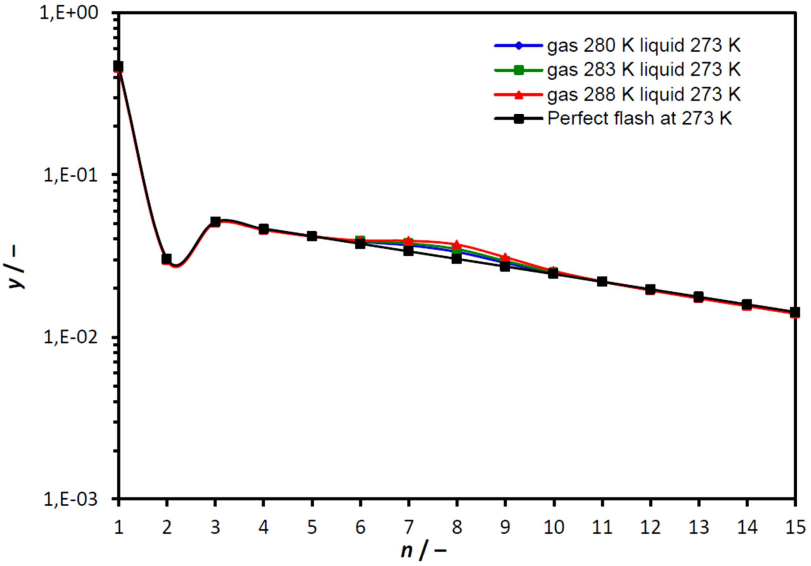

Figure 9. Fractional molar distribution of FTS hydrocarbons (α = 0.9) obtained after a flash separation of liquid and gas phases. Composition of the gas phase at different flash separation temperatures was integrated with that of the liquid phase for a flash separation at 273 K.

2.4. Case study: Assessment of six-flow operation

2.4.1. Catalyst

Co/SiO_2 FTS catalyst was prepared by incipient wetness impregnation in one step, using a Co nitrate aqueous solution. Spherical particles of SiO_2 (CARiACT Q-10, Fuji Silysia Chemical Ltd.) were loaded with 10 wt% of Co in a rotating vessel. The impregnated sample was kept under rotation for *ca.* 0.5 h at room temperature and, subsequently, at 323–333 K for more than 2 h. The catalyst was then dried overnight at 393 K and calcination was followed at 673 K for 2 h in static air conditions.

Textural and chemical properties of SiO_2 support and Co/SiO_2 catalyst are summarized in Table A2/Appendix A. The temperature-programmed reduction profile in H_2 of Co/SiO_2 is presented in Figure A3/Appendix A.

2.4.2. Setup operation

0.5 g of fresh Co/SiO_2 (from the same catalyst batch) was fixed in the six reactor inserts, using quartz wool plugs. Samples were first activated *in situ* by 80 cm^3_{STP} min^{-1} of H_2 at 673 K for 12 h at atmospheric pressure followed by cooling to 453 K under H_2 flow. After setting the total feed flow rate to each reactor (by MFCs 5–10), the pressure was increased to the process value (10 or 15 bar total pressure) and CO was gradually introduced to the feed stream (*via* MFC 3) at 453 K in order to reach its final concentration (5.0 μmol_{CO} s^{-1}, H_2/CO = 2) in 1 h. Subsequently, the reactor system was heated to the process temperature (513 or 533 K). A rate of 2 K min^{-1} was applied for all the heating/cooling steps. During the experiment at 513 K, heavy hydrocarbons (wax) were collected by HTs at 448 K and reaction pressure. After expansion of the product flow to atmospheric pressure, lighter hydrocarbons and water were collected in CTs at *ca.* 278 K. Product analysis was done in operation mode (*ii*) as explained in Section 2.2.3 and following the methodology described in Section 2.3.

A pseudo-steady-state condition was attained after 20 h on-stream when the internal volume of the experimental setup was thoroughly flushed by the (liquid) reaction effluents and the decrease in CO conversion (with time) contracted (see Section 2.4.3). CO conversion, carbon selectivity, and molar fraction of each product were defined by Eqs. (4)-(6), respectively, where X_{CO} stands for CO conversion (%), F indicates the molar flow rate, S is the carbon selectivity (%) toward a product with n carbon atoms, and y is the molar fraction of a hydrocarbon Cn.

$$X_{\mathrm{CO}} = \frac{F_{\mathrm{in,CO}} - F_{\mathrm{out,CO}}}{F_{\mathrm{in,CO}}} \times 100 \quad (4), \qquad S_{\mathrm{C}n} = \frac{nF_{\mathrm{C}n}}{F_{\mathrm{CO_2}} + \sum_{n=1}^{N} nF_{\mathrm{C}n}} \times 100 \quad (5), \qquad y_{\mathrm{C}n} = \frac{F_{\mathrm{C}n}}{\sum_{n=1}^{N} F_{\mathrm{C}n}} \quad (6)$$

The α value was defined in terms of the rate of polymerization (r_{p}) and the rate of termination (r_{t}) of the growing hydrocarbons, according to Eq. (7).

$$\alpha = r_{\mathrm{p}}/(r_{\mathrm{p}}+r_{\mathrm{t}}) \qquad (7)$$

Therefore, Eq. (8) represented the Anderson-Schulz-Flory (ASF) product distribution in terms of molar fractions:

$$y_{\mathrm{C}n} = (1-\alpha)\alpha^{\mathrm{n-1}} \qquad (8)$$

and α value was calculated from the slope of Ln($y_{\mathrm{C}n}$) as a function of n. (*i.e.*, expecting a first order function based of Eq. (8), the slope will be equal to Ln(α).)

2.4.3. Results

Time-on-stream (*TOS*) evolution of CO conversion in FBM 1–6 is depicted in Figure 10. *Ca.* 98% conversion of CO is measured after 1–2 h of reaction. CO conversion decreases with *TOS* by *ca.* 14% after 27 h on-stream. The maximum deviation from the average conversion value (between FBM 1–6) is ±2%, observed in case of FBM 2 and 6.

The collection period of liquid fraction (in CTs) was during 20 to 28 h *TOS*, when CO conversion decreases 3% (Figure 10). Molar flow rates of liquid hydrocarbons, as averaged based on the collection duration and offline analysis, were added to their corresponding values obtained from the online analysis at *ca.* 20 h *TOS*. The added flow rates were used to calculate the carbon selectivity (Eqs. 5) and molar fraction (Eqs. 6) of hydrocarbons that were present in more than one phase (see Section 2.3.2).

FBM 1–6 display very similar product selectivities (Figure 11a). Under the applied process conditions, the highest carbon selectivity is obtained for the C5–C11 fraction, while a minor amount of C21+ is formed over Co/SiO_2. The very low production of C21+ is observed in HTs as almost no wax sample could be collected for offline analysis. The olefin to paraffin ratio in C2–C4 fraction

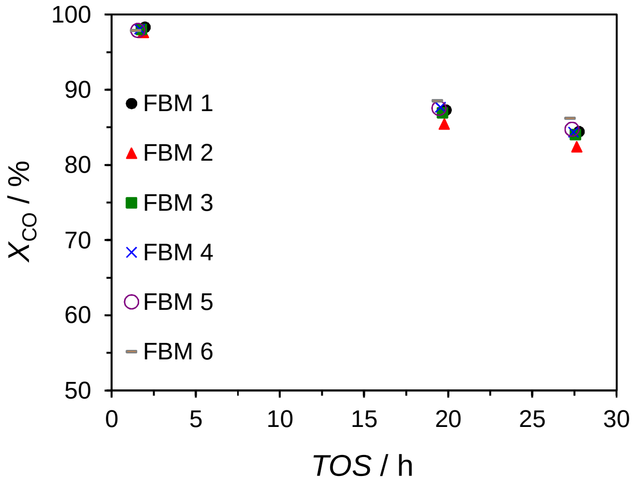

Figure 10. Time-on-stream (*TOS*) evolution of the CO conversion during FTS at 533 K, 10 bar total pressure, feed composition $H_2/CO = 2$, and $GHSV = 2.4\ m^3_{STP}\ kg^{-1}_{cat}\ h^{-1}$. FBM 1–6 were loaded with the same catalyst batch of 10 wt% Co/SiO_2.

(O/P (C2-4)) is *ca.* 0.4 (insert in Figure 11a) which points to prevalence of saturated hydrocarbons throughout the product spectrum (O/P ratio decreases for larger hydrocarbons due to their stronger adsorption [18] followed by hydrogenation [19]). The CO_2 selectivity is above 10 % suggesting a considerable contribution of water-gas-shift (WGS) over the studied Co-catalyst at 533 K.

Relative errors (E) between reactors associated with carbon selectivities to each product range, with respect to the average value (between FBM 1–6, $S_{Cn,\text{average}}$) was calculated by Eq. (9) and is presented in Figure 11b.

$$E_{Cn} = \frac{S_{Cn} - S_{Cn,\text{average}}}{S_{Cn,\text{average}}} \times 100 \tag{9}$$

Note that for each group, the error associated with isoparaffins and olefins is separated from that related to *n*-paraffins. E is maximum 6% for hydrocarbon fractions up to C11 and 10% for C12+.

The molar fraction of FTS hydrocarbons *versus* their carbon number follow a fairly log-linear trend up to C17 (Figure 12a). C1 and C2 are exceptions which show, respectively, higher and lower values than what is anticipated by extrapolating the linear distribution to $n = 1$ and 2. In order to assess the performance of the setup when working at a higher α values (*cf.* inserts in Figure 12a and b), additional experiments were performed at lower temperature (513 K). Figure 12b shows that the linear trend continues for $n > 17$.

2.5. Discussion

The lab-scale six-flow FTS setup, introduced in this report, includes six fixed-bed microreactors of which feed flow rate and process pressure may be adjusted independently. Moreover, each flow is

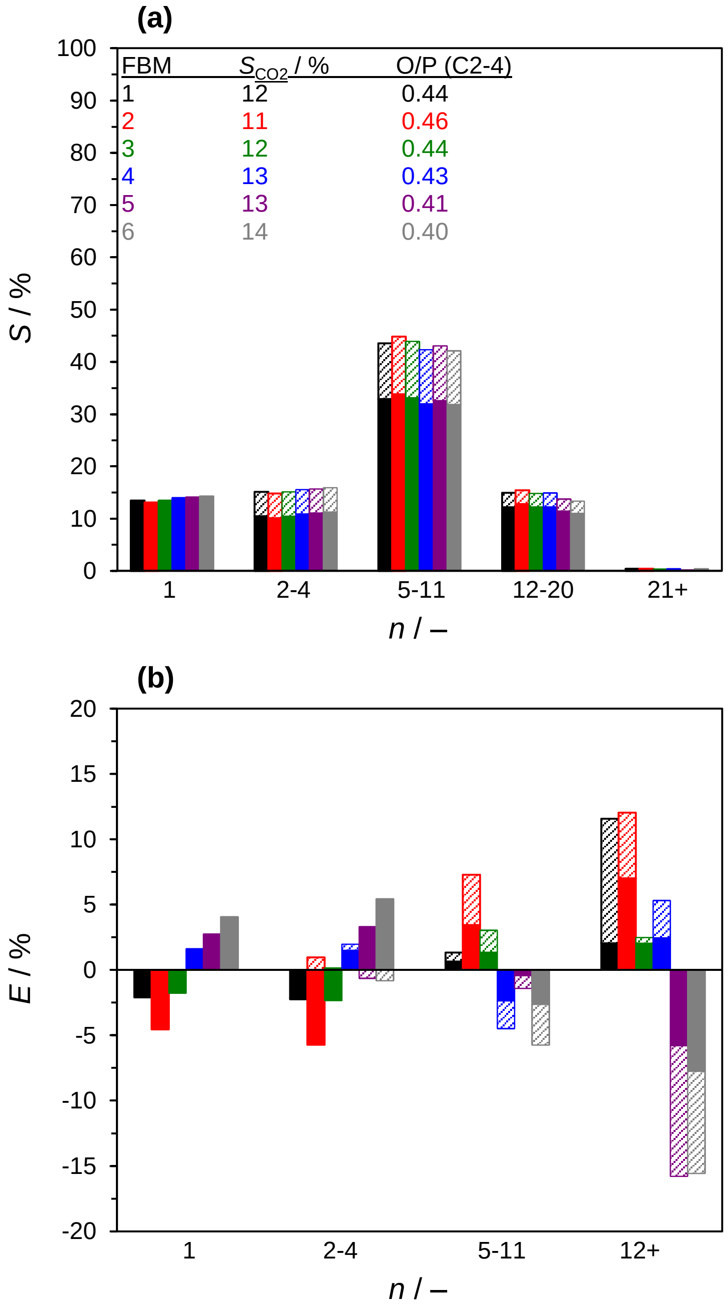

Figure 11. Carbon selectivity of FTS products after 20 h on-stream (a). Relative errors associated with carbon selectivities to each product range with respect to the average value (between FBM 1–6) (b). In each carbon number group from left to right: FBM 1 to FBM 6. ■: *n*-paraffins; ▨: sum of isoparaffins and olefins; S_{CO2}: CO_2 selectivity; O/P (C2-4): olefin to paraffin ratio of C2–C4. Experiment was performed at 533 K, 10 bar total pressure, feed composition $H_2/CO = 2$, and *GHSV* = 2.4 m^3_{STP} kg^{-1}_{cat} h^{-1}. FBM 1–6 were loaded with the same catalyst batch of 10 wt% Co/SiO_2.

equipped with phase separators aiding an independent collection of solid and liquid samples. At the same time, the six-flow unit benefits from operation under similar feed composition, reaction and product separation temperatures, and conditions of the online analytical equipment (*e.g.*, calibration, *etc.*). While the former independent parameters increase the experimentation throughput, the later similarities will certainly improve its accuracy. Enhancements in both throughput and accuracy are the

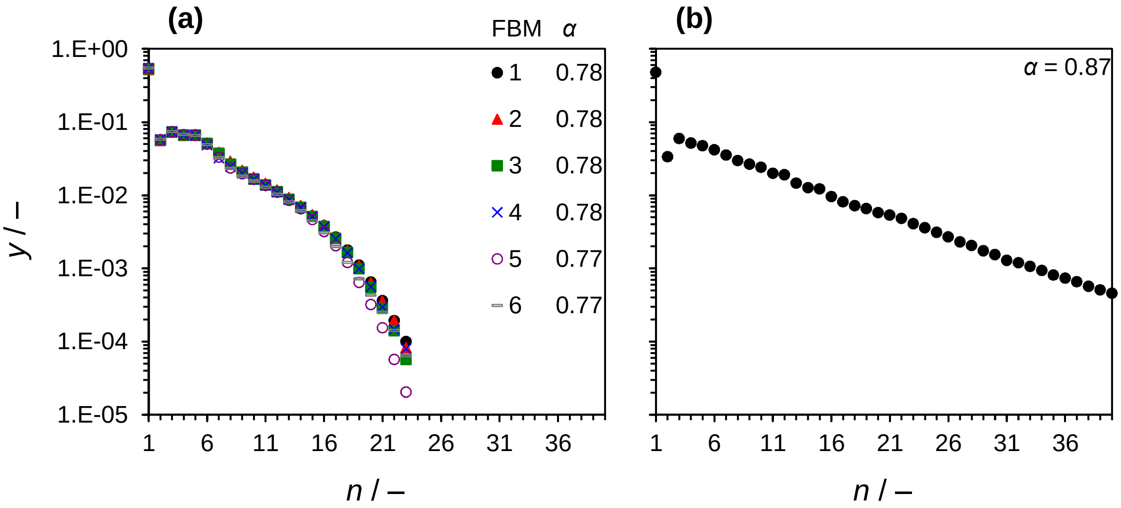

Figure 12. Fractional molar composition of FTS hydrocarbons after 20 h on-stream over Co/SiO_2 at 533 K, 10 bar total pressure (a) and 513 K, 15 bar total pressure (b), feed composition $H_2/CO = 2$, and *GHSV* = 2.4 $m^3_{STP}\ kg^{-1}_{cat}\ h^{-1}$. In (a), FBM 1–6 were loaded with the same catalyst batch. Chain growth probability (α) is calculated in the range of C5–C16.

advantages of such a system over six independent units. The condition is that all the reactors (flows) should behave identical, *i.e.*, provide similar results employing the same catalyst.

Testing the same batch of Co/SiO_2 catalyst in the six-flow setup confirms that the six FBMs operate almost identical in terms of activity and selectivity measurements. With respect to the average CO conversion, FBMs 2 and 6 show about 1–2% lower and higher values, respectively (Figure 10). Carbon selectivity to C1–C4 and CO_2 are lowest in FBM 2 and highest in the case of FBM 6 (Figure 11). At the same time, selectivity to C5+ and O/P (C2-4) are highest in FBM 2 and lowest for FBM 6. Slight fluctuations in local temperatures can potentially lead to such observation since Co-based FTS catalysts are very sensitive to changes in the process temperature in terms of their product selectivity [20]. The construction of the six-flow FBM with five separate heating zones and very narrow reactor inserts results in an identical temperature profile in FBM 1–6 in absence of reaction (Figure 5c and A1/Appendix A). On the other hand, all catalyst beds were carefully packed in the 10 cm isothermal region of FBM 1–6 by means of a dedicated rod followed by tapping. Therefore, the above-mentioned alterations cannot originate from the reactor oven temperature. Indeed deviations in the obtained results are expected when catalytic measurements are duplicated (even with the same reactor). Variances such as those in packing the catalyst beds, inhomogeneity in a catalyst batch, *etc.* may significantly contribute to experimental errors in addition to other sources (*e.g.*, analytical, mass and flow measurements, *etc.*) [10]. The FTS reaction is highly exothermic [21] and the aforementioned catalysts' performance results suggest that small differences in heat dissipation from the catalyst beds and/or occurrence of hotspots may have an important role in this case.

The ASF distribution implies a log-linear trend for fractional molar composition of FTS hydrocarbons when plotted *versus* their carbon number [22]. Although this assumption is fairly relevant for many catalytic systems, several reports deal with non-ASF product distributions [23]. Dissimilar sites or (parallel) growth mechanisms in one catalyst [24], altered α values in different carbon number regions [25], and the so-called 'bifunctional catalysts' that represent a 'break' in ASF plot [26] are among such exceptions. Moreover, the degree of saturation (and/or branching) may vary at different hydrocarbon ranges, even over an ASF-behaving catalyst. Thus, analysis of the whole product spectrum is of crucial importance in order to fully unveil the performance of an FTS catalyst. This asks for running reactions with a sufficient production of liquid and solid amounts in the case of studies dealing with gas-to-liquid conversions (*i.e.*, when high α values are aimed for). Excluding the heavies from the analysis may lead to artifacts in the form of deviation from ASF distribution (Figure 12a) and results in elevated errors in the selectivity data above C11 (Figure 11b).

If process conditions are fixed, productivity of a reaction can be increased by loading more catalyst in the reactor while keeping the space velocity constant. In this case, the necessary amount of sample may reach above a gram, since FTS catalysts in general are not highly productive. Conventional 'one-flow' setups can easily be adopted for such amounts as they are less limited by space. However, upon numbering up the reactors (flows), a compromise should be made between the equipment volume (/capital), operation complexity, and extensive data acquisition. In this respect, a six-flow equipment in the lab-scale bridges the gap between high-throughput setups for primary screening of FTS catalysts and conventional one-flow systems for their detailed performance studies. As a show case, the current setup has been employed for studying a number of zeolite-containing Co-catalysts which are proven to combine FTS and acid-catalyzed reactions [26-30]. The product compositions of these catalysts above C11 cannot be described by an ASF distribution [26, 29]. Therefore, an almost extensive analysis of liquid products was essential (Figure A4/Appendix A) in addition to a time efficient catalyst screening. This was offered by the operation mode (*ii*) (see Section 2.2.3) of the six-flow fixed-bed microreactor FTS setup.

2.6. Conclusions

A relatively long catalyst stabilization period stresses the necessity of high-throughput experimentation in research areas related to FTS catalyst developments. As long as activity and selectivity measurements are concerned, lab-scale six-flow operations offer an increased experimental throughput as well as accuracy. The latter is due to equal conditions (in terms of process temperature, feed composition, equipment conditions, *etc.*) under which the six parallel experiments are performed and is ensured if the flows operate identically. Design, construction, and operation of such an equipment confirm that indeed it is possible to obtain reproducible activity and selectivity data within 6% relative error (with respect to the average value between the six flows). Our results suggest that minor differences in local temperatures may be the major basis of slight deviation from the average activity and selectivity values, in addition to other sources of experimental error.

Incorporation of separate mass flow and pressure controllers as well as product separation units in each flow allows running reactions with high production of solid and liquid fractions. Including these fractions in the product analysis (as in the case of conventional one-flow operations) is of great importance to fully characterize the FTS product spectra. Since the number of reactors is not as many as in high-throughput setups (bearing more than 10 flows) such instrumental considerations will not lead to a dramatic increase in the equipment volume (and as consequence, in the associated capital cost). Therefore, a six-flow fixed-bed microreactor unit combines the advantages of high-throughput and conventional FTS setups at the lab-scale.

Nomenclature

+C1-3	All C1–C3 hydrocarbons
+C4	All C4 hydrocarbons
+C5	All C5 hydrocarbons
α	Chain growth probability
ν	Volumetric flow rate
C2=	Ethylene
C3=	Propylene
Cn	Hydrocarbon with n carbon number
E	Relative error
F	Molar flow rate
*iso*C4	Isobutane
*iso*C5	Isopentane
l	length
n	Carbon number
O/P (C2-4)	Olefin to paraffin ratio in C2–C4 fraction
r	Rate
rf	Response factors
S	Carbon selectivity
T	Temperature
t	Time
TOS	Time-on-stream
X	Conversion
y	Molar fraction

Subscripts

gas	Gas phase
i	Component index
loop	GC sample loop
p	Polymerization

T	Total
t	Termination

References

[1] L. Singoredjo, M. Slagt, J. van Wees, F. Kapteijn, J.A. Moulijn, Catal. Today 7 (1990) 157-165.

[2] J. Pérez-Ramírez, R.J. Berger, G. Mul, F. Kapteijn, J.A. Moulijn, Catal. Today 60 (2000) 93-109.

[3] F. Kapteijn, J.A. Moulijn, Laboratory testing of solid catalysts, in: G. Ertl, H. Knözinger, F. Schüth, J. Weitkamp (Eds.) Handbook of Heterogeneous Catalysis, Wiley-VCH Verlag GmbH & Co. KGaA, Weinheim, 2008, pp. 2019-2045.

[4] H.W. Turner, A.F. Volpe Jr, W.H. Weinberg, Surf. Sci. 603 (2009) 1763-1769.

[5] T. Zech, G. Bohner, O. Laus, J. Klein, M. Fischer, Rev. Sci. Instrum. 76 (2005).

[6] D.A. Wood, C. Nwaoha, B.F. Towler, J. Nat. Gas Sci. Eng. 9 (2012) 196-208.

[7] S.T. Sie, M.M.G. Senden, H.M.H. van Wechem, Catal. Today 8 (1991) 371-394.

[8] A. de Klerk, E. Furimsky, Catalysis in the Refining of Fischer-Tropsch Syncrude, RSCPublishing, Cambridge, UK, 2010.

[9] N.E. Tsakoumis, M. Rønning, Ø. Borg, E. Rytter, A. Holmen, Catal. Today 154 (2010) 162-182.

[10] J.A. Moulijn, J. Pérez-Ramírez, R.J. Berger, G. Hamminga, G. Mul, F. Kapteijn, Catal. Today 81 (2003) 457-471.

[11] R. de Deugd, Fischer-Tropsch synthesis revisited, in: Catalysis Engineering, Department of Chemical Engineering, Delft University of Technology, Netherlands, Delft, Netherlands, 2004.

[12] A.Y. Khodakov, W. Chu, P. Fongarland, Chem. Rev. 107 (2007) 1692-1744.

[13] J.K. van der Waal, G. Klaus, M. Smit, C.M. Lok, Catal. Today 171 (2011) 207-210.

[14] H.M.T. Galvis, J.H. Bitter, C.B. Khare, M. Ruitenbeek, A.I. Dugulan, K.P. de Jong, Science 335 (2012) 835-838.

[15] H.M. Torres Galvis, J.H. Bitter, T. Davidian, M. Ruitenbeek, A.I. Dugulan, K.P. de Jong, J. Am. Chem. Soc. 134 (2012) 16207-16215.

[16] H.M. Torres Galvis, A.C.J. Koeken, J.H. Bitter, T. Davidian, M. Ruitenbeek, A.I. Dugulan, K.P. de Jong, J. Catal. 303 (2013) 22-30.

[17] J.L. Dierickx, P.M. Plehiers, G.F. Froment, J. Chromatogr. A 362 (1986) 155-174.

[18] J. Wei, Ind. Eng. Chem. Res. 33 (1994) 2467-2472.

[19] E.W. Kuipers, I.H. Vinkenburg, H. Oosterbeek, J. Catal. 152 (1995) 137-146.

[20] H. Schulz, Stud. Surf. Sci. Catal. 163 (2007) 177-199.

[21] D. Vervloet, M.R. Kamali, J.J.J. Gillissen, J. Nijenhuis, H.E.A. van den Akker, F. Kapteijn, J.R. van Ommen, Catal. Today 147 (2009) S138-S143.

[22] C.G. Visconti, E. Tronconi, L. Lietti, P. Forzatti, S. Rossini, R. Zennaro, Top. Catal. 54 (2011) 786-800.

[23] E.W. Kuipers, C. Scheper, J.H. Wilson, I.H. Vinkenburg, H. Oosterbeek, J. Catal. 158 (1996) 288-300.

[24] M. Claeys, E. van Steen, Stud. Surf. Sci. Catal. 152 (2004) 601-680.

[25] K.D. Kruit, D. Vervloet, F. Kapteijn, J.R. van Ommen, Catal. Sci. Technol. 3 (2013) 2210-2213.

[26] S. Sartipi, K. Parashar, M. Makkee, J. Gascon, F. Kapteijn, Catal. Sci. Technol. 3 (2013) 572-575.

[27] S. Sartipi, M. Alberts, M.J. Meijerink, T.C. Keller, J. Pérez-Ramírez, J. Gascon, F. Kapteijn, ChemSusChem 6 (2013) 1646-1650.

[28] S. Sartipi, M. Alberts, V.P. Santos, M. Nasalevich, J. Gascon, F. Kapteijn, ChemCatChem 6 (2014) 142-151.

[29] S. Sartipi, K. Parashar, M.J. Valero-Romero, V.P. Santos, B. van der Linden, M. Makkee, F. Kapteijn, J. Gascon, J. Catal. 305 (2013) 179-190.

[30] S. Sartipi, J. van Dijk, J. Gascon, F. Kapteijn, Appl. Catal. A-Gen. 456 (2013) 11-22.

Chapter 3

'Zeolite-coated' *versus* 'zeolite-supported' bifunctional catalysts for the direct production of liquid fuels from syngas

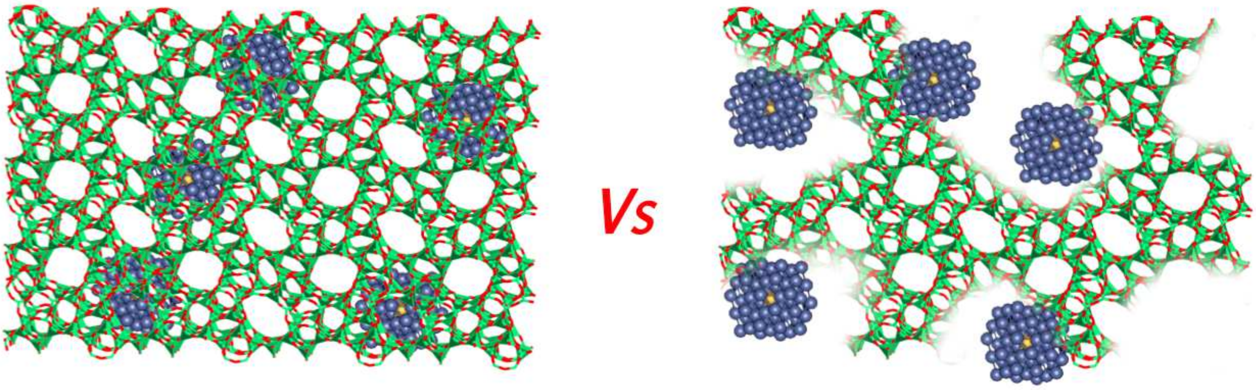

This Chapter is based on the following publication:

S. Sartipi, J.E. van Dijk, J. Gascon, F. Kapteijn, Appl. Catal. A-Gen. 456 (**2013**) 11-22.

Abstract: One step production of gasoline-range hydrocarbons from syngas is demonstrated by combination of Fischer-Tropsch synthesis (FTS) and acid functionalities in one single bifunctional catalyst particle. Two different catalyst configurations were studied in which the acid functionality of H-ZSM-5 zeolite conjoins the cobalt FTS active phase: (*i*) H-ZSM-5 as catalytic coating on Co and (*ii*) H-ZSM-5 as catalytic support for Co. Spherical shaped Co/SiO_2 was chosen as a conventional FTS catalyst for comparison and used as precursor to synthesize the H-ZSM-5-coated Co-catalyst. Various silicalite-1 and H-ZSM-5-coated reference samples were prepared by subjecting Co/SiO_2 to a direct hydrothermal procedure. Thorough characterization and catalytic performance tests reveal that direct hydrothermal synthesis results in transformation of SiO_2 from the Co/SiO_2 particles into an MFI coating on Co agglomerates. The silica support does not only act as precursor but also as nano-mold during the preparation of the zeolite-coated catalysts, as the original Co/SiO_2 particle shape is preserved. The close vicinity of the acid sites and Co function in the zeolite-coated catalysts promotes the acid-catalyzed conversion of the produced FTS hydrocarbons and reduces the production of C12+. Alternatively, mesostructured H-ZSM-5 was used to support Co. Mesoporous hierarchy in the latter case improves both the Co dispersion and the proximity of FTS and acid sites. Thus, Co supported on mesoporous H-ZSM-5 is a much more effective catalyst for the direct production of gasoline-range hydrocarbons than the H-ZSM-5-coated Co-catalyst.

3.1. Introduction

Fischer-Tropsch synthesis (FTS) is an attractive reaction path to produce liquid fuels such as gasoline and diesel oil *via* the transformation of syngas (mixture of H_2 and CO obtained from natural gas, coal, or biomass) to hydrocarbons and water [1].

Cobalt and iron are the two elements industrially employed in commercial FTS catalysts [2-4]. Both Fe and Co can catalyze FTS at temperatures below 523 K, the so-called low-temperature Fischer-Tropsch (LTFT) [5]. In either case, the Fischer-Tropsch synthesis of hydrocarbons follows the Anderson-Schultz-Flory (ASF) polymerization model, implying that the carbon number distribution of these products is a function of the chain growth probability (α) at the catalyst surface [6]. Due to this polymerization type kinetics, the direct selective production of specific hydrocarbon cuts is not feasible by FTS except for methane ($\alpha = 0$) and an infinite chain length ($\alpha = 1$). Therefore, the current strategy toward selective production of hydrocarbons with a narrow carbon number distribution includes the application of LTFT at conditions where α is close to unity followed by downstream conversion where the long chain hydrocarbons are hydrocracked to the desired cut of the barrel [5, 7, 8].

In the past few years quite some research has been conducted to intensify the gas-to-liquid process in terms of both reactor engineering and catalysis engineering: while the use of structured catalysts and reactors based on monolithic [9] or microchannel [8, 10, 11] configurations are very promising to maximize the FTS efficiency by enhancing the mass and heat transport properties of the process, many efforts have been devoted to developing catalyst formulations able to couple FTS with hydrocarbon product upgrading reactions (*i.e.*, hydrocracking and isomerization). The latter approach aims at minimizing the demands on the syncrude refining units, especially hydrocrackers, by maximizing the production of desired liquid fractions (diesel and gasoline) in FTS reactors [12]. To achieve this, a second functionality (other than FTS) should be added to the catalyst formulation to break the ASF selectivity. Since syncrude upgrading is mostly based on acid-catalyzed reactions [5], zeolites are potential candidates for this approach. In an ideal scenario then, hydrocarbons formed on FTS active sites migrate to the acid function and are subsequently chopped to the desired cut [13].

Based on the literature in the field, bifunctional FTS systems can be classified into three main categories in which zeolites are employed as the acid component: (*i*) physically mixed [14-17], (*ii*) zeolite-coated [18-22], and (*iii*) zeolite-supported catalysts [23-26]. In the first category, individual catalyst particles of FTS and zeolite ((hydro)cracking catalyst) can be combined inside one reactor by different configurations such as a homogenously mixed bed [16], a dual bed [17], or using a bed of hybrid catalyst pellets [15]. In a detailed study, different industrial zeolite topologies were physically mixed with Co/SiO_2 FTS catalyst and screened for their deactivation behavior. The deactivation rate of the acid component correlated with the zeolite pore dimensions, and in that respect H-ZSM-5 showed the highest stability in the FTS reaction environment [16, 27]. Moreover, dedicated hydroprocessing reactions over the (hydro)cracking component (of the physically mixed system) confirm that indeed hydrocracking and isomerization reactions are feasible under FTS process conditions and applied space velocities [16, 17, 28, 29]. Nevertheless, such direct observation of the acid-catalyzed reactions is more challenging once the FTS active metal (especially Co) is present in the bifunctional catalysts, where the hydrogenation activity of Co is stronger than that of Fe. Although this (de)hydrogenation functionality is required to promote the activity and stability of the hydrocracking component [30], Co is an active hydrogenolysis catalyst as well (contrary to noble metals) [31, 32]. It is, however, very unlikely for hydrogenolysis to take place effectively during FTS due to competitive adsorption of CO on the metal sites [33], yet this reaction will dominate in the absence of CO [34]. This controversial situation in simulating the FTS reaction environment to evaluate the acid-catalyzed reactions on one hand, and the dependence of intrinsic FTS selectivity to numerous factors, including the catalyst preparation method, type of support, process conditions, *etc.* [35] on the other, calls for extra caution to interpret the effect of the acid component in the product spectrum of bifunctional catalysts belonging to categories (*ii*) and (*iii*).

In this Chapter, two structurally different H-ZSM-5 containing Co-catalysts were synthesized and thoroughly characterized in order to understand their performance as a basis for the development of catalysts for the direct production of liquid fuel. The zeolite acts either as a coating on Co agglomerates (type *ii*) or as a mesoporous Co support (type *iii*). The comparison between both bifunctional configurations and conventional Co/SiO_2 catalyst allowed to demonstrate the importance of site proximity and catalyst structure on the performance of bifunctional FTS catalysts.

3.2. Experimental

3.2.1. Materials

Spherical particles (300–500 µm) of amorphous SiO_2 with specific surface area and pore volume of 293 m^2 g^{-1} and 1.35 cm^3 g^{-1}, respectively, was provided by Fuji Silysia Chemical Ltd. (CARiACT Q-10). Spherical SiO_2-TiO_2 hybrid support was supplied by Ishihara Sangyo Kaisha Ltd. (ST-B21, 87 m^2 g^{-1} surface area and 0.14 cm^3 g^{-1} pore volume). 1 M tetrapropylammonium hydroxide (TPAOH) solution, tetraethyl orthosilicate (TEOS), $Al(NO_3)_3 \cdot 9H_2O$, $Co(NO_3)_2 \cdot 6H_2O$, and NaOH pellets from Sigma-Aldrich were used as received.

Table 1 Abbreviations of samples, prepared by hydrothermal treatment and molar compositions of the corresponding synthesis solutions.

Sample		Synthesis solution composition (mol)				
Description	Abbreviation	TPAOH	$Al(NO_3)_3$	TEOS	EtOH	H_2O
H-ZSM-5 powder	H-ZSM-5	0.25	0.025	1	4	60
H-ZSM-5-coated Co	$Z/Co/SiO_2$	0.25	0.025	1	4	60
H-ZSM-5-coated Co/TiO_2	$Z/Co/SiO_2$-TiO_2	0.25	0.025	1	4	60
Hydrothermally-treated Co/SiO_2	Co/SiO_2-*hydro*	0	0	0	4	74
H-ZSM-5-coated Co without TEOS	$Z/Co/SiO_2$-*noTEOS*	0.25	0.025	0	4	72
silicalite-1-coated Co	$S/Co/SiO_2$	0.25	0	1	4	60
silicalite-1-coated Co without TEOS	$S/Co/SiO_2$-*noTEOS*	0.25	0	0	4	72

3.2.2. Catalyst synthesis

3.2.2.1. Zeolite-coated Co-catalysts

Spherical particles of SiO_2 as well as SiO_2-TiO_2 supports were loaded with 10 wt% of Co, applying incipient wetness impregnation of $Co(NO_3)_2 \cdot 6H_2O$ aqueous solution in one step. Before impregnation, the supports were dried overnight at 393 K. Impregnated samples were kept overnight in a desiccator at room temperature and dried at 393 K for 12 h. Finally, samples were calcined at 673 K for 2 h. For all the above-mentioned drying and calcination steps a heating rate of 2 K min^{-1} and static air conditions were applied.

H-ZSM-5 powder was synthesized by a hydrothermal procedure, employing $Al(NO_3)_3 \cdot 9H_2O$ and TEOS as the alumina and silica sources, respectively. To prepare the synthesis solution, TPAOH, H_2O, and ethanol (EtOH) were mixed and stirred for *ca.* 0.5 h. Subsequently, TEOS was added drop wise to the mixture and the solution was aged and stirred at 333 K for 2 h in a capped bottle to allow the hydrolysis of TEOS. Afterwards, the synthesis solution was sealed in a hydrothermal vessel (autoclave) and heated at 453 K for 24 h without rotation. Once the hydrothermal synthesis was completed, the vessel was cooled to room temperature and the zeolite powder was separated by filtration and washed until neutral pH was reached in the filtrate. The synthesis solution composition, which is analogous to that reported by Tsubaki *et al.* [36] is mentioned in Table 1 (see sample H-ZSM-5).

In order to coat the Co_3O_4 agglomerates by an H-ZSM-5 layer (H-ZSM-5-coated Co-catalyst), 10 wt% Co/SiO_2 particles of 300–500 µm were used and added to the above-mentioned synthesis solution with a ratio of 28.7 $g_{\text{synthesis solution}}\ g^{-1}_{Co/SiO2}$ (sample $Z/Co/SiO_2$ in Table 1). The hydrothermal synthesis was then carried out to form the zeolite coating, following a procedure similar to that of the H-ZSM-5 powder, only under autoclave rotation in this case.

To investigate the effect of this procedure on the intrinsic (chemical and catalytic) properties of the produced Co-catalyst, five additional reference samples were prepared by varying the synthesis mixture composition but with the same coating method. The abbreviations of these samples together with their synthesis solution compositions are reported in Table 1: for the synthesis of ‘Z/Co/SiO_2-TiO_2’, 10 wt% Co/SiO_2-TiO_2 particles (300–500 µm) were used as basis. ‘Co/SiO_2-*hydro*’ represents Co/SiO_2 particles, hydrothermally-treated in H_2O and EtOH when TPAOH and TEOS were substituted (excluded) in the synthesis solution by an equal mass of H_2O. For ‘Z/Co/SiO_2-*noTEOS*’, only TEOS was substituted by H_2O (equal mass). ‘S/Co/SiO_2’ is a silicalite-1-coated Co sample where the alumina source was excluded from the synthesis solution. ‘S/Co/SiO_2-*noTEOS*’ is the sample for which synthesis alumina source was excluded and TEOS was substituted by H_2O in equal mass. After the coating procedure, samples were washed and separated carefully from the loose MFI crystallites, applying sedimentation. After rinsing with H_2O, all the above-mentioned catalysts were kept overnight at room temperature, dried at 393 K for 12 h (2 K min^{-1}) and subsequently calcined at 773 K for 5 h (1 K min^{-1}) in static air.

3.2.2.2. Zeolite-supported Co-catalysts

Part of the synthesized H-ZSM-5 sample was calcined at 823 K for 10 h (2 K min^{-1}) in static air and modified to introduce mesoporous hierarchy applying the desilication approach reported by Groen *et al.* [37]. Alkaline treatment of H-ZSM-5 powder was carried out in 0.2 M NaOH aqueous solution ($\text{volume}_{\text{NaOH solution}}/\text{weight}_{\text{H-ZSM-5}} = 30.3\ cm^3\ g^{-1}$) under stirring at 338 K for 0.5 h. This treatment was followed by immediate quenching in an ice bath and centrifugation to separate the zeolite powder from the solution. The residue of desilicating agent was removed from the zeolite crystallites by subsequent redispersion in deionized water and centrifugation cycles until neutral pH was reached. In order to remove Na traces, a well-known poison for Co-based FTS catalysts [38], the zeolite was ion-exchanged with an excess of 0.1 M NH_4NO_3 at room temperature for 20 min in three additional cycles. Mesoporous H-ZSM-5, denoted as ‘*meso*H-ZSM-5’, was then dried at 393 K for 12 h and calcined at 823 K for 5 h.

Parent H-ZSM-5 as well as *meso*H-ZSM-5 samples were employed as catalyst supports and loaded with 10 wt% of Co, applying incipient wetness impregnation with aqueous solutions of $Co(NO_3)_2 \cdot 6H_2O$. Both supports were dried overnight at 393 K before impregnation. Only in the case of parent H-ZSM-5, two impregnation steps were required (due to its low pore volume) with intermediate sample drying at 333 K for 4 h. After impregnation, samples were kept overnight in a desiccator at room temperature and dried at 393 K for 12 h. Subsequently the catalysts were calcined at 673 K for 2 h. A heating rate of 2 K min^{-1} and static air conditions were applied for all the above-mentioned drying and calcination steps.

3.2.3. Characterization

N_2 physisorption was performed in an Autosorb-6B unit (Quantachrome Instruments) at liquid nitrogen temperature (77 K). Prior to the experiment, *ca.* 0.1 g of the samples were degassed overnight in an Autosorb Degasser unit (Quantachrome Instruments) under vacuum at 623 K.

Elemental analysis was performed with PerkinElmer Optima instruments. Samples were first digested in *ca.* 50 ml of 2.00% HCl, 1.25% H_2SO_4, and 1.00% HF mixture, in a microwave furnace. After dilution, analysis was done by the inductively coupled plasma optical emission spectrometry (ICP-OES).

The X-ray diffraction (XRD) patterns were recorded in Bragg-Brentano geometry by a Bruker D8 Advance diffractometer equipped with a Vantec position sensitive detector and graphite monochromator. Measurements were performed at room temperature, using monochromatic Co Kα radiation (λ = 0.179026 nm) in the 2θ region between 10° and 100° with a step size of 0.038°. All patterns were background-subtracted to eliminate the contribution of air scatter and possible fluorescence radiation.

Scanning electron microscopy (SEM) was performed on a Philips XL 20 microscope. Samples were coated with a layer of gold using an Edwards S150A sputter coater, to make them conductive prior to imaging. In order to study the catalyst particles cross-section, they were mixed with a resin inside a mold before gold sputtering. After solidification, the resin was removed from the mold and polished carefully to reach the particles cross-section. Energy dispersive X-ray (EDX) spectroscopy of the samples cross-section was analyzed by JEOL JSM-7500F field emission scanning electron microscope equipped with a Noran System Six spectral imaging system and a 30 mm^2 Novar detector. Transmission electron microscopy (TEM) was done by a FEI Tecnai TF20 microscope operated at 200 kV using a carbon coated Cu grid.

Temperature-programmed reduction by H_2 (TPR(H_2)) was performed on a homemade equipment. *Ca.* 0.1 g of Co-containing samples was mounted in a temperature controlled reactor where 27 cm^3_{STP} min^{-1} flow of 7.4% H_2 in Ar was fed over the samples. The reactor temperature was then ramped from room temperature to 1123 K with a heating rate of 10 K min^{-1} and the H_2 consumption was monitored by a TCD. Water was removed by a Permapure membrane dryer.

Temperature-programmed NH_3 desorption (NH_3-TPD) was measured by an AutoChem II Chemisorption Analyzer (Micromeritics). *Ca.* 0.2 g of the zeolite-containing samples was first degassed under He flow at 673 K for 1 h and then saturated with NH_3 at 373 K (or 473 K) during 1 h, using a flow of 1.65% NH_3 in He. The gas mixture was then switched back to He and the sample was purged at 373 K (or 473 K) for *ca.* 1 h to remove the weakly adsorbed NH_3 molecules until no ammonia was detected. TP desorption was subsequently recorded in He flow, from 373 (or 473 K) to

773 K. All flow rates were adjusted to 25 cm^3_{STP} min^{-1} and the heating rates were 10 K min^{-1} during different stages of the experiment.

3.2.4. Fischer-Tropsch synthesis

FTS experiments were performed on the six-flow fixed-bed microreactor setup described in Chapter 2. For all experiments, fresh catalyst (0.197–0.556 g) was fixed in the reactor inserts using quartz wool plugs. Samples were first activated *in situ* by 80 cm^3_{STP} min^{-1} of H_2 at 673 K for 12 h at atmospheric pressure followed by cooling to 453 K under H_2 flow. After increasing the pressure to the process value, CO was gradually introduced to the feed stream at 453 K in order to reach its final concentration in 1 h. Subsequently, the reactor was heated to the process temperature. A rate of 2 K min^{-1} was applied for all the heating/cooling steps.

During the experiment, heavy hydrocarbons (wax) were collected by gas/liquid separators at 448 K and reaction pressure. After expansion of the product flow to atmospheric pressure by back pressure controllers, lighter hydrocarbons and water were collected in cold traps at *ca.* 278 K. After separation from water, these liquid hydrocarbons as well as the wax were weighted, dissolved in CS_2, and analyzed offline by a simulated distillation (SimDis) GC (Hewlett Packard 5890, Series II) equipped with an FID and HP-1 column (7.5 m × 0.53 mm, film thickness 2.65 µm), using He as carrier gas. During the analysis, the oven temperature was ramped from 308 to 623 K (14 K min^{-1}) and kept at the final temperature for 5 min.

N_2, CO, and CO_2 as well as light hydrocarbons in the gas phase were analyzed online by a Compact GC (Interscience), equipped with three columns and detectors in parallel, applying He as carrier gas. In the first column (Carboxen 1010, 10 m × 0.32 mm) N_2, CO, CH_4, and CO_2 were separated at 333 K and analyzed by TCD. In the second column (Al_2O_3/KCl, 10 m × 0.32 mm) and FID, separation between all C1–C4 components was achieved at 434 K. In the third column (RTx-1 0.5 µm, 15 m × 0.32 mm) C5–C10 hydrocarbons were separated at 353 K and analyzed by FID.

A pseudo-steady catalytic behavior was attained after 20 h on-stream when selectivity data were collected. CO conversion, carbon selectivity, and molar fraction of each product were defined by Eqs. (1), (2), and (3), respectively, where X_{CO} stands for CO conversion, F indicates the molar flow, S is the carbon selectivity toward a product with n carbon atoms and y is the molar fraction of a hydrocarbon Cn.

$$X_{\mathrm{CO}} = \frac{F_{\mathrm{in,CO}} - F_{\mathrm{out,CO}}}{F_{\mathrm{in,CO}}} \times 100 \quad (1), \qquad S_{\mathrm{C}n} = \frac{nF_{\mathrm{C}n}}{F_{\mathrm{CO_2}} + \sum_{n=1}^{N} nF_{\mathrm{C}n}} \times 100 \quad (2), \qquad y_{\mathrm{C}n} = \frac{F_{\mathrm{C}n}}{\sum_{n=1}^{N} F_{\mathrm{C}n}} \quad (3)$$

3.3. Results

3.3.1. Transformation of Co/SiO_2 to zeolite-coated Co-catalyst

SEM micrographs of the synthesized H-ZSM-5 powder as well as the zeolite-coated catalysts are shown in Figure 1 and 2. In the absence of the supported Co_3O_4 particles (Co/SiO_2 or Co/SiO_2-TiO_2) in the zeolite synthesis solution, H-ZSM-5 crystallites of about 3 µm are formed by the hydrothermal procedure, described in Section 3.2.2.1 (see Figure 1a). Once the supported Co_3O_4 particles are added to the mixture and subjected to the synthesis, their morphology change due to formation of a coating layer which is to some extent inter-grown (*cf.* Figure 1b and c). SiO_2 is not very stable under hydrothermal conditions and is prone to dissolution at high pH [39, 40], so partial dissolution of the SiO_2 support in the basic zeolite synthesis mixture can be expected upon hydrothermal treatment at 453 K. In order to verify this, Co/SiO_2-TiO_2 was used in the synthesis. Since TiO_2 is much more stable under similar conditions, it can be employed as an internal standard in the supported Co_3O_4 particles composition. Elemental analysis by ICP-OES reveals that indeed the Si/Ti ratio of Co/SiO_2-TiO_2 decreases from 3.4 to 2.9 for $Z/Co/SiO_2$-TiO_2 after the hydrothermal synthesis, while the Co/Ti ratio stays unchanged, indicating that Co remains in the structure of the coated catalyst.

Figure 2 shows similar morphological changes of Co/SiO_2 after the coating procedure: while the hydrothermal treatment in the absence of the zeolite precursors does not affect the morphology of the particles and the SEM micrographs of Co/SiO_2-*hydro* (Figure 2b and h) look very similar to that of the Co/SiO_2 (Figure 2a and g), addition of TPAOH to the synthesis solution results in transformation of SiO_2 into crystallites similar to MFI structure. This transformation even occurs when excluding the additional Si source (TEOS), indicating that Co/SiO_2 can supply Si to the zeolite synthesis solution (compare Figure 2i and k with Figure 2j and l). In the absence of an Al source ($Al(NO_3)_3 \cdot 9H_2O$), the crystallites tend to grow, forming well developed silicalite-1 crystals on the surface of $S/Co/SiO_2$-*noTEOS* (see Figure 2f and l).

XRD analysis confirms the presence of MFI topology in the zeolite powder as well as in the Co-containing coated samples (Figure 3). In the latter samples, Co_3O_4 reflections are also identified. In the case of $Z/Co/SiO_2$-*noTEOS*, the MFI peak intensities are somewhat reduced relative to those of Co_3O_4,

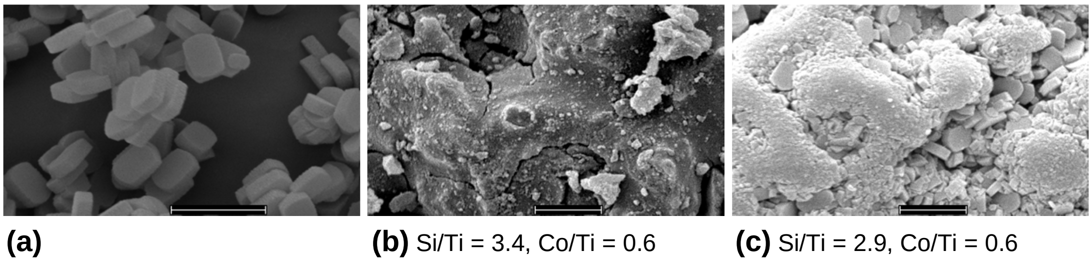
(a) **(b)** Si/Ti = 3.4, Co/Ti = 0.6 **(c)** Si/Ti = 2.9, Co/Ti = 0.6

Figure 1. SEM micrographs of H-ZSM-5 (a), Co/SiO_2-TiO_2 (b), and $Z/Co/SiO_2$-TiO_2 (c). Scale bars correspond to 5 µm.

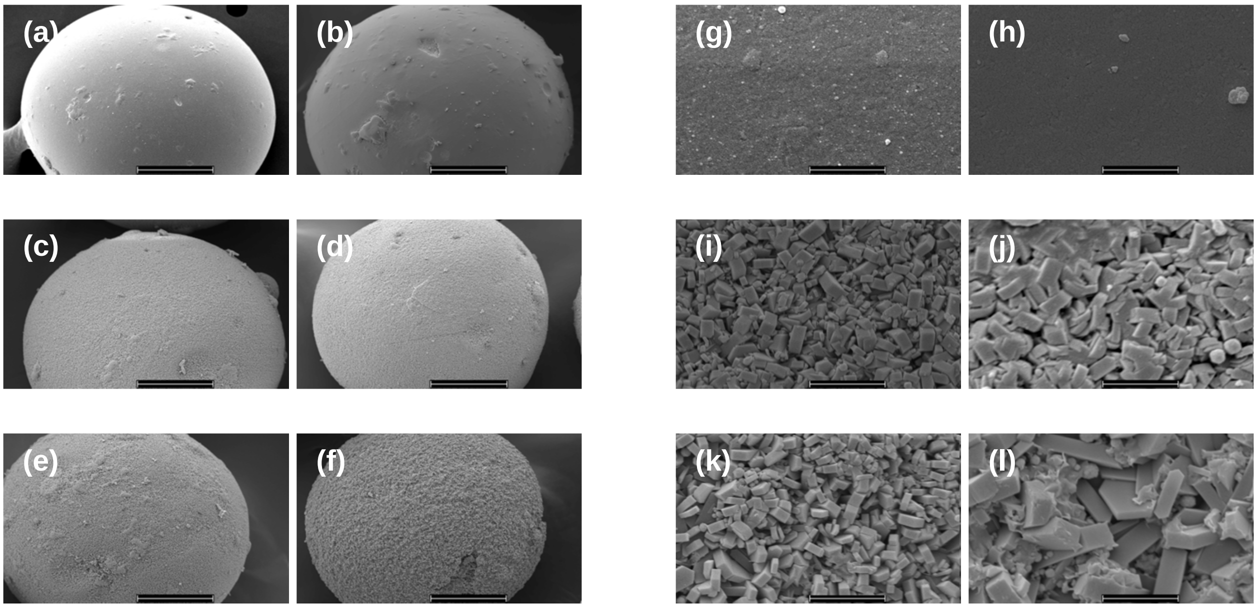

Figure 2. SEM micrographs of Co/SiO_2 (a and g), Co/SiO_2-*hydro* (b and h), $Z/Co/SiO_2$ (c and i), $Z/Co/SiO_2$-*noTEOS* (d and j), $S/Co/SiO_2$ (e and k), and $S/Co/SiO_2$-*noTEOS* (f and l). Scale bars correspond to 100 µm for the left column and 5 µm for the right column micrographs.

implying a lower concentration of zeolite phase in $Z/Co/SiO_2$-*noTEOS* as compared to the other Co containing catalysts. So, the coating layers observed in the SEM micrographs (Figure 2) are H-ZSM-5 in the case of $Z/Co/SiO_2$ and $Z/Co/SiO_2$-*noTEOS* samples and silicalite-1 in $S/Co/SiO_2$ and $S/Co/SiO_2$-*noTEOS*.

N_2 physisorption results (Table 2) reveal that the hydrothermal treatment of Co/SiO_2 in H_2O and EtOH results in surface area loss for Co/SiO_2-*hydro* and a slight increase in its pore volume. When zeolite precursors (including the structure directing agent, TPAOH) are added to the synthesis solution, total surface area of samples increases while the mesopore surface area of Co/SiO_2 decreases by a factor of 10, from 203 to 25 $m^2\ g^{-1}$ for $Z/Co/SiO_2$. A similar trend is observed for all Co-containing catalysts when they are coated with either H-ZSM-5 or silicalite-1. Further, the sample's micropore volume increases from 0.01 to *ca.* 0.1 $cm^3\ g^{-1}$ at the cost of a decrease in their mesopore volume by two orders of magnitude. Clearly, the textural properties of the coated catalysts evolve toward those of the microporous H-ZSM-5. The only exception showing a texture intermediate between Co/SiO_2-*hydro* and H-ZSM-5 is $Z/Co/SiO_2$-*noTEOS,* having the lowest MFI peak intensities in XRD. From the SEM image of the latter sample (Figure 2j) and XRD patterns, it must be concluded that the H-ZSM-5 crystals are formed through transformation of SiO_2 (*cf.* top left area of Figure 2j and h). This transition behavior is noticed in the corresponding N_2 physisorption isotherms as well (see Figure B1/Appendix B) and attributed to the presence of Al, which slows down the crystallization rate of zeolites [41], especially in the absence of TEOS. Figure B1/Appendix B illustrates that the type IV isotherm of SiO_2 changes toward type I after being transformed into the zeolite coating. Nevertheless, the coated

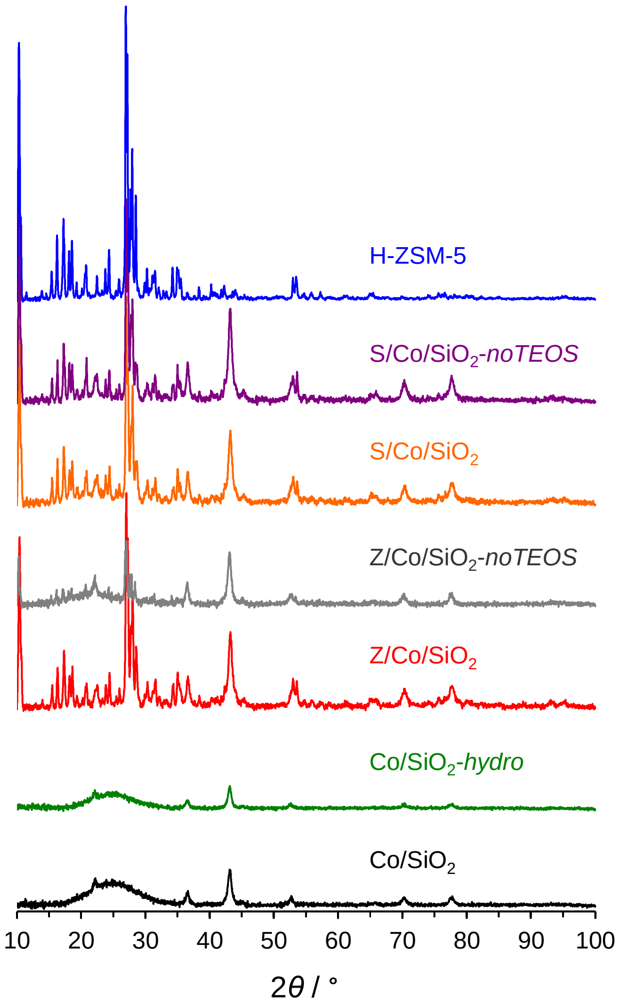

Figure 3. XRD patterns of the samples.

samples still contain an extent of mesoporosity as revealed by the presence of a hysteresis loop in their isotherms which is totally absent in the case of H-ZSM-5.

As visualized by the cross-sectional SEM micrographs of particles the hydrothermal treatment alone does not severely destroy the silica support (*cf.* Figure 4a and b) and Co/SiO$_2$-*hydro* has a morphology very similar to that of Co/SiO$_2$ (in line with what mentioned earlier). However, changes in the surface area and pore volume of Co/SiO$_2$ (see above) suggest a slight dissolution of SiO$_2$ at the hydrothermal conditions. Figure B2/Appendix B shows that the mesopores of Co/SiO$_2$-*hydro* are about four times larger than those of Co/SiO$_2$. The SiO$_2$ dissolution is promoted by addition of the zeolite structure directing agent TPAOH which increases the pH of the hydrothermal environment. As a result, a spongy structure is observed inside the Z/Co/SiO$_2$ particles (Figure 4c). In the latter case, severe dissolution of SiO$_2$ transforms the mesopores into macropores which cannot be detected anymore by N$_2$ physisorption; although, for Z/Co/SiO$_2$-*noTEOS* pores larger than 100 nm can still be noticed in the pore size distribution (Figure B2/Appendix B). A closer look at the edge of Z/Co/SiO$_2$ particle cross-

Table 2 Textural and chemical properties of MFI coated catalysts and their corresponding reference samples.

Sample	S / m^2 g^{-1}		V / cm^3 g^{-1}			Co		Si/Al[f]
	total[a]	meso[b]	total[c]	micro[d]	meso[e]	wt%[f]	d_{Co}[g] / nm	
SiO_2	293	248	1.35	0.02	1.34	n.a.[h]	n.a.	n.a.
Co/SiO_2	231	203	1.04	0.01	1.03	9.3	15	n.a.
Co/SiO_2-*hydro*	101	81	1.11	0.01	1.11	9.9	16	n.a.
$Z/Co/SiO_2$	319	25	0.18	0.13	0.05	13.8	13	193
$Z/Co/SiO_2$-*noTEOS*	134	20	0.12	0.05	0.07	23.6	14	14
$S/Co/SiO_2$	321	25	0.17	0.13	0.04	14.4	14	n.a.
$S/Co/SiO_2$-*noTEOS*	296	27	0.18	0.12	0.06	22.9	14	n.a.
H-ZSM-5	353	12	0.17	0.14	0.03	n.a.	n.a.	41

[a] BET surface area; [b] Mesopore surface area obtained from the *t*-plot applied to the N_2 isotherm; [c] Total pore volume; [d] Micropore volume obtained from the *t*-plot; [e] Mesopore volume calculated as $V_{meso} = V_{total}-V_{micro}$; [f] Obtained from ICP-OES; [g] Co crystallite size calculated from $d(Co^0) = 0.75d(Co_3O_4)$, where $d(Co_3O_4)$ is derived from XRD, applying the Scherrer equation; [h] Not applicable.

section in Figure 5 reveals that its spongy structure is confined in a 3 µm outer shell which holds the catalyst particle together. The hydrothermal transformation of mesoporous silica spheres into hollow zeolite shells is reported in the literature and promoted by attaching zeolite crystallites to the silica particles prior to the hydrothermal synthesis [42-44]. According to EDX analysis, a high concentration of Co is located inside this shell (*cf.* Figure 5b and c).

Consistent with the N_2 physisorption results, TEM images in Figure 6 illustrate that most of the mesoporosity present in Co/SiO_2 disappears in the case of $Z/Co/SiO_2$ where agglomerates of individual Co_3O_4 crystallites are enwrapped in the zeolite coating (*cf.* Figure 6a and b). The above results demonstrate the preservation of the Co/SiO_2 particle shape, in which SiO_2 acts as both mold and Si precursor, transforming into zeolite. As a result, an H-ZSM-5 coating on the Co-catalyst is formed at the level of its active metal crystallites. Apparently, the Co_3O_4 crystallites do not sinter during the coating procedure as the Co crystallite size barely changes during the synthesis (see Table 2). The Co loading on Co/SiO_2 and Co/SiO_2-*hydro* is similar (around 9.6 wt%), while it increases to 13.8 and 23.6 wt% over $Z/Co/SiO_2$ and $Z/Co/SiO_2$-*noTEOS*, respectively (a similar trend is observed for $S/Co/SiO_2$ and $S/Co/SiO_2$-*noTEOS* as well). This considerable increase in the loading is due to the fact that while Co stays in the catalyst structure, part of the dissolved SiO_2 is transformed into loose zeolite crystals that were separated from the spherical catalyst particles. These zeolite particles did not contain Co.

TPR(H_2) profiles of all the Co-catalysts are plotted in Figure 7. Reduction of Co_3O_4 to metallic cobalt takes place through intermediate formation of CoO [45, 46]. These two reduction steps are clearly observed over Co/SiO_2 where Co^{3+} reduces around 640 K to Co^{2+} which further reduces to Co^0 around 685 K. The small shoulder at 615 K may be attributed to the reduction of very active Co species of small size on the catalyst surface [47]. This shoulder disappears in the case of Co/SiO_2-*hydro*. Other than that, there are no major differences between the TPR(H_2) profiles of Co/SiO_2-*hydro*

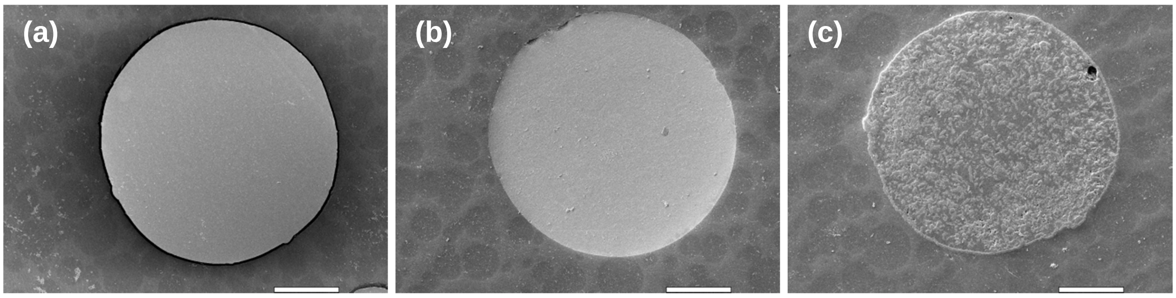

Figure 4. Cross-sectional SEM micrographs of Co/SiO_2 (a), Co/SiO_2-*hydro* (b), and Z/Co/SiO_2 (c) particles. Scale bars correspond to 100 µm.

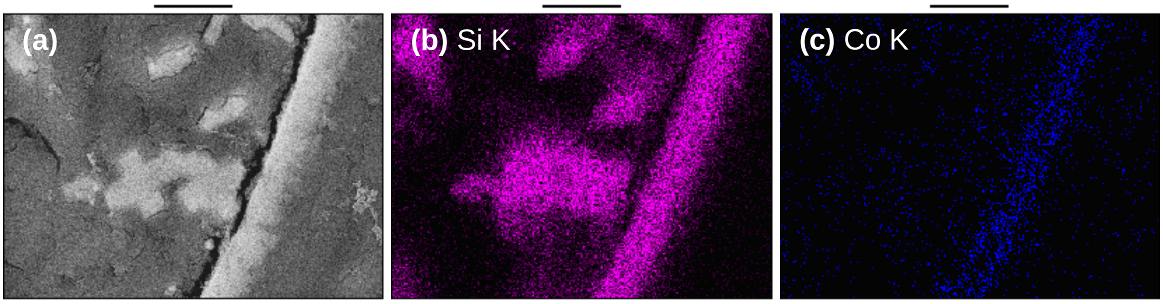

Figure 5. Cross-sectional SEM micrograph (a) and EDX analysis (b and c) of Z/Co/SiO_2. Scale bars correspond to 5 µm.

and Co/SiO_2. In the case of the zeolite-containing catalysts, the reduction shifts toward higher temperatures. As compared with Co/SiO_2 and Co/SiO_2-*hydro*, the higher H_2 consumption of the zeolite-containing catalysts (suggested by their larger reduction peaks), points to their higher Co loading and confirms the elemental analysis results.

NH_3-TPD profiles of H-ZSM-5 powder as well as Z/Co/SiO_2 and S/Co/SiO_2 samples are depicted in Figure 8. Two NH_3 desorption peaks are observed for H-ZSM-5 and Z/Co/SiO_2. The peak appearing below 500 K, weakly visible in the pattern of S/Co/SiO_2 as well, is known to arise from weakly

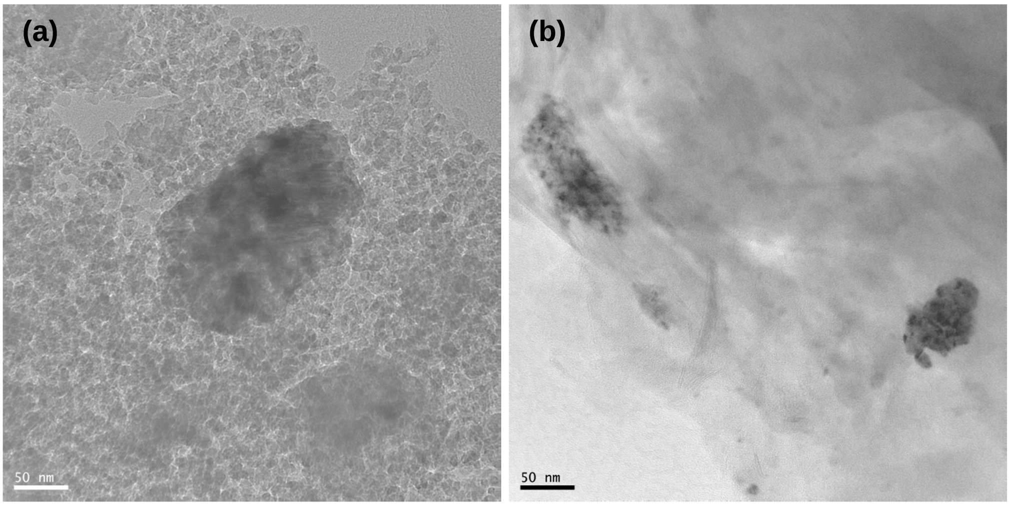

Figure 6. TEM images of Co/SiO_2 (a) and Z/Co/SiO_2 (b) before activation. Scale bars correspond to 50 nm.

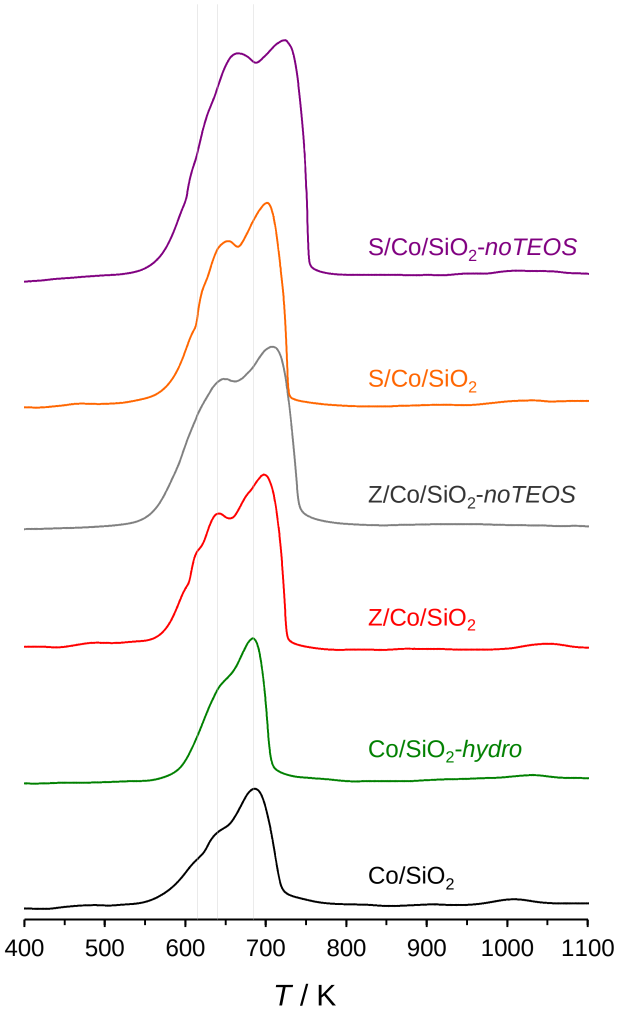

Figure 7. TPR(H_2) profiles (10 K min^{-1}) of Co containing samples.

adsorbed NH_3 molecules, and does not originate from the zeolite acid sites [29]. The characteristic peak reflecting Brønsted acidity is observed at 650–700 K over H-ZSM-5 [48]. This peak shifts to 565–615 K over Z/Co/SiO_2 and is totally absent in the case of S/Co/SiO_2. Although the Si/Al ratio of Z/Co/SiO_2 is about five times greater than that of H-ZSM-5 (193 *versus* 41, see Table 2), the Brønsted acid sites are clearly present in its structure but with a lower strength as compared to the latter catalyst.

3.3.2. Mesoporous zeolite-supported Co-catalyst

Employing Co/SiO_2 as the supported Co_3O_4 precursor followed by a partial hydrothermal transformation, results in the formation of an H-ZSM-5 coating over the Co. This FTS catalyst possesses a combination of zeolite microporosity and a certain mesoporosity in the inter-crystalline space (N_2 physisorption results in Table 2, Figure B1 and B2/Appendix B). In order to synthesize a ‘carbon copy’ of the previous catalyst, where Co would be on top of the zeolite rather than covered by it, mesostructure was created in the crystallites of H-ZSM-5 before being used as Co support.

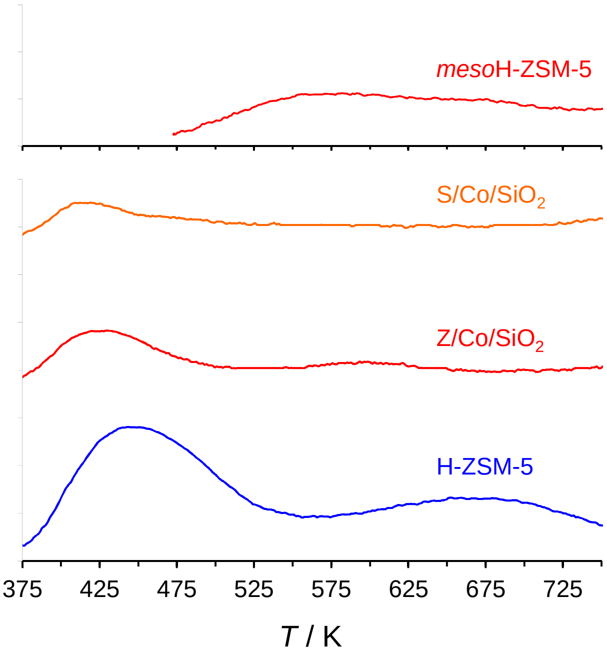

Figure 8. NH_3-TPD profiles (10 K min^{-1}) of zeolite-containing samples where NH_3 was adsorbed at 373 K over H-ZSM-5, Z/Co/SiO$_2$, and S/Co/SiO$_2$ and it was adsorbed at 473 K over *meso*H-ZSM-5.

Textural properties of *meso*H-ZSM-5 and the corresponding supported catalysts are reported in Table 3. By the alkaline treatment the mesopore surface area of the parent H-ZSM-5 increases from 12 to 114 m^2 g^{-1} and its mesopore volume increases by a factor of 10 from 0.03 to 0.21 cm^3 g^{-1}. *meso*H-ZSM-5 displays a type IV N_2 physisorption isotherm with a well-developed hysteresis loop, closing at *ca.* 0.42 relative N_2 pressure, suggesting a high degree of hierarchy in its structure which includes large cavities communicated with smaller mesopores (see Figure B3/Appendix B) [49]. On the other hand, both the microporous and mesoporous zeolites have the same micropore volume (0.14 cm^3 g^{-1}, Table 3) which confirms that the desilication procedure did not result in severe amorphization of the zeolite crystallites.

Elemental analysis shows that the Co loading is the same on both Co/H-ZSM-5 and Co/*meso*H-ZSM-5 and equal to 10.1 wt%. The Co crystallite size has decreased considerably on the latter catalyst,

Table 3 Textural and chemical properties of zeolite-supported catalysts and *meso*H-ZSM-5.

Sample	*S* / m^2 g^{-1}		*V* / cm^3 g^{-1}			Co		Si/Al[f]
	total[a]	meso[b]	total[c]	micro[d]	meso[e]	wt%[f]	d_{Co}[g] / nm	
Co/H-ZSM-5	355	21	0.19	0.14	0.05	10.1	17	42
*meso*H-ZSM-5	448	114	0.35	0.14	0.21	n.a.[h]	n.a.	n.d.[i]
Co/*meso*H-ZSM-5	376	88	0.28	0.12	0.16	10.1	11	26

[a] BET surface area; [b] Mesopore surface area obtained from the *t*-plot applied to the N_2 isotherm; [c] Total pore volume; [d] Micropore volume obtained from the *t*-plot; [e] Mesopore volume calculated as $V_{meso} = V_{total}-V_{micro}$; [f] Obtained from ICP-OES; [g] Co crystallite size calculated from $d(Co^0) = 0.75d(Co_3O_4)$, where $d(Co_3O_4)$ is derived from XRD, applying the Scherrer equation; [h] Not applicable; [i] Not determined.

which implies an improved dispersion over the support with the higher degree of mesoporosity (see Table 3).

NH_3-TPD profile of *meso*H-ZSM-5 is depicted in Figure 8. In order to eliminate the contribution of weakly adsorbed NH_3 molecules, adsorption of ammonia was performed at 473 K. The Brønsted acidity of *meso*H-ZSM-5 is weakened upon desilication (as compared to the parent zeolite) and the acidic strength of this sample is to an extent similar to Z/Co/SiO_2. In this case, the desorption peak of NH_3 is centered around 565 K (analogous to Z/Co/SiO_2) with a shoulder at 675 K. This shoulder corresponds to the stronger Brønsted acid sites, arising from domains in the structure of the original H-ZSM-5 sample, which are partly preserved [50].

3.3.3. Catalyst performance in Fischer–Tropsch synthesis

3.3.3.1. MFI coated Co-catalysts

FTS was performed over the synthesized catalysts after separating the spherical catalyst particles from the loose zeolite crystals that were also formed. Since the Co loading of some samples changed by the coating procedure, catalyst performance testing was carried out with a fixed Co mass rather than with an equal catalyst mass.

Figure 9 compares the carbon selectivity (Figure 9a) as well as the molar distribution (Figure 9b) of FTS hydrocarbons, produced over Co/SiO_2, Co/SiO_2-*hydro*, Z/Co/SiO_2, and a physical mixture of Co/SiO_2 with H-ZSM-5 (Co/SiO_2 + H-ZSM-5). In the latter catalytic system, pressed H-ZSM-5 particles of 300–500 µm were well mixed with Co/SiO_2 particles of the same size, so that the final catalyst mixture contained the same amount of Al as in Z/Co/SiO_2.

FTS results show that the CO conversion is comparable for all the above-mentioned catalysts at 533 K, 10 bar total pressure and feed composition $H_2/CO = 2$ (insert in Figure 9a). C1 selectivity of Co/SiO_2-*hydro* is 7% higher than that of Co/SiO_2. Furthermore, a relative decrease in the chain growth probability α of the former catalyst (Figure 9b) reveals that aging Co/SiO_2 in a hydrothermal environment slightly lowers the catalyst selectivity to long chain hydrocarbons. When the zeolite coating is formed on the Co-catalyst, a considerable deviation from the ASF distribution is observed above C7, resulting in an effective decrease in C12+ selectivity of Z/Co/SiO_2 in comparison with Co/SiO_2 (Figure 9a). The fact that C1 molar fraction over Z/Co/SiO_2 is lower than that over the Co/SiO_2-*hydro* (see insert Figure 9b), implies that this further deviation from the ASF distribution is not a regular decrease in α and has to do with the acid nature of the coating.

The product spectrum of Co/SiO_2 does not change when it is physically mixed with H-ZSM-5 (Co/SiO_2 + H-ZSM-5), although a slight decrease in selectivity to higher hydrocarbons is observed (Figure 9). Considering that the Brønsted acidity of H-ZSM-5 is even stronger than that of Z/Co/SiO_2

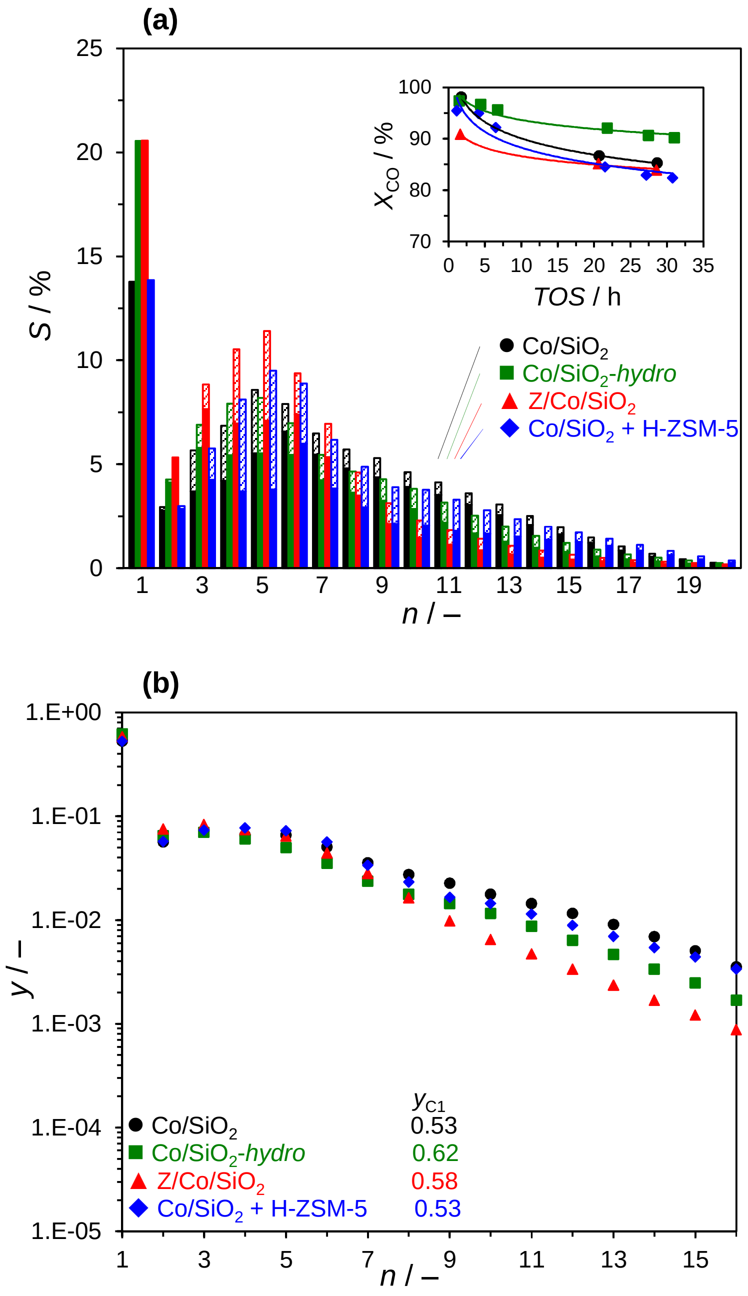

Figure 9. Carbon selectivity (a) and fractional molar composition (b) of FTS products after 20 h on-stream at 533 K, 10 bar total pressure, feed composition H_2/CO = 2, and $GHSV$ = 25.8 m^3_{STP} kg^{-1}_{Co} h^{-1}; ■: *n*-paraffins; ▨: sum of isoparaffins and olefins; y_{C1}: methane molar fraction. Insert in (a) shows the time-on-stream (*TOS*) evolution of CO conversion.

(Figure 8), this result shows that the close vicinity of the FTS active phase and acid sites in the zeolite coating is a crucial factor which increases the effectiveness of Z/Co/SiO$_2$ in lowering the C12+ production. This observation is consistent with what has been reported in literature for similar catalyst structures [18-22].

TEM images of Z/Co/SiO$_2$ suggest that the H-ZSM-5 coating is located over the Co active phase, rather than around the original precursor particle (Figure 6b). So to demonstrate this, Z/Co/SiO$_2$

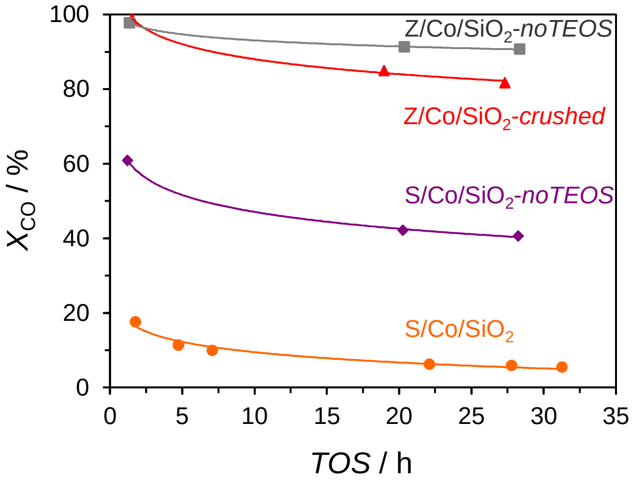

Figure 10. Time-on-stream (*TOS*) evolution of CO conversion during FTS at 533 K, 10 bar total pressure, feed composition H_2/CO = 2, and *GHSV* = 25.8 m^3_{STP} kg^{-1}_{Co} h^{-1}.

catalyst particles were crushed and re-pelletized to their original size ('Z/Co/SiO$_2$-*crushed*') prior to the FTS reaction. Time-on-stream (*TOS*) evolution of CO conversion and carbon selectivity of this sample are included in Figure 10 and 11, respectively, where reaction conditions are similar to those in Figure 9. The catalytic performance of Z/Co/SiO$_2$ does not change considerably upon crushing the particles. This result reveals that the zeolite coating is effective at the level of Co agglomerate size (nm) rather than the catalyst particle size (μm).

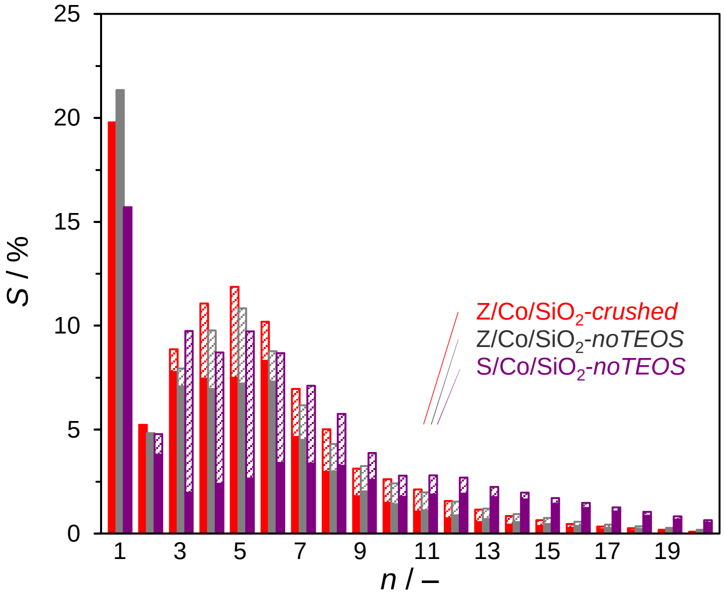

Figure 11. Carbon selectivity of FTS products after 20 h on-stream at 533 K, 10 bar total pressure, feed composition H_2/CO = 2, and *GHSV* = 25.8 m^3_{STP} kg^{-1}_{Co} h^{-1}; ■: *n*-paraffins; ▨: sum of isoparaffins and olefins.

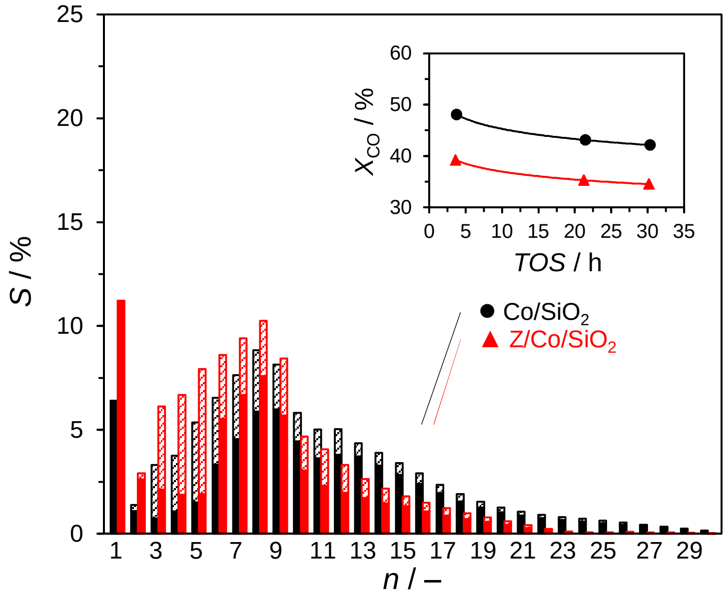

Figure 12. Carbon selectivity of FTS products after 20 h on-stream at 533 K, 10 bar total pressure, feed composition H_2/CO = 1, and *GHSV* = 25.8 m^3_{STP} kg^{-1}_{Co} h^{-1}; ■: *n*-paraffins; ▨: sum of isoparaffins and olefins. Insert shows the time-on-stream (*TOS*) evolution of CO conversion.

Absence of the acid functionality in the case of silicalite-1-coated Co samples leads to a dramatic drop in their activity, where S/Co/SiO_2 deactivates almost in the initial stage of the reaction and the CO conversion of S/Co/SiO_2-*noTEOS* decreases by *ca.* 50% as compared to Z/Co/SiO_2-*noTEOS* (Figure 10). TGA analysis (Figure B4/Appendix B) shows that upon heating in an oxidizing atmosphere, the spent S/Co/SiO_2 loses more weight than the spent Z/Co/SiO_2. This reveals that in spite of its much lower activity and productivity during the FTS reaction, more carbonaceous species stay within the particles of S/Co/SiO_2.

Carbon selectivity and CO conversion of Co/SiO_2 and Z/Co/SiO_2 are compared in Figure 12 at reaction conditions similar to those in Figure 9–11, but at the more demanding H_2/CO feed ratio of 1. Lowering the H_2/CO ratio promotes the wax (C21+) formation over Co/SiO_2, whereas this fraction is minor for Z/Co/SiO_2. CO conversion over Z/Co/SiO_2 is 8% lower than that over Co/SiO_2 (Figure 12 inset). In this case, since H_2 is the limiting reactant, CO conversion cannot exceed 50% (unless water-gas-shift reaction is catalyzed). On the other hand, decreasing the H_2 concentration lowers the rate of hydrogenation reactions and therefore, much less C1 is produced than at an H_2/CO feed ratio of 2.

3.3.3.2. *H-ZSM-5-supported Co-catalysts*

FTS results over H-ZSM-5 directly applied as Co support (Co/H-ZSM- 5) at 513 K, 15 bar total pressure, and feed composition H_2/CO = 2 are reported in Figure 13 and Table 4. The CO conversion level of Co/H-ZSM-5 is considerably lower than that of Co/SiO_2 while it is similar to Z/Co/SiO_2 under

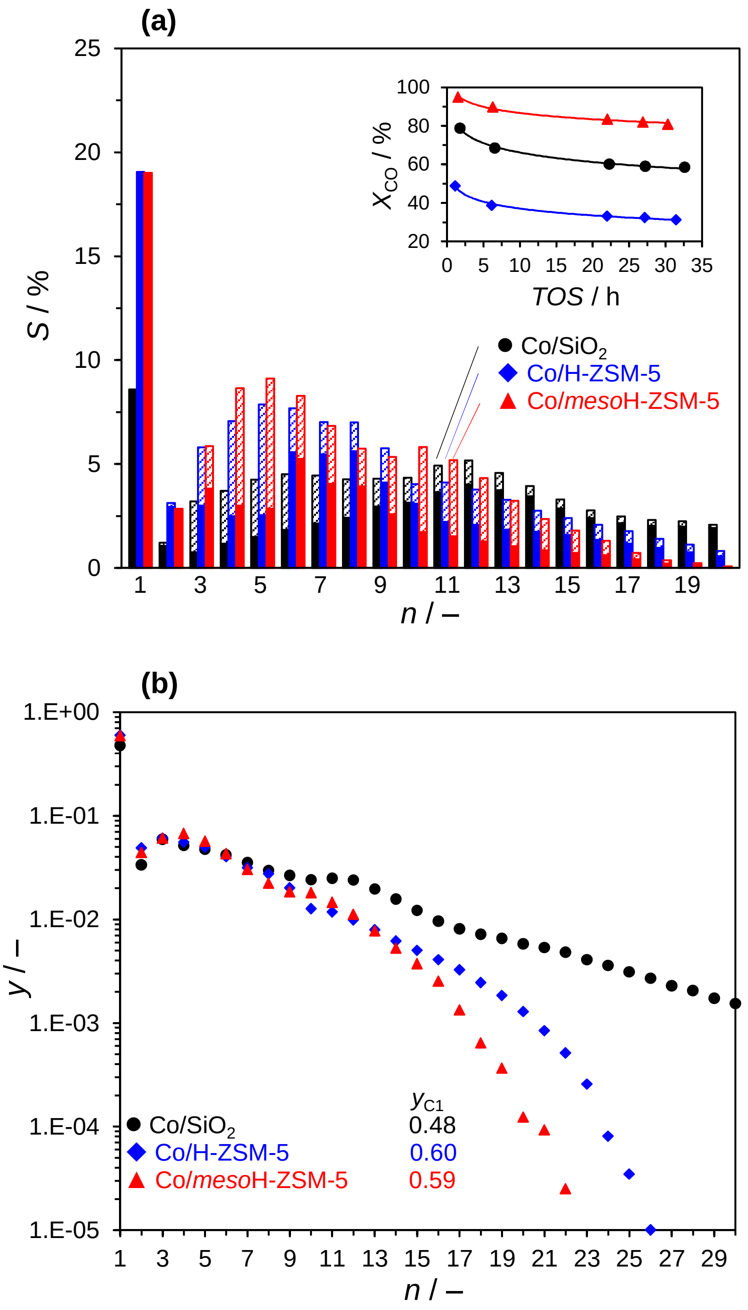

Figure 13. Carbon selectivity (a) and fractional molar composition (b) of FTS products after 20 h on-stream at 513 K, 15 bar total pressure, feed composition $H_2/CO = 2$, and $GHSV = 2.4\ m^3_{STP}\ kg^{-1}_{cat}\ h^{-1}$; ■: *n*-paraffins; ▨: sum of isoparaffins and olefins; y_{C1}: methane molar fraction. Insert in (a) shows the time-on-stream (*TOS*) evolution of CO conversion.

the reaction conditions (see Table 4 and the insert in Figure 13). As compared with Co/SiO$_2$, production of C12+ is reduced over both Z/Co/SiO$_2$ and Co/H-ZSM-5, while the coated catalyst is more effective (Table 4).

Upon introduction of mesoporosity to the H-ZSM-5 crystallites, CO conversion increases dramatically from 32% over Co/H-ZSM-5 to 82% over Co/*meso*H-ZSM-5. Moreover, the latter catalyst is more efficient in lowering the C12+ production, as indicated by the carbon selectivity and

Table 4 CO conversion after 20 h on-stream and carbon selectivities of different FTS product fractions.

Process Conditions	Catalyst	X_{CO} / %	S / %					O/P (C2-4)[a]
			C1	C2–C4	C5–C11	C12+	CO_2	
533 K, 10 bar, H_2/CO = 2, 25.8 m^3_{STP} kg^{-1}_{Co} h^{-1}	Co/SiO_2	87	14	15	43	15	13	0.45
	Co/SiO_2-*hydro*	91	21	19	37	11	13	0.24
	Z/Co/SiO_2	85	21	25	40	6	9	0.23
	Z/Co/SiO_2-*crushed*	85	20	25	42	6	7	0.22
	Z/Co/SiO_2-*noTEOS*	91	21	23	38	7	12	0.18
	S/Co/SiO_2-*noTEOS*	42	16	23	41	15	5	1.84
	Co/SiO_2 + H-ZSM-5	83	14	17	40	14	15	0.55
533 K, 10 bar, H_2/CO = 1, 25.8 m^3_{STP} kg^{-1}_{Co} h^{-1}	Co/SiO_2	43	6	8	47	33	5	1.90
	Z/Co/SiO_2	35	11	16	53	16	4	1.37
513 K, 15 bar, H_2/CO = 2, 2.4 m^3_{STP} kg^{-1}_{cat} h^{-1}	Co/SiO_2	59	9	8	31	49	4	1.72
	Z/Co/SiO_2	31	21	20	40	17	2	0.64
	Co/H-ZSM-5	32	19	16	43	21	1	0.89
	Co/*meso*H-ZSM-5	82	19	17	46	15	3	0.80

[a] Olefin to paraffin ratio of C2–C4.

ASF distribution (Figure 13). Taking into consideration that the *y*-axis in Figure 13b is presented in logarithmic scale, hydrocarbon molar fractions above C16 deviate progressively from the ASF distribution over Co/*meso*H-ZSM-5. Therefore, while being the most active sample, this mesoporous H-ZSM-5-supported Co-catalyst is also the most selective one to the gasoline-range, as compared to the other bifunctional catalysts, including H-ZSM-5-coated Co (see Table 4).

3.4. Discussion

With regard to the recent literature on bifunctional FTS catalysts, H-ZSM-5 is one of the most promising zeolite candidates for use in breaking the ASF selectivity and thus increasing the production of liquid fuels through one-step FTS, for the following reasons: (1) it is one of the few zeolites industrially produced and applied for acid-catalyzed hydrocarbon conversion reactions [51], (2) due to its narrow channel type structure and well distributed acid sites, it represents a (relatively) stable catalytic performance, especially at LTFT process conditions [16, 27], and (3) besides acid-catalyzed cracking, it has a fair isomerization and oligomerization activity at low temperatures [52] which is essential to increase the octane number in case of gasoline cut and improve the cold flow properties of diesel [34].

The concept of coating the FTS catalyst particles with zeolites to tune their product selectivity was first introduced by Tsubaki and co-workers [53, 54] in analogy to earlier work for other reactions [55, 56]. A series of hydrothermal procedures were applied to synthesize acidic or inert zeolite coatings (H-ZSM-5 [18, 36, 53, 54, 57-60], H-Beta [19, 38, 61], and silicalite-1 [62]) over supported cobalt [18, 19, 38, 53, 54, 57-59, 61] and iron [36, 62] catalysts. It is reported that the direct exposure of conventional FTS catalyst particles to the zeolite synthesis solution followed by hydrothermal treatment results in formation of a so-called ‘core-shell’ structure for the subsequent catalyst, where the FTS catalyst ‘core’ is enwrapped in an outer zeolitic ‘shell’. In spite of interesting catalytic results, the catalyst structure description was mainly based on a qualitative characterization by cross-sectional SEM micrographs of the particles, hardly providing detailed information on the sample structure at the Co crystallite level. The physical appearance of coated catalysts depends on parameters such as size of the precursor catalyst particle (‘core’) and its material, in combination with the hydrothermal synthesis conditions. At fixed synthesis durations, less zeolite is reported to form over larger Co/SiO_2 particles [57]. This was attributed to the lower accessible/external surface area of larger metal supported SiO_2 pellets [57, 60] which gave a core-shell appearance to the resulting catalyst. The alternative is selecting supported catalysts that do not transform into zeolites, such as Co/Al_2O_3 [19, 38, 61]. Nevertheless, there is no evidence that Co does not build up in the outer zeolitic ‘shell’ and/or zeolite layers do not form inside the porous structure of these supports after their exposure to the synthesis solution and hydrothermal synthesis. Our work with Co/SiO_2, applying similar hydrothermal procedures for the formation of the zeolite coating on various reference samples, demonstrates that indeed a shell is formed around the catalyst particle and that the core of the particle is partly consumed for this ($Z/Co/SiO_2$). Furthermore, the Co phase is present not only in the core, but also in the shell and seems to be encapsulated by the zeolite (Figure 6). This structure is further confirmed by the similar performance before and after crushing the catalyst particle prior to its use in FTS. No major changes were observed in the selectivity (Figure 11); whereas, for a ‘core-shell’ structure the product slate should shift toward that of the ‘core’ (Co/SiO_2) upon crushing.

It is apparent that the effectiveness of the bifunctional catalytic system, in terms of breaking the ASF selectivity in FTS, correlates with the vicinity of FTS active phase and acid functionality. Schaub *et al.* [17] studied the combination of individual Co/Al_2O_3 and $Ni/ZSM\text{-}5/\gamma\text{-}Al_2O_3$ particles in different catalyst bed configurations. The carbon molar fraction of FTS wax (C21+) was 8 times lower over the physical mixture of the two catalysts compared to a dual bed catalytic system, where the hydrocracking catalyst ($Ni/ZSM\text{-}5/\gamma\text{-}Al_2O_3$) was placed downstream the FTS layer. This efficiency is increased further by bringing the acid functionality in an even closer contact with the FTS active phase in the form of coating compared to a physical mixture (*cf.* $Z/Co/SiO_2$ and Co/SiO_2 + H-ZSM-5 in Figure 9 and Table 4). It is known that larger hydrocarbons are more prone to hydrocarbon conversion reactions including hydrocracking due to their stronger adsorption [34, 63]. The possible origins of the proximity effect can be described as follows: when acid sites are in a close vicinity to FTS reaction environment, at a nanometer scale, the olefinic FTS hydrocarbons may adsorb on them and subsequently crack or isomerize before they are hydrogenated on a neighbor metal [13]. At the same time, an intimate contact between (de)hydrogenation and acid functionalities promotes the hydroprocessing reactions [51]. Further, if acid site domains are far from Co, formed hydrocarbons are more likely to escape from the acid-catalyzed reactions. Comparing the product spectrum of Z/Co/SiO_2-*noTEOS* with S/Co/SiO_2-*noTEOS* (which is devoid of zeolite acid sites), shows that the latter produces much more C12+ (see Figure 11). This result confirms that the product spectrum of the bifunctional catalyst is determined by the acid-catalyzed reactions in addition to an intrinsic FTS chain growth. Otherwise, similar product slates were expected for both H-ZSM-5-coated and silicalite-1-coated Co-catalysts.

In line with literature [18-21, 36, 38, 53, 54, 57-62], the coated catalysts exhibit lower CO conversion levels than the conventional Co/SiO_2. Since FTS catalysts in general are not highly productive, any loss in activity should be considered as a serious obstacle for practical applications. This decrease in the CO conversion is attributed to diffusion limitations, introduced by the coating layer. The mass transport restriction is verified by studying the silicalite-1-coated samples during FTS. In the latter case, an activity loss can be explained by the membrane effect of the coating which slows down the diffusion of large hydrocarbons through the inactive silicalite-1 micropores. This increases the accumulation of long chain hydrocarbons over Co active phase and suppresses the FTS activity. TGA analysis confirms this larger residue on the spent particles of silicalite-1-coated Co-catalyst (Figure B4/Appendix B). If the zeolite coating is acidic, hydrocarbons are chopped to smaller fractions which can leave the catalyst particle easier. Therefore, Z/Co/SiO_2-*noTEOS* exhibits a much higher activity than S/Co/SiO_2-*noTEOS* (see Figure 10).

A closer look at the cumulative representation of FTS product carbon selectivities in Table 4 reveals that formation of C12+ decreases by at least 50% upon coating the FTS active phase with H-ZSM-5 (Co/SiO_2 *versus* Z/Co/SiO_2). However, this decrease is at the cost of a considerable increase in C2–C4 fraction, rather than the gasoline-range hydrocarbons (C5–C11). Although, proximity of the FTS active phase and the acid component is achieved by the coating approach, the membrane effect of the zeolite layer promotes the adsorption of FTS hydrocarbons on acid sites, resulting in their over-exposure to acid-catalyzed reactions and over-cracking to lighter fractions which are less valuable than C5+. In that sense, thinner coatings should result in a better balance between FTS and cracking activity, that is a synthesis optimization problem.

Alternatively, the above-mentioned cooperative action of FTS and acid sites can be enhanced by employing the acidic zeolite as FTS catalyst support. However, due to the low external/mesopore surface area, the Co crystallite size tends to increase when applied to microporous zeolites at high loadings. So, while the syngas conversion over H-ZSM-5-coated Co is restricted by diffusion limitations, it suffers from poor metal dispersion over the H-ZSM-5-supported Co and both catalysts show reduced FTS activity as compared with Co/SiO_2 (see inserts in Figure 12 and 13a and Table 4). By introducing porous hierarchy in the zeolite crystallites, Co dispersion increases due to the presence of mesoporosity, while the diffusive transport to the Co improves. This considerably enhances the CO conversion over Co/*meso*H-ZSM-5, compared to Co/H-ZSM-5 (82% *versus* 32%, respectively).

Furthermore, waxes are more exposed to the acid sites in Co/*meso*H-ZSM-5 where they are formed on Co, located inside the zeolite crystallite rather than on its external surface. Thus, in spite of its weaker acidity (see Figure 8), a more pronounced deviation from ASF selectivity is observed over the mesoporous-supported H-ZSM-5 Co-catalyst compared to the microporous one (see Figure 13b). In other words, Co/*meso*H-ZSM-5 features the advantages of Z/Co/SiO_2, in terms of close proximity between FTS active phase and acid sites, with those of the conventional supported catalysts in terms of a decent mass transport. This results in an active FTS catalyst which breaks the classical ASF distribution, reducing wax formation and yielding directly liquid fuel.

3.5. Conclusions

Two structurally different H-ZSM-5-containing Co-catalysts have been synthesized and thoroughly characterized, where the zeolite acts either as a coating layer over Co agglomerates or as a mesoporous Co support. In the first case, silica in a conventional Co/SiO_2 FTS catalyst transforms into the zeolite when subjected to the hydrothermal synthesis (state of the art method to prepare zeolite coatings) while the original shape of the support is preserved after the transformation. By this synthesis approach, Co_3O_4 agglomerates are enwrapped in an H-ZSM-5 coating on a nanometer scale. In the second catalyst configuration, the close vicinity of the FTS and acid sites is achieved by introducing the FTS active phase into mesoporous zeolite crystallites.

Catalytic performance comparison with physically mixed and non-acidic coated catalysts shows that close proximity between the two phases is essential for improving the bifunctionality of the catalyst to eliminate the heavy FTS hydrocarbons. The membrane effect of the coating, however, results in mass transport resistances, lowering the productivity, and in the absence of acid functionality accumulation of carbonaceous species deactivates the silicalite-1-coated reference catalyst. The H-ZSM-5-coated Co-catalyst shows lower CO conversion levels than the conventional Co/SiO_2 due to the membrane coating. This activity loss should be considered as the major drawback of this approach and can be overcome when the Co active phase is directly deposited on mesoporous H-ZSM-5. This approach improves the Co dispersion and enhances Co accessibility while keeping the important close proximity of the two functionalities. As a result, the catalyst exhibits both a high activity and a high selectivity to gasoline-range hydrocarbons, breaking the ASF distribution. Altogether, our results demonstrate that the use of mesoporous zeolites as FTS supports holds many promises for the direct synthesis of liquid fractions from syngas.

References

[1] M.E. Dry, Appl. Catal. A-Gen. 276 (2004) 1-3.
[2] E. van Steen, M. Claeys, Chem. Eng. Technol. 31 (2008) 655-666.
[3] O.O. James, A.M. Mesubi, T.C. Ako, S. Maity, Fuel Process. Technol. 91 (2010) 136-144.
[4] R. Luque, A.R. de la Osa, J.M. Campelo, A.A. Romero, J.L. Valverde, P. Sanchez, Energy Environ. Sci. 5 (2012) 5186-5202.
[5] A. de Klerk, E. Furimsky, Catalysis in the Refining of Fischer-Tropsch Syncrude, RSCPublishing, Cambridge, UK, 2010.
[6] C.G. Visconti, E. Tronconi, L. Lietti, P. Forzatti, S. Rossini, R. Zennaro, Top. Catal. 54 (2011) 786-800.
[7] S.T. Sie, M.M.G. Senden, H.M.H. Van Wechem, Catal. Today 8 (1991) 371-394.
[8] R. Guettel, U. Kunz, T. Turek, Chem. Eng. Technol. 31 (2008) 746-754.
[9] F. Kapteijn, R.M. de Deugd, J.A. Moulijn, Catal. Today 105 (2005) 350-356.
[10] R.M. de Deugd, F. Kapteijn, J.A. Moulijn, Top. Catal. 26 (2003) 29-39.
[11] S.R. Deshmukh, A.L.Y. Tonkovich, J.S. McDaniel, L.D. Schrader, C.D. Burton, K.T. Jarosch, A.M. Simpson, D.R. Kilanowski, S. LeViness, Biofuels 2 (2011) 315-324.
[12] B. Sun, M. Qiao, K. Fan, J. Ulrich, F. Tao, ChemCatChem 3 (2011) 542-550.
[13] R. Oukaci, J.C.S. Wu, J.G. Goodwin Jr, J. Catal. 110 (1988) 47-57.
[14] K. Jothimurugesan, T. Gordon, S.K. Gangwal, Chem. Lett. CL-970870 (1998) 377-378.
[15] N. Tsubaki, Y. Yoneyama, K. Michiki, K. Fujimoto, Catal. Commun. 4 (2003) 108-111.
[16] A. Martínez, J. Rollán, M.A. Arribas, H.S. Cerqueira, A.F. Costa, E.F. S.-Aguiar, J. Catal. 249 (2007) 162-173.
[17] A. Freitez, K. Pabst, B. Kraushaar-Czarnetzki, G. Schaub, Ind. Eng. Chem. Res. 50 (2011) 13732-13741.
[18] J. He, Z. Liu, Y. Yoneyama, N. Nishiyama, N. Tsubaki, Chem.-Eur. J. 12 (2006) 8296-8304.
[19] X. Li, J. He, M. Meng, Y. Yoneyama, N. Tsubaki, J. Catal. 265 (2009) 26-34.
[20] X. Huang, B. Hou, J. Wang, D. Li, L. Jia, J. Chen, Y. Sun, Appl. Catal. A-Gen. 408 (2011) 38-46.
[21] C. Li, H. Xu, Y. Kido, Y. Yoneyama, Y. Suehiro, N. Tsubaki, ChemSusChem 5 (2012) 862-866.
[22] B. Sun, G. Yu, J. Lin, K. Xu, Y. Pei, S. Yan, M. Qiao, K. Fan, X. Zhang, B. Zong, Catal. Sci. Technol. 2 (2012) 1625-1629.
[23] S. Bessell, Appl. Catal. A-Gen. 96 (1993) 253-268.
[24] G. Calleja, A. de Lucas, R. van Grieken, Fuel 74 (1995) 445-451.
[25] S.H. Kang, J.H. Ryu, J.H. Kim, P.S.S. Prasad, J.W. Bae, J.Y. Cheon, K.W. Jun, Catal. Lett. 141 (2011) 1464-1471.
[26] K. Cheng, J. Kang, S. Huang, Z. You, Q. Zhang, J. Ding, W. Hua, Y. Lou, W. Deng, Y. Wang, ACS Catal. 2 (2012) 441-449.
[27] A. Martínez, S. Valencia, R. Murciano, H.S. Cerqueira, A.F. Costa, E.F. S.-Aguiar, Appl. Catal. A-Gen. 346 (2008) 117-125.
[28] A.M. Subiranas, G. Schaub, Int. J. Chem. React. Eng. 5 (2007) Article A78.
[29] J. Kang, K. Cheng, L. Zhang, Q. Zhang, J. Ding, W. Hua, Y. Lou, Q. Zhai, Y. Wang, Angew. Chem.-Int. Edit. 50 (2011) 5200-5203.
[30] A. Martínez, C. López, Appl. Catal. A-Gen. 294 (2005) 251-259.
[31] C.J. Machiels, R.B. Anderson, J. Catal. 58 (1979) 268-275.
[32] E.A. Medvedkova, Kinet. Catal. 32 (1992) 821-824.
[33] R.J. Gormley, V.U.S. Rao, R.R. Anderson, R.R. Schehl, R.D.H. Chi, J. Catal. 113 (1988) 193-205.

[34] C. Bouchy, G. Hastoy, E. Guillon, J.A. Martens, Oil Gas Sci. Technol. 64 (2009) 91-112.
[35] A.Y. Khodakov, W. Chu, P. Fongarland, Chem. Rev. 107 (2007) 1692-1744.
[36] J. Bao, G. Yang, C. Okada, Y. Yoneyama, N. Tsubaki, Appl. Catal. A-Gen. 394 (2011) 195-200.
[37] J.C. Groen, L.A.A. Peffer, J.A. Moulijn, J. Pérez-Ramírez, Colloid Surf. A-Physicochem. Eng. Asp. 241 (2004) 53-58.
[38] J. Bao, J. He, Y. Zhang, Y. Yoneyama, N. Tsubaki, Angew. Chem.-Int. Edit. 47 (2008) 353-356.
[39] J. Pérez-Ramírez, C.H. Christensen, K. Egeblad, C.H. Christensen, J.C. Groen, Chem. Soc. Rev. 37 (2008) 2530-2542.
[40] D. Verboekend, S. Mitchell, M. Milina, J.C. Groen, J. Pérez-Ramírez, J. Phys. Chem. C 115 (2011) 14193-14203.
[41] M. Noack, P. Kölsch, A. Dittmar, M. Stöhr, G. Georgi, R. Eckelt, J. Caro, Microporous Mesoporous Mat. 97 (2006) 88-96.
[42] A. Dong, N. Ren, W. Yang, Y. Wang, Y. Zhang, D. Wang, J. Hu, Z. Gao, Y. Tang, Adv. Funct. Mater. 13 (2003) 943-948.
[43] J. Shi, N. Ren, Y.H. Zhang, Y. Tang, Microporous Mesoporous Mat. 132 (2010) 181-187.
[44] L.H. Chen, X.Y. Li, J.C. Rooke, Y.H. Zhang, X.Y. Yang, Y. Tang, F.S. Xiao, B.L. Su, J. Mater. Chem. 22 (2012) 17381-17403.
[45] P. Arnoldy, J.A. Moulijn, J. Catal. 93 (1985) 38-54.
[46] W. Chu, P.A. Chernavskii, L. Gengembre, G.A. Pankina, P. Fongarland, A.Y. Khodakov, J. Catal. 252 (2007) 215-230.
[47] B. de Rivas, R. López-Fonseca, C. Jiménez-González, J.I. Gutiérrez-Ortiz, J. Catal. 281 (2011) 88-97.
[48] F. Lónyi, J. Valyon, Microporous Mesoporous Mat. 47 (2001) 293-301.
[49] J.C. Groen, L.A.A. Peffer, J. Pérez-Ramírez, Microporous Mesoporous Mat. 60 (2003) 1-17.
[50] J.C. Groen, W. Zhu, S. Brouwer, S.J. Huynink, F. Kapteijn, J.A. Moulijn, J. Pérez-Ramírez, J. Am. Chem. Soc. 129 (2007) 355-360.
[51] M. Rigutto, Cracking and Hydrocracking, in: J. Čejka, A. Corma, S. Zones (Eds.) Zeolites and Catalysis: Synthesis, Reactions and Applications, WILEY-VCH Verlag GmbH & Co. KGaA, Weinheim, 2010, pp. 547-584.
[52] A. Martínez, G. Prieto, A. García-Trenco, E. Peris, Advanced Catalysts Based on Micro- and Mesoporous Molecular Sieves for the Conversion of Natural Gas to Fuels and Chemicals, in: J. Čejka, A. Corma, S. Zones (Eds.) Zeolites and Catalysis: Synthesis, Reactions and Applications, WILEY-VCH Verlag GmbH & Co. KGaA, Weinheim, 2010, pp. 649-685.
[53] J. He, B. Xu, Y. Yoneyama, N. Nishiyama, N. Tsubaki, Chem. Lett. 34 (2005) 148-149.
[54] J. He, Y. Yoneyama, B. Xu, N. Nishiyama, N. Tsubaki, Langmuir 21 (2005) 1699-1702.
[55] N. Nishiyama, K. Ichioka, D.H. Park, Y. Egashira, K. Ueyama, L. Gora, W. Zhu, F. Kapteijn, J.A. Moulijn, Ind. Eng. Chem. Res. 43 (2004) 1211-1215.
[56] N. Nishiyama, K. Ichioka, M. Miyamoto, Y. Egashira, K. Ueyama, L. Gora, W. Zhu, F. Kapteijn, J.A. Moulijn, Microporous Mesoporous Mat. 83 (2005) 244-250.
[57] G. Yang, J. He, Y. Yoneyama, Y. Tan, Y. Han, N. Tsubaki, Appl. Catal. A-Gen. 329 (2007) 99-105.
[58] G. Yang, J. He, Y. Yoneyama, Y. Tan, Y. Han, N. Tsubaki, Res. Chem. Intermed. 34 (2008) 771-779.
[59] G. Yang, J. He, Y. Zhang, Y. Yoneyama, Y. Tan, Y. Han, T. Vitidsant, N. Tsubaki, Energy Fuels 22 (2008) 1463-1468.
[60] G. Yang, Y. Tan, Y. Han, J. Qiu, N. Tsubaki, Catal. Commun. 9 (2008) 2520-2524.
[61] M. Thongkam, G. Yang, T. Vitidsant, N. Tsubaki, J. Jpn. Pet. Inst 52 (2009) 216-217.
[62] N. Jiang, G. Yang, X. Zhang, L. Wang, C. Shi, N. Tsubaki, Catal. Commun. 12 (2011) 951-954.
[63] J. Wei, Ind. Eng. Chem. Res. 33 (1994) 2467-2472.

Chapter 4

Breaking the Fischer-Tropsch synthesis selectivity: Direct conversion of syngas to gasoline-range hydrocarbons over hierarchical Co/H-ZSM-5 catalysts

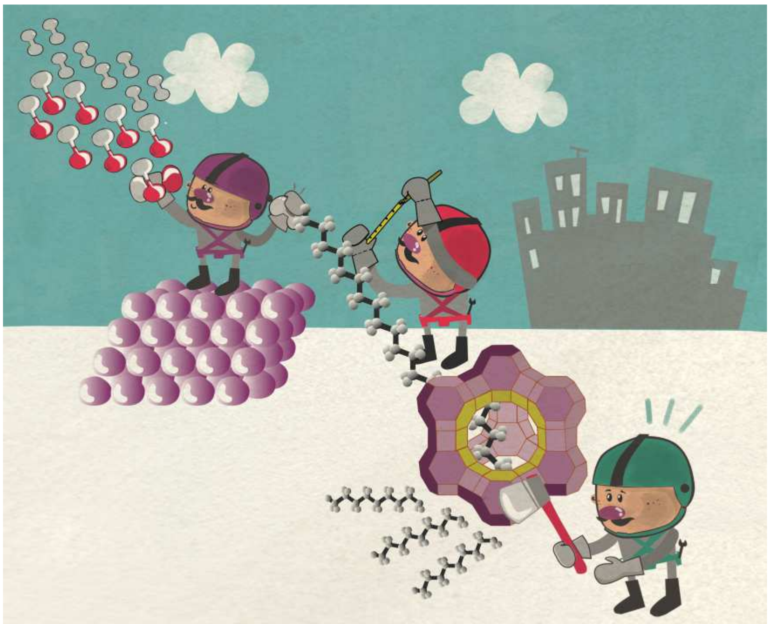

This Chapter is based on the following publication:

S. Sartipi, K. Parashar, M. Makkee, J. Gascon, F. Kapteijn, Catal. Sci. Technol. 3 (**2013**) 572-575.

Abstract: Combination of Fischer-Tropsch synthesis and acid functionalities in one single catalyst particle is reported. The resulting bifunctional catalyst is capable of producing gasoline-range hydrocarbons from synthesis gas in one catalytic step with outstanding activities and selectivities.

4.1. Introduction

The Fischer-Tropsch synthesis (FTS) is a key step in the transformation of various non-petroleum carbon resources such as natural gas, coal, and biomass into clean hydrocarbon fuels and valuable chemicals. Since the FTS product spectrum is believed to follow the Anderson-Schulz-Flory (ASF) distribution, it is theoretically impossible to selectively synthesize hydrocarbon fractions in the diesel and/or gasoline-ranges [1]. Therefore, the state of the art gas-to-liquid (GTL) processes are based on FTS followed by downstream conversion units (predominantly hydrocrackers in the case of Co-based FTS) [2]. This layout is economically feasible once it is applied at large scale, but is less suitable for the production of liquid fuels from remotely dispersed syngas resources such as biomass and offshore flare gas [3].

Recently, the combination of zeolites with FTS catalysts in one reaction step has gained a great deal of attention as a tool to develop smaller scale GTL processes. This approach aims to minimize the demands on the refining units, especially hydrocrackers, by maximizing the production of desired liquid fractions in FTS reactors. The use of acidic zeolites as FTS catalyst supports and/or as co-catalysts deviates from the ASF limitation, yielding products mainly in the gasoline-range with high selectivities to isoparaffins [4]. In these catalytic systems, the primary hydrocarbons, formed on the FTS active sites, migrate to the micropores of the zeolite where (hydro)cracking and isomerization occur. Nevertheless, the low external/mesopore surface area of zeolites, their poor mass transport properties and the fast deposition of coke [5] cause a number of limitations which are addressed in this Chapter.

Along with the development of efficient methods to alleviate diffusion limitations in zeolites [6-8], the first examples of mesoporous zeolites as FTS supports have been published very recently. Co supported on a slightly mesoporous zeolite Beta is reported to give a better FTS catalytic performance in terms of CO conversion with lower methane and higher C6+ selectivities. However, the improvement was insignificant in comparison with the unmodified Beta sample [9]. A comprehensive study on 3 wt% Ru supported on desilicated ZSM-5 and Beta zeolites revealed that the activity for hydrocarbon reactions of FTS products correlates with the extent of support mesoporosity as well as with its acid strength [10, 11]. In spite of the promising results, it is fair to admit that Ru is not the preferred metal of choice for large scale applications due to its high prise and the formation of volatile Ru-carbonyls under reaction conditions [12].

In this Chapter, the performance of Co-based FTS catalysts supported on hierarchical H-ZSM-5 is presented. The performance of the new bifunctional catalyst is compared with Co supported on SiO_2 as a conventional FTS catalyst.

4.2. Experimental

4.2.1. Materials

Amorphous SiO_2 with surface area and pore volume of 293 m^2 g^{-1} and 1.35 cm^3 g^{-1}, respectively, was provided by Fuji Silysia Chemical Ltd. (CARiACT Q-10). ZSM-5 zeolite in ammonium form with nominal Si/Al of 40 was purchased from Zeolyst (CBV 8014). NaOH pellets, 1 M tetrapropylammonium hydroxide (TPAOH) solution, and $Co(NO_3)_2 \cdot 6H_2O$ were purchased from Sigma-Aldrich. NH_4NO_3 was provided by Merck. All chemicals were used without any further purification steps.

4.2.2. Synthesis

Ammonium form of ZSM-5 was calcined at 823 K for 5 h to obtain the parent H-ZSM-5. Desilication of H-ZSM-5 powder was carried out in 1 M NaOH or TPAOH aqueous solutions in a capped vessel ($\text{volume}_{\text{base solution}}/\text{weight}_{\text{parent H-ZSM-5}}$ = 8 cm^3 g^{-1}) and under stirring at 343 K for 1 h in an oil bath. This treatment was followed by immediate quenching in an ice bath and centrifugation to separate the zeolite powder from solution. The residue of the desilicating agent was removed from zeolite crystallites by subsequent redispersion in deionized water and centrifugation cycles until neutral pH was reached. In the case of NaOH treatment, the zeolite was ion-exchanged with an excess of 0.1 M NH_4NO_3 at room temperature for 15 min in three additional cycles and thoroughly washed. Mesoporous H-ZSM-5 samples were then kept overnight at 333 K followed by drying at 393 K for 12 h and calcination at 823 K for 5 h. The mesoporous H-ZSM-5, obtained *via* alkaline and organic treatments, are denoted as *meso*H-ZSM-5*(a)* and *meso*H-ZSM-5*(o),* respectively.

Amorphous SiO_2, parent H-ZSM-5 as well as mesoporous zeolite samples were employed as catalyst supports and loaded with 10 wt% of Co, applying incipient wetness impregnation with a $Co(NO_3)_2 \cdot 6H_2O$ aqueous solution. Before impregnation, all the supports were dried overnight at 393 K. Only in the case of parent H-ZSM-5, two impregnation steps were required (due to its low pore volume) in between of which the sample was dried at 333 K for 5 h. After impregnation, samples were kept overnight in a desiccator at room temperature and dried at 393 K for 12 h. Finally, the catalysts were calcined at 673 K for 2h. For all the above-mentioned drying and calcination steps a heating rate of 2 K min^{-1} and static air conditions were applied.

4.2.3. Characterization

N_2 physisorption experiments were performed in an Autosorb-6B unit (Quantachrome Instruments) at liquid nitrogen temperature (77 K). Prior to the experiment, all samples were degassed overnight in an Autosorb Degasser unit (Quantachrome Instruments) under vacuum at 623 K.

4.2.4. Fischer-Tropsch synthesis

FTS experiments were performed on the six-flow fixed-bed microreactor setup described in Chapter 2. For all experiments, 0.5 g of fresh catalyst particles were fixed in the reactor inserts using quartz wool. Samples were first activated *in situ* with 80 cm^3_{STP} min^{-1} of H_2 at 673 K for 12 h at atmospheric pressure followed by cooling to 453 K under H_2 flow. After increasing the pressure to the process value (15 bar total pressure), CO was gradually introduced to the feed stream at 453 K in order to reach its final concentration ($H_2/CO = 2$) in 1 h. Subsequently, the reactor was heated to the process temperature (513 K). A rate of 2 K min^{-1} was applied for all the heating/cooling steps.

During the experiment, heavy hydrocarbons (wax) were collected by gas/liquid separators at 448 K and reaction pressure. Lighter hydrocarbons and water were collected in cold traps at *ca.* 278 K and atmospheric pressure. After separation from water, these hydrocarbons as well as the wax were weighted, dissolved in CS_2, and analyzed offline by a simulated distillation (SimDis) GC (Hewlett Packard 5890, Series II) equipped with an FID and HP-1 column (7.5 m × 0.53 mm, Film Thickness 2.65 μm), using He as carrier gas. During the analysis, the oven temperature was ramped from 308 to 623 K (14 K min^{-1}) and kept at the final temperature for 5 min.

N_2, CO, and CO_2 as well as light hydrocarbons in the gas phase were analyzed online by a Compact GC (Interscience), equipped with three columns and detectors in parallel, applying He as carrier gas. In the first column (Carboxen 1010, 10 m × 0.32 mm) N_2, CO, CH_4, and CO_2 were separated at 333 K and analyzed by TCD. In the second column (Al_2O_3/KCl, 10 m × 0.32 mm) and FID detection, separation between all C1–C4 components was achieved at 434 K. In the third column (RTx-1 0.5μm, 15 m × 0.32 mm) C5–C10 hydrocarbons were separated at 353 K and analyzed by FID.

A pseudo-steady-state catalytic behavior was attained after 20 h on-stream when selectivity data were collected and the carbon balance was satisfied by 100 ± 5%. CO conversion, carbon selectivity, and molar fraction of each product were defined by Eqs. (1), (2), and (3), respectively, where X_{CO} stands for CO conversion, F indicates the molar flow, S is the carbons selectivity of a product with n carbon number and y is its molar fraction.

$$X_{\mathrm{CO}} = \frac{F_{\mathrm{in,CO}} - F_{\mathrm{out,CO}}}{F_{\mathrm{in,CO}}} \times 100 \quad (1), \qquad S_{\mathrm{C}n} = \frac{nF_{\mathrm{C}n}}{F_{\mathrm{CO_2}} + \sum_{n=1}^{N} nF_{\mathrm{C}n}} \times 100 \quad (2), \qquad y_{\mathrm{C}n} = \frac{F_{\mathrm{C}n}}{\sum_{n=1}^{N} F_{\mathrm{C}n}} \quad (3)$$

4.2.5. Acid-catalyzed reactions

Acidic catalyzed reactions of *n*-C6 were performed in a fixed-bed stainless-steel reactor. 0.25 g of the alkaline treated H-ZSM-5 (*meso*H-ZSM-5*(a)*) particles were fixed in the reactor center (3.9 mm inner diameter) by quartz wool. The catalyst was treated overnight under H_2 flow at 673 K and atmospheric pressure. After cooling to 513 K the total pressure was increased to 15 bar and subsequently a mixture of *n*-C6, H_2, and N_2 was fed to the reactor (SV = 13 mol_{C6} kg^{-1}_{cat} h^{-1}, molar composition: $H_2/n\text{-C6} = 9.0$, $N_2/H_2 = 2.0$). After 20 h on-stream, data collection started at different reaction temperatures. The reactor was kept for 3 h at each temperature before measurements. The product stream was analyzed online by a Compact GC (Interscience), equipped with Porabond Q column at 363 K (10 m × 0.32 mm) and FID, using He as the carrier gas. Yield of the hydrocarbon products ($Y_{\mathrm{C}n}$) was defined by Eq. (4):

$$Y_{\mathrm{C}n} = \frac{n}{6}\frac{F_{\mathrm{C}n}}{F_{\mathrm{in},n\text{-C6}}}\times 100\% \tag{4}$$

4.3. Results and discussion

The textural properties of these supports are presented in Table 1. Under similar treatment conditions, NaOH results in a more severe desilication than TPAOH, creating mesostructures with pore sizes and volumes very similar to the amorphous SiO_2 reference support. This difference is visible in the textural properties (Table 1) as well as in the TEM images of the corresponding catalysts (*cf.* Figure C4e and f/Appendix C). In line with previous observations [13], a more controlled desilication with TPAOH gives rise to more mesoporosity with pores in the range of 4–8 nm. *meso*HZSM-5*(o)* shows a clear type IV hysteresis upon N_2 adsorption at 77 K (see Figure C1/Appendix C). Closure of the hysteresis at $p/p_\circ \approx 0.42$ (*i.e.*, N_2 cavitation) suggests a high degree of hierarchy with large cavities communicated with smaller mesopores.

Temperature-programmed NH_3 desorption profiles (Figure C2/Appendix C) show a maximum at around 700 K for both parent and *meso*H-ZSM-5*(a)* supports which is characteristic of strong Brønsted acidity in H-ZSM-5 [10, 11]. Moreover, a shoulder appears at around 550 K for *meso*H-ZSM-5*(a)*, corresponding to weaker acid sites which are predominantly present in the *meso*H-ZSM-5*(o)*.

All four supports mentioned in Table 1 were loaded with *ca.* 10 wt% Co *via* incipient wetness impregnation. CO conversion as well as carbon selectivity of different products on the catalysts (at 513 K) are compared in Figure 1.

Figure 1a shows that Co/SiO_2 and Co/H-ZSM-5 display similar CO conversion levels after 20 h; however, once mesoporosity is created in the zeolite support, the conversion increases considerably

Table 1 Textural properties of supports, obtained from N_2 physisorption at 77 K.

Support	$S_{\mathrm{meso}}{}^{a}$ / m^2 g^{-1}	$V_{\mathrm{meso}}{}^{b}$ / cm^2 g^{-1}	$d_{\mathrm{meso}}{}^{c}$ / nm
SiO_2	248	1.34	23–32
H-ZSM-5	52	0.08	n.d.[d]
*meso*H-ZSM-5*(a)*	309	1.08	15–32
*meso*H-ZSM-5*(o)*	414	0.52	*ca.* 4–8

[a] Mesopore surface area obtained from the *t*-plot applied to the N_2 isotherm; [b] Mesopore volume calculated as $V_{\mathrm{meso}} = V_{\mathrm{total}}\text{-}V_{\mathrm{micro}}$ where micropore volume is obtained from the *t*-plot; [c] Mesopore diameter, derived from the adsorption branch employing the BJH method; [d] Not determined.

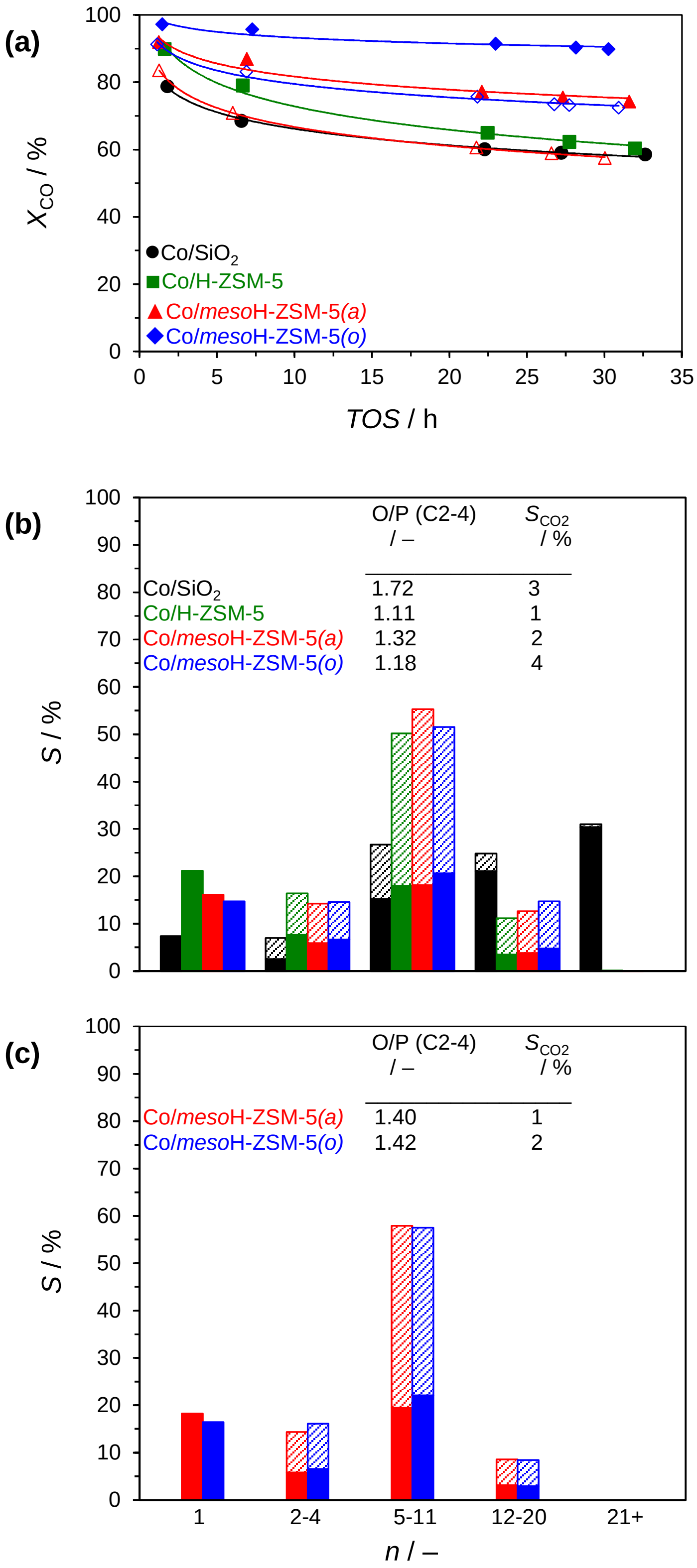

Figure 1. Time-on-stream (*TOS*) evolution of CO conversion during FTS where *GHSV* / m^3_{STP} kg^{-1}_{cat} h^{-1} = 2.4 (solid symbols) and 6.0 (open symbols) (a). Carbon selectivity of FTS products after 20 h on-stream at *GHSV* / m^3_{STP} kg^{-1}_{cat} h^{-1} = 2.4 (b) and 6.0 (c). In each carbon number group from left to right: Co/SiO_2, Co/H-ZSM-5, Co/*meso*H-ZSM-5*(a)*, and Co/*meso*H-ZSM-5*(o)*. ■: *n*-paraffins, ▨: sum of isoparaffins and olefins, O/P (C2-4): olefin to *n*-paraffin ratio of C2–C4, S_{CO2}: CO_2 selectivity. Experiments were performed at 513 K, 15 bar total pressure, and feed composition H_2/CO = 2.

(by *ca.* 13 and 28% in the case of Co/*meso*H-ZSM-5*(a)* and *-(o)*, respectively) under similar process conditions. Time-on-stream (*TOS*) evolution of CO conversion reveals that Co/H-ZSM-5 deactivates faster as compared with the mesoporous zeolite-supported catalysts (Figure 1a). TGA analysis of the spent catalysts gives comparable weight losses and patterns for the zeolite-supported samples upon heat treatment in air (Figure C5/Appendix C). This result points to the formation of similar amounts and type of carbon residues on the spent zeolite-containing catalysts, indicating that coke deposition cannot explain their different deactivation behavior. In general, microporous zeolites are devoid of mesopore surface area, essential for an optimal dispersion of Co particles at high metal loadings. On the other hand, formation of metal clusters in the micropores is undesired, as Co particles smaller than 6 nm are not optimal for FTS in terms of activity and selectivity [14, 15]. Therefore, the first advantage of introducing hierarchy in H-ZSM-5, for the current application, is providing the proper mesopore surface area to support Co particles of proper size in close vicinity to acid sites. TEM images (Figure C4/Appendix C) show that Co oxide crystallites of about 17 nm are located on the external surface of parent H-ZSM-5 particles, whereas considerably smaller Co crystallites are present in the mesoporous zeolite supports (see also Table C1/Appendix C). Further, Co crystallites visibly tend to cluster more on the parent zeolite support (Figure C4/Appendix C). These Co agglomerates are prone to sinter which results in a lower *TOS* stability of Co/H-ZSM-5 than that of the mesoporous zeolite-supported catalysts at higher operating temperatures (Figure 1).

Although after desilication by NaOH, *meso*H-ZSM-5*(a)* was ion-exchanged and the amount of Na in this support is lower than our detection limit (0.01 wt%), alkaline treatment is a less preferred route, as Na^+ is a well-known poison for Co-based FTS catalysts where trace amounts can result in the loss of activity [16]. Under similar process conditions, CO conversion over Co/*meso*H-ZSM-5*(o)* is almost 15% higher than that over Co/*meso*H-ZSM-5*(a)* (Figure 1a). Since no major differences are observed between Co crystallite sizes of these two catalysts (see Table C1 and Figure C4/Appendix C), we attribute this difference in activity to the effect of Na traces.

Figure 1b shows that Co/SiO_2 and Co/H-ZSM-5 produce a considerably different product spectrum at similar conversion levels. In contrast to Co/SiO_2, formation of C21+ (wax) is eliminated on Co/H-ZSM-5 (see also Figure 2) and gasoline-range hydrocarbons are produced, but with increased C1–C4 selectivities. Methane selectivity on Co/H-ZSM-5 is almost three times higher than that on Co/SiO_2. Due to the higher diffusivity of H_2 (than that of CO), the local H_2 concentration in the zeolitic particle is higher than that in the mesoporous SiO_2. The higher intra-particle H_2/CO ratio contributes to an enhanced CH_4 production over the Co/H-ZSM-5 catalyst [17].

Comparison of the Co/H-ZSM-5 and Co/*meso*H-ZSM-5*(a)* performances under iso-conversion conditions reveals that the selectivity to gasoline cut (C5–C11) is higher for the mesoporous sample and that to C1 is lower (*cf.* Figure 1b and c). This selectivity improvement over Co/*meso*H-ZSM-5*(a)* is attributed to reduced diffusion limitations, which eliminate the overexposure of the FTS hydrocarbons to strong acid sites and keep the local H_2/CO closer to bulk conditions inside the catalyst particle. Indeed, the positive effect of reduced diffusion limitations in hierarchical zeolites is known to increase the yield towards middle distillates with a decreased coke formation [18].

Figure 2 compares the FTS product distributions (molar fractions) over conventional and bifunctional catalysts. Under the applied process conditions, long chain hydrocarbons (wax) are formed on Co/SiO_2 according to an ASF distribution with a chain growth probability (α) of 0.87. In contrast, a clear deviation from ASF distribution is observed for H-ZSM-5-supported catalysts, resulting in a cut-off above C11, breaking the Fischer-Tropsch synthesis ASF distribution at the upper limit of gasoline cut, as longer hydrocarbons are more prone to conversion reactions [19, 20]. The reduced wax production on the zeolite-containing samples is confirmed by TGA analysis of the spent catalysts where their weight loss is *ca.* 8 times lower than that of the spent Co/SiO_2 (Figure C5/Appendix C). In line with other reports [21], the methane level, higher than that of the ASF distribution, implies that a secondary reaction of CO hydrogenation takes place (in addition to FTS) for all the Co-catalysts. As compared to Co/SiO_2, the higher CH_4 molar fraction obtained over Co/*zeolite* catalysts (see inset in Figure 2), and their lower olefin selectivity (see insets in Figure 1b and c), reveals that this hydrogenation functionality is more pronounced in the case of zeolite-supported catalysts.

Limiting the FTS product spectrum to C5–C11 cut has often been reported in the literature over bifunctional FTS catalysts. Researchers predominantly ascribed this phenomenon to the

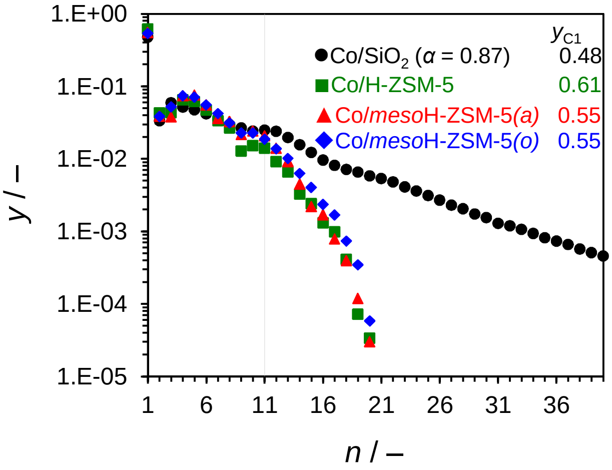

Figure 2. Fractional molar composition of FTS products after 20 h on-stream at 513 K, 15 bar total pressure, feed composition H_2/CO = 2, and *GHSV* = 2.4 m^3_{STP} kg^{-1}_{cat} h^{-1}. α: chain growth probability, y_{C1}: methane molar fraction.

(hydro)cracking activity of the acid function [10, 11, 16, 22-26]. In contrast to the hydrocracking of petroleum-derived feeds, where the aromatic content of the feed determines the processing conditions, hydrocracking of low-temperature FT (LTFT) wax (often referred to as ‘mild hydrocracking’) is less demanding. The optimal process temperature of mild hydrocrackers is *ca.* 100 K higher than that of the LTFT [2, 19, 27]. Comparison of various catalytic systems reveals that the key factor, determining the product distribution over bifunctional FTS catalysts, is the close vicinity of the FTS active phase to the acid functionality. In that sense, hybrid catalyst particles (such as the so-called ‘core-shell’ catalysts [22-25]) are more effective than physical mixtures which perform in turn better than the layered beds of FTS and acid catalyst particles [28].

An even more intimate contact between the FTS and acid sites increases the chance of primary olefinic FTS products to adsorb on the acid sites for further hydrocracking and isomerization reactions [29]. The operating temperature window of isomerization overlaps better with that of the LTFT than hydrocracking, and considerable amounts of branched hydrocarbons are produced over our zeolite-containing catalysts, in good agreement with the literature [10, 11, 16, 22-26]. Formation of skeletal and double bond isomers that do not re-incorporate into the chain growth process as fast as linear α-olefins would prevent the formation of wax simply by lowering the α value, but without any contribution of hydrocracking, isomerization alone cannot explain the nonlinear break in the ASF distribution observed in Figure 2. Our results show that the *iso*- to *n*-C4 ratio increases by one order of magnitude from 0.02 over Co/SiO_2 to 0.24 over Co/*meso*H-ZSM-5*(a)* (513 K, 15 bar total pressure, feed composition $H_2/CO = 2$, $GHSV = 2.4$ m^3_{STP} kg^{-1}_{cat} h^{-1}). C4 isomers are typically formed during acid-catalyzed cracking reactions, and not produced to a large extent in skeletal isomerization at the above-mentioned temperature [27]. Therefore, this result already indicates that some hydrocracking reactions take place over our zeolite-containing catalysts.

In order to investigate the feasibility of acid-catalyzed reactions under FTS process conditions and space velocities (as those described in Figure 1 and 2), *meso*H-ZSM-5*(a)* was subjected to a mixture of *n*-hexane, H_2, and N_2. As depicted in Figure 3, both hydrocracking and hydroisomerization occur under reaction conditions, with C4 as the major product. It is also important to mention that together with isomerization and cracking products, higher hydrocarbons (C8–C10) were also found among the products (Figure C7/Appendix C), demonstrating that C6 first dimerizes and then cracks to C4, C5, C8, and C7. These results together with the fact that larger hydrocarbons are even more reactive (than C6) for hydrocarbon conversion reactions [19, 20] explain the cutoff shown in Figure 2 where the molar fraction of hydrocarbon products drops as their carbon number increases. The similar formation level of C6 isomers (Figure 3) implies that the effect of isomerization reactions on the product slate of bifunctional catalysts should not be neglected either, as mentioned earlier. Gas-phase hydroprocessing

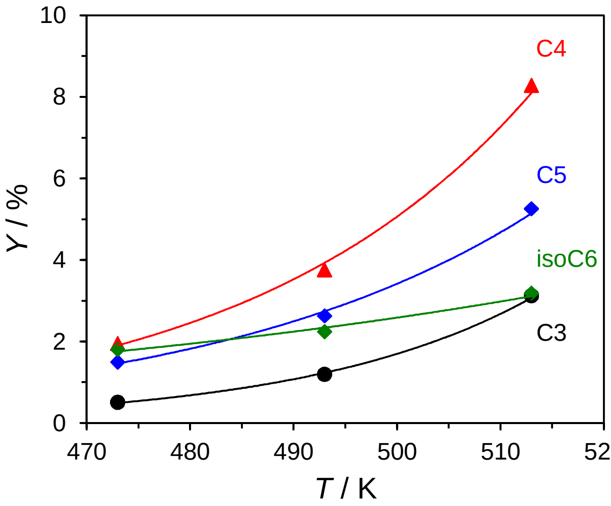

Figure 3. Product yields of *n*-C6 hydroconversion over *meso*H-ZSM-5*(a)* at different temperatures, 15 bar total pressure, H_2/*n*-C6 = 9.0, N_2/H_2 = 2.0, and SV = 13 $\mathrm{mol_{C6}\,kg^{-1}_{cat}\,h^{-1}}$.

experiments with hydrocarbon model compounds show that hydrocracking reactions take place in the presence of CO and H_2O as well [28, 30].

It is also important to notice that compared to the large amounts of methane formed over the FTS catalysts, this product was not detected when feeding *n*-hexane to *meso*H-ZSM-5*(a)* in the absence of Co. This observation suggests that formation of C1 does not directly correlate with the support acidity but is related to the direct CO hydrogenation and/or hydrogenolysis reactions at the metal sites [31, 32].

4.4. Conclusions

The combination of FTS activity and acid functionality and a high degree of mesoporous hierarchy results in catalysts that produce gasoline-range hydrocarbons from syngas in one step with selectivities close to 60%. This high selectivity towards gasoline is the result of the cooperative action of the different active sites that are in close vicinity. Introduction and control of mesoporosity in the zeolite support turned out to be a crucial parameter in increasing the yield towards C5–C11, as well as the catalyst activity and stability.

References

[1] S.T. Sie, M.M.G. Senden, H.M.H. Van Wechem, Catal. Today 8 (1991) 371-394.
[2] A. de Klerk, E. Furimsky, Catalysis in the Refining of Fischer-Tropsch Syncrude, RSCPublishing, Cambridge, UK, 2010.
[3] S.R. Deshmukh, A.L.Y. Tonkovich, J.S. McDaniel, L.D. Schrader, C.D. Burton, K.T. Jarosch, A.M. Simpson, D.R. Kilanowski, S. LeViness, Biofuels 2 (2011) 315-324.
[4] B. Sun, M. Qiao, K. Fan, J. Ulrich, F. Tao, ChemCatChem 3 (2011) 542-550.

[5] A. Martínez, G. Prieto, A. García-Trenco, E. Peris, Advanced Catalysts Based on Micro- and Mesoporous Molecular Sieves for the Conversion of Natural Gas to Fuels and Chemicals, in: J. Čejka, A. Corma, S. Zones (Eds.) Zeolites and Catalysis: Synthesis, Reactions and Applications, WILEY-VCH Verlag GmbH & Co. KGaA, Weinheim, 2010, pp. 649-685.
[6] J.C. Groen, W. Zhu, S. Brouwer, S.J. Huynink, F. Kapteijn, J.A. Moulijn, J. Pérez-Ramírez, J. Am. Chem. Soc. 129 (2007) 355-360.
[7] J. Pérez-Ramírez, C.H. Christensen, K. Egeblad, C.H. Christensen, J.C. Groen, Chem. Soc. Rev. 37 (2008) 2530-2542.
[8] D. Verboekend, S. Mitchell, M. Milina, J.C. Groen, J. Pérez-Ramírez, J. Phys. Chem. C 115 (2011) 14193-14203.
[9] A.L.C. Pereira, J.M. González-Carballo, F.J. Pérez-Alonso, S. Rojas, J.L.G. Fierro, M.D.C. Rangel, Top. Catal. 54 (2011) 179-189.
[10] J. Kang, K. Cheng, L. Zhang, Q. Zhang, J. Ding, W. Hua, Y. Lou, Q. Zhai, Y. Wang, Angew. Chem.-Int. Edit. 50 (2011) 5200-5203.
[11] K. Cheng, J. Kang, S. Huang, Z. You, Q. Zhang, J. Ding, W. Hua, Y. Lou, W. Deng, Y. Wang, ACS Catal. 2 (2012) 441-449.
[12] A.Y. Khodakov, W. Chu, P. Fongarland, Chem. Rev. 107 (2007) 1692-1744.
[13] S. Abelló, A. Bonilla, J. Pérez-Ramírez, Appl. Catal. A-Gen. 364 (2009) 191-198.
[14] G.L. Bezemer, J.H. Bitter, H.P.C.E. Kuipers, H. Oosterbeek, J.E. Holewijn, X. Xu, F. Kapteijn, A.J. van Dillen, K.P. De Jong, J. Am. Chem. Soc. 128 (2006) 3956-3964.
[15] J.P. den Breejen, P.B. Radstake, G.L. Bezemer, J.H. Bitter, V. Frøseth, A. Holmen, K.P. de Jong, J. Am. Chem. Soc. 131 (2009) 7197-7203.
[16] J. Bao, J. He, Y. Zhang, Y. Yoneyama, N. Tsubaki, Angew. Chem.-Int. Edit. 47 (2008) 353-356.
[17] D. Vervloet, F. Kapteijn, J. Nijenhuis, J.R. Van Ommen, Catal. Sci. Technol. 2 (2012) 1221-1233.
[18] K.P. de Jong, J. Zečević, H. Friedrich, P.E. de Jongh, M. Bulut, S. Van Donk, R. Kenmogne, A. Finiels, V. Hulea, F. Fajula, Angew. Chem.-Int. Edit. 49 (2010) 10074-10078.
[19] C. Bouchy, G. Hastoy, E. Guillon, J.A. Martens, Oil Gas Sci. Technol. 64 (2009) 91-112.
[20] J. Wei, Ind. Eng. Chem. Res. 33 (1994) 2467-2472.
[21] C.G. Visconti, E. Tronconi, L. Lietti, P. Forzatti, S. Rossini, R. Zennaro, Top. Catal. 54 (2011) 786-800.
[22] J. He, Z. Liu, Y. Yoneyama, N. Nishiyama, N. Tsubaki, Chem.-Eur. J. 12 (2006) 8296-8304.
[23] X. Li, J. He, M. Meng, Y. Yoneyama, N. Tsubaki, J. Catal. 265 (2009) 26-34.
[24] X. Huang, B. Hou, J. Wang, D. Li, L. Jia, J. Chen, Y. Sun, Appl. Catal. A-Gen. 408 (2011) 38-46.
[25] C. Li, H. Xu, Y. Kido, Y. Yoneyama, Y. Suehiro, N. Tsubaki, ChemSusChem 5 (2012) 862-866.
[26] B. Sun, G. Yu, J. Lin, K. Xu, Y. Pei, S. Yan, M. Qiao, K. Fan, X. Zhang, B. Zong, Catal. Sci. Technol. 2 (2012) 1625-1629.
[27] J.A. Moulijn, M. Makkee, A. van Diepen, Chemical Process Technology, John Wiley & Sons, Chichester, 2001.
[28] A. Freitez, K. Pabst, B. Kraushaar-Czarnetzki, G. Schaub, Ind. Eng. Chem. Res. 50 (2011) 13732-13741.
[29] R. Oukaci, J.C.S. Wu, J.G. Goodwin Jr, J. Catal. 110 (1988) 47-57.
[30] A. Martínez, J. Rollán, M.A. Arribas, H.S. Cerqueira, A.F. Costa, E.F. S.-Aguiar, J. Catal. 249 (2007) 162-173.
[31] C.J. Machiels, R.B. Anderson, J. Catal. 58 (1979) 268-275.
[32] R.J. Gormley, V.U.S. Rao, R.R. Anderson, R.R. Schehl, R.D.H. Chi, J. Catal. 113 (1988) 193-205.

Chapter 5

Modification of H-ZSM-5 crystallites for cobalt-based catalyst applications in Fischer-Tropsch synthesis

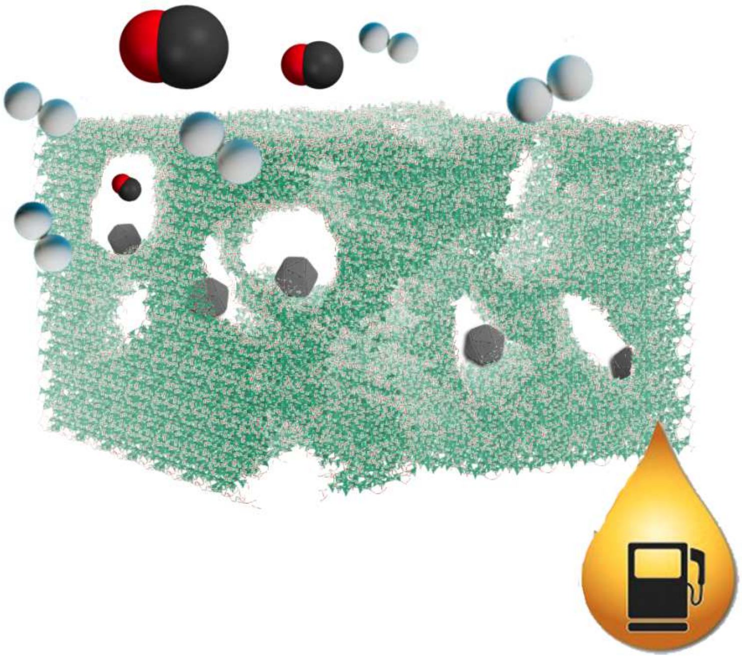

This Chapter is based on the following publication:

S. Sartipi, K. Parashar, M.J. Valero-Romero, V.P. Santos, B. van der Linden, M. Makkee, F. Kapteijn, J. Gascon, J. Catal. 305 (**2013**) 179-190.

Abstract: The main advantages and limitations of the use of mesoporous H-ZSM-5 as Co support in Fischer-Tropsch synthesis (FTS) are identified by combining a detailed catalyst performance evaluation with a thorough characterization.

Mesostructures were created in H-ZSM-5 crystallites by demetalation *via* subsequent base and acid treatments. Desilication through base treatment provides H-ZSM-5 with pore sizes and volumes similar to amorphous SiO_2 (a conventional carrier), while acid treatment removes the produced extraframework aluminum and boosts the FTS catalyst activity. Model acid-catalyzed reactions and induced deactivation of zeolite acid sites confirm that hydrocracking of primary FTS hydrocarbons at the zeolite strongly increases the selectivity toward C5–C11 (gasoline fraction). On the other hand, the strong Co-zeolite interaction as revealed by TPR(H_2) results in the stabilization of lower coordinated Co sites (as revealed by IR-assisted CO adsorption) and in a higher selectivity toward methane. *n*-Hexane conversion reactions suggest that the latter is due to increased activity for hydrogenation and hydrocarbon hydrogenolysis reactions at such coordinatively unsaturated Co sites.

5.1. Introduction

Fischer-Tropsch synthesis (FTS) is the core of the gas-to-liquid (GTL) technology. During FTS, a mixture of CO and H_2 (syngas) is catalytically converted into a wide spectrum of hydrocarbon chains through a surface polymerization reaction. Industrially two types of processes are employed for FTS: (*i*) the so-called high-temperature Fischer-Tropsch (HTFT) and (*ii*) low-temperature Fischer-Tropsch (LTFT) [1]. In the former, application of Fe-based catalysts at high temperatures (> 573 K) is typically aimed to produce short-chain hydrocarbons, olefins (Fischer-Tropsch to olefins, FTO), and oxygenates [2]. Moreover, high selectivities toward gasoline-range hydrocarbons can be reached over Fe catalysts under HTFT operation [3]. On the other hand, at LTFT conditions (< 573 K), mostly long-chain paraffins (wax) are produced over either Fe- or Co-containing catalysts. This wax is subsequently (hydro)cracked into the desired product spectrum [4, 5].

When high purity syngas is used, Co-based catalysts are preferred since Co brings together chain propagation ability and intrinsic activity that are higher than those of Fe (at similar conditions). Moreover, Co is more active for hydrogenation and consequently produces less unsaturated hydrocarbons and oxygenates, while having a longer lifetime [4, 6]. Recently, much effort has been put to tune the LTFT product selectivity of Co-based catalysts, which is dictated by the ASF polymerization model. In this respect, adding an acid functionality to the FTS catalyst formulation increases the product yields toward the C5–C11 cut [7] and may therefore be considered as a new generation of catalysts for direct production of gasoline from syngas. It is proposed that FTS wax is hydrocracked to shorter chain hydrocarbons on the acid sites of these bifunctional catalysts [8-13].

LTFT hydrocarbons mainly contain paraffins and no aromatics [4]; therefore, hydrocracking of FTS wax is less demanding (often referred to as ‘mild hydrocracking’ [14]) than that of crude oil. As the aromatic content of the feed to hydrocrackers increases, the higher propensity for coke formation calls for higher hydrogen pressures and more severe process conditions [15]. Nevertheless, the optimal process temperature of mild hydrocrackers is still *ca.* 100 K higher than that of the LTFT process. Moreover, their operation requires higher H_2 partial pressures than that in FTS reactors [14].

In spite of the above-mentioned facts, several studies on the combination of H-ZSM-5 zeolites with FTS active phases have demonstrated that bifunctional catalysts may benefit from a close proximity of the two active components. The intimate contact between the FTS metal and the acid sites turned out to be the key parameter, determining the performance of such catalysts in tuning the product selectivity. When acid site domains are in a close vicinity to FTS sites at a nanometer scale, the produced olefinic FTS hydrocarbons may crack or isomerize before they are hydrogenated [16]. However, limited knowledge is available on the actual role of zeolite acidity and on the influence of the zeolite support on the Co active phase. In this work, a detailed catalyst performance assessment is combined with a thorough characterization to make a quantum leap in understanding the bifunctional FTS catalysts. With this information in hand, the main advantages and limitations of the use of mesoporous zeolites as FTS supports are delineated.

5.2. Experimental

5.2.1. Materials

Amorphous SiO_2 with surface area and pore volume of 293 $m^2\ g^{-1}$ and 1.35 $cm^3\ g^{-1}$, respectively, was provided by Fuji Silysia Chemical Ltd. (CARiACT Q-10). ZSM-5 zeolite in ammonium form with nominal Si/Al ratio of 40 was purchased from Zeolyst (CBV 8014). NaOH, 70 wt% HNO_3 solution, $Co(NO_3)_2{\cdot}6H_2O$, and $Co(CH_3COO)_2{\cdot}4H_2O$ were purchased from Sigma-Aldrich. NH_4NO_3 was provided by Merck. All chemicals were used without any further purification steps.

5.2.2. Support preparation and catalyst synthesis

5.2.2.1. Preparation of mesoporous H-ZSM-5

Mesoporous H-ZSM-5 was prepared by desilication, a technique already demonstrated in technical scale that is shown to be an affordable method for scale up [17]. Ammonium form of ZSM-5 was calcined at 823 K for 5 h to obtain the parent H-ZSM-5. Desilication of H-ZSM-5 powder was carried out in 1 M NaOH aqueous solution in a capped vessel ($\text{volume}_{\text{base solution}}/\text{weight}_{\text{parent H-ZSM-5}}$ = 8.0 $cm^3\ g^{-1}$) and under stirring at 343 K for 1 h in an oil bath. This treatment was followed by immediate quenching in a water-ice bath and centrifugation to separate the zeolite powder from the solution. The residue of the desilicating agent was removed from the zeolite crystallites by subsequent redispersion in deionized water and centrifugation cycles until neutral pH was reached. In order to remove Na traces, a well-known poison for Co-based FTS catalysts [18], the zeolite was ion-exchanged with an excess of 0.1 M NH_4NO_3 at room temperature for 15 min in three additional cycles and thoroughly washed. Mesoporous H-ZSM-5, denoted as '*meso*H-ZSM-5', was then kept overnight at 333 K followed by drying at 393 K for 12 h and calcination at 823 K for 5 h. Yield of the desilication procedure was 25% (averaged from four experiments starting from *ca.* 20 g of H-ZSM-5).

A fraction of the parent H-ZSM-5 as well as the *meso*H-ZSM-5 zeolites were acid treated in 1 M HNO_3 aqueous solution ($\text{volume}_{\text{acid solution}}/\text{weight}_{\text{zeolite}}$ = 28.6 $cm^3\ g^{-1}$) at 343 K for 2 h under stirring in an oil bath. After quenching, the samples were thoroughly washed with deionized water, dried, and calcined the same as after the above-mentioned desilication procedure. The acid-washed zeolites are denoted as 'H-ZSM-5*(w)*' and '*meso*HZSM-5*(w)*'. Yield of the acid treatment procedure was 90% to *meso*H-ZSM-5*(w)* (averaged from four experiments starting from 5–7 g of *meso*H-ZSM-5).

Amorphous SiO_2 and the zeolite samples were employed as catalyst supports and loaded with *ca.* 8–10 wt% of Co, applying incipient wetness impregnation with an aqueous $Co(NO_3)_2 \cdot 6H_2O$ solution. All the supports were dried overnight at 393 K before impregnation. Only in the case of parent H-ZSM-5, two impregnation steps were required (due to its low pore volume) with intermediate sample drying at 333 K for 5 h. After impregnation, samples were kept overnight in a desiccator at room temperature and dried at 393 K for 12 h. Subsequently, the catalysts were calcined at 673 K for 2 h. A heating rate of 2 K min^{-1} and static air conditions were applied for all the above-mentioned drying and calcination steps.

2 g of *meso*H-ZSM-5*(w)* was exchanged with 250 cm^3 of 0.01 M $Co(CH_3COO)_2 \cdot 4H_2O$ aqueous solution (pH = *ca.* 6) at 343 K for *ca.* 24 h. After two identical consecutive exchanges, the sample was washed with 1 l of deionized water *via* subsequent centrifugation and redispersion cycles. Finally, the resulting zeolite was kept overnight at 333 K, dried at 393 K for 12 h, and calcined at 673 K for 2 h. The ion-exchanged zeolite contained 1.3 wt% of Co and is denoted as '*meso*H-ZSM-5*(wCo)*'.

5.2.2.2. Carbon deposition over the mesoporous H-ZSM-5

In order to study the catalytic effect of *meso*H-ZSM-5 on the overall performance of the corresponding bifunctional catalyst (Co/*meso*H-ZSM-5), the acid sites of this support were (partially) deactivated by pyrolytic carbon [19, 20]. The pyrolytic carbon was deposited by decomposition of propene over *meso*H-ZSM-5 in a continuous fixed-bed reactor: First, the reactor temperature was ramped to 823 or 973 K under N_2 flow, and subsequently, 4% C_3H_6 was added to the feed stream ($GHSV$ = 14.4 $m^3_{STP}\ kg^{-1}_{zeolite}\ h^{-1}$). The carbon amount was controlled by varying the deposition duration and temperature. The modified zeolites are denoted as '*meso*H-ZSM-5*(nnc)*' where '*nn*' is a two digit number, which indicates the carbon percentage ($g_{carbon}\ g^{-1}_{zeolite+carbon}$).

*meso*H-ZSM-5*(nnc)* samples were loaded with *ca.* 10 wt% Co according to the impregnation method described before. In this case, the impregnated samples were dried under air flow at 343 K for 12 h followed by calcination at 523 K for 2 h. A heating rate of 0.5 K min^{-1} and air flow rate of 1.8 m^3 $kg^{-1}_{Co(NO3)2 \cdot 6H2O}\ h^{-1}$ were employed during the heating steps.

5.2.3. Characterization

N_2 physisorption was performed in an Autosorb-6B unit (Quantachrome Instruments) at liquid nitrogen temperature (77 K). Prior to the experiment, *ca.* 0.1 g of the samples was degassed overnight in an Autosorb Degasser unit (Quantachrome Instruments) under vacuum at 623 K (473 K in the case of Co/*meso*H-ZSM-5*(nnc)*).

Elemental analysis was performed with PerkinElmer Optima instruments. Samples were first digested in *ca.* 50 ml of 1.25% H_2SO_4 and 1.00% HF mixture. After dilution, analysis was done by inductively coupled plasma optical emission spectrometry (ICP-OES).

The X-ray diffraction (XRD) patterns were recorded in Bragg-Brentano geometry in a Bruker D8 Advance diffractometer equipped with a Vantec position sensitive detector and graphite monochromator. Measurements were performed at room temperature, using monochromatic Co Kα radiation (λ = 0.179026 nm) in the 2θ region between 10° and 90°. The samples were placed on a Si {510} substrate and rotated during measurements. All patterns were background-subtracted to eliminate the contribution of air scatter and possible fluorescence radiation.

Transmission electron microscopy (TEM) was done by a FEI Tecnai TF20 microscope operated at 200 kV using a carbon coated Cu grid.

Temperature-programmed NH_3 desorption (NH_3-TPD) was measured by an AutoChem II chemisorption analyzer (Micromeritics). *Ca.* 0.2 g of the zeolite-containing samples was first degassed under He flow at 673 K for 1 h and then saturated with NH_3 at 473 K during 1 h, using a flow of 1.65% NH_3 in He. The gas mixture was then switched back to He, and the sample was purged at 473 K for *ca.* 1 h to remove the weakly adsorbed NH_3 molecules until no ammonia was detected. TP desorption was subsequently recorded under He flow, from 473 to 873 K. All flow rates were adjusted to 25 cm^3_{STP} min^{-1}, and the heating rates were 10 K min^{-1} during different stages of the experiment.

Temperature-programmed reduction by H_2 (TPR(H_2)) was performed on a homemade equipment. *Ca.* 0.1 g of Co-containing samples was mounted in a temperature-controlled reactor where 27 cm^3_{STP} min^{-1} flow of 7.4% H_2 in Ar was fed over the samples. The reactor temperature was then ramped from room temperature to 1223 K with a heating rate of 5 K min^{-1}, and the H_2 consumption was monitored by a TCD.

5.2.3.1. Fourier transform infrared (FT-IR) transmission spectroscopy

5.2.3.1.1. Pyridine adsorption

The amount of Brønsted and Lewis acid sites in zeolite samples was evaluated by pyridine adsorption, assisted by a Nicolet 6700 FT-IR (Thermo Scientific) equipped with a MCT/B detector. *Ca.* 0.05 g of a zeolite sample was pressed at 1132 kg cm^{-2} for 5 s to form self-supporting wafer of 1.5 cm diameter. The sample was then degassed at 393 K for 2 h under vacuum (2×10^{-5} mbar). Pyridine vapor was dosed to the sample stepwise *via* a known volume and pressure. After each step, the sample was heated at 458 K to allow diffusion of the probe molecule and subsequently cooled to room temperature for spectra collection [21]. This procedure was repeated to estimate the extinction coefficient till no further increase was observed in the areas of adsorbed pyridine upon dosage.

Ultimately, the sample was heated at 458 K for 10 min, and the final spectra were recorded at room temperature. During each measurement, 128 scans were recorded in 1000–4000 cm^{-1} range at 4 cm^{-1} resolution. Spectra of degassed samples were collected as background.

5.2.3.1.2. CO adsorption-Diffuse Reflectance Infrared Fourier Transform Spectroscopy (DRIFTS)

Employing CO as a probe molecule, the nature of surface metallic sites and different Co species in the zeolite-supported catalysts was studied by DRIFTS. Catalysts in the powder form were dried inside the DRIFTS cell under He flow at 673 K for 1 h and reduced for 5 h in H_2 at the same temperature. After cooling the sample to room temperature under He flow (and removal of adsorbed H_2 molecules), 10% CO in He was fed to the cell for 0.5 h to allow the adsorption of CO. Subsequently, the sample was flushed overnight by He at room temperature to remove the physisorbed CO. Then, the cell temperature was elevated under the He flow, and IR spectra were collected at different temperatures by a Nicolet 6700 FT-IR (Thermo Scientific) equipped with a MCD/A detector. All the flow rates were adjusted to 20 cm^3_{STP} min^{-1} at different stages of the experiment, and the measurements were performed after 10 min on-stream at each temperature by 280 scans in the range of 650–4000 cm^{-1} at 4 cm^{-1} resolution. Spectra of KBr at room temperature were recorded as background, and those of the samples were subtracted from their corresponding spectra after 5 h H_2 reduction.

5.2.4. Catalytic performance experiments

5.2.4.1. Acid-catalyzed reactions

Acid-catalyzed reactions were performed in a fixed-bed stainless steel reactor employing *n*-C6 as a hydrocarbon model compound. 0.25 g of catalyst particles was fixed in the reactor (3.9 mm inner diameter) between quartz wool plugs. The samples were treated overnight under H_2 flow at 673 K and atmospheric pressure. After cooling to 513 K, the pressure was increased to 15 bar, and subsequently, a mixture of *n*-C6, H_2, and N_2 was fed to the reactor ($SV = 13\ \mathrm{mol_{C6}\ kg^{-1}_{cat}\ h^{-1}}$, $H_2/n\text{-C6} = 9.0$, $N_2/H_2 = 2.0$). After 20 h on-stream, data collection started at different reaction temperatures. The reactor was kept for 3 h at each temperature before product analysis. The product stream was analyzed online by a Compact GC (Interscience), equipped with Porabond Q column at 363 K (10 m × 0.32 mm) and FID, using He as the carrier gas. Selectivity (S_{Cn}) and yield (Y_{Cn}) of the hydrocarbon products were defined by Eqs. (1) and (2), respectively:

$$S_{\mathrm{C}n} = \frac{n}{6}\frac{F_{\mathrm{C}n}}{\left(F_{\mathrm{in},n\text{-C6}} - F_{n\text{-C6}}\right)}\times 100\% \qquad (1), \qquad Y_{\mathrm{C}n} = \frac{n}{6}\frac{F_{\mathrm{C}n}}{F_{\mathrm{in},n\text{-C6}}}\times 100\% \qquad (2)$$

5.2.4.2. Fischer–Tropsch synthesis

FTS experiments were performed on the six-flow fixed-bed microreactor setup described in Chapter 2. For all experiments, 0.5 g of fresh catalyst was fixed in the reactor inserts using quartz wool plugs. Samples were first activated in situ by 80 cm^3_{STP} min^{-1} of H_2 at 673 K for 12 h at atmospheric pressure followed by cooling to 453 K under H_2 flow. After increasing the pressure to the process value (15 bar total pressure), CO was gradually introduced to the feed stream at 453 K in order to reach its final concentration (H_2/CO = 2) in 1 h. Subsequently, the reactor was heated to the process temperature (493 or 513 K). A rate of 2 K min^{-1} was applied for all the heating/cooling steps.

During the experiment, heavy hydrocarbons (wax) were collected by gas/liquid separators at 448 K and reaction pressure. Once expanded to atmospheric pressure, lighter hydrocarbons and water were collected in cold traps at *ca.* 278 K. After separation from water, these liquid hydrocarbons as well as the wax were weighted, dissolved in CS_2, and analyzed offline by a simulated distillation (SimDis) GC (Hewlett Packard 5890, Series II) equipped with an FID and HP-1 column (7.5 m × 0.53 mm, film thickness 2.65 µm), using He as carrier gas. During the analysis, the oven temperature was ramped from 308 to 623 K (14 K min^{-1}) and kept at the final temperature for 5 min.

H_2, N_2, CO, and CO_2 as well as light hydrocarbons in the gas phase were analyzed online by a Compact GC (Interscience), equipped with three columns and detectors in parallel, applying He as carrier gas. In the first column (Carboxen 1010, 10 m × 0.32 mm), N_2, CO, CH_4, and CO_2 were separated at 333 K and analyzed by TCD. In the second column (Al_2O_3/KCl, 10 m × 0.32 mm) and FID detection, separation between all C1–C4 components was achieved at 434 K. In the third column (RTx-1 0.5 µm, 15 m × 0.32 mm), C5–C10 hydrocarbons were separated at 353 K and analyzed by FID.

A pseudo-steady-state catalytic behavior was attained after 20 h on-stream when selectivity data were collected. CO conversion, carbon selectivity, and molar fraction of each product were defined by Eqs. (3)–(5), respectively, where X_{CO} stands for CO conversion, F indicates the molar flow, S is the carbon selectivity toward a product with n carbon atoms, and y is the molar fraction of a hydrocarbon Cn.

$$X_{\mathrm{CO}} = \frac{F_{\mathrm{in,CO}} - F_{\mathrm{out,CO}}}{F_{\mathrm{in,CO}}} \times 100 \qquad (3), \qquad S_{\mathrm{C}n} = \frac{nF_{\mathrm{C}n}}{F_{\mathrm{CO_2}} + \sum_{n=1}^{N} nF_{\mathrm{C}n}} \times 100 \qquad (4), \qquad y_{\mathrm{C}n} = \frac{F_{\mathrm{C}n}}{\sum_{n=1}^{N} F_{\mathrm{C}n}} \qquad (5)$$

5.3. Results

5.3.1. Catalyst characterization

5.3.1.1. Support base/acid treatments

In agreement with previous reports [22], the morphology of the H-ZSM-5 crystallites does not change considerably upon desilication (Figure D1/Appendix D), although its crystallite size decreases slightly. The N_2 physisorption isotherms of these zeolites and the SiO_2 support are presented in Figure D2a/Appendix D. The isotherm of the parent H-ZSM-5 shows a plateau starting at a very low relative pressure (type I), the characteristic of microporous zeolite structures. On the other hand, the type IV isotherm and the remarkable hysteresis loop of amorphous silica confirm the mesoporous structure of the SiO_2 support. Similarly, after desilication, the shape of the zeolite isotherm changes from type I to type IV, and mesostructures are created with pore sizes in similar range as the SiO_2 (Figure D3a/Appendix D). Textural properties of all supports are summarized in Table 1. The mesopore surface area of H-ZSM-5 increases from 52 to 309 $m^2\ g^{-1}$ for *meso*H-ZSM-5, and its total pore volume increases from 0.26 to 1.20 $cm^3\ g^{-1}$, which is very close to that of the SiO_2 (1.35 $cm^3\ g^{-1}$). This increase is due to creation of mesopores at the cost of a slight decrease in the zeolite micropore volume (0.18 *versus* 0.12 $cm^3\ g^{-1}$ for H-ZSM-5 and *meso*H-ZSM-5, respectively). The decrease in micropore volume suggests some minor amorphization during the base treatment which is the consequence of desilication [23]. Nevertheless, the overall MFI structure is preserved, as confirmed by XRD patterns of the corresponding catalysts (Figure D4/Appendix D).

The Si/Al ratio of H-ZSM-5 decreases from 41 to 16 for *meso*HZSM-5 after alkaline treatment and Si extraction from the zeolite framework (Table 1). This ratio can be readjusted by acid treatment; thus, *meso*H-ZSM-5*(w)* represents an Si/Al ratio of 39, which is almost identical to that of the parent zeolite. In contrast, similar treatment results in a minor increase in the Si/Al ratio of the parent zeolite (41 *versus* 46 for H-ZSM-5 and H-ZSM-5*(w)*, respectively). Moreover, the textural properties of

Table 1 Textural and chemical properties of the supports employed for FTS catalyst preparation.

Support	S / $m^2\ g^{-1}$		V / $cm^3\ g^{-1}$			Si/Al[f]
	total[a]	meso[b]	total[c]	micro[d]	meso[e]	
SiO_2	293	248	1.35	0.02	1.34	n.a.[g]
H-ZSM-5	460	52	0.26	0.18	0.08	41
H-ZSM-5*(w)*	435	56	0.25	0.17	0.08	46
*meso*H-ZSM-5	580	309	1.20	0.12	1.08	16
*meso*H-ZSM-5*(w)*	575	314	1.20	0.11	1.09	39
*meso*H-ZSM-5*(07c)*	484	265	1.11	0.09	1.02	n.d.[h]
*meso*H-ZSM-5*(21c)*	369	229	0.84	0.06	0.78	n.d.

[a] BET surface area; [b] Mesopore surface area obtained from the *t*-plot applied to the N_2 isotherm; [c] Total pore volume; [d] Micropore volume obtained from the *t*-plot; [e] Mesopore volume calculated as $V_{meso} = V_{total}-V_{micro}$; [f] Obtained from ICP-OES; [g] Not applicable; [h] Not determined.

H-ZSM-5 and *meso*H-ZSM-5 are barely altered upon the acid treatment (Table 1, Figure D2 and D3/Appendix D), which indicates that the employed acid wash does not leach Al out of the zeolite framework.

5.3.1.2. Carbon deposition

TGA patterns of *meso*H-ZSM-5 zeolite are presented in Figure D5a/Appendix D after treatment with 4% C_3H_6 in N_2 at different temperatures and durations. The total weight loss, associated with the presence of pyrolytic carbon [19], is increased when increasing the treatment temperature and duration. As a result, *ca.* 7% and 21% ($g_{carbon}\ g^{-1}_{zeolite+carbon}$) of carbon is loaded over *meso*H-ZSM-5 after the treatment at 973 K for 6 and 18 h, respectively.

The SEM images of *meso*H-ZSM-5*(07c)* and *meso*H-ZSM-5*(21c)* reveal that apart from agglomeration of the zeolite crystallites, their individual size and morphology do not change after the carbon deposition (*cf.* Figure D6 and D1b/Appendix D). N_2 physisorption results show a lower N_2 uptake (Figure D2c/Appendix D) and decreased micro- and mesopore volumes for carbon-containing samples as compared with *meso*H-ZSM-5, while the decrease in the micropore volume is more pronounced (Table 1). The mesopore size distribution of *meso*HZSM-5 does not change significantly after carbon deposition (*cf.* Figure D3a and c/Appendix D). These results indicate that by C_3H_6 decomposition, carbon is deposited inside the framework more than on the external surface of the zeolite, confirming a higher density of acid sites in the zeolite micropores.

5.3.1.3. Acid properties of supports

NH_3-TPD of H-ZSM-5 and *meso*H-ZSM-5 are compared in Figure D7/Appendix D. The desorption profile of H-ZSM-5 shows two maxima, at around 460 and 700 K. The first is known to arise from the weakly adsorbed NH_3 molecules, whereas the second one originates from the strong Brønsted acid sites [11]. In case of *meso*H-ZSM-5, weaker acid sites are more pronounced than in parent H-ZSM-5. In order to make the contribution of these acid sites more visible, the weakly adsorbed NH_3 molecules were eliminated by performing the adsorption step at 473 K (Figure 1). In this case, the peak at 700 K appears with a tail at lower temperatures for H-ZSM-5 and a shoulder at around 550 K for *meso*H-ZSM-5. While the desorption profiles of H-ZSM-5 and H-ZSM-5*(w)* look very similar (Figure 1a), these weak acid sites disappear to a large extent after subsequent acid treatment of the desilicated sample (Figure 1b). After carbon deposition, the concentration of Brønsted acid sites decreases considerably (Figure 1c). NH_3-TPD profiles of Co-containing zeolites (Figure D8/Appendix D) show that strong Brønsted acid sites are present in the zeolite after Co impregnation. However, *meso*H-ZSM-5*(wCo)* which was exchanged with Co is devoid of Brønsted acidity, and only the weak

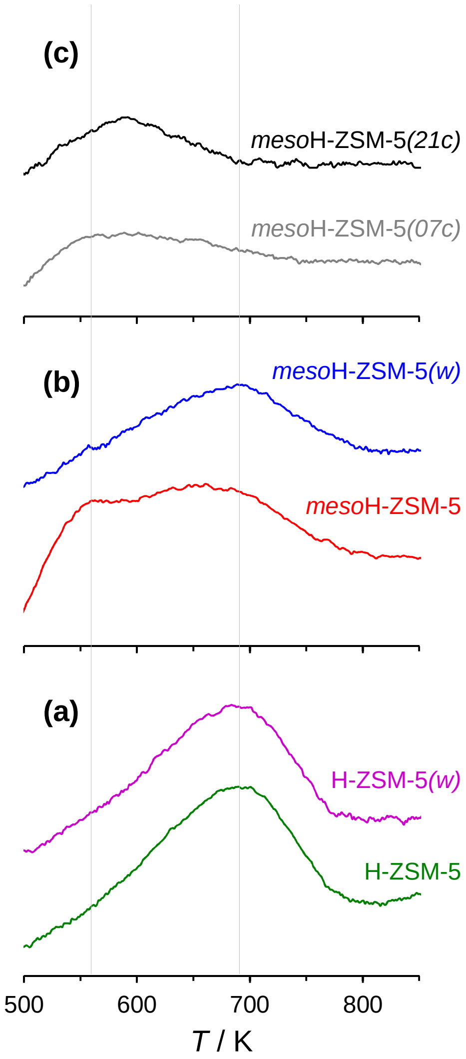

Figure 1. NH_3-TPD profiles (10 K min^{-1}) of the microporous zeolites (a), mesoporous zeolites (b), and carbon deposited mesoporous zeolites. NH_3 was adsorbed at 473 K.

Lewis acid sites can be detected over this sample.

The nature of acid sites over the zeolite samples was further investigated by FT-IR-assisted pyridine adsorption (Figure 2). The IR band at 1456 cm^{-1} arises from the pyridine molecule interacting with Lewis acid sites [24]. The intensity of this peak increases for *meso*H-ZSM-5, while in the case of *meso*H-ZSM-5*(w)*, it is almost similar to that of H-ZSM-5. Apparently, a large number of Lewis acid sites is formed in the zeolite after desilication (Table 2). This result reveals that the weak acidity observed with NH_3-TPD (Figure 1) has a clear Lewis nature and can be ascribed to extraframework Al (EFAl), produced during desilication [23]. EFAl may be washed off by means of acid treatment, as mentioned in Section 5.3.1.1 and as clearly observed by both pyridine adsorption (Figure 2 and Table 2) and NH_3-TPD (*cf.* Figure 1a and b).

The IR absorption at 1545 cm^{-1} in Figure 2 is attributed to adsorption of pyridine on Brønsted acid sites, while the band at 1491 cm^{-1} results from both Brønsted and Lewis sites [24, 25]. Quantification

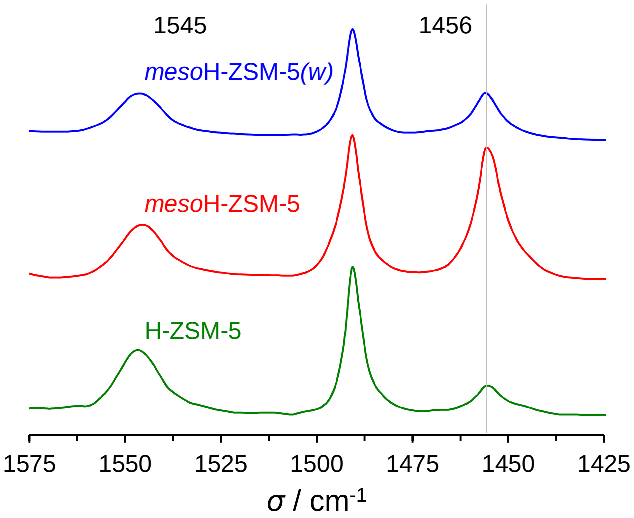

Figure 2. IR spectra of the zeolites upon pyridine adsorption.

of the former peak areas with the amount of adsorbed pyridine reveals that the Brønsted acid density (µmol g^{-1}) decreases upon desilication and even further by acid treatment (Table 2). However, the total number of Brønsted acid sites of *meso*H-ZSM-5*(w)* per mol Al is higher than that of *meso*H-ZSM-5. In other words, Al present in *meso*H-ZSM-5*(w)* contributes more to Brønsted acidity than it does in *meso*H-ZSM-5.

Surface hydroxyl groups of the zeolite samples are clearly visualized by direct observation of the zeolite IR spectra (Figure D9/Appendix D). The Brønsted OH groups show a stretching band at 3310 cm^{-1} [26]. The most intense peak in the OH stretching region at 3747 cm^{-1} can be attributed to terminal SiOH [27]. The concentration of these silanol groups is the highest on *meso*H-ZSM-5*(w)*. It is apparent that more silanol groups form on the zeolite surface by acid treatment.

5.3.1.4. Co-catalysts

Co loadings and crystallite sizes of Co/SiO_2, Co/H-ZSM-5 as well as the modified zeolite-supported catalysts are reported in Table 3. A Co loading of about 10 wt% was obtained on SiO_2, H-ZSM-5, and *meso*H-ZSM-5 supports. The average Co crystallite size of Co/SiO_2 and Co/H-ZSM-5 catalysts is comparable and about 13–14 nm, while it decreases considerably to 7 nm for Co/*meso*H-ZSM-5. The

Table 2 Acid densities of zeolite supports obtained from pyridine adsorption.

Support	Brønsted acid		Lewis acid	
	µmol g^{-1}	µmol $µmol_{Al}^{-1}$	µmol g^{-1}	µmol $µmol_{Al}^{-1}$
H-ZSM-5	138	0.35	37	0.09
*meso*H-ZSM-5	99	0.10	173	0.18
*meso*H-ZSM-5*(w)*	77	0.21	49	0.13

Table 3 Textural and chemical properties of the prepared FTS catalysts.

Catalyst	S / m^2 g^{-1}		V / cm^3 g^{-1}			Co	
	total^a	meso^b	total^c	micro^d	meso^e	wt%^{f}	d_{Co}^{g} / nm
Co/SiO$_2$	223	200	1.03	0.01	1.03	9.7	14
Co/H-ZSM-5	388	38	0.22	0.16	0.06	9.6	13
Co/H-ZSM-5*(w)*	380	45	0.23	0.15	0.08	8.2	8
Co/*meso*H-ZSM-5	467	257	0.87	0.09	0.78	9.9	7
Co/*meso*H-ZSM-5*(w)*	487	279	0.85	0.09	0.76	8.7	8
Co/*meso*H-ZSM-5*(07c)*	364	205	0.77	0.07	0.70	10.9	7
Co/*meso*H-ZSM-5*(21c)*	295	182	0.69	0.05	0.64	11.2	8

[a] BET surface area; [b] Mesopore surface area obtained from the *t*-plot applied to the N$_2$ isotherm; [c] Total pore volume; [d] Micropore volume obtained from the *t*-plot; [e] Mesopore volume calculated as $V_{meso} = V_{total}-V_{micro}$; [f] Obtained from ICP-OES; [g] Co crystallite size calculated from $d(Co^0) = 0.75d(Co_3O_4)$, where $d(Co_3O_4)$ is derived from XRD, applying the Scherrer equation.

mesopore surface area of Co/*meso*H-ZSM-5 is *ca.* 7 times greater than that of Co/H-ZSM-5 (Table 3). The TEM images of the two catalysts (Figure 3) show a spongy morphology for Co/*meso*H-ZSM-5 as compared with Co/H-ZSM-5, which is due to mesoporous structure of the former. Large areas with considerably high concentration of Co oxide are observed at the external surface of H-ZSM-5 crystallites (Figure 3a) and verified by EDX (Figure D10/Appendix D), which suggests an inhomogeneous distribution of the active phase over this support. On the contrary, small Co oxide agglomerates can be identified in the mesopores of *meso*H-ZSM-5 (Figure 3d–f). The positive impact of mesoporosity on metal dispersion has been reported for zeolite-supported catalysts [13, 16, 28].

Lower Co loadings of about 8 wt% on the acid-washed zeolites resulted in an average Co crystallite size of 8 nm for both Co/H-ZSM-5*(w)* and Co/*meso*H-ZSM-5*(w)* catalysts.

In summary (Table 3), Co/SiO$_2$ and Co/H-ZSM-5 have comparable Co crystallite size of around 14 nm, while a size of *ca.* 8 nm is obtained for Co crystallites on Co/*meso*H-ZSM-5, Co/H-ZSM-5*(w)*, Co/*meso*H-ZSM-5*(w)*, Co/*meso*H-ZSM-5*(07c)*, and Co/*meso*H-ZSM-5*(21c)* catalysts.

TPR(H$_2$) profiles of the above-mentioned calcined samples are presented in Figure 4. Two overlapping reduction peaks can be distinguished in the profile of Co/SiO$_2$ below 700 K where the first peak corresponds to reduction of Co^{3+} to Co^{2+} and the second one to the reduction of Co^{2+} to metallic Co [29] (Figure 4a). Co oxide reduction occurs in a wider temperature range for the zeolite-supported catalysts. In the case of microporous zeolite-supported catalysts (*i.e.*, Co/H-ZSM-5 and Co/H-ZSM-5*(w)*), a reduction profile similar to SiO$_2$ is observed at temperatures below 700 K. In addition, two peaks at about 800 and 950 K are also observed, showing the presence of Co species that are more difficult to reduce (Figure 4b), resulting from a stronger interaction of Co with the zeolite than with the amorphous SiO$_2$. Contribution of the high-temperature peaks is more pronounced in the case of Co/H-ZSM-5*(w)* probably due to smaller Co crystallite size. Co oxide inside *meso*H-ZSM-5 and *meso*H-ZSM-5*(w)* supports, exhibits a sharp reduction around 550 K and a broad pattern with several

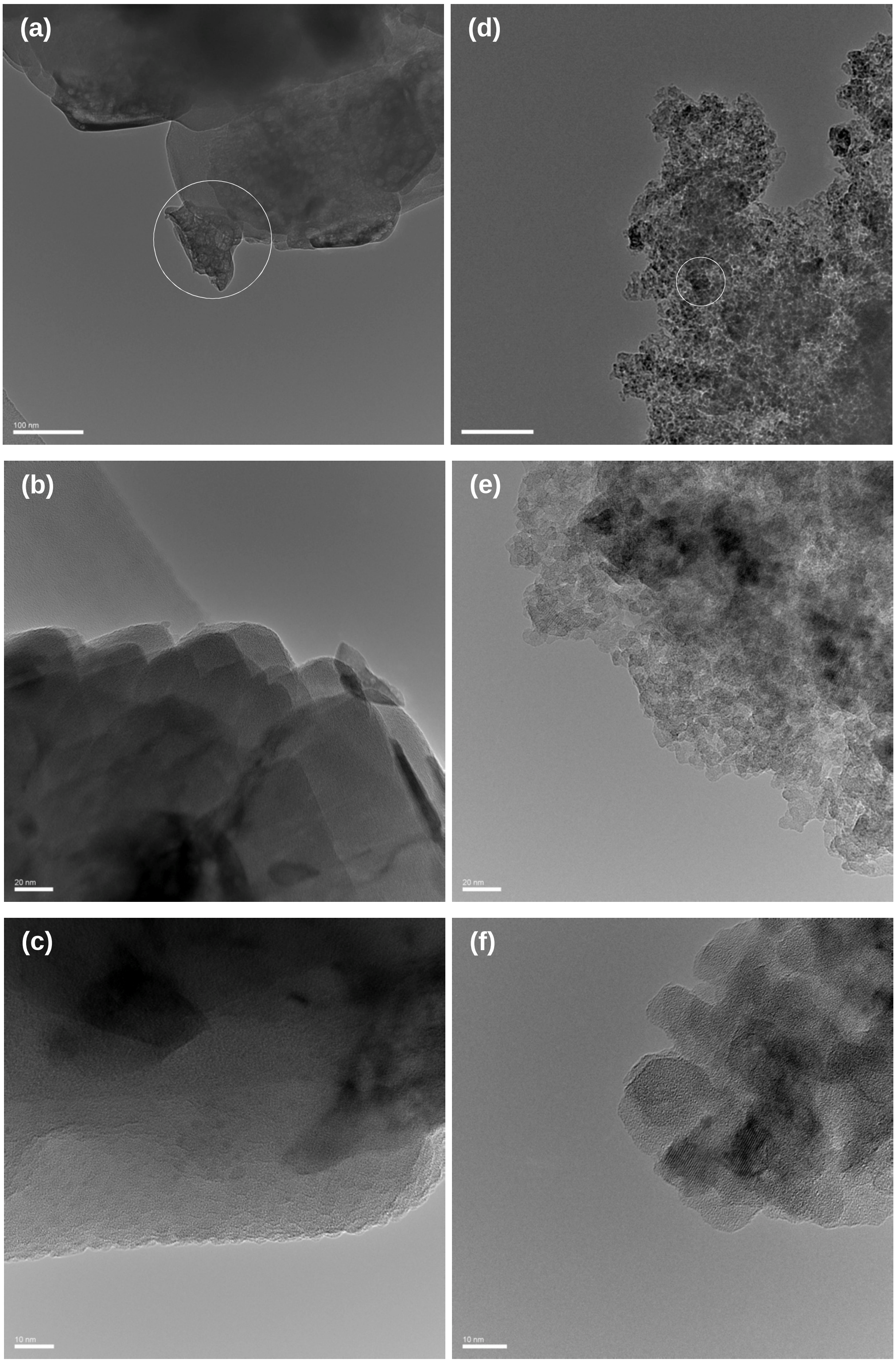

Figure 3. TEM images of Co/H-ZSM-5 (a–c) and Co/*meso*H-ZSM-5 (d–f) before activation. Scale bars correspond to 100 nm (a and d), 20 nm (b and e) and 10 nm (c and f). Circles show Co oxide clusters.

overlapping peaks at 600–1000 K (Figure 4c). In order to determine the reducibility of Co/*meso*H-ZSM-5, this catalyst was reduced at 673 K under conditions similar to those applied prior to FTS experiments (see Section 5.2.4.2), and a TPR(H_2) was recorded afterward. H_2 consumption above

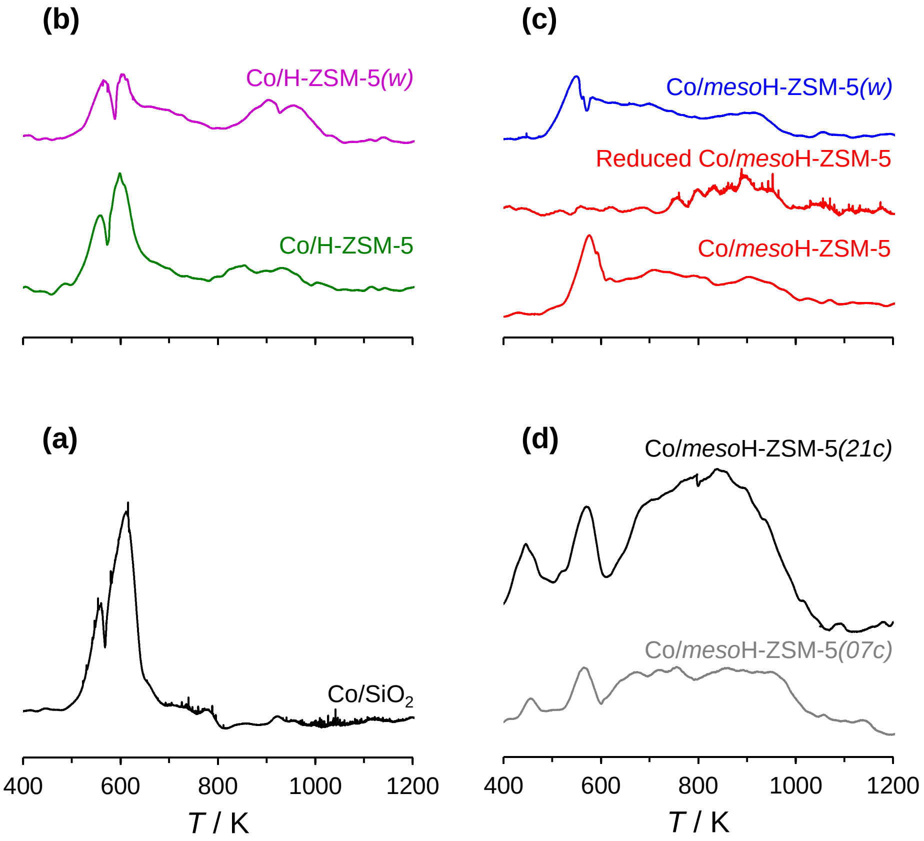

Figure 4. TPR(H_2) profiles (5 K min^{-1}) of Co-catalysts, supported on SiO_2 (a), microporous zeolites (b), mesoporous zeolites (c), and carbon deposited mesoporous zeolites (d).

700 K in the profile of this ‘reduced’ Co/*meso*H-ZSM-5 catalyst (Figure 4c) reveals the presence of Co species which are barely reducible under the applied FTS activation conditions.

TPR(H_2) profiles of Co/*meso*H-ZSM-5*(07c)* and Co/*meso*H-ZSM-5*(21c)* catalysts are different from those of the above-mentioned samples (*cf.* Figure 4c and d). An additional peak is observed at 400–500 K in this case, which might arise from residual nitrate precursors, as the calcination temperature of these catalysts was 150 K lower than that of the other samples. Moreover, the broad peak at 600–1000 K expands progressively as the catalyst contains more carbon. The weight losses of Co/*meso*H-ZSM-5*(07c)* and Co/*meso*H-ZSM-5*(21c)* catalysts upon TGA analysis are similar to those of *meso*H-ZSM-5*(07c)* and *meso*H-ZSM-5*(21c)*, respectively (*cf.* Figure D5a and b/Appendix D). This confirms that calcination at 523 K does not result in major removal of the deposited carbon. In H_2 atmosphere, Co may catalyze the gasification of pyrolytic carbon at higher temperatures [30]. The intensity of the broad TPR(H_2) reduction profile at 600–1000 K that correlates with the amount of carbon on the Co/*meso*H-ZSM-5*(07c)* and Co/*meso*H-ZSM-5*(21c)* catalysts strongly suggests such a gasification [31]. This is corroborated by methane formation observed upon activating Co/*meso*H-ZSM-5*(nnc)* (not shown).

CO adsorption infrared studies were employed to characterize the nature and reactivity of Co active sites over amorphous SiO_2 and the zeolite supports (Figure 5). IR spectra of pre-adsorbed CO on the bare supports show that carbon monoxide desorbs completely at 473 K from the zeolites (not shown), eliminating the acid sites contribution from the presented spectra in Figure 5. Two regions can be observed in the IR spectra of pre-adsorbed CO over the supported Co-catalysts: The IR bands at 2000–2100 cm^{-1} are attributed to side-on adsorption of CO on the Co sites, while the stretchings at 1890 cm^{-1} arise from bridged CO adsorption to Co sites [32-35]. In the linear adsorption region, the spectrum of Co/SiO_2 represents one major stretching band at 2054 cm^{-1}, which is assigned to CO adsorbed on face-centered cubic (fcc) Co phase [35]. The same band is also observed for the zeolite-supported catalysts. However, this type of Co sites is dominant on the SiO_2 support, while various Co species can be distinguished on the zeolite: A band at 2077 cm^{-1} in the spectrum of Co/H-ZSM-5 is attributed to Co sites with lower surface electron density [36] (Figure 5). The intensity of this band is higher at lower temperatures (not shown) in comparison with the absorption at 2054 cm^{-1}. At low temperatures, more

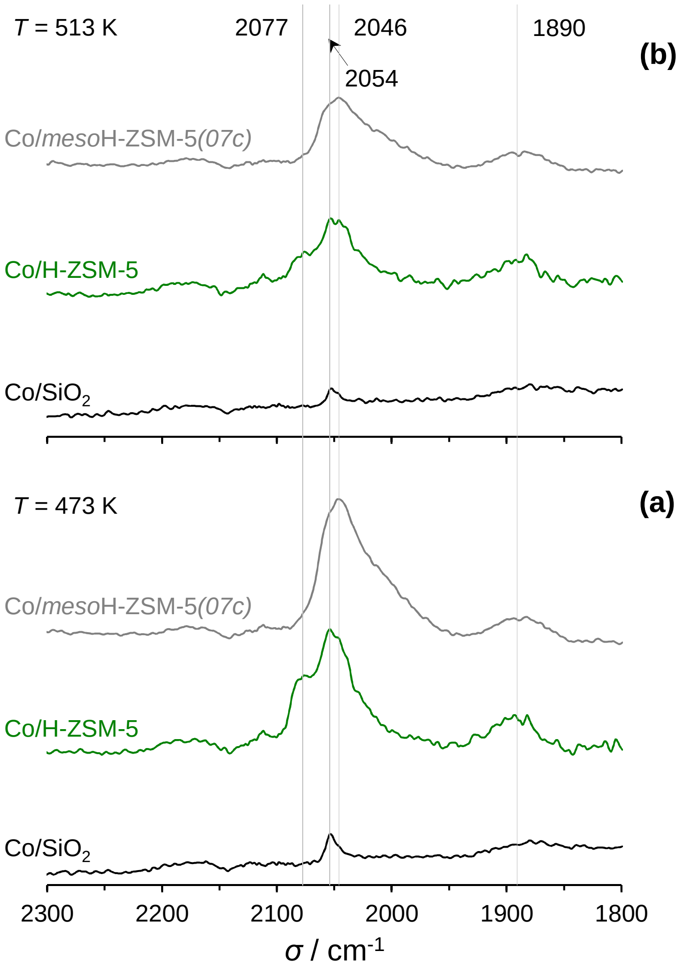

Figure 5. IR spectra of pre-adsorbed CO on Co-catalysts after increasing the temperature to 473 K (a) and 513 K (b) in a DRIFTS cell.

CO coordinates to the surface. Therefore, fewer cobalt atoms without electron withdrawing CO ligands are available that can donate electron density to nearby cobalt atoms (that are coordinated to CO). Increasing the temperature and desorbing more CO, results in a decrease in electron withdrawing π-backbonding carbonyls and causes a general increase in surface electron density and thus stronger cobalt-carbonyl bonding [36]. Therefore, at higher desorption temperatures (Figure 5), contribution of the band at 2077 cm^{-1} decreases, whereas that of lower wavenumbers becomes more pronounced. Besides the peak at 2054 cm^{-1}, linear adsorption of CO on the zeolite-supported Co sites associates with various stretchings appear as a tail between 2000 and 2050 cm^{-1}. The low frequency IR bands, which are hardly observed for Co/SiO_2, have been assigned to lower coordinated cobalt surface sites located on more open low index surface crystallographic planes or steps and corners. An enhanced electron back-donation from the metal *d* orbitals to the π^* antibonding molecular orbital of CO is expected on these sites [37-39].

5.3.2. Catalytic performance

5.3.2.1. Acid-catalyzed reactions

In order to investigate the hydrocarbon conversion reactions under FTS process conditions, the zeolite supports, as well as the supported Co-catalysts, were subjected to a mixture of *n*-C6 and H_2. Product yields as a function of process temperature over H-ZSM-5 are presented in Figure 6a. Increasing yields toward lower hydrocarbons with temperature confirm that hydrocracking is feasible over H-ZSM-5 under typical FTS process conditions and space velocities. Minor amounts of higher hydrocarbons which are not detectable in the feed (C7–C8, not shown) reveal that *n*-C6 hydroconversion proceeds *via* the bimolecular mechanism [4, 40, 41].

n-C6 conversion is lower over *meso*H-ZSM-5 than over H-ZSM-5 (Figure 6b), due to the lower amount of Brønsted acid sites in the former. Product selectivities over H-ZSM-5 and *meso*H-ZSM-5 are similar, with C4 hydrocarbons being the most significant products. The level of C6 isomers in the product implies that the contribution of skeletal isomerization should not be neglected on these catalysts. The fact that no C1 was detected in the products suggests that *n*-C6 hydroconversion involves rearrangement of a classical secondary carbocation into a protonated dialkylcyclopropane where methane cannot be produced [4].

In contrast, considerable selectivities to C1 and C2 are obtained over the supported Co-catalysts (Figure 6b). Since the product selectivity of Co/H-ZSM-5 is comparable to that of Co/SiO_2 (which is devoid of acid sites), *n*-C6 hydroconversion is dominated by hydrogenolysis over the Co sites in this case [42, 43]. The conversion over Co/H-ZSM-5 is four times higher than that over Co/SiO_2 which points to a higher hydrogenolysis activity of the former catalyst. *n*-C6 conversion as well as C1 and C2

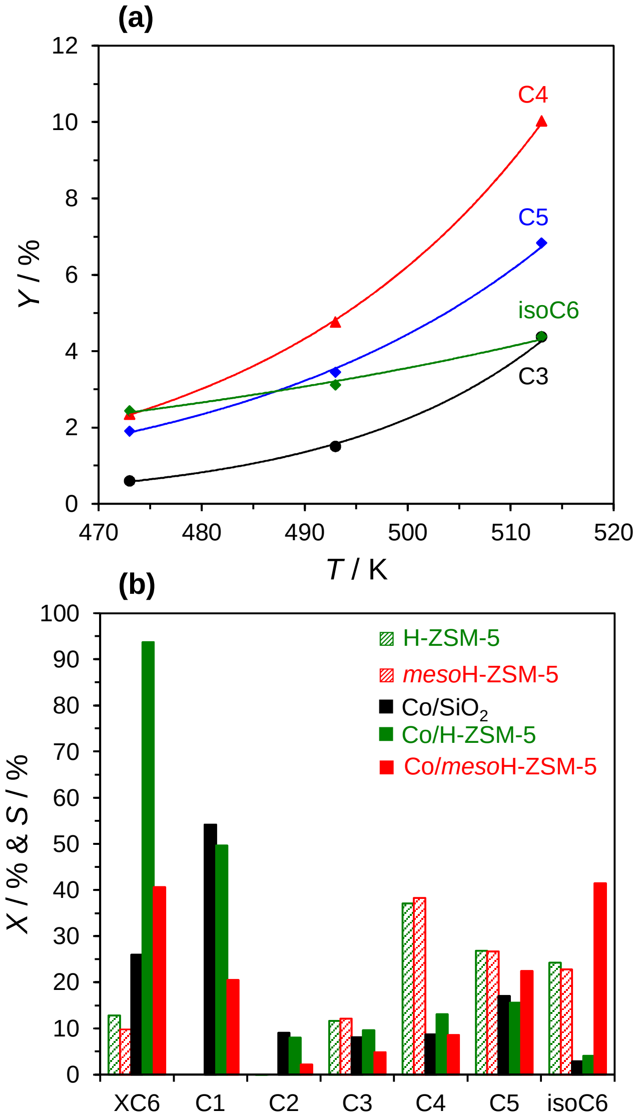

Figure 6. Product yields during *n*-C6 hydroconversion over H-ZSM-5 at different temperatures (a). Conversion and product selectivities in *n*-C6 hydroconversion over zeolites and Co-containing catalysts at 493 K (b). In each group from left to right: H-ZSM-5, *meso*H-ZSM-5, Co/SiO_2, Co/H-ZSM-5, and Co/*meso*H-ZSM-5. Data were collected after 20 h on-stream at 15 bar total pressure, H_2/*n*-C6 = 9.0, N_2/H_2 = 2.0, and *SV* = 13 mol_{C6} kg^{-1}_{cat} h^{-1}.

selectivities decrease considerably over Co/*meso*H-ZSM-5 as compared with Co/H-ZSM-5 while selectivity to C6 isomers is highest over the former.

5.3.2.2. Fischer-Tropsch synthesis

Time-on-stream (*TOS*) evolution of CO conversion over Co/SiO_2, Co/H-ZSM-5, and Co/*meso*H-ZSM-5 is presented in Figure 7a. While the conversion over Co/SiO_2 and Co/H-ZSM-5 is at the same level after 20 h on-stream, that of Co/*meso*H-ZSM-5 is at least 12% higher. The carbon selectivity to different product ranges over these three catalysts is compared in Figure 7b at iso-conversion conditions (as depicted in the Figure insert). Under the applied process conditions, Co/SiO_2 is mostly selective to C12+ hydrocarbons and wax. The carbon selectivities to C5–C11 (gasoline-

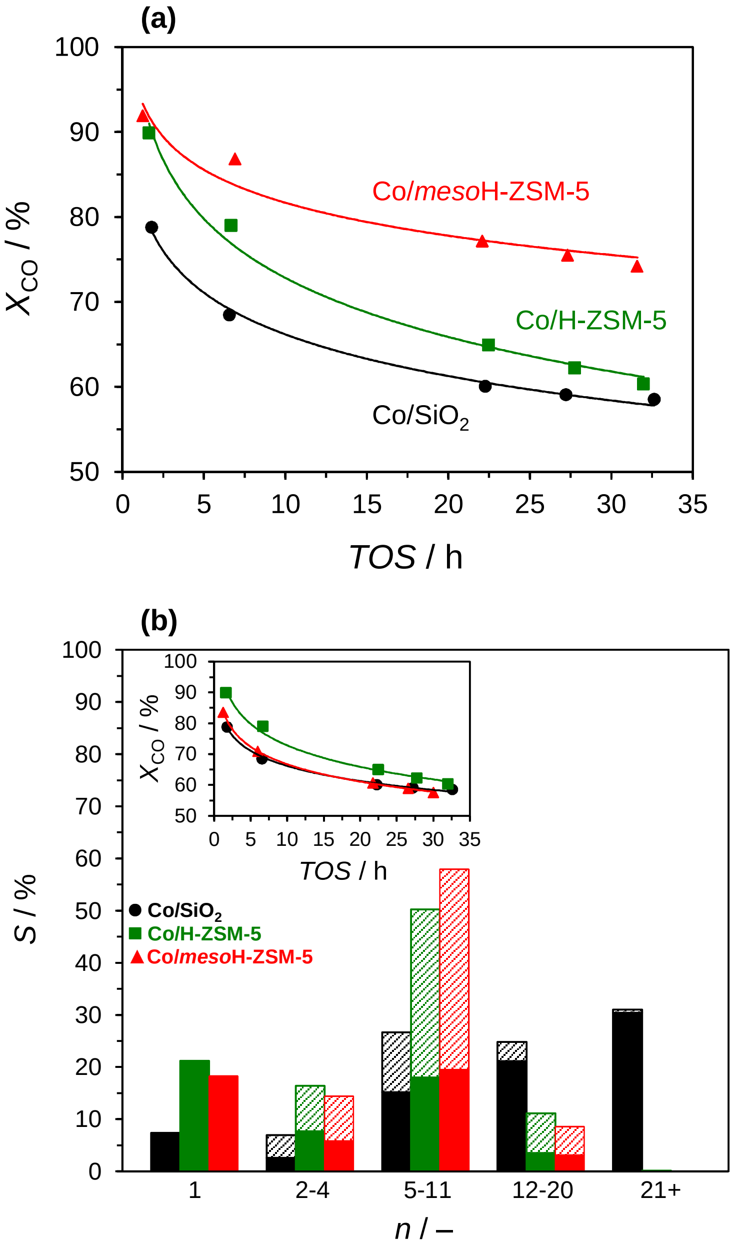

Figure 7. Time-on-stream (*TOS*) evolution of CO conversion during FTS where $GHSV = 2.4\ m^3_{STP}\ kg^{-1}_{cat}\ h^{-1}$ (a). Carbon selectivity of FTS products after 20 h on-stream at iso-conversion conditions (as depicted in the insert) where $GHSV\ /\ m^3_{STP}\ kg^{-1}_{cat}\ h^{-1} = 6.0$ for Co/*meso*H-ZSM-5 and 2.4 for the rest of the catalysts (b). In each carbon number group from left to right: Co/SiO$_2$, Co/H-ZSM-5, and Co/*meso*H-ZSM-5. ■: *n*-paraffins, ▨: sum of isoparaffins and olefins. Experiments were performed at 513 K, 15 bar total pressure, and feed composition $H_2/CO = 2$.

range) and C1 are 27% and 7%, respectively. On the other hand, C21+ (wax) production is reduced over Co/H-ZSM-5, while the selectivity to the C5–C11 fraction has increased considerably to 50%. Carbon selectivity of this catalyst to C1 (21%) is almost three times greater than that over Co/SiO$_2$. For Co/*meso*H-ZSM-5, the C5–C11 selectivity increases to 58% and that to C1 decreases to 18%. Moreover, this catalyst is less selective to lower hydrocarbons (C2–C4) and diesel range (C12–C20).

The CO$_2$ carbon selectivity is less than 8% over the Co-catalysts (Table 4), evidencing a very low

Table 4 CO conversion, C1, C5–C11, and CO_2 carbon selectivities, *iso*- to *n*-paraffin and olefin to paraffin ratios of FTS products after 20 h on-stream.

Process Conditions	Catalyst	X_{CO}	S / %			I/N (C4)[a]	O/P (C2-4)[b]
		%	C1	C5–C11	CO_2		
513 K, 15 bar, $H_2/CO = 2$	Co/SiO_2	59	7	27	3	0.02	1.72
2.4 $m^3_{STP}kg^{-1}_{cat}\ h^{-1}$	Co/H-ZSM-5	62	21	50	1	0.13	1.11
	Co/H-ZSM-5*(w)*	83	21	49	2	0.09	1.02
	Co/*meso*H-ZSM-5	75	16	55	2	0.24	1.32
	Co/*meso*H-ZSM-5*(w)*	87	18	56	4	0.22	1.05
513 K, 15 bar, $H_2/CO = 2$	Co/*meso*H-ZSM-5	59	18	58	1	0.24	1.40
6.0 $m^3_{STP}kg^{-1}_{cat}\ h^{-1}$	Co/*meso*H-ZSM-5*(07c)*	57	19	59	1	0.16	1.48
	Co/*meso*H-ZSM-5*(21c)*	70	19	52	1	0.06	1.12
493 K, 15 bar, $H_2/CO = 2$	Co/SiO_2	31	5	16	2	0.02	2.19
2.4 $m^3_{STP}kg^{-1}_{cat}\ h^{-1}$	Co/H-ZSM-5	41	24	40	2	0.08	0.93
	Co/*meso*H-ZSM-5	49	15	47	0.4	0.11	1.38
513 K, 15 bar, $H_2/CO = 2$ 0.4 $m^3_{STP}kg^{-1}_{cat}\ h^{-1}$	*meso*H-ZSM-5*(wCo)*	6	51	19	7	2.05	0.03

[a] *Iso*- to *n*-C4 ratio; [b] Olefin to paraffin ratio of C2–C4.

water-gas-shift activity at the applied reaction temperatures. The olefin to paraffin ratio of C2–C4 (O/P (C2-4)) hydrocarbons is highest over Co/SiO_2 and decreases by 35% and 19% for Co/H-ZSM-5 and Co/*meso*H-ZSM-5, respectively, at iso-conversion conditions. On the other hand, the *iso*- to *n*-C4 ratio (I/N (C4)) increases by a factor of ten over the Co/*zeolite* catalysts as compared to Co/SiO_2, while it is highest over the mesoporous supported sample (Table 4).

Molar product distributions over Co/SiO_2, Co/H-ZSM-5, and Co/*meso*H-ZSM-5 at iso-conversion conditions are presented in Figure 8. The molar fraction of FTS hydrocarbons *versus* their carbon number follows a linear trend over Co/SiO_2 which points to an ASF distribution with a chain growth probability (α) of 0.87 for this catalyst. In contrast, hydrocarbon distribution over Co/H-ZSM-5 and Co/*meso*H-ZSM-5 is not bounded by one linear chain growth. The ASF distribution breaks at around C11 and molar fractions of hydrocarbons drop dramatically (note the logarithmic scale on *y*-axis in Figure 8) as their carbon number exceeds the upper limit of gasoline cut.

Figure 9 represents the catalytic performances of the three above-mentioned catalysts at lower reaction temperature of 493 K. In addition to a lower CO conversion level, the selectivity to C21+ increases considerably over Co/SiO_2 in comparison with that at 513 K (Figure 7b). At the same time, the selectivities toward all other hydrocarbon fractions decrease, which points to an increase in the chain growth probability of this catalyst at lower reaction temperatures [44]. For the zeolite-supported catalyst, the selectivities to C2–C4 and C5–C11 (Figure 9) as well as I/N (C4) ratio (Table 4) decrease,

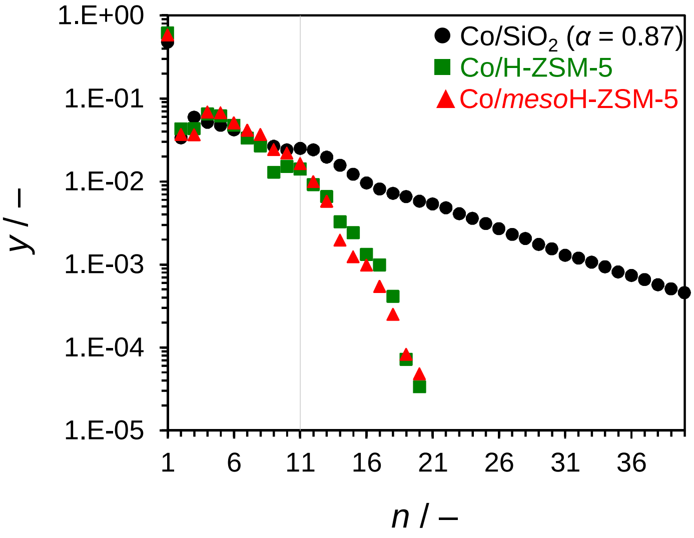

Figure 8. Molar distribution of FTS products after 20 h on-stream at 513 K, 15 bar total pressure, H_2/CO = 2, and iso-conversion conditions where *GHSV* / m^3_{STP} kg^{-1}_{cat} h^{-1} = 6.0 for Co/*meso*H-ZSM-5 and 2.4 for the rest of the catalysts.

while the selectivity to C12+ increases.

The CO conversion and carbon selectivities of catalysts supported on acid-washed H-ZSM-5 and *meso*H-ZSM-5 zeolites are compared in Figure 10. The CO conversion over Co/H-ZSM-5*(w)* is 20% higher than that over Co/H-ZSM-5 (*cf.* inserts in Figure 7b and Figure 10). This catalytic activity

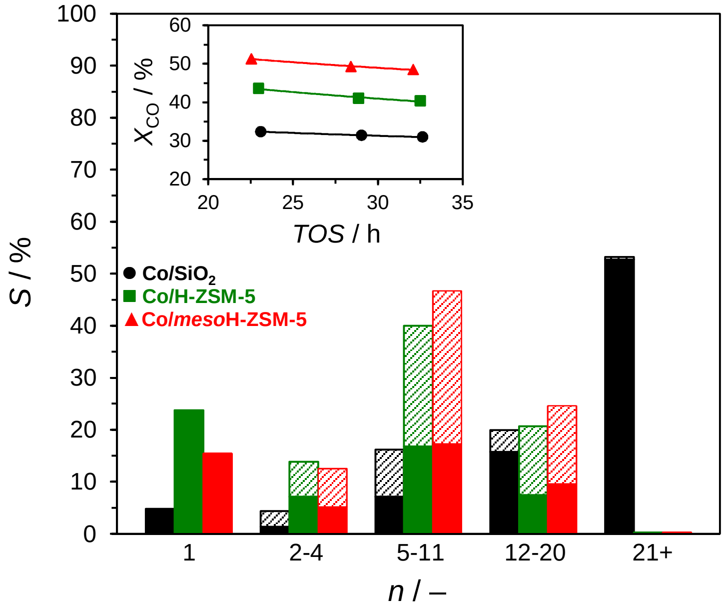

Figure 9. Carbon selectivity of FTS products after 20 h on-stream at 493 K, 15 bar total pressure, feed composition H_2/CO = 2, and *GHSV* = 2.4 m^3_{STP} kg^{-1}_{cat} h^{-1}. In each carbon number group from left to right: Co/SiO_2, Co/H-ZSM-5, and Co/*meso*H-ZSM-5. ■: *n*-paraffins, ▨: sum of isoparaffins and olefins. Insert shows the time-on-stream (*TOS*) evolution of CO conversion.

improvement is also observed for Co/*meso*H-ZSM-5*(w)* over Co/*meso*H-ZSM-5 (Figure 10). Nevertheless, the product distributions of Co/H-ZSM-5*(w)* and Co/*meso*H-ZSM-5*(w)* are to a large extent similar as those of Co/H-ZSM-5 and Co/*meso*H-ZSM-5, respectively.

Figure 11 depicts the catalytic performances of Co-catalysts supported on carbon loaded *meso*H-ZSM-5. The CO conversion levels off with an increase in carbon content of the employed support (Figure insert); thus, Co/*meso*H-ZSM-5*(21c)* is more active than Co/*meso*H-ZSM-5*(07c)*. The C5–C11 fraction decreases over Co/*meso*H-ZSM-5*(21c)* yielding an increase in C12–C20 as compared with Co/*meso*H-ZSM-5*(07c)*. Moreover, both O/P and I/N ratios get lower with increasing the carbon content (Table 4, Figure 11).

5.4. Discussion

The use of hierarchical ZSM-5 as cobalt support for Fischer-Tropsch synthesis results in a deviation of the ASF distribution: production of long-chain hydrocarbons is strongly reduced by secondary reactions over the bifunctional catalyst. Modifying the zeolite texture and surface chemistry by desilication and acid washing alters its accessibility and interaction with the cobalt phase and consequently the CO adsorption behavior and FTS product distribution.

Increasing the mesoporosity *via* desilication provides the microporous zeolite with essential surface area to support small metal particles and indeed, Co crystallites are much smaller on *meso*H-ZSM-5

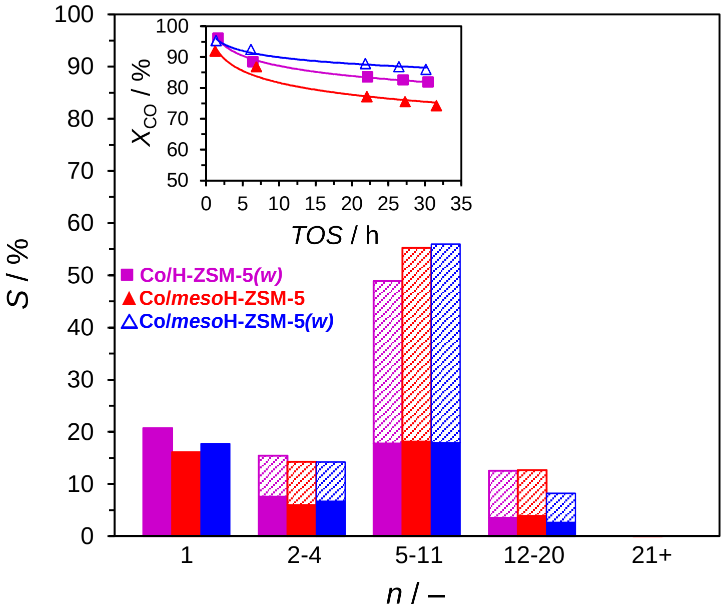

Figure 10. Carbon selectivity of FTS products after 20 h on-stream at 513 K, 15 bar total pressure, feed composition H_2/CO = 2, and *GHSV* = 2.4 m^3_{STP} kg^{-1}_{cat} h^{-1}. In each carbon number group from left to right: Co/H-ZSM-5*(w)*, Co/*meso*H-ZSM-5, and Co/*meso*H-ZSM-5*(w)*. ■: *n*-paraffins, ▨: sum of isoparaffins and olefins. Insert shows the time-on-stream (*TOS*) evolution of CO conversion.

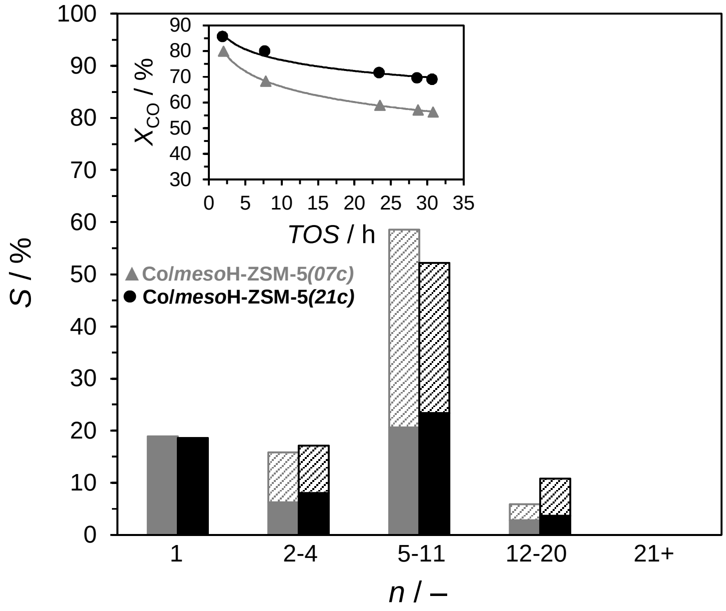

Figure 11. Carbon selectivity of FTS products after 20 h on-stream at 513 K, 15 bar total pressure, H_2/CO = 2, and *GHSV* = 6.0 m^3_{STP} kg^{-1}_{cat} h^{-1}. In each carbon number group from left to right: Co/*meso*H-ZSM-5*(07c)* and Co/*meso*H-ZSM-5*(21c)*. ■: *n*-paraffins, ▨: sum of isoparaffins and olefins. Insert shows the time-on-stream (*TOS*) evolution of CO conversion.

(Table 3). This improves the metal dispersion, and hence, the activity of Co/*meso*H-ZSM-5 is higher than that of Co/H-ZSM-5 (Figure 7a).

After desilication, high concentrations of EFAl are formed in *meso*H-ZSM-5 as evidenced by pyridine adsorption (Figure 2). EFAl species may react with Co to form cobalt aluminates which are barely reducible [29] and thus inactive in Fischer-Tropsch synthesis. Acid washing the H-ZSM-5 and *meso*H-ZSM-5 supports removes the EFAl, especially from the latter. Therefore, the FTS activity of Co/*meso*H-ZSM-5*(w)* is higher than that of Co/*meso*H-ZSM-5, in spite of their similar crystallite size and lower Co content of the former (insert in Figure 10).

Furthermore, the concentration of terminal silanol groups on the support surface increases after acid treatment (Figure D9/Appendix D), which may promote the adsorption of Co nitrate precursor during impregnation. At lower metal loadings, small Co crystallites are obtained on H-ZSM-5*(w)* resulting in similar conversion levels as Co/*meso*H-ZSM-5*(w)* (insert in Figure 10). These results further confirm that Co dispersion improvement is the main origin of enhanced catalytic activity of Co/*meso*H-ZSM-5 relative to that of Co/H-ZSM-5 at elevated Co loadings.

Deposition of carbon on the zeolite support prior to impregnation enhances the FTS activity. The catalytic activity correlates with the amount of carbon deposited over the zeolite, since CO conversion is at least 12% higher over Co/*meso*H-ZSM-5*(21c)* than over Co/*meso*H-ZSM-5*(07c)* (insert in Figure 11). Presence of carbon on the support may generate cobalt carbide during the catalyst preparation.

Cobalt carbide is not active in FTS; however, reducing the supported cobalt carbide promotes the formation of hexagonal cobalt phase (hcp) [45, 46] which is more active than face-centered cubic cobalt phase (fcc) in FTS [46, 47]. The higher contribution of hcp Co phase in Co/*meso*H-ZSM-5*(07c)* with respect to Co/H-ZSM-5 can be verified by the IR spectra of pre-adsorbed CO on Co-catalysts in Figure 5: A band at 2050 cm^{-1} has been previously assigned to linearly coordinated CO to fcc phase of Co^0 on the surface of the catalyst [35], which agrees with the prevalence of this crystalline phase in Co/SiO_2 and Co/H-ZSM-5. On the other hand, bands observed at a lower wavenumber of 2035 cm^{-1} have been assigned to CO adsorbed in linear form on hcp phase of Co^0. The shift of the maxima from 2054 in case of Co/H-ZSM-5 to 2046 for Co/*meso*H-ZSM-5*(07c)* confirms the dominance of hcp phase over the latter catalyst. The use of carbon and organic modifiers has also been reported in the literature to enhance the Co dispersion [48-50].

Increased selectivities to gasoline-range hydrocarbons and isoparaffins by combining the FTS active phase and zeolites has been reported by several groups [10, 11, 13, 16, 51, 52]. In line with the literature, our results with H-ZSM-5 (Figure 7) show that this improvement is due to a non-linear trend in the molar distribution of hydrocarbon products (Figure 8). A break in this ASF distribution at about C11 results in decreased selectivities to C12+ which cannot be explained solely by a low intrinsic FTS chain growth. Acid sites in the vicinity of Co clearly promote acid-catalyzed reactions, *i.e.*, cracking and isomerization [16]. It is speculated that close vicinity of these sites is especially effective to convert the olefinic FTS products, before they are hydrogenated to paraffins.

Hydrocracking under FTS process conditions and comparable space velocities is obvious over H-ZSM-5 and *meso*H-ZSM-5 (Figure 6). However, in the case of supported Co samples, this is harder to prove, since Co is an active hydrogenolysis catalyst [53, 54]. Although hydrogenolysis may be suppressed during FTS by competitive adsorption of CO on the metal sites [55], this reaction dominates in absence of CO (Figure 6b). On the other hand, C4 isomers are typical products of (hydro)cracking [56], and indeed, the *iso*- to *n*-C4 hydrocarbons increases considerably in the product spectrum of the zeolite-supported catalysts (Table 4). Instant hydrocracking of FTS products on the acid sites explains the observed cutoff in FTS product distribution of bifunctional catalysts in Figure 8: Hydrocarbons become more prone to hydrocracking as their carbon number increases due to their increased adsorption strength [14, 57], and consequently, their molar fractions progressively deviate from a classical ASF distribution such as that exhibited by Co/SiO_2.

The acid sites of Co/*meso*H-ZSM-5*(07c)* and Co/*meso*H-ZSM-5*(21c)* are (partially) deactivated by carbonaceous species, resulting in a decreased selectivity to the C5–C11 cut (Figure 11) and isoparaffins (Table 4) which is more pronounced for Co/*meso*H-ZSM-5*(21c)*. This further confirms the role of acid-catalyzed reactions in the altered product slate for Co/*meso*H-ZSM-5 catalyst.

As shown in previous works [13, 16, 58], the improved C1 and C5–C11 selectivities of Co/*meso*H-ZSM-5 (or Co/*meso*H-ZSM-5*(w)*) with respect to the Co/H-ZSM-5 (or Co/H-ZSM-5*(w)*) (Figure 7b and Figure 10) are attributed to mass transport improvements in the former catalyst particles. Lower *n*-C6 conversion and C1–C2 selectivities over Co/*meso*H-ZSM-5 as compared with Co/H-ZSM-5 (Figure 6b) suggest that hydrocarbon hydrogenolysis is suppressed over the former. This is due to an enhancement in diffusion of hydrocarbons out of the catalyst particle and demonstrates the above-mentioned mass transport improvement.

In Figure 8, the methane level for all the Co-catalysts (including Co/SiO_2) is higher than what is anticipated by extrapolating the ASF distribution to $n = 1$, which points to a separate reaction that generates C1 in parallel to FTS [59]. Co is known to be an active hydrogenation metal, and therefore, direct CO hydrogenation to methane is expected over the Co-based catalysts [60]. The lower O/P ratio of all the zeolite-containing catalysts than that of Co/SiO_2 (Table 4) suggests that this hydrogenation functionality is stronger when Co is loaded on H-ZSM-5 supports. Moreover, zeolite-supported Co-catalysts are more active than Co/SiO_2 in the hydrogenolysis reaction (Figure 6b) which further confirms this hypothesis.

According to our IR characterization by CO adsorption (Figure 5), more lower coordinated Co surface sites are observed over the zeolite supports as compared to amorphous silica. The density of lower index surface crystallographic planes or steps and corners increases as Co crystallite size decreases [61], and indeed, Co oxide particles of *ca.* 2 nm can be observed on H-ZSM-5 (Figure 3c and D11/Appendix D). From these results, it is clear that mesoporous H-ZSM-5 promotes the dispersion of Co particles, resulting in a larger amount of such coordinatively unsaturated sites. Small Co crystallites are very active in CO hydrogenation [62] and hydrogenolysis reactions (Fig. 6b) which explain the higher C1 selectivity of Co/*zeolite* than that of Co/SiO_2 (Fig. 7b). So to demonstrate this conclusion, *meso*H-ZSM-5*(wCo)* was tested in FTS reaction. A 51% carbon selectivity to C1 and an O/P ratio of almost zero, obtained over this sample (Table 4), further confirms that low coordinated Co sites (in this case promoted to form *via* ion-exchange) are indeed very active in hydrogenation.

As a consequence of the stronger hydrogenation functionality, the (on average) higher H_2 concentrations at lower conversion levels over the catalyst bed also result in higher C1 selectivities over the zeolite-supported catalysts (*cf.* Co/*meso*H-ZSM-5 in Figure 7b and Figure 10). Therefore, a lower reaction temperature (lower conversion) may still result in similar C1 selectivity as a higher temperature (493 *versus* 513 K) operation in contrast to Co/SiO_2.

Similarly, this increased hydrogenation activity is observed in the olefin selectivities where O/P ratio increases for Co/SiO_2 by decreasing the reaction temperature, whereas it only slightly decreases for the zeolite-supported Co-catalysts (Table 4).

5.5. Conclusions

H-ZSM-5-supported Co-catalysts combine Fischer-Tropsch and acid functionalities. Introducing mesopores in H-ZSM-5 by desilication provides it with sufficient mesopore surface area to be used as FTS catalyst supports. Application of this bifunctional catalyst in FTS results in a high selectivity to liquid fractions and reduces the wax production as compared to Co/SiO_2. The high selectivity to gasoline-range products over H-ZSM-5-supported catalysts is visible as a cutoff in the molar distribution above C11 in terms of the ASF distribution of conventional catalysts (Co/SiO_2). This is due to hydrocracking of primary FTS hydrocarbons as evidenced by model hydroconversion experiments. Partial deactivation of the acid site by carbonaceous species during catalyst synthesis decreases the *iso*- to *n*-paraffin ratio and selectivity to gasoline fraction which further confirms the abovementioned role of acid-catalyzed reactions in tuning the product selectivity. On the other hand, the strong Co-zeolite interaction results in formation of more Co particles with lower coordination sites and a higher selectivity toward methane. The latter is attributed to the higher activity for CO hydrogenation and hydrocarbon hydrogenolysis reactions at such Co species.

References

[1] R. Guettel, U. Kunz, T. Turek, Chem. Eng. Technol. 31 (2008) 746-754.
[2] H.M.T. Galvis, J.H. Bitter, C.B. Khare, M. Ruitenbeek, A.I. Dugulan, K.P. de Jong, Science 335 (2012) 835-838.
[3] A.P. Steynberg, R.L. Espinoza, B. Jager, A.C. Vosloo, Appl. Catal. A-Gen. 186 (1999) 41-54.
[4] A. de Klerk, E. Furimsky, Catalysis in the Refining of Fischer-Tropsch Syncrude, RSCPublishing, Cambridge, UK, 2010.
[5] R. Luque, A.R. de la Osa, J.M. Campelo, A.A. Romero, J.L. Valverde, P. Sanchez, Energy Environ. Sci. 5 (2012) 5186-5202.
[6] E. van Steen, M. Claeys, Chem. Eng. Technol. 31 (2008) 655-666.
[7] B. Sun, M. Qiao, K. Fan, J. Ulrich, F. Tao, ChemCatChem 3 (2011) 542-550.
[8] R. Oukaci, J.C.S. Wu, J.G. Goodwin, J. Catal. 110 (1988) 47-57.
[9] A. Martínez, J. Rollán, M.A. Arribas, H.S. Cerqueira, A.F. Costa, E.F. S.-Aguiar, J. Catal. 249 (2007) 162-173.
[10] A. Freitez, K. Pabst, B. Kraushaar-Czarnetzki, G. Schaub, Ind. Eng. Chem. Res. 50 (2011) 13732-13741.
[11] J. Kang, K. Cheng, L. Zhang, Q. Zhang, J. Ding, W. Hua, Y. Lou, Q. Zhai, Y. Wang, Angew. Chem.-Int. Edit. 50 (2011) 5200-5203.
[12] S. Sartipi, M. Alberts, M.J. Meijerink, T.C. Keller, J. Pérez-Ramírez, J. Gascon, F. Kapteijn, ChemSusChem 6 (2013) 1646-1650.
[13] S. Sartipi, K. Parashar, M. Makkee, J. Gascon, F. Kapteijn, Catal. Sci. Technol. 3 (2013) 572-575.
[14] C. Bouchy, G. Hastoy, E. Guillon, J.A. Martens, Oil Gas Sci. Technol. 64 (2009) 91-112.
[15] D. Leckel, Energy Fuels 21 (2007) 1425-1431.
[16] S. Sartipi, J. van Dijk, J. Gascon, F. Kapteijn, Appl. Catal. A-Gen. 456 (2013) 11-22.
[17] S. Mitchell, N.L. Michels, K. Kunze, J. Pérez-Ramírez, Nat. Chem. 4 (2012) 825-831.
[18] J. Bao, J. He, Y. Zhang, Y. Yoneyama, N. Tsubaki, Angew. Chem.-Int. Edit. 47 (2008) 353-356.
[19] J. Rodriguez-Mirasol, T. Cordero, L.R. Radovic, J.J. Rodriguez, Chem. Mat. 10 (1998) 550-558.
[20] T. Kyotani, Z. Ma, A. Tomita, Carbon 41 (2003) 1451-1459.

[21] J.A.Z. Pieterse, S. Veefkind-Reyes, K. Seshan, L. Domokos, J.A. Lercher, J. Catal. 187 (1999) 518-520.

[22] J. Pérez-Ramírez, S. Mitchell, D. Verboekend, M. Milina, N.L. Michels, F. Krumeich, N. Marti, M. Erdmann, ChemCatChem 3 (2011) 1731-1734.

[23] D. Verboekend, S. Mitchell, M. Milina, J.C. Groen, J. Pérez-Ramírez, J. Phys. Chem. C 115 (2011) 14193-14203.

[24] K. Cheng, J. Kang, S. Huang, Z. You, Q. Zhang, J. Ding, W. Hua, Y. Lou, W. Deng, Y. Wang, ACS Catal. 2 (2012) 441-449.

[25] J.B. Koo, N. Jiang, S. Saravanamurugan, M. Bejblová, Z. Musilová, J. Čejka, S.E. Park, J. Catal. 276 (2010) 327-334.

[26] J. Szanyi, M.T. Paffett, Microporous Mesoporous Mat. 7 (1996) 201-218.

[27] S. Bordiga, E. Escalona Platero, C. Otero Areán, C. Lamberti, A. Zecchina, J. Catal. 137 (1992) 179-185.

[28] D. Verboekend, R. Caicedo-Realpe, A. Bonilla, M. Santiago, J. Pérez-Ramírez, Chem. Mat. 22 (2010) 4679-4689.

[29] P. Arnoldy, J.A. Moulijn, J. Catal. 93 (1985) 38-54.

[30] A. Nieto-Márquez, S. Gil, A. Romero, J.L. Valverde, S. Gómez-Quero, M.A. Keane, Appl. Catal. A-Gen. 363 (2009) 188-198.

[31] J. van Doorn, H.A.A. Barbolina, J.A. Moulijn, Ind. Eng. Chem. Res. 31 (1992) 101-107.

[32] S. Sun, N. Tsubaki, K. Fujimoto, Appl. Catal. A-Gen. 202 (2000) 121-131.

[33] G. Bian, A. Oonuki, Y. Kobayashi, N. Koizumi, M. Yamada, Appl. Catal. A-Gen. 219 (2001) 13-24.

[34] J. Zhang, J. Chen, J. Ren, Y. Sun, Appl. Catal. A-Gen. 243 (2003) 121-133.

[35] D. Song, J. Li, Q. Cai, J. Phys. Chem. C 111 (2007) 18970-18979.

[36] N. Kumar, K. Jothimurugesan, G.G. Stanley, V. Schwartz, J.J. Spivey, J. Phys. Chem. C 115 (2011) 990-998.

[37] G. Blyholder, J. Phys. Chem. 68 (1964) 2772-2778.

[38] G. Blyholder, L.D. Neff, J. Phys. Chem. 73 (1969) 3494-3496.

[39] L.E.S. Rygh, C.J. Nielsen, J. Catal. 194 (2000) 401-409.

[40] J.A.Z. Pieterse, K. Seshan, J.A. Lercher, J. Catal. 195 (2000) 326-335.

[41] F. Bauer, E. Bilz, W.H. Chen, A. Freyer, V. Sauerland, S.B. Liu, Stud. Surf. Sci. Catal. 170 (2007) 1096-1103.

[42] W. Juszczyk, Z. Karpinski, J. Pielaszek, Z. Paal, J. Catal. 143 (1993) 583-593.

[43] W. Böhringer, A. Kotsiopoulos, M. de Boer, C. Knottenbelt, J.C.Q. Fletcher, Stud. Surf. Sci. Catal. 163 (2007) 345-365.

[44] D. Vervloet, F. Kapteijn, J. Nijenhuis, J.R. van Ommen, Catal. Sci. Technol. 2 (2012) 1221-1233.

[45] A.Y. Khodakov, W. Chu, P. Fongarland, Chem. Rev. 107 (2007) 1692-1744.

[46] O. Ducreux, B. Rebours, J. Lynch, M. Roy-Auberger, D. Bazin, Oil Gas Sci. Technol. 64 (2009) 49-62.

[47] D.I. Enache, B. Rebours, M. Roy-Auberger, R. Revel, J. Catal. 205 (2002) 346-353.

[48] J. van de Loosdrecht, M. van der Haar, A.M. van der Kraan, A.J. van Dillen, J.W. Geus, Appl. Catal. A-Gen. 150 (1997) 365-376.

[49] J.S. Girardon, E. Quinet, A. Griboval-Constant, P.A. Chernavskii, L. Gengembre, A.Y. Khodakov, J. Catal. 248 (2007) 143-157.

[50] N. Koizumi, T. Mochizuki, M. Yamada, Catal. Today 141 (2009) 34-42.

[51] V.U.S. Rao, R.J. Gormley, A. Shamsi, T.R. Petrick, J.M. Stencel, R.R. Schehl, R.D.H. Chi, R.T. Obermyer, J. Mol. Catal. 29 (1985) 271-283.

[52] J. He, Z. Liu, Y. Yoneyama, N. Nishiyama, N. Tsubaki, Chem.-Eur. J. 12 (2006) 8296-8304.

[53] C.J. Machiels, R.B. Anderson, J. Catal. 58 (1979) 268-275.

[54] E.A. Medvedkova, Kinet. Catal. 32 (1992) 821-824.

[55] R.J. Gormley, V.U.S. Rao, R.R. Anderson, R.R. Schehl, R.D.H. Chi, J. Catal. 113 (1988) 193-205.

[56] J.A. Moulijn, M. Makkee, A. van Diepen, Chemical Process Technology, John Wiley & Sons, Chichester, 2001.

[57] J. Wei, Ind. Eng. Chem. Res. 33 (1994) 2467-2472.

[58] D. Vanhove, Z. Zhuyong, L. Makambo, M. Blanchard, Appl. Catal. 9 (1984) 327-342.

[59] C.G. Visconti, E. Tronconi, L. Lietti, P. Forzatti, S. Rossini, R. Zennaro, Top. Catal. 54 (2011) 786-800.

[60] H. Schulz, Stud. Surf. Sci. Catal. 163 (2007) 177-199.

[61] R. van Hardeveld, F. Hartog, Surf. Sci. 15 (1969) 189-230.

[62] J.P. den Breejen, P.B. Radstake, G.L. Bezemer, J.H. Bitter, V. Frøseth, A. Holmen, K.P. de Jong, J. Am. Chem. Soc. 131 (2009) 7197-7203.

Chapter 6

Insights into the catalytic performance of mesoporous H-ZSM-5-supported cobalt in Fischer-Tropsch synthesis

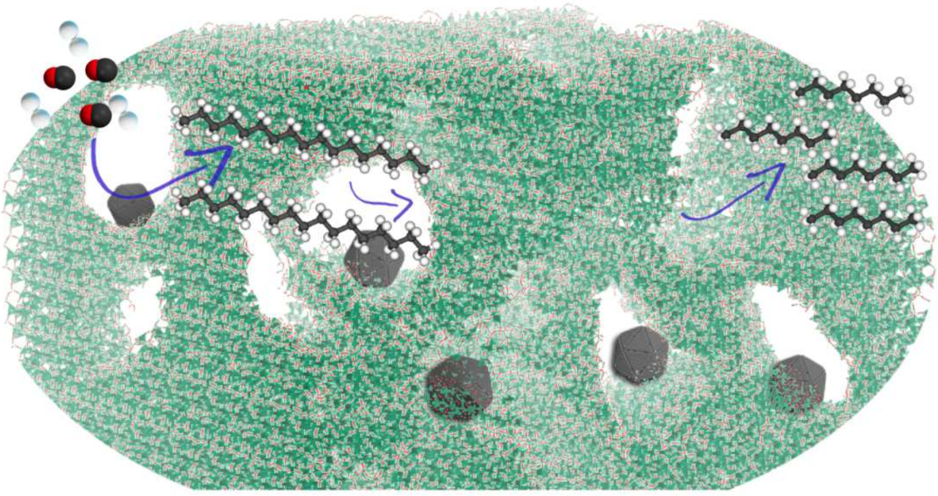

This Chapter is based on the following publication:

S. Sartipi, M. Alberts, V.P. Santos, M. Nasalevich, J. Gascon, F. Kapteijn, ChemCatChem 6 (**2014**) 142-151.

Abstract: Mesoporous H-ZSM-5 (‘*meso*H-ZSM-5’) was used as a carrier for a series of bifunctional Co-based catalysts for Fischer-Tropsch synthesis with ZrO_2 and/or Ru added as promoters. The reducibility of the catalysts was studied in detail by using temperature-programmed reduction and X-ray absorption spectroscopy. A comparison of the catalytic performance of Co/*meso*H-ZSM-5 and Co/SiO_2 (a conventional catalyst), after 140 h on-stream, reveals that the former is two times more active and three times more selective to the C5–C11 fraction with a large content of unsaturated hydrocarbons, next to α-olefins. The acid-catalyzed conversion of *n*-hexane and 1-hexene, as model reactions, demonstrates that the improvement in the selectivity toward gasoline-range hydrocarbons is due to the acid-catalyzed reactions of the Fischer-Tropsch α-olefins over the acidic zeolite. The formation of methane over the zeolite-supported Co-catalysts originates from direct CO hydrogenation and hydrocarbon hydrogenolysis on coordinatively unsaturated Co sites, which are stabilized as a consequence of a strong metal-zeolite interaction. Although the addition of either ZrO_2 or Ru increases the catalyst reducibility considerably, it does not affect the product selectivity significantly.

6.1. Introduction

Fischer-Tropsch synthesis (FTS) is one of the most important achievements of chemical industry in the 20th century. The depletion of fossil resources over the last few decades, the increasing price of crude oil, the rapid increase in methane reserves, and environmental concerns have generated a worldwide interest in practical applications of FTS-based technologies. Different types of fossil- (natural gas and coal) and renewable-based feedstocks can be converted into industrially relevant chemicals, such as lower olefins and alcohols as well as ultraclean fuels, through the FTS reaction [1]. The latter case is already commercialized through the so-called low-temperature Fischer-Tropsch (LTFT; catalyzed by Co or Fe) and high-temperature Fischer-Tropsch (HTFT; catalyzed by Fe) processes [2]. However, these technologies are economically feasible only at large scales [3, 4] and therefore process intensification is needed in applications with limited (and scattered) availability of feedstock (*e.g.*, biomass) and/or space (*e.g.*, offshore flare gas).

Both LTFT and HTFT reactors are followed by product upgrading units in which hydrocracking and/or isomerization of the products of FTS are performed [5]. Therefore, one way to attain the above-mentioned process intensification is to tune the FTS product selectivity to eliminate the demand for downstream conversion units [6].

Such efforts date to 1980s when combinations of zeolites with the FTS active phase were reported to “break” the classical Anderson-Schulz-Flory (ASF) product distribution [7, 8] Since then, the integration of both Co- and Fe-based catalysts with various zeolite topologies has been studied at different levels, such as catalyst bed layers [9, 10], physical mixtures of catalyst particles [11, 12], and coated catalysts [13]. A 7.5 wt% Co-0.2 wt% Ru-catalyst supported on alumina-bound ZSM-5 has been reported recently to demonstrate a stable performance and high selectivity toward C5–C20 up to 1500 h on-stream [14]. Co is claimed to be present mainly on the alumina binder of this hybrid catalyst.

A systematic comparison of different Co-zeolite catalyst configurations reveals that the selectivity toward liquid hydrocarbons increases as the proximity between FTS and acid sites increases in these hybrid systems [15]. Such a contact can be maximized by directly dispersing Co over the zeolite. Because high metal loadings are typically required in the catalyst formulations for FTS and zeolites lack a sufficient external surface area, the use of mesoporous zeolites as catalyst carriers gave promising results [16, 17]. On the one hand, the improved transport properties of hierarchically structured zeolites increase the selectivity toward liquid hydrocarbons [18, 19]; on the other hand, their high mesopore surface area improves dispersion at elevated metal loadings [15, 18-20]. Insights into the catalytic performance of these bifunctional catalysts would enable us to fine-tune their product selectivity, making these catalysts attractive for practical applications.

Next Chapter (7) demonstrates that in an attempt to maximize the performance of bifunctional catalysts by steering the product selectivity toward liquid hydrocarbons, the topology of the zeolite and, most importantly, the number and strength of acid sites are key parameters [20]. Herein, mesoporous H-ZSM-5-supported Co (*ca.* 20 wt%) catalysts are studied further. Special attention is given to thoroughly characterize metal reducibility and to its improvement upon promoter addition. Hydrocarbon conversion mechanisms over acid sites and Co are investigated by using the conversion of C6 as a model reaction. The effect of such reactions on the product selectivity and origins of methane formation over the zeolite-containing Co-catalyst is discussed in detail. In all, through an advanced catalyst characterization along with a detailed catalyst assessment, a clear relationship is drawn between structural characteristics of Co (if supported on the zeolite) and its FTS activity and selectivity.

6.2. Experimental

6.2.1. Synthesis

Amorphous SiO_2 (CARiACT Q-10) with surface area and pore volume of 293 m^2 g^{-1} and 1.35 cm^3 g^{-1}, respectively, was provided by Fuji Silysia Chemical Ltd. (Japan). ZSM-5 zeolite in the ammonium form with a nominal Si/Al ratio of 40 was purchased from Zeolyst (CBV 8014) and calcined at 823 K for 5 h to obtain H-ZSM-5. TPAOH (1 M), HNO_3 (70 wt%), ruthenium(III) nitrosyl nitrate (1.5 wt%), and zirconyl nitrate (5 wt%) solutions as well as the cobalt(II) nitrate hexahydrate salt were purchased from Sigma-Aldrich. All chemicals were used without any further purification.

Mesoporous H-ZSM-5 was prepared through base and acid treatments, as described earlier [19]: In brief, desilication was performed in TPAOH aqueous solution (1 M) placed in a capped vessel ($\text{volume}_{\text{base solution}}/\text{weight}_{\text{zeolite}}$ = 8.0 cm^3 g^{-1}) and at 343 K for 1 h under stirring in an oil bath. This treatment was followed by immediate quenching in an ice water bath and centrifugation to separate the zeolite powder from the solution. The residue of the desilicating agent was removed from the zeolite crystallites through subsequent redispersion in deionized water and centrifugation cycles until neutral pH was reached. The samples were then kept overnight at 333 K followed by drying at 393 K for 12 h and calcination at 823 K for 5 h. After heat treatments, the mesoporous H-ZSM-5 samples were acid treated in aqueous HNO_3 (1 M; $\text{volume}_{\text{acid solution}}/\text{weight}_{\text{zeolite}}$ = 28.6 cm^3 g^{-1}) at 343 K for 2 h under stirring in an oil bath. After quenching, the samples were washed thoroughly with deionized water, dried, and calcined similarly as after the abovementioned desilication method. Mesoporous H-ZSM-5 before acid treatment is labeled as '*meso*H-ZSM-5*(o)*', and the acid-washed zeolite is labeled as '*meso*H-ZSM-5'.

The catalysts for FTS were prepared through incipient wetness impregnation. All the supports were dried overnight at 393 K before impregnation. To study the promoting effect of ZrO_2, a fraction of *meso*H-ZSM-5 was loaded with Zr (*ca.* 5 wt%) by using a zirconyl nitrate solution. This sample was then kept overnight in a desiccator at room temperature, dried at 393 K for 12 h, and calcined at 823 K for 5 h; the resulting sample was labeled as 'ZrO_2/*meso*H-ZSM-5'. Amorphous SiO_2, *meso*H-ZSM-5*(o)*, *meso*H-ZSM-5, and ZrO_2/*meso*H-ZSM-5 were used as carriers and loaded with Co (*ca.* 20 wt% or 10 wt%, in one case, for each sample) by using aqueous cobalt(II) nitrate hexahydrate solutions as precursors. To investigate Ru as a catalyst promoter, ruthenium nitrosyl nitrate was added to the precursor solution and co-impregnated with Co to obtain a Ru loading of 0.3 wt%. After impregnation, the samples were dried in a desiccator at 393 K as explained above. Then, the catalysts were calcined at 673 K for 2 h. All the above-mentioned drying and calcination steps were performed at a heating rate of 2 K min^{-1} and under static air conditions.

6.2.2. Characterization

N_2 physisorption was performed in an Autosorb 6B unit (Quantachrome Instruments) at liquid nitrogen temperature (77 K). Before the experiment, the samples (*ca.* 0.1 g) were degassed overnight in an Autosorb Degasser unit (Quantachrome Instruments) under vacuum at 623 K.

Elemental analysis was performed with Perkin-Elmer Optima instruments. The samples were digested in an acid mixture. After dilution, analysis was performed by using inductively coupled plasma optical emission spectrometry (ICP-OES).

The X-ray diffraction (XRD) patterns were recorded in Bragg-Brentano geometry with a Bruker D8 Advance X-ray diffractometer equipped with a LynxEye position-sensitive detector. Measurements were performed at room temperature by using monochromatic Co Kα (λ = 1.788970 Å) radiation in the 2θ range from 5° to 90°. All patterns were background subtracted to eliminate the contribution of air scatter and possible fluorescence radiation.

Temperature-programmed desorption of ammonia (NH_3-TPD) was measured with an AutoChem II chemisorption analyzer (Micromeritics). The zeolite-containing samples (*ca.* 0.2 g) were first degassed under He flow at 673 K for 1 h and then saturated with NH_3 at 473 K during 1 h by using a flow of 1.65% NH_3 in He. The gas mixture was then switched back to He, and the sample was purged at 473 K for 1 h to remove the weakly adsorbed NH_3 molecules until no NH_3 was detected. Temperature-programmed desorption was subsequently recorded under He flow from 473 to 873 K. All flow rates were adjusted to 25 cm^3_{STP} min^{-1} and the heating rates were 10 K min^{-1} during different stages of the experiment.

The amount of Brønsted and Lewis acid sites in H-ZSM-5 and *meso*H-ZSM-5 were evaluated by using pyridine adsorption, which was performed with a Nicolet 6700 FT-IR spectrometer (Thermo Scientific) equipped with a MCT/B detector. A zeolite sample (*ca.* 0.05 g) was pressed at 1132 kg cm^{-2} for 5 s to form a self-supporting wafer of 1.5 cm diameter. The sample was then degassed at 673 K for 2 h under vacuum [2×10^{-5} mbar (1 bar = 100 kPa)]. Pyridine vapor was added stepwise to the sample at a known volume and pressure. After each step, the sample was heated at 433 K to allow diffusion of the probe molecules and then cooled to room temperature for spectra collection [21]. This method was repeated to estimate the extinction coefficient until no further increase was observed in the areas of adsorbed pyridine upon pyridine addition. Finally, the sample was heated at 433 K under vacuum and the final spectrum was recorded at room temperature. During each measurement, 128 scans were recorded in 1000–4000 cm^{-1} range at a resolution of 4 cm^{-1}. The degassed sample was recorded as a background spectrum.

Transmission electron microscopy (TEM) was performed with an FEI Tecnai TF20 microscope using a carbon-coated Cu grid. Before analysis, the samples were reduced in an H_2 flow of 80 cm^3_{STP} min^{-1} at 773 K for 13 h (heating rate = 2 K min^{-1}) and transferred to the grid in a glove box. For the introduction of the samples into the microscope, a transfer unit was used to prevent any contact with air.

Temperature-programmed reduction by H_2 (TPR(H_2)) was performed with a homemade equipment. The Co-containing samples (*ca.* 0.1 g) were subjected to a 7.4% H_2 flow of 27 cm^3_{STP} min^{-1} in Ar in a temperature-controlled reactor. The reactor temperature was ramped from room temperature to 1223 K (heating rate = 5 K min^{-1}), and the H_2 consumption was monitored with a thermal conductivity detector. Water was removed with a Permapure membrane dryer. Calibration was performed with CuO (Alfa Aesar), and total H_2 consumption values were obtained from TPR(H_2) patterns. The ratio between the H_2 consumption and the corresponding theoretical value, calculated for the full reduction of each catalyst (assuming all Co atoms to be initially in the form of Co_3O_4), was reported as the degree of reduction.

X-ray absorption spectroscopy (XAS) was performed at beamline X18A of National Synchrotron Light Source in Brookhaven National Laboratory (NY, USA). The beamline used the Si(111) channel-cut monochromator and provided an energy range of 5–25 keV. All the measurements were performed at room temperature in the transmittance mode. Incident and transmitted X-rays were detected with ion chambers. Extended X-ray absorption fine structure (EXAFS) and X-ray absorption near-edge structure (XANES) data were collected on the K-edge of Co. All Co-containing samples were measured against the Co foil used as a reference. In typical XAS experiments, the powder samples were placed into a 1.27 cm stainless steel washer and sealed from both sides with the Kapton tape.

This configuration enabled us to keep the sample thickness constant. Air-sensitive samples (*i.e.*, activated catalysts) were loaded into a dedicated cell. The cell consisted of an airtight stainless steel chamber equipped with two Kapton windows for the beam passing and a clamped cap for loading. The sample holder was located in the middle of this cell under N_2 atmosphere in a glove box and sealed. The EXAFS data were processed by Athena (version 0.8.056). The background subtraction was performed by using the automated single-variable fit implemented in Athena. The Fourier transform of the reciprocal space data was performed by using the Hanning window in the k range of 2–10 Å^{-1}.

6.2.3. Acid-catalyzed reactions

The acid-catalyzed reactions were performed in a fixed-bed stainless steel reactor with *n*-hexane and 1-hexene as hydrocarbon model compounds. The fresh catalyst particles (0.250 g, 100–212 μm in size) were fixed in the reactor (3.9 mm inner diameter) between quartz wool plugs. The samples were treated overnight under H_2 flow at 673 K and atmospheric pressure. After cooling the samples to 513 K, the pressure was increased to 15 bar, and subsequently, a mixture of C6, H_2, and N_2 was fed to the reactor (space velocity (SV) = 13 mol_{C6} kg^{-1}_{cat} h^{-1}, H_2/C6 = 9.0, and N_2/H_2=2.0). After 20 h on-stream, the product was analyzed on-line at 363 K with a Compact GC (Interscience) equipped with a Porabond Q column (10 m × 0.32 mm) and a flame ionization detector (FID) and using He as the carrier gas.

6.2.4. Fischer-Tropsch synthesis

FTS experiments were performed on the six-flow fixed-bed microreactor setup described in Chapter 2. For all experiments, the fresh catalyst (0.250 g, 100–212 μm in size) was diluted with SiC of similar size to attain a constant bed volume of approximately 1.3 cm^3. Catalysts were activated *in situ* before the FTS reaction by H_2 at 773 K for 13 h at atmospheric pressure followed by cooling to 453 K under H_2 flow. After increasing the pressure to the process value (15 bar total pressure), CO was gradually introduced into the feed stream at 453 K to reach its final concentration (H_2/CO = 1 or 2) in 1 h. Subsequently, the reactor was heated to the process temperature (513 K).

To regenerate the catalysts, CO was excluded from the feed and the operating pressure was decreased to atmospheric pressure under H_2 flow. Upon increasing the reactor temperature to 773 K, the samples were reactivated *in situ* (as described) and a second FTS experiment was started as per the above-mentioned method. All the above heating and cooling steps were performed at a heating rate of 2 K min^{-1}.

During FTS experiments, heavy hydrocarbons (wax) were collected with gas/liquid separators at 448 K and the reaction pressure. After expanding the product flow to atmospheric pressure by using

Table 1 Textural and chemical properties of the supports used for catalyst preparation for FTS.

Support	Treatment sequence	S / m^2 g^{-1}		V / cm^3 g^{-1}			Si/Al[f]
		total[a]	meso[b]	total[c]	micro[d]	meso[e]	
SiO_2	None	293	248	1.35	0.02	1.34	n.a.[g]
H-ZSM-5	None	460	52	0.26	0.18	0.08	41
*meso*H-ZSM-5*(o)*	TPAOH	653	426	0.68	0.10	0.58	22
*meso*H-ZSM-5	TPAOH/HNO_3	691	470	0.67	0.09	0.58	41
ZrO_2/*meso*H-ZSM-5	TPAOH/HNO_3/Impregnation	602	412	0.57	0.08	0.48	n.d.[h]

[a] BET surface area; [b] Mesopore surface area obtained from the *t*-plot applied to the N_2 isotherm; [c] Total pore volume; [d] Micropore volume obtained from the *t*-plot; [e] Mesopore volume calculated as $V_{meso} = V_{total}-V_{micro}$; [f] Obtained from ICP-OES; [g] Not applicable; [h] Not determined.

back pressure controllers, lighter hydrocarbons and water were collected in cold traps at approximately 278 K. After separation from water, these liquid hydrocarbons as well as the wax were weighted, dissolved in CS_2, and analyzed offline with a simulated distillation (SIMDIS) gas chromatograph (Hewlett Packard HP 5890, Series II) equipped with an FID and HP-1 column (7.5 m × 0.53 mm; film thickness = 2.65 µm) and using He as carrier gas. During the analysis, the oven temperature was ramped from 308 to 623 K (ramp rate = 14 K min^{-1}) and maintained at the final temperature for 5 min. N_2, CO, and CO_2 as well as light hydrocarbons in the gas phase were analyzed on-line with a Compact GC (Interscience) equipped with three columns and detectors in parallel and using He as a carrier gas. In the first column (Carboxen 1010, 10 m × 0.32 mm), N_2, CO, CH_4, and CO_2 were separated at 333 K and analyzed with a thermal conductivity detector. In the second column (Al_2O_3/KCl, 10 m × 0.32 mm) and detection with an FID, separation between all C1–C4 components was achieved at 434 K. In the third column (RTx-1, 0.5 µm, 15 m × 0.32 mm), C5–C10 hydrocarbons were separated at 353 K and analyzed with an FID.

6.3. Results and discussion

6.3.1. Catalyst characterization

The total and mesopore surface area of H-ZSM-5 increases by 40 and 720 %, respectively, and its Si/Al ratio decreases from 41 to 22 after desilication with tetrapropylammonium hydroxide (TPAOH) owing to the creation of mesopores [22] (Table 1). Moreover, the mesopore volume of *meso*H-ZSM-5*(o)* is approximately 7 times larger than that of H-ZSM-5. This increase is at the cost of a slight decrease in micropore volume (0.18 and 0.10 cm^3 g^{-1} for H-ZSM-5 and *meso*H-ZSM-5*(o)*, respectively), which indicates a minor collapse of the zeolite structure under basic conditions [23]. Nevertheless, the XRD patterns of the corresponding catalysts (Figure E1/Appendix E) confirm that the characteristic MFI structure is preserved after desilication [24]. The surface area and pore volume of *meso*H-ZSM-5 are barely altered with respect to those of *meso*H-ZSM-5*(o)*; however, the zeolite Si/Al ratio is readjusted to the original value (41) after acid treatment (Table 1). It was shown earlier

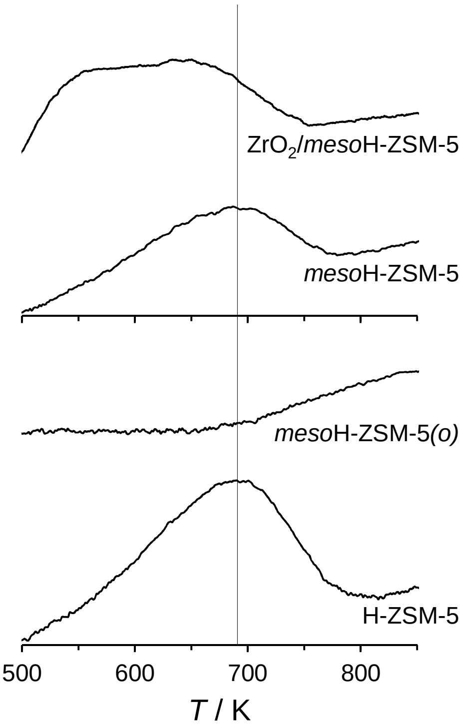

Figure 1. NH$_3$-TPD profiles (10 K min^{-1}) of H-ZSM-5 zeolites. NH$_3$ was adsorbed at 473 K.

that (the used) treatment with 1 M HNO$_3$ is effective only in removing the extra-framework aluminum species and does not leach out aluminum from the H-ZSM-5 framework [19].

NH$_3$-TPD profile of H-ZSM-5 shows the characteristic peak of strong Brønsted acidity [16] at approximately 700 K (Figure 1). This “high-temperature” peak is initiated by a tail at lower temperatures, which originates from weaker Lewis acid sites [19]. Although *meso*H-ZSM-5*(o)* does not show any desorption of NH$_3$, *meso*H-ZSM-5 shows a profile similar to that of H-ZSM-5 (notably, the peak at temperatures above 800 K corresponds to framework collapse, not to strong acidity) [20]. We conclude that the initial treatment with TPAOH results in the partial ion-exchange of the framework protons, which are recovered after acid treatment and calcination. The quantification of acidity through pyridine adsorption (Table 2) shows that the Brønsted acid density of *meso*H-ZSM-5 is lower than that of H-ZSM-5; nevertheless, the concentrations of Lewis acid sites are equal for both samples. The addition of ZrO$_2$ slightly modifies the acidic properties of supports: the high-temperature peak shifts slightly to lower temperatures in the NH$_3$-TPD profile of ZrO$_2$/*meso*H-ZSM-5 (4.6 wt%

Table 2 Acid-type densities of H-ZSM-5 zeolites obtained through pyridine adsorption.

Support	Brønsted acid		Lewis acid	
	µmol g^{-1}	µmol µmol$_{Al}^{-1}$	µmol g^{-1}	µmol µmol$_{Al}^{-1}$
H-ZSM-5	138	0.35	37	0.09
*meso*H-ZSM-5	74	0.18	38	0.09

Table 3 Textural and chemical properties of the catalysts for FTS.

Catalyst	S / m^{2} g^{-1}		V / cm^{3} g^{-1}			d_{Co}[f] / nm	Loading[g] / wt%		
	total[a]	meso[b]	total[c]	micro[d]	meso[e]		Co	Ru	Zr
Co/SiO_2	199	180	0.89	0.01	0.88	16	18.6	n.a.[h]	n.a.
Co/*meso*H-ZSM-5*(o)*	442	272	0.45	0.07	0.38	11	20.7	n.a.	n.a.
Co/*meso*H-ZSM-5	509	311	0.50	0.08	0.41	10	23.8	n.a.	n.a.
10 wt% Co/*meso*H-ZSM-5	564	371	0.55	0.08	0.47	10	10.7	n.a.	n.a.
CoRu/*meso*H-ZSM-5	464	288	0.40	0.07	0.33	10	17.7	0.3	n.a.
Co/ZrO_2/*meso*H-ZSM-5	420	260	0.37	0.07	0.30	12	18.0	n.a.	3.5
CoRu/ZrO_2/*meso*H-ZSM-5	433	273	0.39	0.07	0.32	13	17.8	0.3	3.7

[a] BET surface area; [b] Mesopore surface area obtained from the *t*-plot applied to the N_2 isotherm; [c] Total pore volume; [d] Micropore volume obtained from the *t*-plot; [e] Mesopore volume calculated as $V_{meso} = V_{total} - V_{micro}$; [f] Co crystallite size calculated from $d(Co^0) = 0.75d(Co_3O_4)$, where $d(Co_3O_4)$ is derived from XRD, applying the Scherrer equation; [g] Obtained from ICP-OES; [h] Not applicable.

Zr). Moreover, a shoulder appears at approximately 550 K, which indicates a considerable increase in the Lewis acidity of this sample owing to the presence of ZrO_2 [25] (Figure 1).

All the mesoporous supports given in Table 1 were loaded with 18–24 wt% of Co (Table 3), except

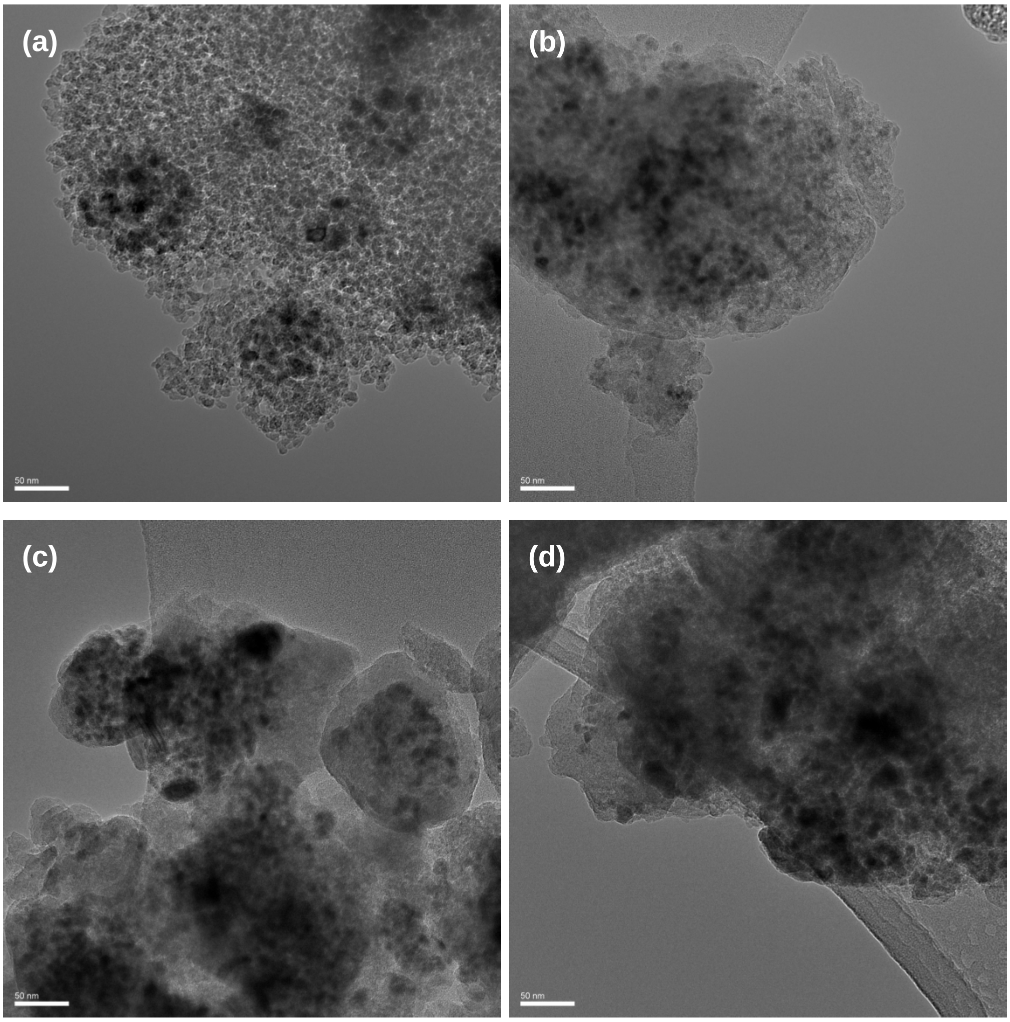

Figure 2. *Quasi in situ* TEM images of catalysts for FTS after reduction in H_2 at 773 K for 13 h. Scale bars correspond to 50 nm.

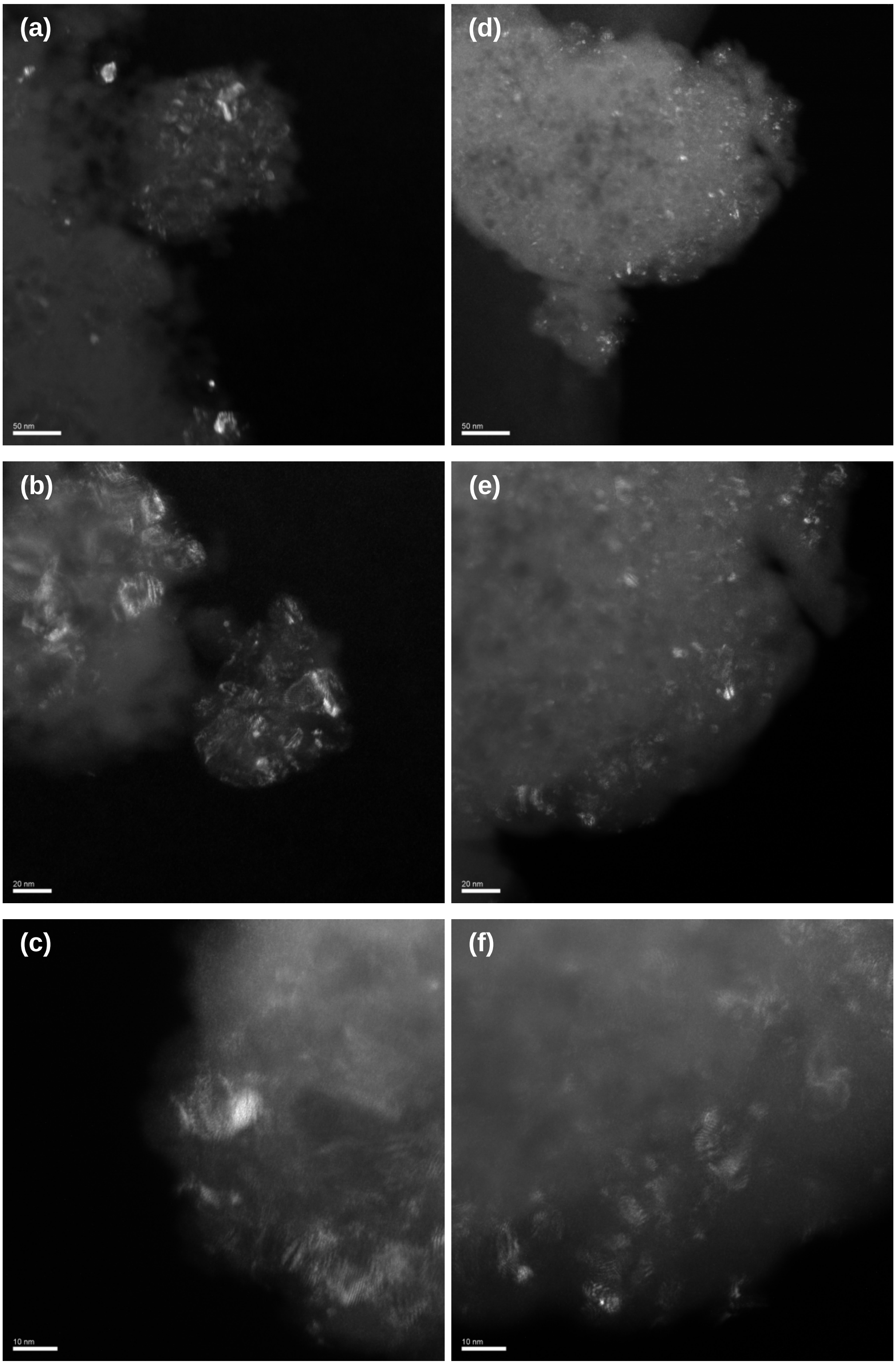

Figure 3. *Quasi in situ* dark-field TEM images of Co/SiO_2 (left column: a, b, and c) and Co/*meso*H-ZSM-5 (right column: d, e, and f) after reduction in H_2 at 773 K for 13 h. Scale bars correspond to 50 nm (top row: a and d), 20 nm (middle row: b and e) and 10 nm (bottom row: c and f).

10 wt% Co/*meso*HZSM-5, which was prepared with a lower Co loading of 10.7 wt%. In addition, 0.3 wt% Ru-promoted catalysts were prepared over *meso*H-ZSM-5 and ZrO_2/*meso*H-ZSM-5 supports. The N_2 physisorption results reveal that at least 70% of the micropore volume is maintained after the

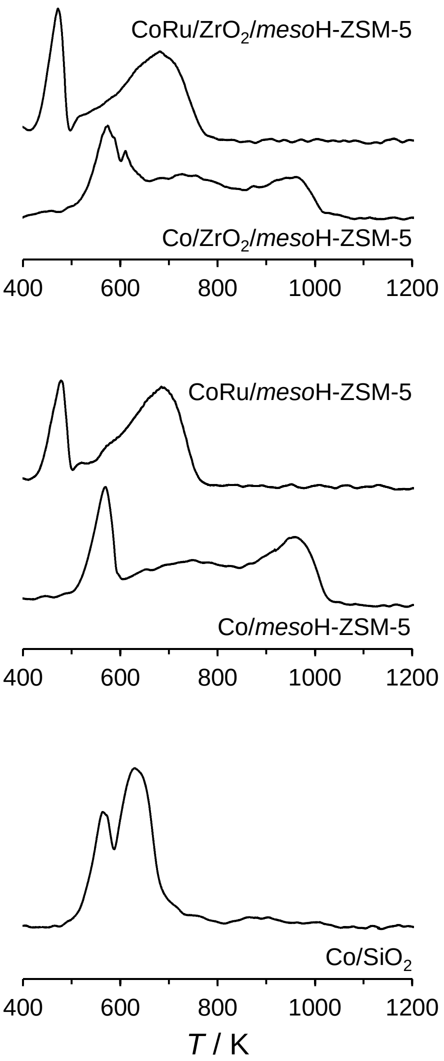

Figure 4. TPR(H_2) profiles (5 K min^{-1}) of fresh catalysts for FTS.

impregnation of the active phase (*cf.* Tables 1 and 3).

The average Co crystallite size, as calculated from the XRD data, is the largest for Co/SiO_2 (16 nm) and similar for all zeolite-supported catalysts (10–13 nm) (Table 3). According to TEM analysis, Co particles form clusters over amorphous SiO_2, which results in an inhomogeneous distribution of the FTS active phase on this support (Figure 2a). This spatial distribution is to some extent improved in the zeolite-supported catalysts; yet, regions with higher Co concentration can be observed in all the TEM micrographs (Figure 2 b–d).

The dark-field TEM images (Figure 3) of Co/SiO_2 and *meso*HZSM-5 supports show smaller Co particles that are dispersed more over *meso*H-ZSM-5 than over Co/SiO_2. Any Co particle can hardly be observed at the outer surface (edge) of the zeolite crystallites, which indicates that most of the FTS active phase is introduced into the mesopore space of *meso*H-ZSM-5. TPR(H_2) profiles of supported Co-catalysts are shown in Figure 4. The classical two-step reduction of Co_3O_4 *via* CoO to Co^0 [26, 27]

Table 4 Degree of reduction of the catalysts for FTS obtained by using TPR(H_2).

Catalyst	Degree of reduction / %
Co/SiO_2	> 95
Co/*meso*H-ZSM-5	67
CoRu/*meso*H-ZSM-5	92
Co/ZrO_2/*meso*H-ZSM-5	> 95
CoRu/ZrO_2/*meso*H-ZSM-5	> 95

occurs for Co/SiO_2 below 800 K. A sharp peak at approximately 550 K is also observed in the profile of Co/*meso*H-ZSM-5, which is followed by two broad peaks: one at 600–900 K and the other above 900 K. The latter two peaks merge in the case of CoRu/*meso*H-ZSM-5 and form a large peak at approximately 700 K with a shoulder at approximately 600 K. Moreover, the onset temperature of reduction and the positions of the peak maxima shift by approximately 100 K to lower temperatures, which suggests that the presence of Ru increases the rate of Co reduction. Co/ZrO_2/*meso*H-ZSM-5 demonstrates a pattern similar to that of Co/*meso*H-ZSM-5, although it is apparent that hydrogen consumption above 900 K has decreased upon ZrO_2 addition. These results reveal that the reducibility of Co is lower over H-ZSM-5 than over amorphous SiO_2 owing to a stronger metal-support interaction. In addition, the presence of multiple reduction peaks on zeolite-supported catalysts indicates Co species with different reactivities.

Degrees of reduction, as calculated from the total consumption of H_2, are listed in Table 4. Co is fully reduced over SiO_2, whereas the degree of reduction is 67% for Co/*meso*H-ZSM-5. With the addition of either Ru or ZrO_2, this value increases considerably and reaches above 90 %. Different mechanisms have been proposed for the promoting effects of precious metals (Ru) and ZrO_2. Small amounts of Ru in the catalyst composition promote H_2 spillover and thus increase the rate of reduction [28]. ZrO_2 forms an intermediate layer between the metal and the support, which reduces the metal-support interaction [29]. Such mechanistic differences are indicated by the observed changes in the TPR(H_2) profiles of CoRu/*meso*H-ZSM-5 and Co/ZrO_2/*meso*H-ZSM-5 compared with those of Co/*meso*H-ZSM-5.

The reducibility and coordination of Co on zeolite-supported catalysts were also studied by using XAS. EXAFS Fourier transform and XANES spectra of fresh and activated catalysts as well as reference compounds at Co K-absorption edges are shown in Figure 5.

The EXAFS data of fresh (supported) Co species are characterized by the presence of two peaks, which are characteristic of Co–O and Co–Co coordination, respectively. The Co–O coordination can still be observed in the EXAFS spectrum of the activated Co/*meso*H-ZSM-5 catalyst, demonstrating an incomplete reduction of Co, which is in agreement with the TPR(H_2) results. In contrast, activated

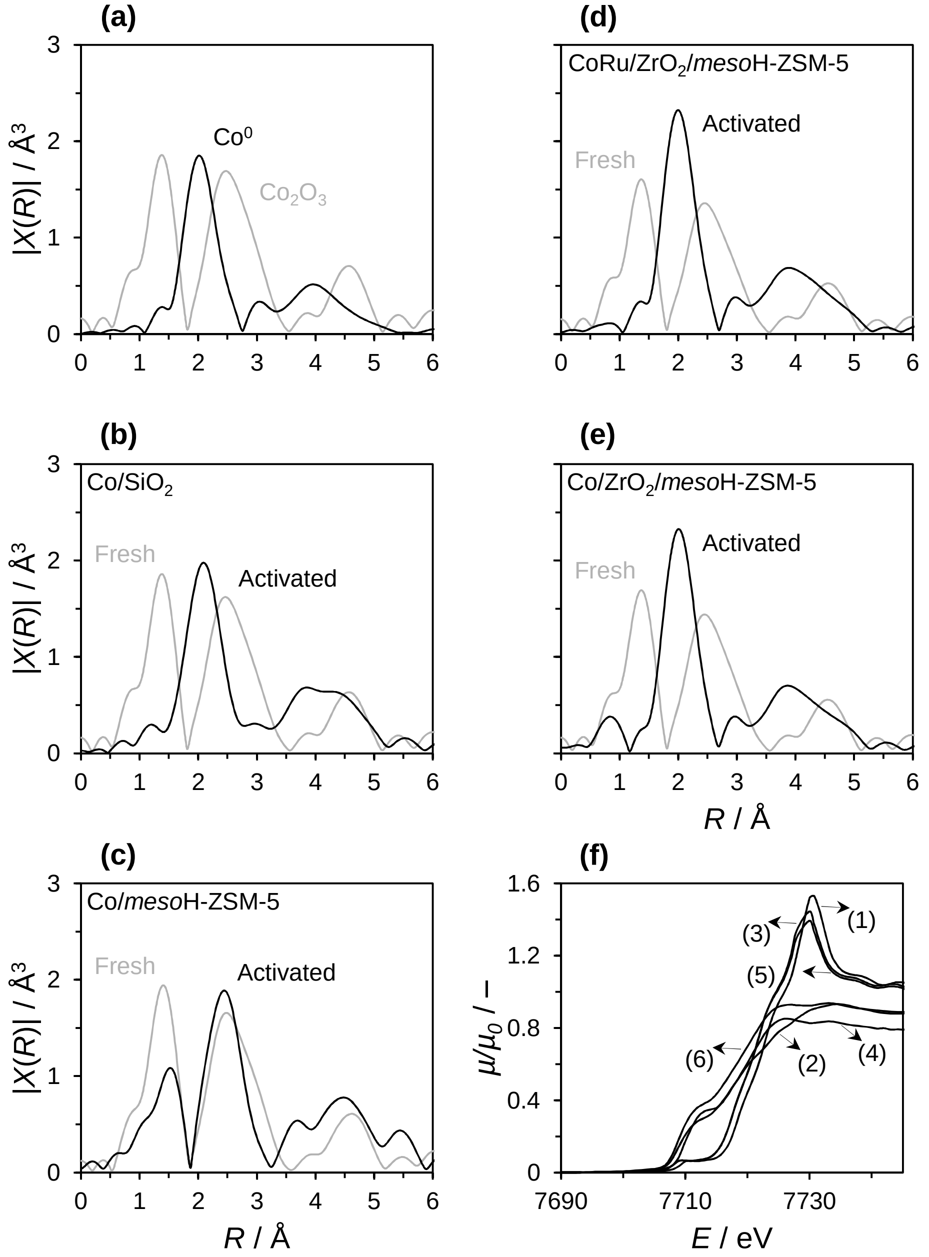

Figure 5. Fourier-transformed EXAFS (Co K-edge, not phase corrected) (a–e) and XANES (f) spectra of fresh and activated catalysts for FTS (reduced *quasi in situ* in H_2). Spectra f correspond to Co_2O_3 (1), Co^0 (2), fresh Co/ZrO_2/*meso*H-ZSM-5 (3), activated Co/ZrO_2/*meso*H-ZSM-5 (4), fresh $CoRu/ZrO_2$/*meso*H-ZSM-5 (5), and activated $CoRu/ZrO_2$/*meso*H-ZSM-5 (6).

Co/ZrO_2/*meso*H-ZSM-5, $CoRu/ZrO_2$/*meso*H-ZSM-5, and $CoSiO_2$ catalysts all have a local atomic structure similar to that of the Co foil, which confirms a full reduction of Co.

The XANES spectra of Co/ZrO_2/*meso*H-ZSM-5 and $CoRu/ZrO_2$/*meso*H-ZSM-5 are characterized by a pre-edge peak at approximately 7710 eV, arising from the 1*s*→3*d* transition, which is only quadrupole allowed for coordination sites without centric symmetry, and an edge peak at 7717 eV [30-32]. According to the edge position, Co_3O_4 is the major Co phase in these promoted catalysts; this observation is in agreement with the XRD and TPR(H_2) results. After activation, the XANES spectra of Co/ZrO_2/*meso*H-ZSM-5 and $CoRu/ZrO_2$/*meso*H-ZSM-5 resemble that of the Co foil. The slight

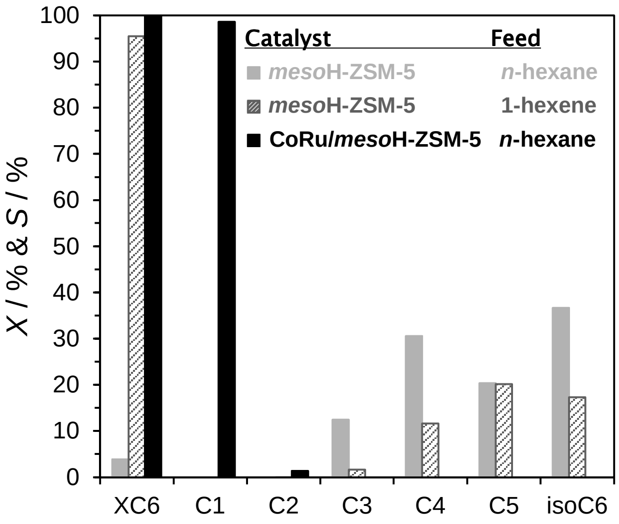

Figure 6. Conversion and product selectivities in C6 hydroconversion over *meso*H-ZSM-5 and CoRu/*meso*H-ZSM-5. Data were collected after 20 h on-stream at 513 K, 15 bar total pressure, H_2/C6=9.0, N_2/H_2 = 2.0, and *SV* =13 mol_{C6} kg^{-1}_{cat} h^{-1}. Either *n*-hexane or 1-hexene was used, as indicated in the legend.

difference can be due to the metal-support interactions that can induce a perturbation on the electronic structure and hence on the spectral features [32]. The results obtained from XAS are consistent with the improved reducibility and degree of reduction of Co upon promotion with ZrO_2 (Table 4), which reveal that Ru addition to the ZrO_2-promoted catalyst is not necessary for activation temperatures above 773 K.

6.3.2. Catalytic performance

Lower hydrocarbons (C3–C5) are detected in the product streams upon feeding C6 (in a mixture with H_2) over *meso*H-ZSM-5 (Figure 6). C6 conversion increases from 4% to 96% if *n*-hexane is replaced by 1-hexene in the feed stream. This difference in conversion implies that olefins are much more reactive in the acid-catalyzed reactions over the zeolite support. Hydrocarbon conversion reactions over *meso*H-ZSM-5 do not lead to methane formation. However, nearly full conversion of *n*-hexane and a 99% methane selectivity are obtained by incorporating Co into *meso*H-ZSM-5. These results reveal that hydrocarbon hydrogenolysis is predominant over Co.

In FTS, the cobalt-time-yield (*CTY*; number of CO moles converted per kilogram of Co per hour) of Co/*meso*H-ZSM-5 is almost two times higher than that of Co/SiO_2 (Figure 7). At the same time, calculations assuming spherical Co particles with diameters equal to those reported in Table 3 show that the ratio of CO turnover frequencies between Co/*meso*H-ZSM-5 and Co/SiO_2 is approximately 1.1, which is in line with the general belief that Co-based FTS is not structure sensitive if particles are larger than 6–10 nm [33]. The initial activity of Co/*meso*H-ZSM-5 increases with the addition of either Ru or ZrO_2 to the catalyst composition. However, *CTY*s of all the zeolite-supported catalysts become

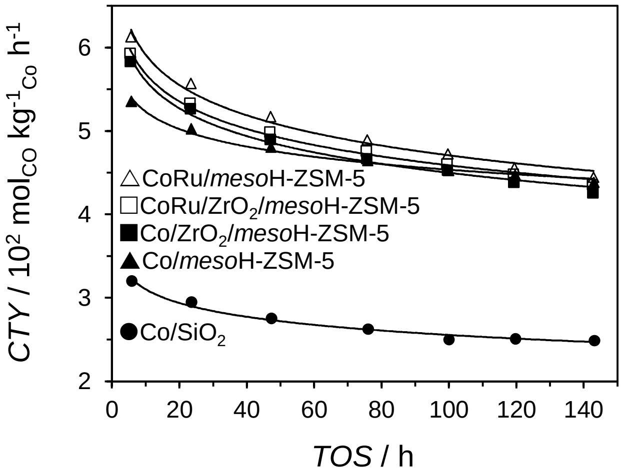

Figure 7. *TOS* evolution of the *CTY* during FTS at 513 K, 15 bar total pressure, feed composition H_2/CO = 1, and *GHSV* = 12 m^3_{STP} kg^{-1}_{cat} h^{-1}.

similar after approximately 80 h on-stream.

The carbon selectivities to different FTS product ranges over promoted and unpromoted catalysts are shown in Figure 8. Under the applied process conditions, Co/SiO_2 is highly selective to C21+ (wax). Wax production is suppressed considerably over the zeolite-containing catalysts, which results in higher carbon selectivity toward gasoline-range hydrocarbons (C5–C11) as well as to C1. A

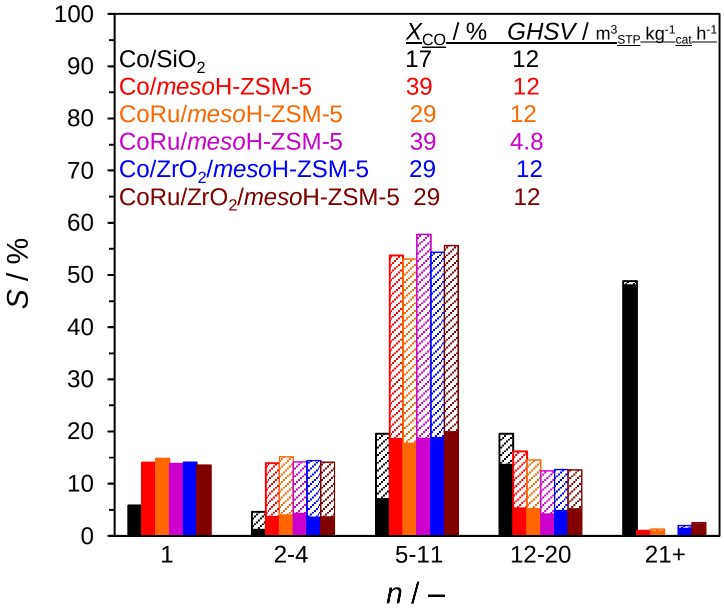

Figure 8. Carbon selectivity toward products of FTS after 140 h on-stream. In each carbon number group from left to right: Co/SiO_2, Co/*meso*H-ZSM-5, CoRu/*meso*H-ZSM-5, CoRu/*meso*H-ZSM-5, Co/ZrO_2/*meso*H-ZSM-5, and CoRu/ZrO_2/*meso*H-ZSM-5. ■: *n*-paraffins, ▨: sum of isoparaffins and olefins. Experiments were performed at 513 K, 15 bar total pressure, and feed composition H_2/CO = 1.

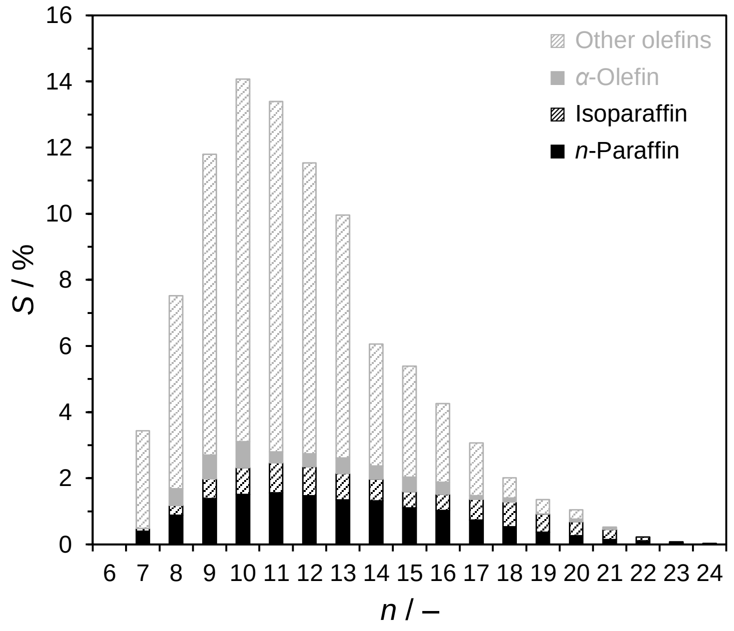

Figure 9. Carbon Selectivity distribution of liquid hydrocarbons formed over Co/*meso*H-ZSM-5. Liquid products were collected after 140 h on-stream at 513 K, 15 bar total pressure, feed composition $H_2/CO = 1$, $GHSV = 12\ m^3_{STP}\ kg^{-1}_{cat}\ h^{-1}$, and were analyzed by 2D GC. The associated 2D chromatogram is presented in Figure E2/Appendix E.

comparison of Co/*meso*H-ZSM-5 and CoRu/*meso*H-ZSM-5 catalysts under iso-conversion conditions shows a minor effect of Ru in terms of altering the catalyst product distribution (Figure 8). In general, the selectivity toward C1 (S_{C1}) decreases only slightly by introducing Ru and/or ZrO_2. A detailed analysis of liquid products formed over Co/*meso*H-ZSM-5 (in the FTS reaction) shows a large fraction of unsaturated hydrocarbons, other than α-olefins, in the sample (Figure 9). (Notably, a contribution of aromatics plus oxygenates to the liquid products was < 0.3 wt%.)

The time-on-stream (*TOS*) evolution of CO conversion (X_{CO}) during 140 h on-stream demonstrates that the stability of Co/*meso*H-ZSM-5 in terms of activity is comparable to that of Co/SiO_2 (Figure 10). Methane selectivity is fairly constant over Co/SiO_2 during 140 h on-stream (*ca.* 6%), whereas it increases from 11 to 14% with time as X_{CO} decreases by 9% over Co/*meso*HZSM-5. Once the catalytic activity is restored after regeneration, S_{C1} decreases again (Figure 10). In contrast to Co/*meso*H-ZSM-5, no C4 isomers are produced over Co/SiO_2. The iso- to *n*-C4 ratio (I/N (C4)) over the former catalyst decreases with *TOS* and reaches a steady-state level after approximately 80 h on-stream. The I/N (C4) of the reactivated catalyst is similar to that of the fresh catalyst, which indicates that the acid sites are recovered.

To investigate the effect of conversion level on S_{C1} over the zeolite-supported catalyst, X_{CO} was varied by changing the space velocities at different H_2/CO ratios of 1 and 2. Data reported in Table 5 indicate that increasing the H_2 concentration by changing the H_2/CO ratio from 1 to 2 results in 5–10%

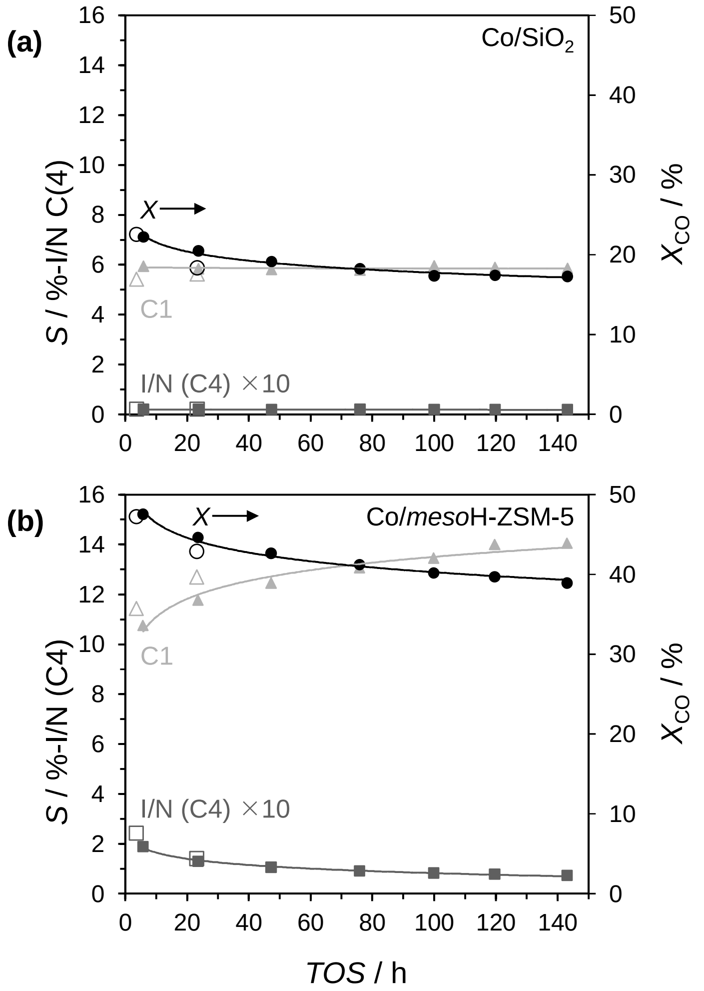

Figure 10. *TOS* evolution of CO conversion (X_{CO}), methane (C1) selectivity, and iso- to *n*-C4 ratio (I/N (C4)) over Co/SiO_2 (a) and Co/*meso*H-ZSM-5 (b) during FTS at 513 K, 15 bar total pressure, feed composition H_2/CO = 1, and *GHSV* = 12 $m^3_{STP}kg^{-1}_{cat}$ h^{-1}. Solid symbols correspond to the first reaction run; open symbols correspond to the second reaction run over *in situ* reactivated catalysts (in H_2 at 773 K for 13 h).

increase in S_{C1}. Furthermore, this value is higher at lower X_{CO} for both H_2/CO ratios.

6.3.3. Discussion

The acid-catalyzed hydroconversion of C6 confirms that hydrocracking is feasible under the applied LTFT process conditions (Figure 6), which is consistent with the literature [10, 11]. This finding explains the increased selectivities to liquid fractions over the H-ZSM-5-containing catalysts (Figure 8). A close contact between the metal for FTS and acid sites is reported to be of crucial importance in this respect: [15] if acid site domains are in the vicinity of FTS sites at a nanometer scale, α-olefins, which are the primary products of FTS, may crack or isomerize before they are hydrogenated. The closer these sites, the higher the probability for cracking to occur. The conversion of 1-hexene is much higher than that of *n*-hexane over *meso*H-ZSM-5 (Figure 6). The classical mechanism of such acid-

Table 5 CO conversion and carbon selectivity to products of FTS over Co/*meso*H-ZSM-5 after 22 h on-stream at 513 K, 15 bar total pressure, and different feed composition H_2/CO ratios and space velocities.

H_2/CO	*GHSV* m^3_{STP} kg^{-1}_{cat} h^{-1}	X_{CO} / %	*S* / %					
			C1	C2–C4	C5–C11	C12–C20	C21+	CO_2
1	4.8	48	10	12	62	12	1	3
1	12	42	12	14	56	16	1	1
2	12	83	17	15	51	15	0	2
2	24	55	20	17	48	14	0	1

catalyzed reactions, through the rearrangement of a secondary carbocation into a protonated dialkylcyclopropane, increases the degree of branching of hydrocarbons [34]. Because FTS may mainly produce linear α-olefins, a considerable fraction of other unsaturated hydrocarbons shown in Figure 9 are formed over the acid sites.

Ru has (de)hydrogenation activity, which promotes the acid-catalyzed hydrocarbon reactions [35]. At the same time, Ru increases the reducibility of small Co particles (Figure 4), which are active for hydrogenolysis [36]. Thus, Ru promotes hydrogenolysis (indirectly) and, in the absence of CO, this reaction over the 20 wt% Co-catalyst is prevalent (Figure 6). As a consecutive reaction, hydrogenolysis may even convert the products of the acid-catalyzed reactions into C1 (and C2).

The higher activity of Co/*meso*H-ZSM-5 compared with that of Co/SiO_2 (Figures 7 and 10) is a result of a smaller Co crystallite size (Table 3 and Figure 3). Both catalysts demonstrate a similar *TOS* stability in terms of CO conversion. Sintering is an important cause for the deactivation of Co-based catalysts for FTS [37, 38] and can be suppressed by maximizing the spatial distribution of active phase particles over the support surface [38, 39]. Therefore, the availability of accessible surface area is an advantage in the design of stable catalysts (supported on mesoporous H-ZSM-5) for FTS [18]. The representative TEM images in Figures 2 and 3 show that the Co distribution in the mesopores of the hierarchical zeolite is slightly better than that in amorphous SiO_2.

The TPR(H_2) and EXAFS results (Figure 5) reveal that the addition of promoters (Ru and/or ZrO_2) increases the reducibility and degree of reduction of smaller cobalt oxide crystallites over *meso*H-ZSM-5. Although large Co particles do not re-oxidize in the FTS reaction environment, the re-oxidation of smaller crystallites (< 4 nm) starts in an early course of the reaction [40, 41]. Therefore, the *CTY* of the promoted catalysts, which is initially higher, reaches values similar to that of the unpromoted catalysts after a gradual decrease (Figure 7). The fact that both Co/ZrO_2/*meso*H-ZSM-5 and CoRu/ZrO_2/*meso*H-ZSM-5 (with similar Co loadings and crystallite sizes; Table 3) present fairly identical values and trends in the *TOS* evolution of *CTY* (Figure 7) supports the EXAFS data in the sense that the addition of ZrO_2 is sufficient to fully reduce Co by using the activation method.

The carbon selectivity toward C1 over Co/*meso*H-ZSM-5 is more than two times larger than that over Co/SiO_2 (Figure 8). The possible sources for such a high methane selectivity are as follows: (*i*) a poor catalyst reducibility, (*ii*) a low chain growth probability (α) in FTS, (*iii*) acid-catalyzed hydroconversion reactions, and (*iv*) side reactions over Co. Sources 1 and 2 increase the rate of methane formation through FTS, whereas in the case of sources 3 and 4, other reactions generate C1 along with FTS. The contribution of each source is discussed below:

(i) Figure 8 shows that promoter addition and reducibility enhancement do not significantly change the methane selectivity.

(ii) In line with previous reports [15, 18-20], the fractional molar distribution of products of FTS has a nonlinear shape for the H-ZSM-5-containing catalysts (Figure E3a/Appendix E). The only exception is Co/*meso*H-ZSM-5*(o)*, which is devoid of strong Brønsted acidity (Figure 1) and represents a linear ASF product distribution, which is similar to the case of Co/SiO_2. A 'break' in the ASF product selectivity at about C12 (Figure E3a/Appendix E) can be translated into a lower α for higher hydrocarbons, which can eventually increase the formation of methane. The S_{C1} of Co/*meso*H-ZSM-5 is 2% higher than that of Co/*meso*H-ZSM-5*(o)* at iso-conversion (Figure E3b/Appendix E).

(iii) No methane was detected during the conversion of C6 over the bare zeolite (Figure 6), which agrees with the general belief that the hydrocracking mechanism over acid sites does not lead to C1 [34]. Furthermore, if over-cracking inside the zeolite pores was the main origin of the large production of methane over the Co-containing catalysts, then Co/*meso*H-ZSM-5*(o)* should have represented a much lower carbon selectivity toward C1. However, the catalytic performance results shown in Figure E3/Appendix E rule out this possibility. Therefore, alleviating the effect of the above-mentioned sources (1–3) may lower S_{C1} (over Co/*meso*H-ZSM-5) only by a few percent at maximum.

(iv) Among Fe and Co, the hydrogenation activity of Co is stronger [42]. The Co-based catalysts for FTS are more sensitive (than Fe) to changes in the process conditions [42] (such as temperature and H_2/CO ratio). Moreover, the C1 level is typically higher for Co-based catalysts than what is anticipated by extrapolating the ASF distribution to $n = 1$ (Figure E3a/Appendix E). In the case of our zeolite-supported Co-catalysts, both direct CO hydrogenation to methane ($CO + 3H_2 \rightarrow CH_4 + H_2O$) and hydrogenolysis are expected to occur because both side reactions become important on smaller Co particles. This is a result of the larger H_2 coverage over lower index surface crystallographic planes or steps and corners [43] (of which the density increases as Co crystallite size decreases) [44]. Hydrogenolysis is a structure-sensitive reaction that will compete with direct CO hydrogenation over the small metal particles [45]. Although

this reaction could be suppressed at low CO conversions owing to competitive CO adsorption [46], it can be observed from Figure 6 that in the absence of CO, the zeolite-supported Co converts hydrocarbons into methane in a yield of 99% at 513 K.

In line with our previously reported CO adsorption results [19], the TPR(H_2) results reveal that the nature and thus the reactivity of Co sites is more heterogeneous over the zeolite-supported catalysts than over Co/SiO_2 (Figure 4). We conclude that owing to the strong Co-zeolite interaction (Figure 4), lower coordinated Co sites are stabilized over the zeolite support. Therefore, this catalyst is sensitive to changes in H_2 concentration as well and demonstrates an increased selectivity toward C1 as the H_2 concentration is higher at lower conversion levels (Table 5). This observation explains why in contrast to Co/SiO_2, S_{C1} increases with time over Co/*meso*H-ZSM-5 with a decrease in CO conversion (Figure 10).

At similar conversion levels, a catalyst with a lower Co loading of 10.7 wt% has 4% more selectivity toward C1 (Figure E3b/Appendix E). At a lower Co loading, more defects are expected on the metal crystallites; therefore, this result further confirms the above-mentioned hypothesis on the main source of methane formation over the zeolite-supported Co-catalysts.

6.4. Conclusions

Mesoporous H-ZSM-5 (*meso*H-ZSM-5) is prepared through base and acid treatments of a commercial ZSM-5 zeolite (Si/Al = 40). The base treatment with tetrapropylammonium hydroxide increases the mesopore surface area considerably and deactivates the Brønsted acidity of the zeolite. The decreased Si/Al ratio, caused by zeolite desilication, is set back to the original value through the succeeding treatment with HNO_3, which also regenerates the Brønsted acidity. If loaded with Co, the resulting *meso*H-ZSM-5-supported Co-catalyst is much more active than the conventional Co/SiO_2 catalyst. After 140 h on-stream, Co/*meso*H-ZSM-5 is three times more selective to the C5–C11 fraction than is Co/SiO_2. A large contribution of unsaturated hydrocarbons, other than α-olefins, to the liquid products as well as the conversion of *n*-hexane and 1-hexene indicate that the improved selectivity toward the gasoline fraction owes to the secondary acid-catalyzed reactions of Fischer-Tropsch α-olefins over the zeolite.

With the addition of either Ru or ZrO_2 promoters, the reducibility of zeolite-supported Co increases considerably, which leads to an increased initial catalytic activity, that disappears at longer *TOS*. Nevertheless, promoters do not affect the product distribution significantly. The TPR(H_2) and CO adsorption (Chapter 5) results reveal that the reactivity of Co is diverse as supported on mesoporous H-ZSM-5. In this respect, a large contribution of lower coordinated Co sites promotes methane formation through the direct hydrogenation of CO and hydrogenolysis and makes the catalyst sensitive to changes in H_2 concentration in terms of selectivity toward C1.

References

[1] D.A. Wood, C. Nwaoha, B.F. Towler, J. Nat. Gas Sci. Eng. 9 (2012) 196-208.

[2] R. Guettel, U. Kunz, T. Turek, Chem. Eng. Technol. 31 (2008) 746-754.

[3] S.R. Deshmukh, A.L.Y. Tonkovich, J.S. McDaniel, L.D. Schrader, C.D. Burton, K.T. Jarosch, A.M. Simpson, D.R. Kilanowski, S. LeViness, Biofuels 2 (2011) 315-324.

[4] O.O. James, B. Chowdhury, M.A. Mesubi, S. Maity, RSC Adv. 2 (2012) 7347-7366.

[5] A. de Klerk, E. Furimsky, Catalysis in the Refining of Fischer-Tropsch Syncrude, RSCPublishing, Cambridge, UK, 2010.

[6] Q. Zhang, J. Kang, Y. Wang, ChemCatChem 2 (2010) 1030-1058.

[7] V.U.S. Rao, R.J. Gormley, A. Shamsi, T.R. Petrick, J.M. Stencel, R.R. Schehl, R.D.H. Chi, R.T. Obermyer, J. Mol. Catal. 29 (1985) 271-283.

[8] V. Udaya, S. Rao, R.J. Gormley, Catal. Today 6 (1990) 207-234.

[9] A.N. Pour, M. Zare, S.M. Kamali Shahri, Y. Zamani, M.R. Alaei, J. Nat. Gas Sci. Eng. 1 (2009) 183-189.

[10] A. Freitez, K. Pabst, B. Kraushaar-Czarnetzki, G. Schaub, Ind. Eng. Chem. Res. 50 (2011) 13732-13741.

[11] A. Martínez, J. Rollán, M.A. Arribas, H.S. Cerqueira, A.F. Costa, E.F. S.-Aguiar, J. Catal. 249 (2007) 162-173.

[12] A. Martínez, S. Valencia, R. Murciano, H.S. Cerqueira, A.F. Costa, E.F. S.-Aguiar, Appl. Catal. A-Gen. 346 (2008) 117-125.

[13] G. Yang, C. Xing, W. Hirohama, Y. Jin, C. Zeng, Y. Suehiro, T. Wang, Y. Yoneyama, N. Tsubaki, Catal. Today 215 (2013) 29-35.

[14] C. Kibby, K. Jothimurugesan, T. Das, H.S. Lacheen, T. Rea, R.J. Saxton, Catal. Today 215 (2013) 131-141.

[15] S. Sartipi, J. van Dijk, J. Gascon, F. Kapteijn, Appl. Catal. A-Gen. 456 (2013) 11-22.

[16] J. Kang, K. Cheng, L. Zhang, Q. Zhang, J. Ding, W. Hua, Y. Lou, Q. Zhai, Y. Wang, Angew. Chem.-Int. Edit. 50 (2011) 5200-5203.

[17] K. Cheng, J. Kang, S. Huang, Z. You, Q. Zhang, J. Ding, W. Hua, Y. Lou, W. Deng, Y. Wang, ACS Catal. 2 (2012) 441-449.

[18] S. Sartipi, K. Parashar, M. Makkee, J. Gascon, F. Kapteijn, Catal. Sci. Technol. 3 (2013) 572-575.

[19] S. Sartipi, K. Parashar, M.J. Valero-Romero, V.P. Santos, B. van der Linden, M. Makkee, F. Kapteijn, J. Gascon, J. Catal. 305 (2013) 179-190.

[20] S. Sartipi, M. Alberts, M.J. Meijerink, T.C. Keller, J. Pérez-Ramírez, J. Gascon, F. Kapteijn, ChemSusChem 6 (2013) 1646-1650.

[21] J.A.Z. Pieterse, S. Veefkind-Reyes, K. Seshan, L. Domokos, J.A. Lercher, J. Catal. 187 (1999) 518-520.

[22] S. Abelló, A. Bonilla, J. Pérez-Ramírez, Appl. Catal. A-Gen. 364 (2009) 191-198.

[23] D. Verboekend, G. Vilé, J. Pérez-Ramírez, Cryst. Growth Des. 12 (2012) 3123-3132.

[24] S. Mitchell, N.L. Michels, K. Kunze, J. Pérez-Ramírez, Nat. Chem. 4 (2012) 825-831.

[25] X.B. Li, X.Y. Jiang, Chem. Tech. Fuels Oils 49 (2013) 156-164.

[26] P. Arnoldy, J.A. Moulijn, J. Catal. 93 (1985) 38-54.

[27] S. Sartipi, A.A. Khodadadi, Y. Mortazavi, Appl. Catal. B-Environ. 83 (2008) 214-220.

[28] F. Diehl, A.Y. Khodakov, Oil Gas Sci. Technol. 64 (2009) 11-24.

[29] A.Y. Khodakov, W. Chu, P. Fongarland, Chem. Rev. 107 (2007) 1692-1744.

[30] R.B. Greegor, F.W. Lytle, R.L. Chin, D.M. Hercules, J. Phys. Chem. 85 (1981) 1232-1235.

[31] W. Chu, P.A. Chernavskii, L. Gengembre, G.A. Pankina, P. Fongarland, A.Y. Khodakov, J. Catal. 252 (2007) 215-230.
[32] G. Jacobs, Y. Ji, B.H. Davis, D. Cronauer, A.J. Kropf, C.L. Marshall, Appl. Catal. A-Gen. 333 (2007) 177-191.
[33] G.L. Bezemer, J.H. Bitter, H.P.C.E. Kuipers, H. Oosterbeek, J.E. Holewijn, X. Xu, F. Kapteijn, A.J. van Dillen, K.P. De Jong, J. Am. Chem. Soc. 128 (2006) 3956-3964.
[34] C. Bouchy, G. Hastoy, E. Guillon, J.A. Martens, Oil Gas Sci. Technol. 64 (2009) 91-112.
[35] M. Rigutto, Cracking and Hydrocracking, in: J. Čejka, A. Corma, S. Zones (Eds.) Zeolites and Catalysis: Synthesis, Reactions and Applications, WILEY-VCH Verlag GmbH & Co. KGaA, Weinheim, 2010, pp. 547-584.
[36] W. Juszczyk, Z. Karpinski, J. Pielaszek, Z. Paal, J. Catal. 143 (1993) 583-593.
[37] N.E. Tsakoumis, M. Rønning, Ø. Borg, E. Rytter, A. Holmen, Catal. Today 154 (2010) 162-182.
[38] T.M. Eggenhuisen, P. Munnik, H. Talsma, P.E. De Jongh, K.P. De Jong, J. Catal. 297 (2013) 306-313.
[39] G. Prieto, J. Zečević, H. Friedrich, K.P. De Jong, P.E. De Jongh, Nat. Mater. 12 (2013) 34-39.
[40] E. Van Steen, M. Claeys, M.E. Dry, J. Van De Loosdrecht, E.L. Viljoen, J.L. Visagie, J. Phys. Chem. B 109 (2005) 3575-3577.
[41] J. van de Loosdrecht, B. Balzhinimaev, J.A. Dalmon, J.W. Niemantsverdriet, S.V. Tsybulya, A.M. Saib, P.J. van Berge, J.L. Visagie, Catal. Today 123 (2007) 293-302.
[42] H. Schulz, Stud. Surf. Sci. Catal. 163 (2007) 177-199.
[43] J.P. den Breejen, P.B. Radstake, G.L. Bezemer, J.H. Bitter, V. Frøseth, A. Holmen, K.P. De Jong, J. Am. Chem. Soc. 131 (2009) 7197-7203.
[44] R. van Hardeveld, F. Hartog, Surf. Sci. 15 (1969) 189-230.
[45] H.J. Jung, S.S. Park, C.H. Shin, Y.K. Park, S.B. Hong, J. Catal. 245 (2007) 65-74.
[46] R.J. Gormley, V.U.S. Rao, R.R. Anderson, R.R. Schehl, R.D.H. Chi, J. Catal. 113 (1988) 193-205.

Chapter 7

Effect of zeolite structure in hierarchical zeolite-supported cobalt-catalysts for the direct conversion of biosyngas into liquid fuels

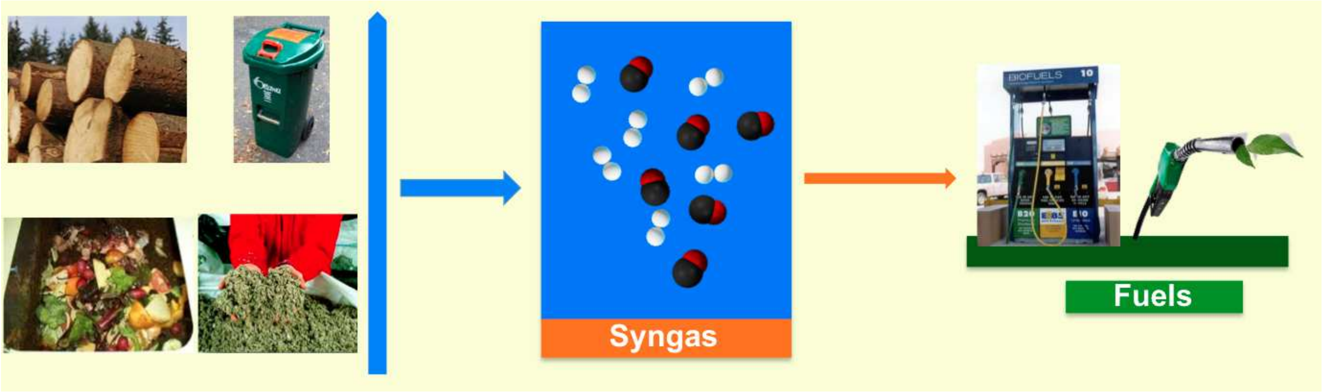

This Chapter is based on the following publication:

S. Sartipi, M. Alberts, M.J. Meijerink, T.C. Keller, J. Pérez-Ramírez, J. Gascon, F. Kapteijn, ChemSusChem 6 (**2013**) 1646-1650.

Abstract: Bifunctional Co-based catalysts on zeolite supports are applied for the valorization of biosyngas through Fischer-Tropsch synthesis (FTS). By using these catalysts, wax can be hydrocracked to shorter-chain hydrocarbons, increasing the selectivity towards the C5–C11 (gasoline-range) fraction. The zeolite topology and the amount and strength of acid sites are key parameters to maximize the performance of these bifunctional catalysts, steering FTS product selectivity towards liquid hydrocarbons.

7.1. Introduction

The growing concerns about oil depletion have spurred worldwide interest in finding alternative feedstocks for important petrochemical commodities and fuels. In this context, the development of efficient routes to transform biomass into useful chemicals and fuels is of primary importance. Among possible options for the valorization of biomass, gasification (followed by syngas cleaning) [1] and Fischer-Tropsch synthesis (FTS) hold much promise for widespread application in the near future, given the maturity reached by both technologies [2]. Currently, however, gas-to-liquid (GTL) technologies are only economically attractive at very large scales. Process intensification is a must if these tools are to be applied for biomass-to-liquid (BTL) conversions, where the on-site availability of the feedstock is an obstacle [3].

Both reactor and catalysis engineering have been explored in GTL process intensification: while the use of structured catalysts and reactors maximizes the FTS efficiency by improving mass and energy transport [3-6], many efforts have been devoted to formulating catalysts that maximize the direct production of liquid fuels (desired products) by combining FTS, hydrocarbon cracking, and isomerization into one single catalyst particle [7, 8]. A promising approach involves the use of mesoporous (hierarchical) zeolites as supports for FTS catalysts [9-11]. For example, bringing H-ZSM-5 acid sites in close proximity to the FTS active phase results in bifunctional catalysts that exhibit a high selectivity to the gasoline fraction [12]. Most studies dealing with the use of ZSM-5 as catalyst carrier proposed that hydrocarbon cracking and isomerization contribute to a non-Anderson-Schulz-Flory (ASF) product distribution [9, 13-15]. However, very little is known about the quantitative effect of both of these acid-catalyzed reactions, and even less about how the properties of the zeolite influence the product distribution. This Chapter demonstrates that when seeking to maximize the performance of bifunctional catalysts by steering FTS product selectivity towards liquid hydrocarbons, the topology of the zeolite and, most importantly, the number and strength of acid sites are key parameters.

7.2. Experimental

7.2.1. Synthesis

Amorphous SiO_2 was provided by Fuji Silysia Chemical Ltd. (CARiACT Q-10). Mesoporous H-ZSM-5 (‘*meso*H-ZSM-5’) was prepared by demetalation *via* consecutive base and acid treatments: H-ZSM-5 powder (Zeolyst, CBV 8014, Si/Al = 40) was desilicated by 1 M tetrapropylammonium hydroxide (Sigma-Aldrich) at 343 K for 1 h. After separation from the base solution, the sample was thoroughly washed with deionized water and kept overnight at 333 K, followed by drying at 393 K for 12 h and calcination in static air at 823 K for 5 h. The desilicated zeolite was treated with 1 M HNO_3

aqueous solution at 343 K for 2 h to remove Al and readjust its Si/Al ratio. After separation from the acid solution, the sample was thoroughly washed with deionized water, dried, and calcined as after the above-mentioned desilication procedure. The H-ITQ-2 sample was prepared according to the procedure described by Corma *et al.* [16, 17]. Mesoporous H-USY zeolite ('*meso*H-USY') was obtained through alkaline treatment of a commercial zeolite sample in presence of a pore-directing agent, as described previously [18]. H-USY powder (Zeolyst, CBV 780, Si/Al = 40) was treated with 0.075 M NaOH (Sigma-Aldrich) and 0.1 M tetrapropylammonium bromide (ABCR Chemicals Karlsruhe) in a Mettler Toledo EasyMax batch reactor system at 338 K for 0.5 h. After filtration and drying, the sample was transformed into the proton form by three subsequent ion-exchanges in 0.1 M NH_4NO_3 solution at room temperature for 8 h and calcination in static air at 823 K for 5 h.

The amorphous SiO_2 and zeolite samples were loaded with *ca.* 20 wt% of Co, by applying incipient wetness impregnation using an aqueous solution of $Co(NO_3)_2 \cdot 6H_2O$ (Sigma-Aldrich). After impregnation, samples were kept overnight in a desiccator at room temperature and dried at 393 K for 12 h. Subsequently, the catalysts were calcined in static air at 673 K for 2 h.

7.2.2. Characterization

Elemental analysis was performed with PerkinElmer Optima instruments. After sample dilution, analysis was done by inductively coupled plasma optical emission spectrometry (ICP-OES).

Pyridine adsorption was followed by a Nicolet 6700 FT-IR (Thermo Scientific) instrument equipped with a MCT/B detector. Zeolite samples (self-supporting wafers) were degassed at 673 K for 2 h under vacuum. Pyridine vapor was dosed to the sample stepwise. After each step, the sample was heated to 433 K to allow diffusion of the probe molecule and subsequently cooled to room temperature for collection of spectra. This procedure was repeated to estimate the extinction coefficient until no further increase was observed in the areas of adsorbed pyridine upon dosage. Finally, the samples were heated to 433 K under vacuum and the final spectrum was recorded at room temperature. During each measurement 128 scans were recorded in the range 1000–4000 cm^{-1} at a resolution of 4 cm^{-1}. Spectra of degassed samples were collected as background.

Temperature-programmed NH_3 desorption (NH_3-TPD) was measured by using an AutoChem II Chemisorption Analyzer (Micromeritics). *Ca.* 0.2 g of the each zeolite sample was first degassed under He flow at 673 K for 1 h and then saturated with NH_3 at 473 K during 1 h, using a flow of 1.65% NH_3 in He. The gas mixture was then switched back to He and the sample was purged at 473 K for *ca.* 1 h to remove the weakly adsorbed NH_3 molecules. TPD was subsequently recorded under He flow, from 473 to 850 K. The heating rates were 10 K min^{-1} during different stages of the experiment.

Transmission electron microscopy (TEM) was done by using a FEI Tecnai TF20 microscope and a carbon-coated Cu grid. Prior to analysis, samples were reduced in H_2 at 773 K for 13 h (2 K min^{-1}) and transferred to the grid in a glove-box.

7.2.3. Fischer-Tropsch synthesis

FTS experiments were performed on the six-flow fixed-bed microreactor setup described in Chapter 2. For all experiments, 0.25 g of fresh catalyst (100–212 µm) was diluted with SiC of similar size to attain a constant bed volume of *ca.* 1.3 cm^3. Catalysts were activated *in situ* prior to FTS reaction by H_2, at 773 K for 13 h at atmospheric pressure followed by cooling to 453 K under H_2 flow. After increasing the pressure to the process value (15 bar total pressure), CO was gradually introduced to the feed stream at 453 K in order to reach its final concentration ($H_2/CO = 1$) in 1 h. Subsequently, the reactor was heated to the process temperature (513 K). A rate of 2 K min^{-1} was applied for all the heating/cooling steps.

7.2.4. Acid-catalyzed reactions

Acid-catalyzed reactions were performed in a fixed-bed reactor over 0.25 g of catalyst particles (100–212 µm). The samples were dried overnight under H_2 flow at 673 K and atmospheric pressure. After cooling to 513 K the total pressure was increased to 15 bar and subsequently a mixture of *n*-C6, H_2, and N_2 was fed to the reactor. After 20 h on-stream, data collection started at different reaction temperatures. The reactor was kept at each temperature for 3 h before product analysis. The product stream was analyzed online by a Compact GC (Interscience), equipped with a Porabond Q column at 363 K (10 m × 0.32 mm) and FID, using He as carrier gas.

7.3. Results and discussion

Three zeolites were chosen, with different framework topologies, in proton form: MFI (H-ZSM-5), delaminated MWW (H-ITQ-2), and FAU (H-USY). The zeolites were used as supports for Co-based FTS catalysts. H-ITQ-2 was used (as support) without further modification, while H-ZSM-5 and H-USY (both obtained commercially) were leached in basic solutions to increase their external surface area by *ca.* 800 and 250 %, respectively (Table F1/Appendix F, see Section 7.2.1). The increased mesopore surface areas of the hierarchical zeolites enables to load larger amounts of Co onto the samples [11, 12] and also improves their accessibility for reactant molecules, benefitting the activity and selectivity of the bifunctional reactions compared to their purely microporous counterparts [19].

*meso*H-ZSM-5, *meso*H-USY, and H-ITQ-2 have very similar bulk Si/Al ratios (of about 40) but different acid properties. H-ITQ-2 has the highest density of acid sites and Lewis-to-Brønsted acidity

Table 1 Textural and chemical properties of the supports.

Support	S_{meso}[a] / m^2 g^{-1}	Si/Al[b] / mol mol^{-1}	Brønsted[c] / µmol g^{-1}	Lewis[c] / µmol g^{-1}
SiO_2	248	n.a.[e]	n.a.	n.a.
*meso*H-ZSM-5	470	43	74	38
H-ITQ-2	604	43	109	111
*meso*H-USY	324	38	53	21

[a] Mesopore surface area obtained from the *t*-plot applied to the N_2 isotherm; [b] Obtained from ICP-OES; [c] Amount of Brønsted acid sites obtained from pyridine adsorption; [d] Amount of Lewis acid sites obtained from pyridine adsorption; [e] Not applicable.

ratio (Table 1). However, in TPD experiments, NH_3 desorbs from this zeolite at lower temperatures than from *meso*H-ZSM-5 (Figure 1). This indicates that H-ITQ-2 has weaker acidity than *meso*H-ZSM-5 [20] (note that the 'high-temperature' peak of H-ITQ-2 corresponds to framework collapse, not to strong acidity). On the other hand, *meso*H-USY was severely steamed and acid-leached prior to desilication and thus has the lowest concentration of acid sites (Table 1), the strength of which is comparable to H-ITQ-2 (Figure 1).

The hierarchical zeolites were loaded with *ca.* 20 wt% of Co and evaluated as FTS catalysts at 513 K using a model syngas mixture with a H_2/CO ratio of 1, similar to that of gasified biomass [21]. Co/SiO_2 (no acidity) served as reference, representing a conventional FTS catalyst [12].

The catalytic activities of Co/*meso*H-USY and Co/*meso*H-ZSM-5 proved similar, and higher than the activities of Co/H-ITQ-2 and Co/SiO_2 (Figure 2a). When considering that the average sizes of the Co crystallites of the Co/*meso*H-ZSM-5 and Co/*meso*H-USY samples are smaller than the average size of the crystallites of Co/SiO_2 (Table F1), the trend in FTS activities can be attributed to better dispersion of the active phase over the zeolite supports. Moreover, the time-on-stream evolution of cobalt-time-yield (number of CO moles converted per kilogram of Co per hour) during 140 h of

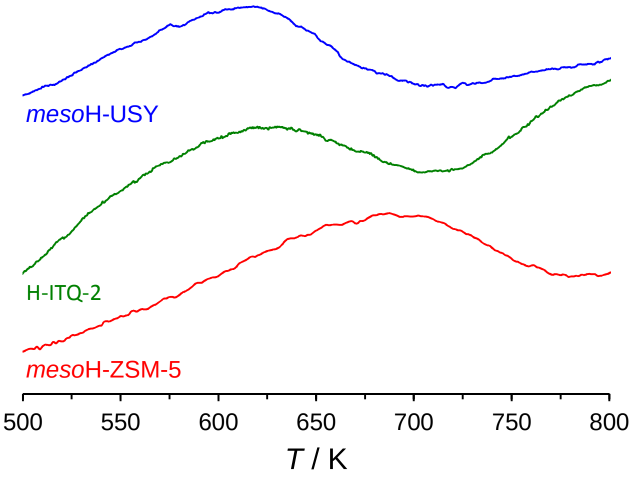

Figure 1. NH_3-TPD profiles (10 K min^{-1}) of *meso*H-ZSM-5, H-ITQ-2, and *meso*H-USY. The NH_3 was adsorbed at 473 K.

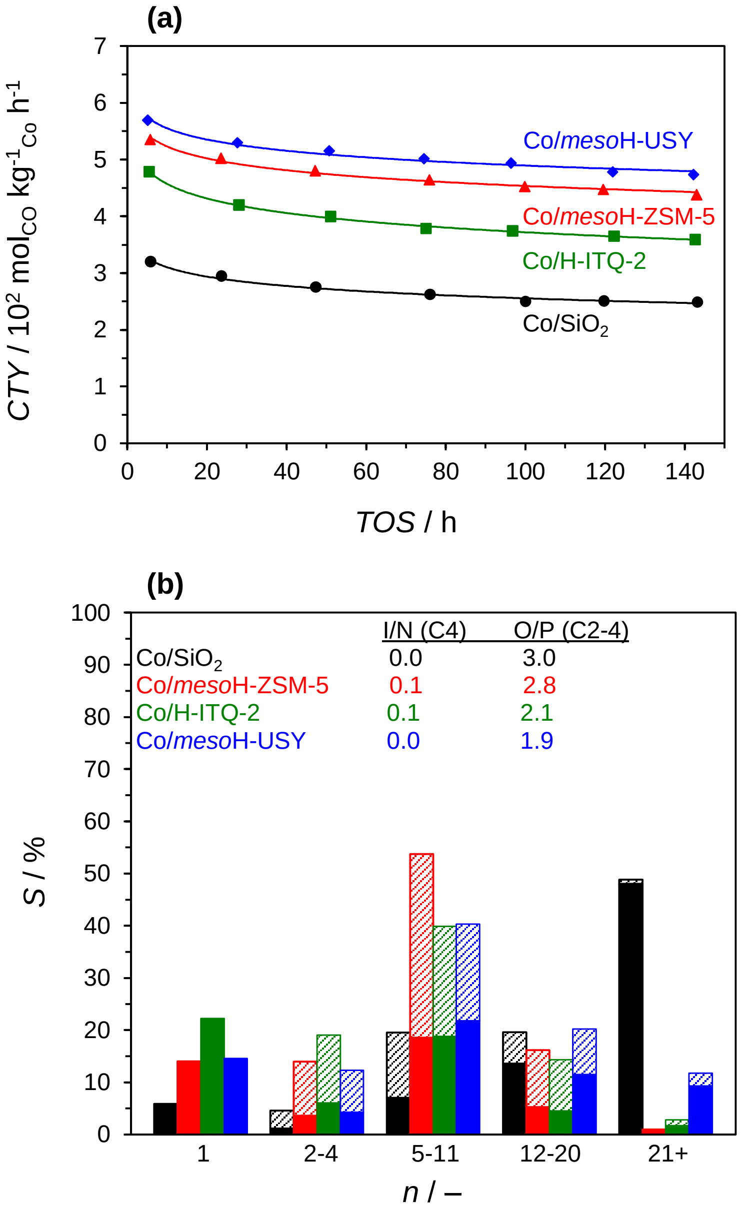

Figure 2. Time-on-stream (*TOS*) evolution of cobalt-time-yield (*CTY*) during FTS (a). Carbon selectivity of FTS products after 140 h on-stream (b). In each carbon number group from left to right: Co/SiO$_2$, Co/*meso*H-ZSM-5, Co/H-ITQ-2, and Co/*meso*H-USY; ■: *n*-paraffins; ▨: sum of isoparaffins and olefins; I/N (C4): *iso*- to *n*-C4 ratio; O/P (C2-4): olefin to paraffin ratio of C2–C4. Experiments were performed at 513 K, 15 bar total pressure, feed composition H$_2$/CO=1, and *GHSV* = 12 m$^3_{STP}$ kg$^{-1}_{cat}$ h^{-1}.

reaction demonstrates that the stability of the zeolite-supported catalysts in terms of CO conversion is comparable to the conventional Co/SiO$_2$ catalyst (Figure 2a). Sintering, the major cause of deactivation for Co-based FTS catalysts [22, 23] can be suppressed by maximizing the spatial distribution of active-phase crystallites over the support surface [23, 24]. Therefore, the availability of accessible surface area is crucial when aiming to design stable FTS catalysts. Representative TEM images in Figure 3 show that the distribution of Co inside the mesopores of the hierarchical zeolite is similar to that in the amorphous SiO$_2$.

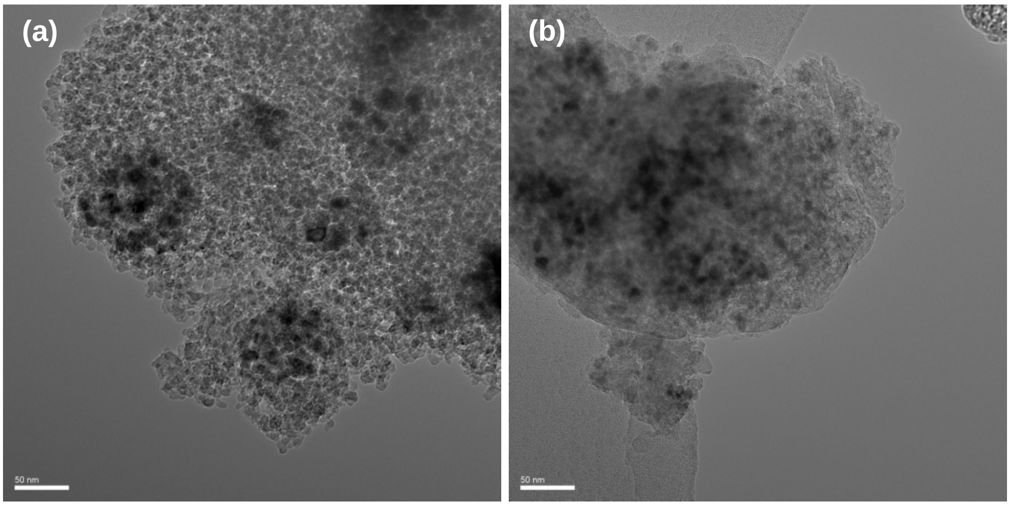

Figure 3. *Quasi in situ* TEM images of Co/SiO_2 (a) and Co/*meso*H-ZSM-5 (b) upon reduction in H_2 at 773 K for 13 h. Scale bars correspond to 50 nm.

Figure 2b shows the carbon selectivities to different FTS product ranges for the four catalysts under study. Under the applied process conditions, Co/SiO_2 proved highly selective to C21+ (wax). In good agreement with data reported earlier [9, 11, 12, 15, 25], wax production is suppressed considerably over the zeolite-containing catalysts, resulting in a higher selectivity to gasoline-range hydrocarbons (C5–C11). Co/*meso*H-USY still produces 12% of wax, while selectivity to this fraction is minimal over Co/*meso*H-ZSM-5 and Co/H-ITQ-2. Notably, the selectivity to the C5–C11 fraction of Co/*meso*H-ZSM-5 is *ca.* 14% higher than the selectivities of Co/*meso*H-USY and Co/H-ITQ-2 to this fraction.

The molar distribution of FTS hydrocarbons followes a fairly linear trend for Co/SiO_2, Co/*meso*H-USY, and Co/H-ITQ-2, implying an ASF product distribution for these catalysts (Figure 4). This reveals that the change in carbon selectivities of *meso*H-USY- and H-ITQ-2-supported catalysts compared Co/SiO_2 (Figure 2b) is due to a lower chain growth probability (α). Co/*meso*H-ZSM-5, in

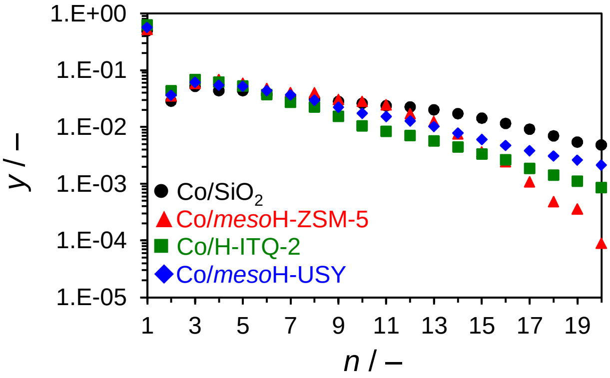

Figure 4. Molar fractional distribution of FTS products after 140 h on-stream at 513 K, 15 bar total pressure, feed composition H_2/CO = 1, and *GHSV* = 12 m^3_{STP} kg^{-1}_{cat} h^{-1}.

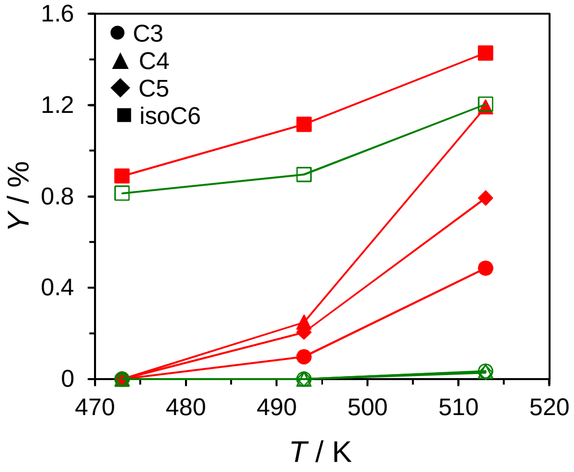

Figure 5. Product yields of *n*-C6 hydroconversion over *meso*H-ZSM-5 (solid symbols) and H-ITQ-2 (open symbols) at different temperatures. Data were collected after 20 h on-stream at 15 bar total pressure, H_2/*n*-C6 = 9.0, $N_2/H_2 = 2.0$, and *SV* = 13 $\mathrm{mol_{C6}\ kg^{-1}_{cat}\ h^{-1}}$.

contrast, does not display a linear chain growth trend. The catalyst displays an *α* value similar to that of Co/SiO_2 up to C11, but there is a progressive deviation from an ASF distribution for the molar fractions of heavier hydrocarbons (Figure 4).

This non-ASF trend has been attributed to secondary reactions, catalyzed by the acid functionality of the zeolite [8]. To gain more insight into possible acid-catalyzed reactions occurring under FTS conditions, additional experiments were performed using *n*-hexane as a C6 model hydrocarbon in a mixture with H_2 at a temperature and pressure similar to the FTS experiments (Figure 5). In the reaction temperature range (473–513 K) we studied, *meso*H-USY does not show any conversion (data not included in Figure 5). On the other hand, C6 isomers are observed when examining the H-ITQ-2 and *meso*H-ZSM-5 samples. Also, in contrast to H-ITQ-2, increasing amounts of lighter hydrocarbons are detected over *meso*H-ZSM-5 as the reaction temperature increases. Therefore, under the conditions applied here, *meso*H-ZSM-5 catalyzes both hydroisomerization and hydrocracking, H-ITQ-2 is mostly active for hydroisomerization, while *meso*H-USY is either inactive or deactivates rapidly.

These results explain the different product slates of the three zeolite-based samples compared to the conventional catalyst reported in Figure 2b: *meso*H-USY has a low density of weak acid sites, which are not capable of catalyzing the hydrocarbon conversion reactions at a low temperature (513 K). Therefore, Co/*meso*H-USY displays only FTS functionality (similar to Co/SiO_2); however, when using this catalyst the product distribution is shifted to lower hydrocarbons due to a lower *α* value. H-ITQ-2 has a high density of acid sites active for isomerization. Thus, Co/H-ITQ-2 combines both FTS and acid functionalities and, indeed, the ratio of *iso*- to *n*-C4 (I/N (C4)) products obtained when using this catalyst is higher than the ratios obtained when using Co/*meso*H-USY and Co/SiO_2 (insert in Figure

2b). Branched hydrocarbons may not participate in the chain propagation as effectively as linear ones, further decreasing the chain growth probability. Although wax production can be eliminated at lower α values, as dictated by the ASF distribution this will lead to increased selectivities towards C1 and C2–C4, which are not as valuable as liquid hydrocarbons (Figure 2b). Finally, *meso*H-ZSM-5 exhibits a stronger acidity (relative to *meso*H-USY and H-ITQ-2, Figure 1) resulting in activity for both isomerization and hydrocracking at 513 K (Figure 5), and hence hydrocracking of primary FTS products takes place on Co/*meso*H-ZSM-5. As a result, the fraction of gasoline-range hydrocarbons is considerably larger when using Co/*meso*HZSM-5 than when using the other catalysts.

H-ITQ-2 and *meso*H-ZSM-5 show comparable yields to C6 isomers in *n*-hexane hydroisomerization (Figure 5). Moreover, both the corresponding Co-catalysts have the same ratio of I/N (C4) in FTS (insert in Figure 2b). However, only Co/*meso*H-ZSM-5 deviates from an ASF product distribution (Figure 4). This implies that hydrocarbon isomerization alone is not enough to lead to non-ASF catalytic behavior, and points to the crucial role of cracking activity in the performance of bifunctional FTS catalysts.

7.4. Conclusions

Co-catalysts supported on hierarchical zeolites show a stable catalytic activity in FTS using model biosyngas mixtures. Zeolite acid density and strength are essential parameters to tune the FTS product selectivity towards liquid hydrocarbons. Only strong acid sites, active for hydrocracking at the operating temperature window of Co-based FTS catalysts, give rise to deviations from a conventional ASF product distribution. Altogether, this Chapter highlights the importance of carefully selecting the zeolite topology when developing intensified processes for the direct production of liquid fuels from biosyngas.

References

[1] A.M. Ribeiro, J.C. Santos, A.E. Rodrigues, Adsorption 17 (2011) 443-452.

[2] R. Luque, A.R. de la Osa, J.M. Campelo, A.A. Romero, J.L. Valverde, P. Sanchez, Energy Environ. Sci. 5 (2012) 5186-5202.

[3] S.R. Deshmukh, A.L.Y. Tonkovich, J.S. McDaniel, L.D. Schrader, C.D. Burton, K.T. Jarosch, A.M. Simpson, D.R. Kilanowski, S. LeViness, Biofuels 2 (2011) 315-324.

[4] R.M. de Deugd, F. Kapteijn, J.A. Moulijn, Top. Catal. 26 (2003) 29-39.

[5] F. Kapteijn, R.M. de Deugd, J.A. Moulijn, Catal. Today 105 (2005) 350-356.

[6] R. Guettel, U. Kunz, T. Turek, Chem. Eng. Technol. 31 (2008) 746-754.

[7] V.U.S. Rao, R.J. Gormley, A. Shamsi, T.R. Petrick, J.M. Stencel, R.R. Schehl, R.D.H. Chi, R.T. Obermyer, J. Mol. Catal. 29 (1985) 271-283.

[8] B. Sun, M. Qiao, K. Fan, J. Ulrich, F. Tao, ChemCatChem 3 (2011) 542-550.

[9] J. Kang, K. Cheng, L. Zhang, Q. Zhang, J. Ding, W. Hua, Y. Lou, Q. Zhai, Y. Wang, Angew. Chem.-Int. Edit. 50 (2011) 5200-5203.

[10] K. Cheng, J. Kang, S. Huang, Z. You, Q. Zhang, J. Ding, W. Hua, Y. Lou, W. Deng, Y. Wang, ACS Catal. 2 (2012) 441-449.
[11] S. Sartipi, K. Parashar, M. Makkee, J. Gascon, F. Kapteijn, Catal. Sci. Technol. 3 (2013) 572-575.
[12] S. Sartipi, J. van Dijk, J. Gascon, F. Kapteijn, Appl. Catal. A-Gen. 456 (2013) 11-22.
[13] A. Martínez, J. Rollán, M.A. Arribas, H.S. Cerqueira, A.F. Costa, E.F. S.-Aguiar, J. Catal. 249 (2007) 162-173.
[14] A.M. Subiranas, G. Schaub, Int. J. Chem. React. Eng. 5 (2007) Article A78.
[15] A. Freitez, K. Pabst, B. Kraushaar-Czarnetzki, G. Schaub, Ind. Eng. Chem. Res. 50 (2011) 13732-13741.
[16] A. Corma, V. Fornés, J. Martínez-Triguero, S.B. Pergher, J. Catal. 186 (1999) 57-63.
[17] A. Corma, V. Fornés, J.M. Guil, S. Pergher, T.L.M. Maesen, J.G. Buglass, Microporous Mesoporous Mat. 38 (2000) 301-309.
[18] D. Verboekend, G. Vilé, J. Pérez-Ramírez, Adv. Funct. Mater. 22 (2012) 916-928.
[19] J.A. Martens, D. Verboekend, K. Thomas, G. Vanbutsele, J.P. Gilson, J. Pérez-Ramírez, ChemSusChem 6 (2013) 421-425.
[20] H.K. Min, M.B. Park, S.B. Hong, J. Catal. 271 (2010) 186-194.
[21] O.O. James, A.M. Mesubi, T.C. Ako, S. Maity, Fuel Process. Technol. 91 (2010) 136-144.
[22] N.E. Tsakoumis, M. Rønning, Ø. Borg, E. Rytter, A. Holmen, Catal. Today 154 (2010) 162-182.
[23] T.M. Eggenhuisen, P. Munnik, H. Talsma, P.E. De Jongh, K.P. De Jong, J. Catal. 297 (2013) 306-313.
[24] G. Prieto, J. Zečević, H. Friedrich, K.P. de Jong, P.E. de Jongh, Nat. Mater. 12 (2013) 34-39.
[25] J. He, Z. Liu, Y. Yoneyama, N. Nishiyama, N. Tsubaki, Chem.-Eur. J. 12 (2006) 8296-8304.

Chapter 8

Summary and outlook

Design and development of catalyst formulations that maximize the direct production of liquid fuels by combining Fischer-Tropsch synthesis (FTS), hydrocarbon cracking, and isomerization into one single catalyst particle (bifunctional FTS catalyst) have been investigated in this thesis.

To achieve this aim, a second functionality (other than FTS) has to be added to the catalyst formulation to break the limitation of a classical Anderson-Schulz-Flory (ASF) distribution of FTS products. Since upgrading the FTS hydrocarbons is mostly based on acid-catalyzed reactions, zeolites are potential candidates for this approach. In this relation, recent literature highlights the use of H-ZSM-5 for the following reasons: (1) it is one of the few zeolites industrially produced and applied for acid-catalyzed hydrocarbon conversion reactions, (2) due to its narrow channel type structure and well distributed acid sites, it represents a (relatively) stable catalytic performance, especially at low-temperature Fischer-Tropsch process conditions, and (3) besides acid-catalyzed cracking, it has a fair isomerization and oligomerization activity at low temperatures which is essential to increase the octane number in case of gasoline cut and improve the cold flow properties of diesel (Chapter 1).

All the FTS experiments in this thesis were performed on a homemade lab-scale unit described in Chapter 2. The experimental setup is based on ‘six-flow fixed-bed microreactor’ concept which offers an increased experimental throughput as well as accuracy. The latter is due to equal conditions (in terms of process temperature, feed composition, equipment conditions, *etc.*) under which the six parallel experiments are performed. The condition is that all the reactors (flows) should behave identical, *i.e.*, provide similar results employing the same catalyst. Design and operation of such piece of equipment confirm that indeed it is possible to obtain reproducible activity and selectivity data within an acceptable experimental error (Chapter 2). Incorporation of separate mass flow and pressure controllers as well as product separation units in each flow allows running reactions with high production of liquid fractions (as in conventional single-flow operations). This is crucial for a complete quantification of FTS product compositions and will represent an advantage over high-throughput setups with more than ten flows where such instrumental considerations lead to elevated equipment volume, cost, and operation complexity. Therefore, **a six-flow fixed-bed microreactor unit combines the advantages of high-throughput and conventional FTS setups at the lab-scale** (Chapter 2).

In Chapter 3, combination of cobalt FTS active phase and acid functionality of H-ZSM-5 zeolite is explored in two different catalyst configurations: (*i*) H-ZSM-5 as catalytic coating on Co and (*ii*) H-ZSM-5 as catalytic support for Co. Spherical shaped Co/SiO_2 is chosen as a conventional FTS catalyst for comparison and used as precursor to synthesize the H-ZSM-5-coated Co-catalyst.

In the first case, various silicalite-1 and H-ZSM-5-coated reference samples were prepared by subjecting Co/SiO_2 to a direct hydrothermal procedure (state of the art method to prepare zeolite coatings). Silica in the Co/SiO_2 catalyst transforms into the zeolite when subjected to the hydrothermal synthesis while the original shape of the support is preserved after the transformation. By this synthesis approach, Co_3O_4 agglomerates are enwrapped in an H-ZSM-5 coating on a nanometer scale. The resulting bifunctional catalyst considerably lowers the production of FTS wax (C21+), as compared with Co/SiO_2. The membrane effect of this coating, however, results in mass transport limitations that lower the productivity. In the absence of acid functionality, accumulation of carbonaceous species deactivates the silicalite-1-coated reference catalyst. The H-ZSM-5-coated Co-catalyst shows lower CO conversion levels than the conventional Co/SiO_2 due to the membrane coating. This lower activity and modification of Co crystallites because of the hydrothermal treatment should be considered as the major drawbacks of this approach.

On the other hand, **systematic comparison of catalytic performances between physically mixed, coated catalyst, and non-acidic coated catalysts shows that the close proximity between the FTS and acid components is essential for improving the bifunctionality of the catalyst to increase the selectivity towards liquid products and eliminate the FTS heavy hydrocarbons** (Chapter 3). Such contact can be maximized when Co is directly dispersed over the zeolite (configuration (*ii*)). Since the Co accessibility is better in this configuration, limitations associated with the membrane effect of a zeolite coating can be overcome while preserving the important close proximity of the two functionalities.

To compensate for the relatively low intrinsic activity of FTS catalysts and to increase their productivity, high metal loadings are typically required in FTS catalyst formulations. In general, microporous zeolites are devoid of mesopore surface area, essential for an optimal dispersion of Co particles at high metal loadings. On the other hand, formation of metal clusters in the micropores is undesired, as Co particles smaller than 6 nm are not optimal for FTS in terms of activity and selectivity. Therefore, mesoporous H-ZSM-5 ('*meso*H-ZSM-5') is studied as carrier for Co-based FTS catalysts in Chapters 4 to 7.

Synthesis optimization of *meso*H-ZSM-5 involved demetalation *via* consecutive base and acid treatments. NaOH (alkaline) and tetrapropylammonium hydroxide (TPAOH, organic) bases were employed as desilicating agents. Consecutive basic-acid treatments provides H-ZSM-5 with high mesopore surface areas and volumes. Under similar treatment conditions, NaOH results in a more severe desilication than TPAOH, creating mesostructures with pore sizes and volumes very similar to the amorphous SiO_2 reference support. A more controlled desilication with TPAOH gives rise to more mesoporosity suggesting a higher degree of hierarchy with large cavities communicated with smaller mesopores. Further, TPAOH is preferred over NaOH, since Na^+ is a well-known poison for Co-based

FTS catalysts and trace amounts results in a lower FTS activity as compared with the organic base treated samples (Chapter 4).

The consecutive acid treatment (with HNO_3) removes the produced extraframework aluminum, caused by zeolite desilication, and boosts the FTS activity. Moreover, the acid treatment restores the Brønsted acidity of *meso*H-ZSM-5 (Chapter 5).

The large mesopore surface area of *meso*H-ZSM-5 improves the metal dispersion at elevated Co loadings. **The Co/*meso*H-ZSM-5 catalyst is a much more active catalyst than Co/H-ZSM-5 and the conventional Co/SiO_2. Moreover, time-on-stream stability of Co/*meso*H-ZSM-5 and Co/SiO_2 is comparable in terms of CO conversion, during 140 h of FTS reaction.** As compared with Co/H-ZSM-5, the improved transport properties of *meso*H-ZSM-5 increase the selectivity of the supported Co-catalyst towards liquid hydrocarbons and lowers that to methane. **The high selectivity to liquid hydrocarbons over H-ZSM-5-supported catalysts is visible as a cutoff in the molar distribution above C11 in terms of the ASF distribution of conventional catalysts (*e.g.*, Co/SiO_2). Measurements after 140 h on-stream show that Co/*meso*H-ZSM-5 is *ca.* three times more selective than Co/SiO_2 towards the C5–C11 cut, producing a large fraction of unsaturated hydrocarbons, other than α-olefins. Moreover, wax production is considerably suppressed over the zeolite-containing catalyst** (513 K, 15 bar total pressure, feed composition H_2/CO = 1, and *GHSV* = $12\ m^3_{STP}\ kg^{-1}_{cat}\ h^{-1}$) (Chapters 5 and 6).

Origins of methane selectivity over zeolite-supported Co-catalysts are also investigated. *meso*H-ZSM-5 was used as carrier for a series of Co-based FTS catalysts of different loadings with ZrO_2 and/or Ru added as promoters. By means of advanced catalyst characterization techniques (including *quasi in situ* dark field transmission electron microscopy, CO adsorption-diffuse reflectance infrared fourier transform spectroscopy, synchrotron-based X-ray absorption spectroscopy (EXAFS and XANES), *etc.*) in addition to a detailed catalyst performance assessment, a relationship is drawn between structural characteristics of Co (when supported on the zeolite) and its FTS activity and selectivity. Addition of either ZrO_2 or Ru considerably increases the Co reducibility upon activation at 773 K and improves the FTS activity during the first 80 h of reaction after which the activity is returned to that of the unpromoted catalyst. This catalyst promotion does not significantly affect the product selectivity (Chapter 6). **Methane selectivity over the zeolite-supported Co-catalysts originates from direct CO hydrogenation and hydrocarbon hydrogenolysis as the most important side reactions on coordinatively unsaturated Co sites, which are stabilized as consequence of a strong metal-zeolite interaction** (Chapters 5 and 6).

In addition to *meso*H-ZSM-5, other zeolite topologies were investigated as FTS catalyst carriers: delaminated MWW (H-ITQ-2) and mesoporous FAU (Chapter 7). All the zeolite supports were carefully characterized for their number and strength of acid sites by temperature-programmed NH_3 desorption and pyridine adsorption. To explore the role of acid-catalyzed reactions, including hydrocracking and isomerization, in the altered product distribution of zeolite-containing catalysts (with respect to conventional ones), acid-catalyzed model reactions of C6 (*n*-hexane or 1-hexene) were performed. **Zeolite acid density and strength are essential parameters to tune the FTS product selectivity towards liquid hydrocarbons. Only strong acid sites, active for hydrocracking at the operating temperature window of Co-based FTS catalysts, give rise to deviations from a conventional ASF product distribution** (Chapter 7). On purpose (partial) deactivation of Brønsted acidity in *meso*H-ZSM-5 by carbonaceous species (during catalyst synthesis) decreases the *iso*- to *n*-paraffin ratio and selectivity to gasoline fraction which further confirms the above-mentioned role of acid-catalyzed reactions in tuning the product selectivity (Chapter 5). **When acid site domains are in a close vicinity of FTS sites at a nanometer scale, α-olefins, which are primary FTS products, may crack or isomerize before they are hydrogenated. Indeed 1-hexene conversion is considerably higher than that of *n*-hexane over *meso*H-ZSM-5** (Chapter 6). The classical mechanism of such acid-catalyzed reactions, through rearrangement of a secondary carbocation into a protonated dialkylcyclopropane or through a bimolecular mechanism, increases the hydrocarbons' degree of branching. Since FTS may mainly produce linear α-olefins, considerable amounts of other unsaturated hydrocarbons in the liquid products are formed over the acid sites.

Altogether, our results demonstrate that the use of mesoporous zeolites as FTS supports holds many promises for the direct synthesis of liquid fuels from syngas. The challenges that still need to be addressed include a better control over the product selectivity of bifunctional catalysts. In this respect, it is essential to tackle the aforementioned origin(s) of methane production on the zeolite-supported Co-catalysts. In addition, more insight is required to further separate and define the contributions of 'the metal' and 'the zeolite/acid' functions in the overall product spectrum of these catalysts. While neglected or poorly described in the open literature, such insight is necessary for further catalyst optimization in relation to the product spectrum and practical applications. Detailed acid-catalyzed hydrocarbon conversion studies, under conditions relevant to that of FTS, together with reference experiments and detailed kinetic investigations are considered essential for a better understanding of bifunctional FTS systems. Finally, the long term stability of these catalysts is largely unexplored.

As an ongoing research, a new PhD project has recently started on this topic at the Catalysis Engineering section of Delft University of technology.

Appendix A

Six-flow operations for catalyst development in Fischer-Tropsch synthesis: Bridging the gap between high-throughput experimentation and extensive product evaluation

Presentation of equipment descriptions and models associated with Figure 2 and 3/Chapter 2, additional temperature profiles and schematic drawings, catalyst characterization, and additional product chromatograms, associated with Chapter 2.

Setup configuration

Table A1 Equipment descriptions and models associated with Figure 2 and 3 of Chapter 2.

Equipment	Description
Feed and mixing section	
SV 1–4	Solenoid valves for N_2, H_2, CO, and ‘a fourth gas’ supplies; pneumatically actuated; Swagelok SS–43S4
Filter 1–4	Filters for N_2, H_2, CO, and ‘a fourth gas’ supplies; VICI ZBUFR2F
PR 1–4	Pressure reducers for N_2, H_2, CO, and ‘a fourth gas’ supplies; DRAGER TESCOM 44–1862–24–816
PR 5	Pressure reducer for N_2, supplied downstream to the FBMs; VERIFLO 44100622
SRV 1–4	Safety relief valves; relief at 65 bar total pressure; Swagelok 55–4R3A1
SRV 5	Safety relief valve; relief at 55 bar total pressure; Swagelok 55–4R3A1
OWT 1–4	Traps for O_2 and H_2O removal from N_2, H_2, CO, and ‘a fourth gas’ supplies; AIR LIQUIDE Oxisorb 1001882
MFC 1–4	Mass flow controllers for N_2, H_2, CO, and ‘a fourth gas’ supplies; Bronkhorst F–211C–RA–11–V
MFC 11–16	Mass flow controllers for N_2, supplied downstream to the FBMs; Bronkhorst F–201CV–100–RAD–11–V
CV 1–4	Check valves for N_2, H_2, CO, and ‘a fourth gas’ supply lines; Swagelok SS–2C1
CV 5–10	Check valves for N_2 supply lines, connected downstream to the FBMs; Swagelok SS–2C–1/3
TWV 1–4	Three-way valves, switching N_2, H_2, CO, and ‘a fourth gas’ between the reactor manifold and vent; pneumatically actuated; Swagelok SS–41XS2
EH	Electrical heater for CO supply; T < 573 K; custom design
WCU	Water cooling unit for CO supply; custom design
FS (1)	Flow sensor installed downstream the SRVs
FS (2)	Flow sensor installed upstream of the WCU to monitor the cooling water flow
BPC 1	Back pressure controller for the vent line; GO BP3–1D01Q5K11L
PR 6	Pressure reducer for the low-pressure N_2 supply; GO PR1–1C11A3C111
R 1–3	Rotameters for controlling the flow rates of low-pressure N_2 supply
CV 26	Check valve for the low-pressure N_2 supply line; S–2C–1/3
Flow division section	
BPC 2	Back pressure controller for the feed line; GO BP3–1D01Q5K11L
MFC 5–10	Mass flow controllers for feeding the FBMs; Bronkhorst F–201C–RA–11–V
CV 11–16	Check valves for the feed supply lines to the FBMs; Swagelok SS–2C–1/3
SRV 6–11	Safety relief valves; relief at 40 bar total pressure; Swagelok 55–4R3A1
Reaction section	
Oven	Large heating box with a door, providing a hot zone for the feed, six-flow fixed-bed microreactor, and products; Heraeus T/UT 6420
FBM 1–6	Fixed-bed microreactors in an electrica1 oven; custom design, constructed in-house
BPC 3–8	Back pressure controllers for pressure adjustment in the reactors; GO LB1–1A01Q5J272
Separation/analysis	
HT 1–6	Hot traps for wax separation; 30 cm^3; custom design, constructed in-house
AOV 1–6A-B	Air operated valves to empty HT 1–6; pneumatically actuated; VICI ASFVO2HT4
LCV 1–6	Liquid collection vessels for collecting the heavy wax; 50 cm^3; Duran 21 801 17 5
CV 17–23	Check valves functioning as relief; cracking pressure: 1.7 bar total pressure
MV	Manual operated on/off valve, closed at the liquid collection period; Swagelok SS–4P4T–BK
FWV 1–7	Four-way valves; Swagelok SS–43YTFS2
Refrigerator	Cooling box with a door, providing a cold environment for the products (in CTs); Frigor

Continued

Continued

Equipment	Description
CT 1–7	Cold traps for collecting water and light hydrocarbons; 250 cm^3; Duran 10 922 34
EWSV 1	Eight-way selection valve for sampling from FBM 1–6 in operation mode (*i*); pneumatically actuated; VICI A6SF8MWE–BCD
EWSV 2	Eight-way selection valve for sampling from FBM 1–6 in operation mode (*ii*); pneumatically actuated; VICI A4SF8MWE–BCD
CV 24	Check valve for GC line
CV 25	Check valve for inlet line to FM
FM	Flow meter; Ritter TG05/5
Heated Line	Line heated by a heating tape
GC	Compact Gas Chromatograph; Interscience

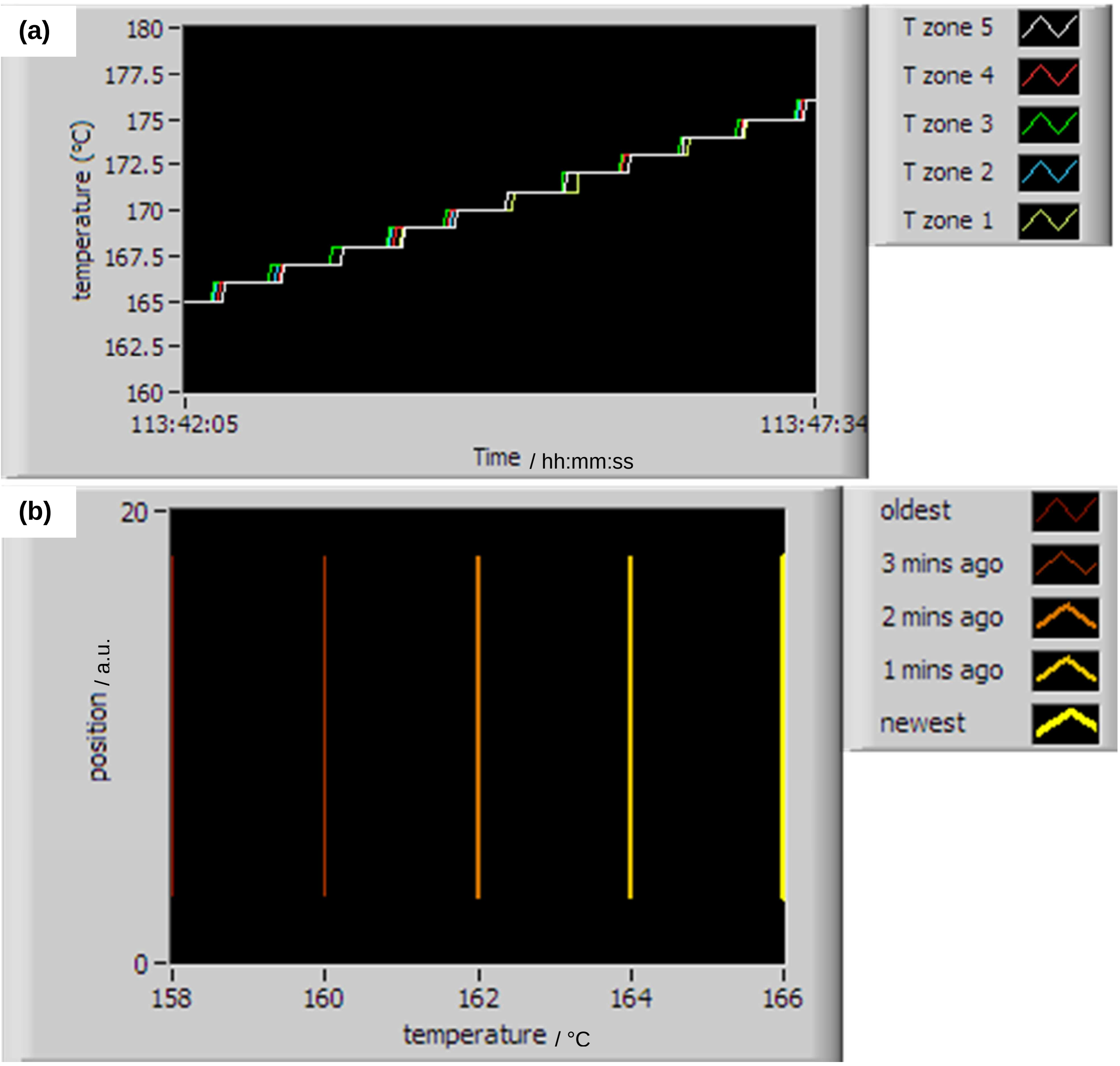

Figure A1. Temperature of individual heating sections (‘zones’ 1–5) of the six-flow fixed-bed microreactor *versus* time (a). Temperature along the six-flow fixed-bed microreactor at a time interval of 1 min (b). The temperature program included equal set points and a heating rate of 2 K min^{-1} for the five heating sections. Temperatures of all the five heating sections stay fairly equal during the program.

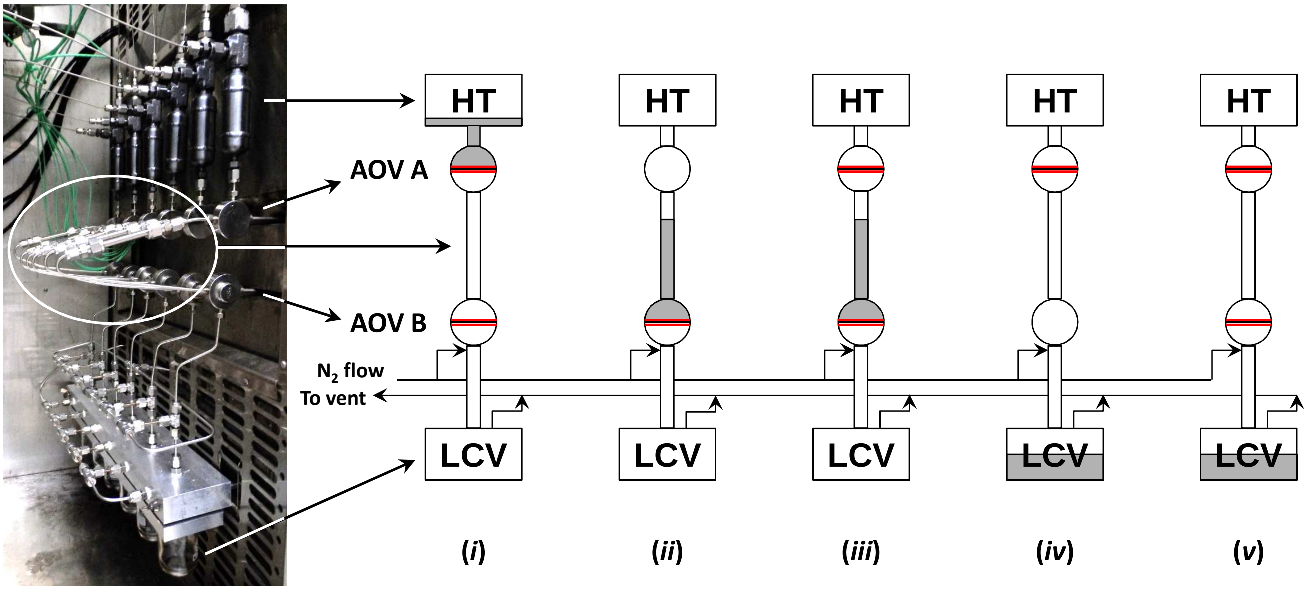

Figure A2. Schematic drawing showing how the hydrocarbon sample is drained from HTs into LCVs by a subsequent sequence of opening and closure of AOVs A and B (two normally-closed air-operated on/off valves): The system pressure allows discharging the wax, first from HTs into a piece of tube that is illustrated by the white oval in the left photograph (sequence *i*–*iii*), and consequently in LCVs (sequence *iii*–*v*). This draining operation is done every 6–24 h, depending on the wax production, during the course of FTS reaction. After the reaction, the draining operation is done every 2–3 h while the setup is flushed overnight by N_2. An inert environment is kept inside LCVs by *ca.* 100 cm^3 min^{-1} flow of N_2 at atmospheric pressure.

Catalyst

Characterization

N_2 physisorption was performed in an Autosorb-6B unit (Quantachrome Instruments) at liquid nitrogen temperature (77 K). Prior to the experiment, *ca.* 0.2 g of the samples were degassed overnight in an Autosorb Degasser unit (Quantachrome Instruments) under vacuum at 473 K.

Elemental analysis was performed with PerkinElmer Optima 5300dv instrument. Sample was first digested in a mixture of 2.00% HCl, 1.00% HF and 1.25% H_2SO_4. Analysis was done by inductively coupled plasma optical emission spectrometry (ICP-OES).

The X-ray diffraction (XRD) pattern was recorded in Bragg-Brentano geometry in a Bruker D8 Advance diffractometer equipped with a Vantec position sensitive detector and graphite monochromator. Measurement was performed at room temperature, using monochromatic Co Kα radiation (λ = 0.179026 nm) in the 2θ region between 10° and 100° with step size of 0.041° and step time of 1 s. The sample was placed on a Si {510} substrate and rotated during the measurement. The XRD pattern was background-subtracted to eliminate the contribution of air scatter and possible fluorescence radiation. Data evaluation was done with the Bruker program EVA.

Temperature-programmed reduction by H_2 (TPR(H_2)) was performed on an in-house constructed equipment. *Ca.* 0.1 g of Co/SiO_2 was subjected to 27 cm^3_{STP} min^{-1} flow of 7.4% H_2 in Ar in a temperature controlled reactor. The reactor temperature was ramped from room temperature to 1173 K with a heating rate of 10 K min^{-1} and the H_2 consumption was monitored by a TCD. Water was removed by a Permapure membrane dryer.

Results

Table A2 Textural and chemical properties of SiO_2 support and Co/SiO_2 catalyst.

Support/Catalyst	S / m^2 g^{-1}		V / cm^3 g^{-1}			Co	
	total[a]	meso[b]	total[c]	micro[d]	meso[e]	wt%[f]	d_{Co}[g] / nm
SiO_2	293	248	1.35	0.02	1.34	n.a.[h]	n.a.
Co/SiO_2	231	203	1.04	0.01	1.03	9.3	15

[a] BET surface area; [b] Mesopore surface area obtained from the *t*-plot applied to the N_2 isotherm; [c] Total pore volume; [d] Micropore volume obtained from the *t*-plot; [e] Mesopore volume calculated as $V_{meso} = V_{total}$-V_{micro}; [f] Obtained from ICP-OES; [g] Co crystallite size calculated from $d(Co^0) = 0.75d(Co_3O_4)$, where $d(Co_3O_4)$ is derived from XRD, applying the Scherrer equation; [h] Not applicable.

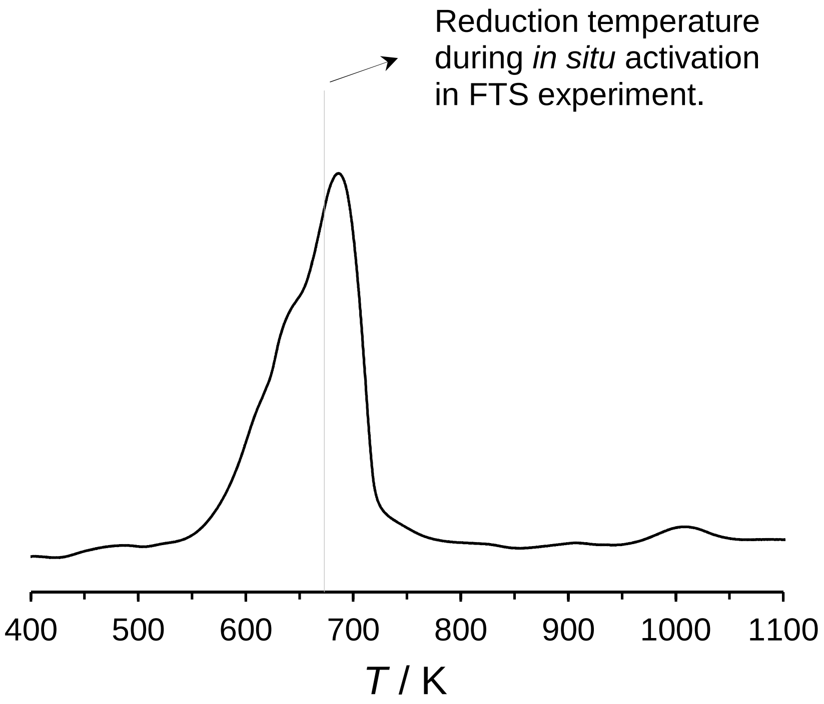

Figure A3. TPR(H_2) profile (10 K min^{-1}) of fresh Co/SiO_2 catalyst.

Product analysis

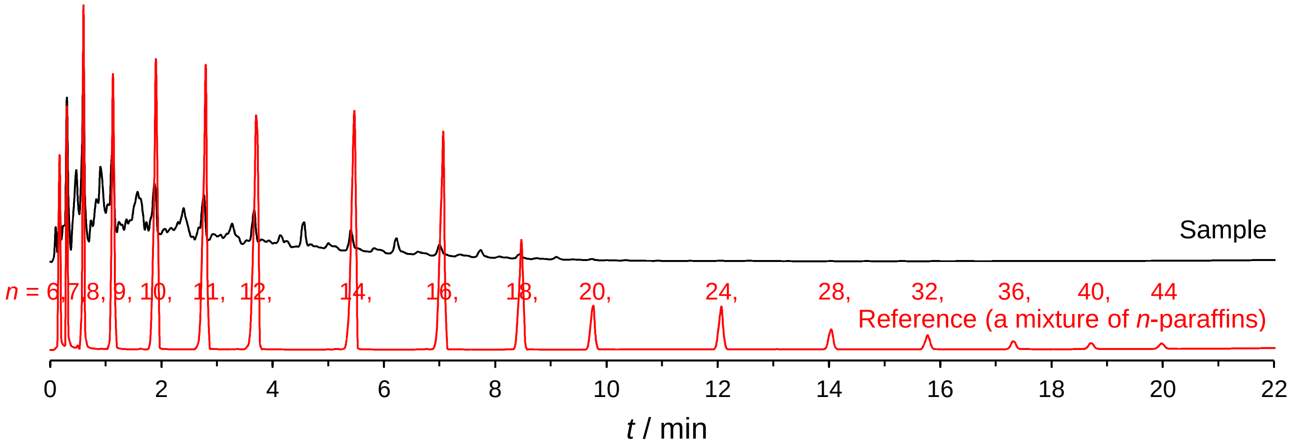

Figure A4. SimDis GC chromatogram of liquid FTS hydrocarbons, collected after 20 h on-stream over 10 wt% Co/H-ZSM-5 at 513 K, 15 bar total pressure, feed composition H_2/CO = 2, and *GHSV* = 2.4 m^3_{STP} kg^{-1}_{cat} h^{-1}. *n*: carbon number. The SimDis GC (Hewlett Packard 5890, Series II) is equipped with an FID and HP-1 column (7.5 m × 0.53 mm, film thickness 2.65 µm), using He as carrier gas. During the analysis, the oven temperature is ramped from 308 to 623 K (14 K min^{-1}) and kept at the final temperature for 5 min. Samples are diluted with CS_2 before injection.

Appendix B

'Zeolite-coated' *versus* 'zeolite-supported' bifunctional catalysts for the direct production of liquid fuels from syngas

Presentation of additional N_2 physisorption data and thermogravimetric analysis, associated with Chapter 3.

Experimental

Characterization

N_2 physisorption was performed in an Autosorb-6B unit (Quantachrome Instruments) at liquid nitrogen temperature (77 K). Prior to the experiment, *ca.* 0.1 g of the samples were degassed overnight in an Autosorb Degasser unit (Quantachrome Instruments) under vacuum at 623 K.

Thermogravimetric analysis (TGA) was performed on a Mettler Toledo TGA/SDTA851^e equipment, where 0.014–0.021 g of fresh and spent catalysts was screened for the change in its mass while heated from 298 to 1123 K with a heating rate of 5 K min^{-1} under 100 cm$^3_{STP}$ min^{-1} of air flow.

Results

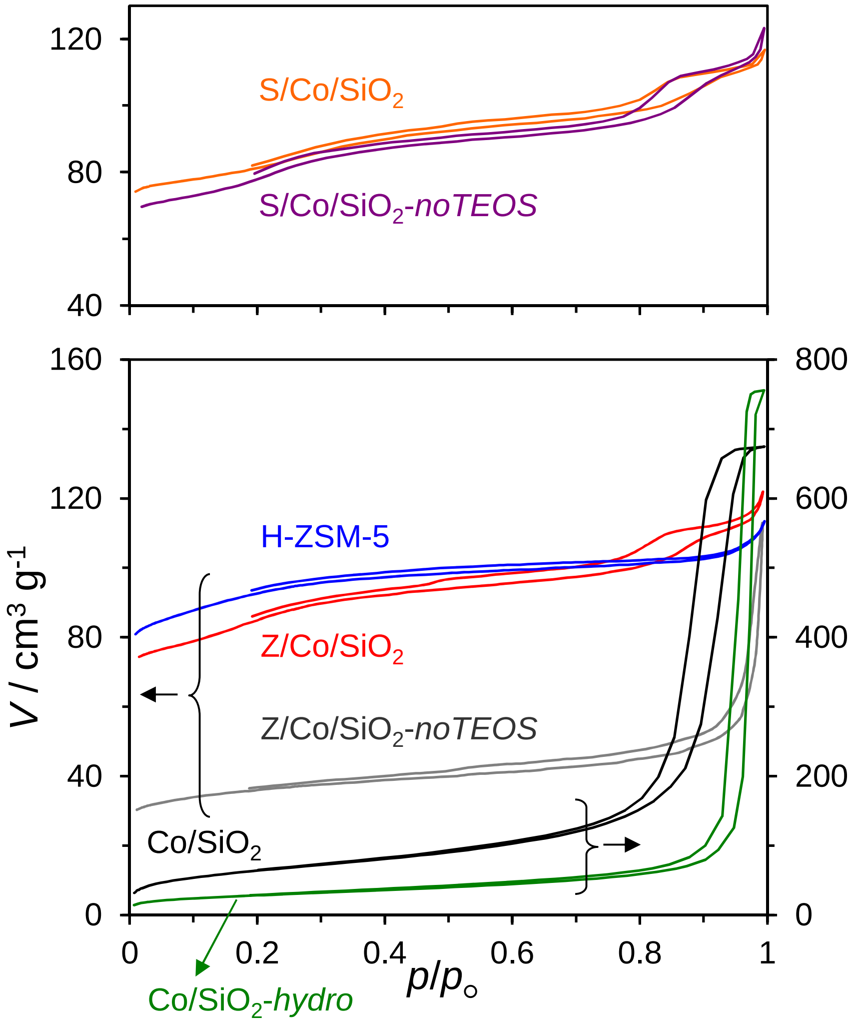

Figure B1. N_2 physisorption isotherms of the samples at 77 K.

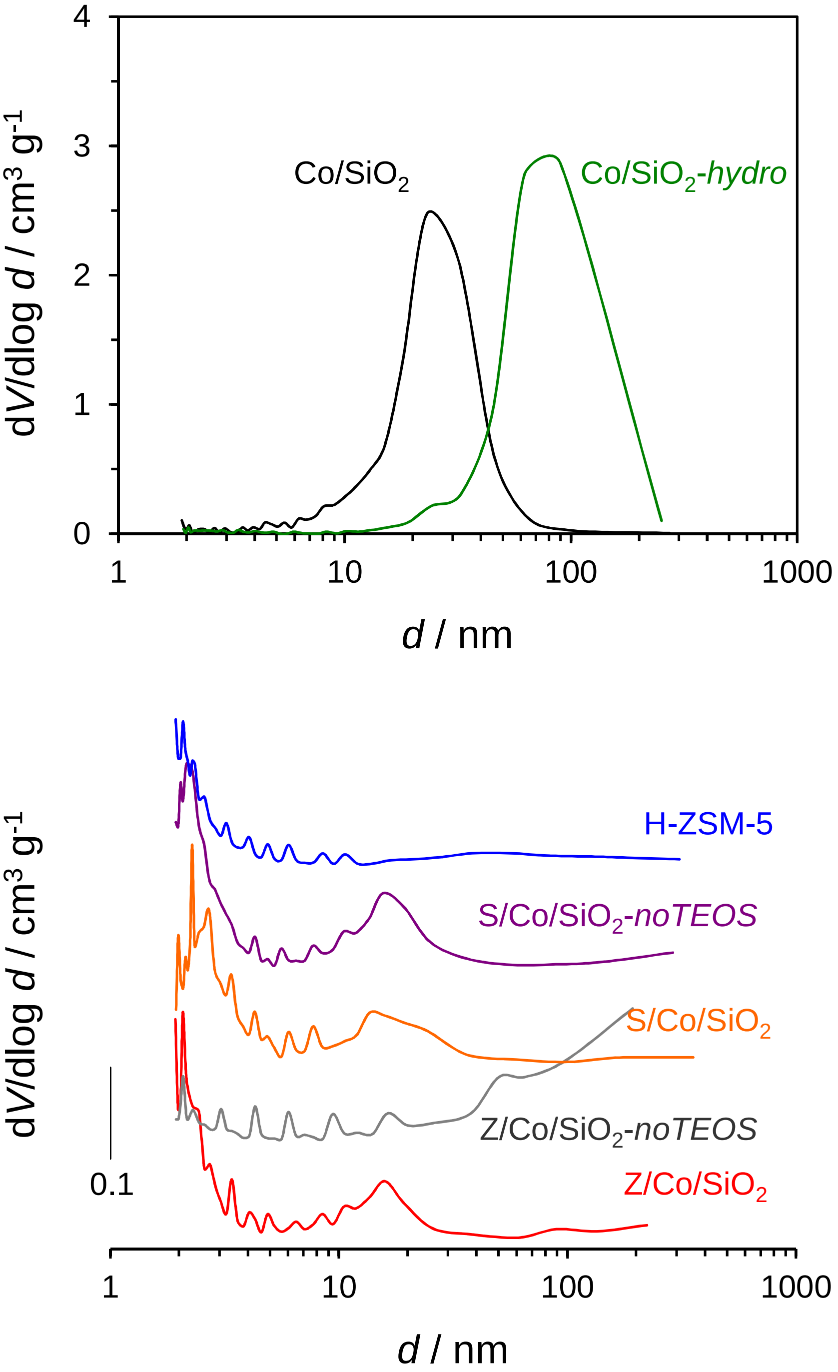

Figure B2. Pore size distribution of samples, derived from the adsorption branch of N_2 physisorption isotherms at 77 K, employing BJH method.

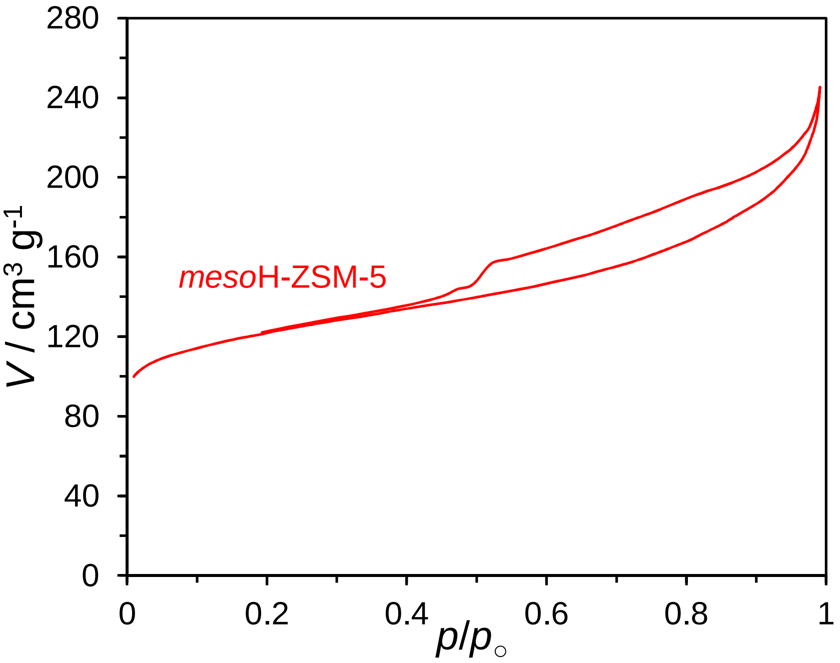

Figure B3. N_2 physisorption isotherm of *meso*H-ZSM-5 at 77 K.

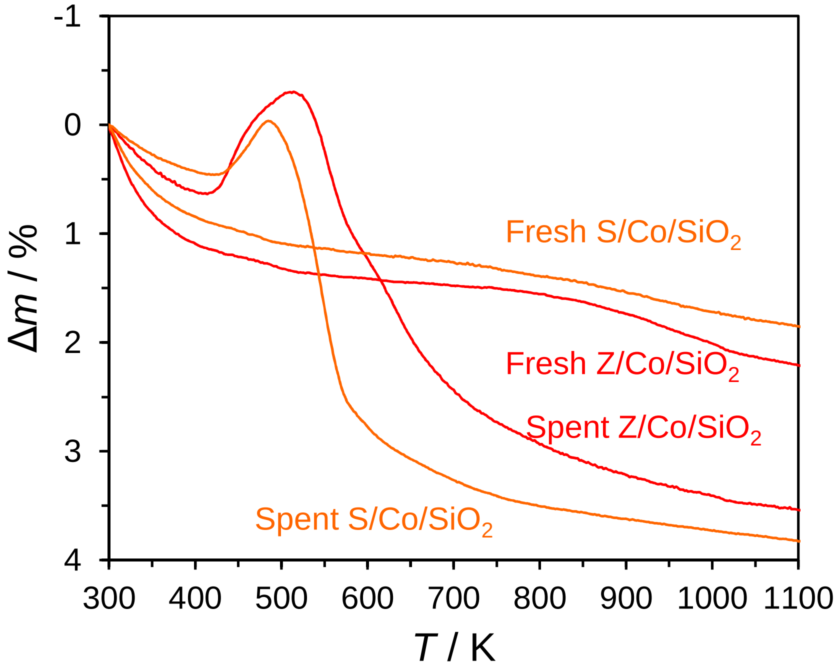

Figure B4. TGA analysis of fresh and spent catalysts after 29 h on-stream at 533 K, 10 bar total pressure, feed composition H_2/CO = 2 and $GHSV$ / m^3_{STP} kg^{-1}_{Co} h^{-1} = 25.8. During the TGA experiment, samples were heated under air flow with a heating rate of 5 K min^{-1}.

Appendix C

Breaking the Fischer-Tropsch synthesis selectivity: Direct conversion of syngas to gasoline-range hydrocarbons over hierarchical Co/H-ZSM-5 catalysts

Presentation of additional N_2 physisorption data, X-ray diffraction patterns, temperature-programmed NH_3 desorption profiles, transmission electron microscopy images, thermogravimetric analysis, and additional catalyst performance data, associated with Chapter 4.

Experimental

Characterization

N_2 physisorption experiments were performed in an Autosorb-6B unit (Quantachrome Instruments) at liquid nitrogen temperature (77 K). Prior to the experiment, all samples were degassed overnight in an Autosorb Degasser unit (Quantachrome Instruments) under vacuum at 623 K.

The X-ray diffraction (XRD) patterns were recorded in Bragg-Brentano geometry in a Bruker D8 Advance diffractometer equipped with a Vantec position sensitive detector and graphite monochromator. Measurements were performed at room temperature, using monochromatic Co Kα radiation (λ = 0.179026 nm) in the 2θ region between 10° and 100° with a step size of 0.035°. The samples were placed on a Si {510} substrate and rotated during measurements. All patterns were background-subtracted to eliminate the contribution of air scatter and possible fluorescence radiations.

Elemental analysis was done by inductively coupled plasma optical emission spectrometry (ICP-OES technique) with PerkinElmer Optima instruments. Transmission electron microscopy (TEM) with a field emission gun was done by a FEI Tecnai TF20 microscope operated at 200kV using a carbon coated Cu grid.

Temperature-programmed NH_3 desorption (NH_3-TPD) was measured by an AutoChem II Chemisorption Analyzer (Micromeritics). *Ca.* 0.2 g of the zeolite support was first degassed under He flow at 673 K for 1 h and then saturated with NH_3 at 473 K during 1 h, under 1.65% NH_3 in He flow. The gas mixture was then switched back to He and the sample was purged at 473 K for 1 h to remove the weakly adsorbed NH_3 molecules. TP desorption was recorded afterwards under He flow, from 473 to 873 K with a heating rate of 10 K min^{-1}. All the flow rates were adjusted to 25 cm^3_{STP} min^{-1}.

Thermogravimetric analysis (TGA) was performed on a Mettler Toledo TGA/SDTA851^e equipment, where 0.018–0.044 g of fresh and spent catalysts was screened for the change in its mass while heated from 298 to 1123 K with a heating rate of 5 K min^{-1} under 100 cm^3_{STP} min^{-1} of air flow.

Fischer-Tropsch synthesis

FTS experiments were performed on the six-flow fixed-bed microreactor setup described in Chapter 2. For all experiments, 0.5 g of fresh catalyst particles were fixed in the reactor inserts using quartz wool. Samples were first activated *in situ* by 80 cm^3_{STP} min^{-1} of H_2 at 673 K for 12 h at atmospheric pressure followed by cooling down to 453 K under H_2 flow. After increasing the pressure to the process value (15 bar total pressure), CO was gradually introduced to the feed stream at 453 K in order to reach its final concentration ($H_2/CO = 2$) in 1 h. Subsequently, the reactor was heated to the process temperature (493 K). A rate of 2 K min^{-1} was applied for all the heating/cooling steps.

During the experiment, heavy hydrocarbons (wax) were collected by gas/liquid separators at 448 K and reaction pressure. Lighter hydrocarbons and water were collected in cold traps at *ca.* 278 K and atmospheric pressure. After separation from water, these hydrocarbons as well as the wax were weighted, dissolved in CS_2, and analyzed offline by a simulated distillation (SimDis) GC (Hewlett Packard 5890, Series II) equipped with an FID and HP-1 column (7.5 m × 0.53 mm, Film Thickness 2.65 μm), using He as carrier gas. During the analysis, the oven temperature was ramped from 308 to 623 K (14 K min^{-1}) and kept at the final temperature for 5 min.

N_2, CO, and CO_2 as well as light hydrocarbons in the gas phase were analyzed online by a Compact GC (Interscience), equipped with three columns and detectors in parallel, applying He as carrier gas. In the first column (Carboxen 1010, 10 m × 0.32 mm) N_2, CO, CH_4, and CO_2 were separated at 333 K and analyzed by TCD. In the second column (Al_2O_3/KCl, 10 m × 0.32 mm) and FID detection, separation between all C1–C4 components was achieved at 434 K. In the third column (RTx-1 0.5μm, 15 m × 0.32 mm) C5–C10 hydrocarbons were separated at 353 K and analyzed by FID.

A pseudo-steady catalytic behavior was attained after 20 h on-stream when selectivity data were collected and the carbon balance was satisfied by 100 ± 5%. CO conversion, carbon selectivity and molar fraction of each product were defined by Eqs. (1), (2), and (3), respectively, where X_{CO} stands for CO conversion, F indicates the molar flow, S is the carbons selectivity of a product with n carbon number and y is its molar fraction.

$$X_{\mathrm{CO}} = \frac{F_{\mathrm{in,CO}} - F_{\mathrm{out,CO}}}{F_{\mathrm{in,CO}}} \times 100 \quad (1), \qquad S_{\mathrm{C}n} = \frac{nF_{\mathrm{C}n}}{F_{\mathrm{CO_2}} + \sum_{n=1}^{N} nF_{\mathrm{C}n}} \times 100 \quad (2), \qquad y_{\mathrm{C}n} = \frac{F_{\mathrm{C}n}}{\sum_{n=1}^{N} F_{\mathrm{C}n}} \quad (3)$$

Results

Table C1 Textural and chemical properties of the supports and catalysts.

Catalyst	S / m^2 g^{-1}		V / cm^3 g^{-1}			Co		Si/Al[f]
	total[a]	meso[b]	total[c]	micro[d]	meso[e]	wt%[f]	d_{Co}[g] / nm	
SiO_2	293	248	1.35	0.02	1.34	n.a.[h]	n.a.	n.a.
Co/SiO_2	223	200	1.03	0.01	1.03	9.7	14	n.a.
H-ZSM-5	460	52	0.26	0.18	0.08	n.a.	n.a.	41
Co/H-ZSM-5	388	38	0.22	0.16	0.06	9.6	13	40
*meso*H-ZSM-5*(a)*	580	309	1.20	0.12	1.08	n.a.	n.a.	16
Co/*meso*H-ZSM-5*(a)*	467	257	0.87	0.09	0.78	9.9	7	16
*meso*H-ZSM-5*(o)*	683	414	0.64	0.12	0.52	n.a.	n.a.	24
Co/*meso*H-ZSM-5*(o)*	574	344	0.53	0.10	0.43	9.0	10	22

[a] BET surface area; [b] Mesopore surface area obtained from the *t*-plot applied to the N_2 isotherm; [c] Total pore volume; [d] Micropore volume obtained from the *t*-plot; [e] Mesopore volume calculated as $V_{\mathrm{meso}} = V_{\mathrm{total}}$-$V_{\mathrm{micro}}$; [f] Obtained from ICP-OES; [g] Co crystallite size calculated from $d(\mathrm{Co}^0) = 0.75d(\mathrm{Co_3O_4})$, where $d(\mathrm{Co_3O_4})$ is derived from XRD, applying the Scherrer equation; [h] Not applicable.

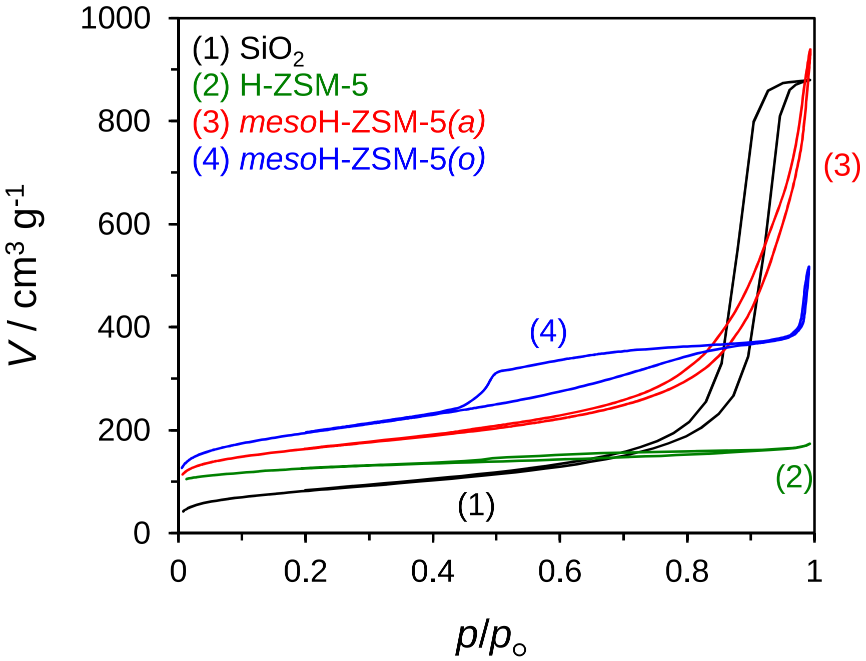

Figure C1. N_2 physisorption isotherms of supports at 77 K.

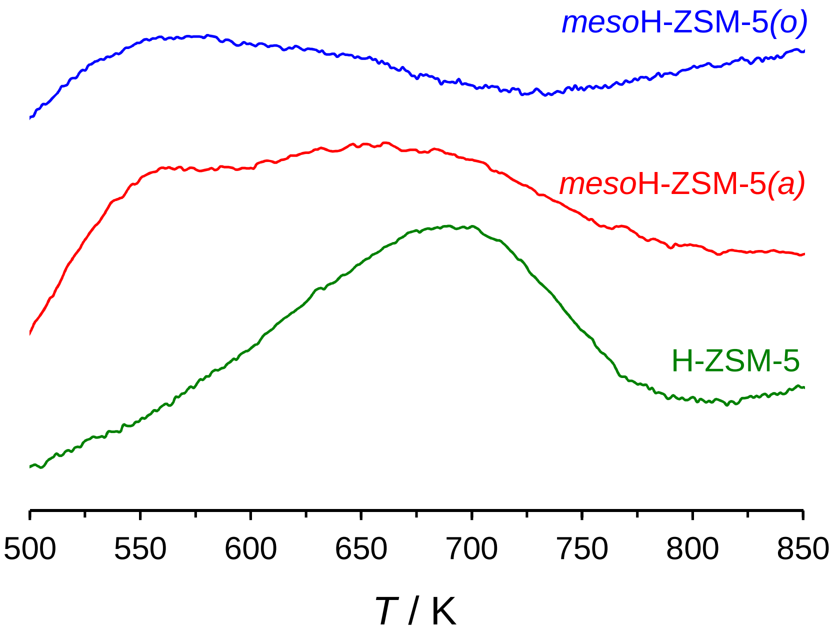

Figure C2. NH_3-TPD profiles (10 K min^{-1}) of zeolite supports.

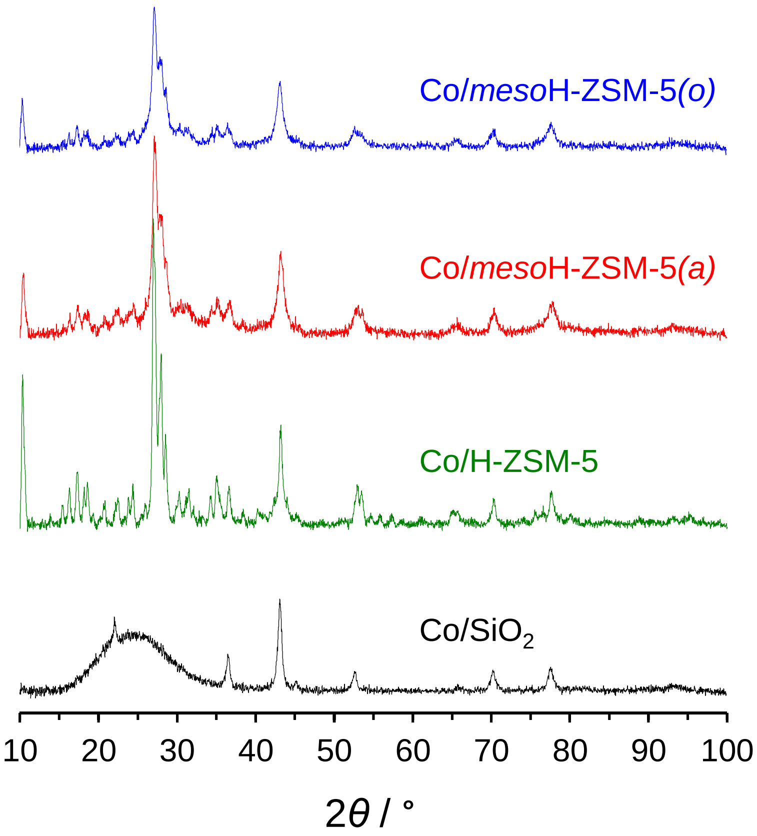

Figure C3. XRD patterns of the catalysts.

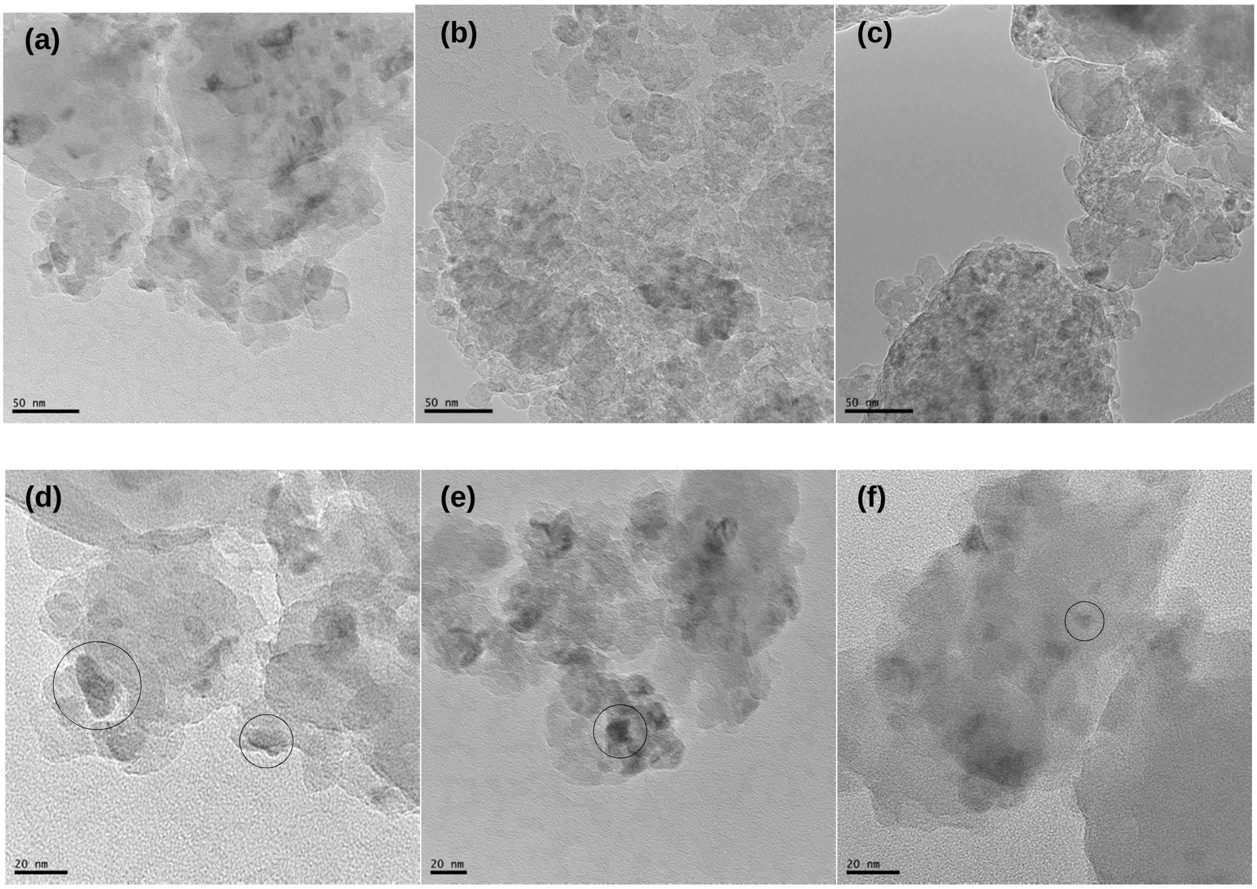

Figure C4. TEM images of the zeolite-supported Co-catalysts (before activation). In each row from left to right: Co/H-ZSM-5 (a and d), Co/*meso*H-ZSM-5*(a)* (b and e), and Co/*meso*H-ZSM-5*(o)* (c and f). Circles show Co oxide clusters/particles. Scale bars correspond to 50 nm for the top row and 20 nm for the bottom row images.

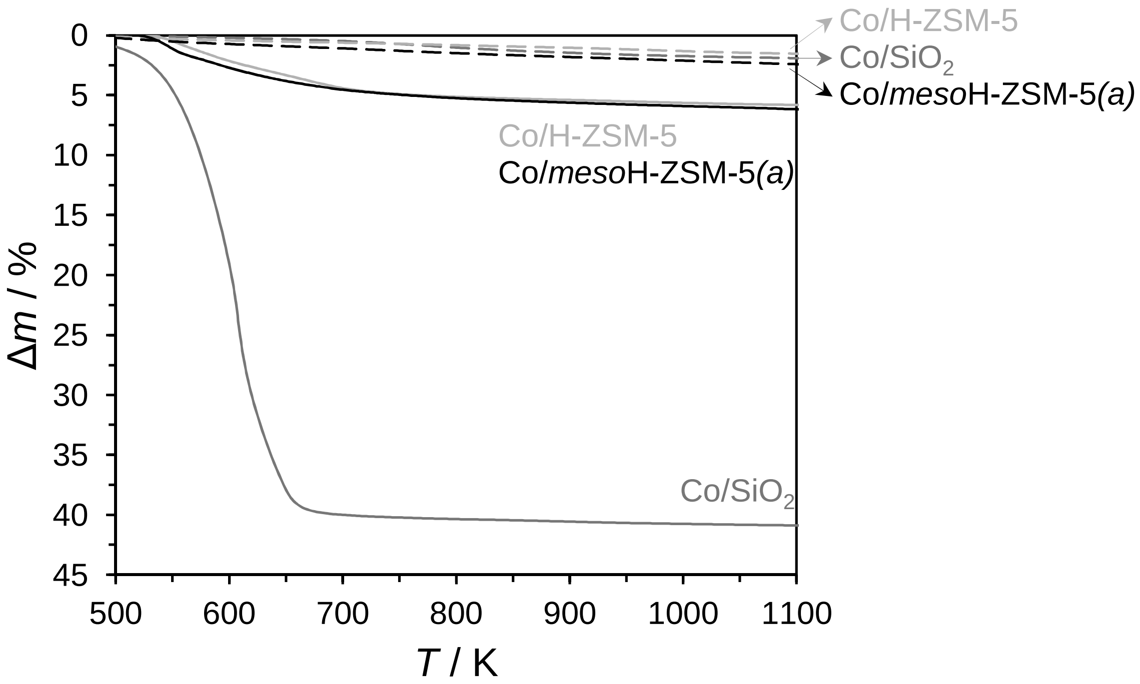

Figure C5. TGA analysis of fresh (dashed lines) and spent (solid lines) catalysts after 30 h FTS reaction at 513 K, 15 bar total pressure, feed composition $H_2/CO = 2$, and *GHSV* = 2.4 $m^3_{STP}\ kg^{-1}_{cat}\ h^{-1}$. During the TGA experiment, samples were heated under air flow with a heating rate of 5 K min^{-1}.

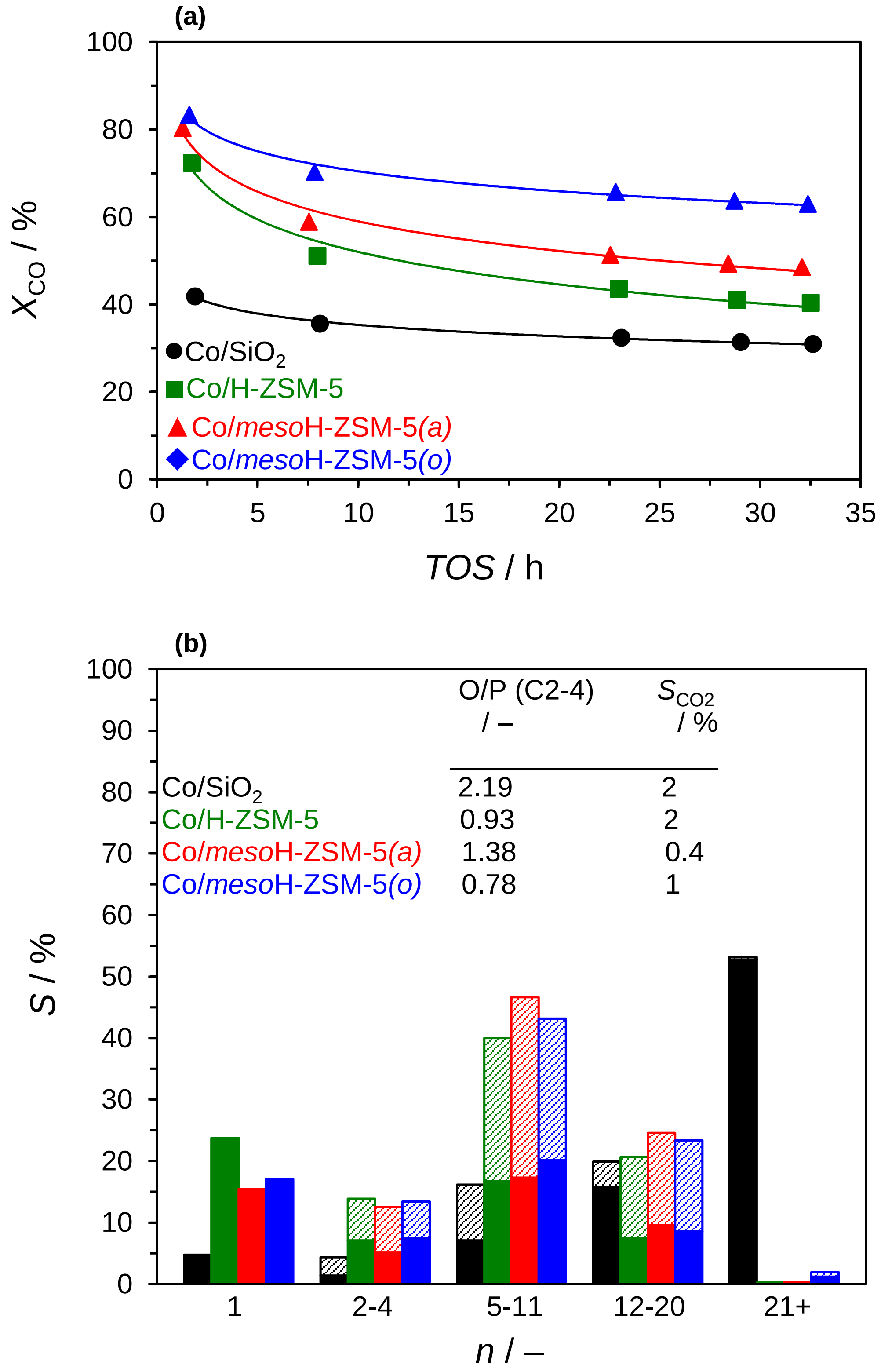

	O/P (C2-4) / –	S_{CO2} / %
Co/SiO$_2$	2.19	2
Co/H-ZSM-5	0.93	2
Co/*meso*H-ZSM-5*(a)*	1.38	0.4
Co/*meso*H-ZSM-5*(o)*	0.78	1

Figure C6. Time-on-stream (*TOS*) evolution of CO conversion during FTS (a). Carbon selectivity of FTS products after 20 h on-stream. In each carbon number group from left to right: Co/SiO$_2$, Co/H-ZSM-5, Co/*meso*H-ZSM-5*(a)*, and Co/*meso*H-ZSM-5*(o)*. ■: *n*-paraffins, ▨: Sum of isoparaffins and olefins, O/P (C2-4): olefin to *n*-paraffin ratio of C2–C4, S_{CO2}: CO$_2$ selectivity. Experiments were performed at 493 K, 15 bar total pressure, feed composition H$_2$/CO = 2, and *GHSV* = 2.4 m^3_{STP} kg^{-1}_{cat} h^{-1}.

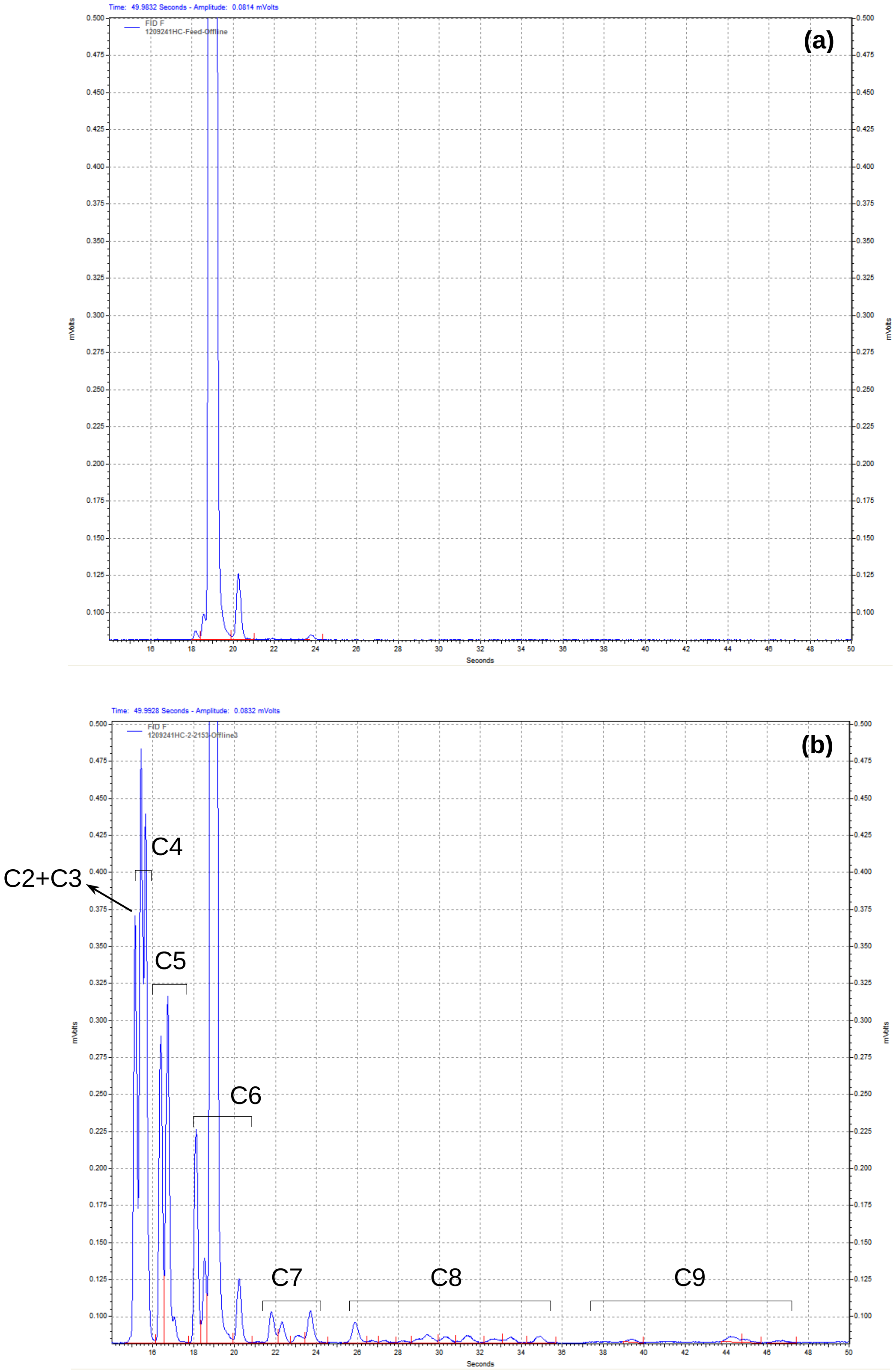

Figure C7. GC analysis chromatograms of the hydrocarbon feed (a) and products (b) obtained from the *n*-C6 hydroconversion experiments over *meso*H-ZSM-5*(a)* at 513 K, 15 bar total pressure, H_2/*n*-C6 = 9.0, N_2/H_2 = 2.0, and *SV* = 13 mol_{c6} kg^{-1}_{cat} h^{-1}. Analysis was performed offline, by Compact GC (Interscience) equipped with an RTx-1 column at 353 K (0.5µm, 15 m × 0.32 mm) and FID as a supplement to the online analysis (see Section 4.2.5/Chapter 4).

Appendix D

Modification of H-ZSM-5 crystallites for cobalt-based catalyst applications in Fischer-Tropsch synthesis

Presentation of scanning electron microscopy images, additional N_2 physisorption data, X-ray diffraction patterns, thermogravimetric analysis, additional temperature-programmed NH_3 desorption profiles, Fourier transform infrared (FT-IR) transmission spectroscopy spectra, energy dispersive X-ray spectroscopy, and dark-field transmission electron microscopy images, associated with Chapter 5.

Experimental

Characterization

Scanning electron microscopy (SEM) was performed on a Philips XL 20 microscope. Samples were coated with a layer of gold using an Edwards S150A sputter coater, to make them conductive prior to imaging.

N_2 physisorption was performed in an Autosorb-6B unit (Quantachrome Instruments) at liquid nitrogen temperature (77 K). Prior to the experiment, *ca.* 0.1 g of the samples was degassed overnight in an Autosorb Degasser unit (Quantachrome Instruments) under vacuum at 623 K (473 K in the case of Co/*meso*H-ZSM-5*(nnc)*).

The X-ray diffraction (XRD) patterns were recorded in Bragg-Brentano geometry in a Bruker D8 Advance diffractometer equipped with a Vantec position sensitive detector and graphite monochromator. Measurements were performed at room temperature, using monochromatic Co Kα radiation (λ = 0.179026 nm) in the 2θ region between 10° and 90°. The samples were placed on a Si {510} substrate and rotated during measurements. All patterns were background-subtracted to eliminate the contribution of air scatter and possible fluorescence radiation.

Thermogravimetric analysis (TGA) was performed on a Mettler Toledo TGA/SDTA851^e equipment, where 0.009–0.011 g of samples was screened for the change in its mass while heated from 298 to 1123 K under 100 cm^3_{STP} min^{-1} of air flow.

Temperature-programmed NH_3 desorption (NH_3-TPD) was measured by an AutoChem II chemisorption analyzer (Micromeritics). *Ca.* 0.2 g of the zeolite-containing samples was first degassed under He flow at 673 K for 1 h and then saturated with NH_3 at 373 or 473 K during 1 h, using a flow of 1.65% NH_3 in He. The gas mixture was then switched back to He, and the sample was purged at 373 or 473 K for *ca.* 1 h to remove the weakly adsorbed NH_3 molecules until no ammonia was detected. TP desorption was subsequently recorded under He flow, from 373 or 473 to 873 K. All flow rates were adjusted to 25 cm^3_{STP} min^{-1}, and the heating rates were 10 K min^{-1} during different stages of the experiment.

Transmission electron microscopy (TEM) was done by a FEI Tecnai TF20 microscope operated at 200 kV using a carbon coated Cu grid.

Fourier Transform Infrared (FT-IR) transmission spectroscopy

Surface hydroxyl groups of the zeolite samples were identified in a homemade setup consisting of a Nexus FT-IR (Thermo Nicolet) equipped with an extended KBr beam splitting and a mercury cadmium telluride (MCT) cryodetector. *Ca.* 0.01 g of the samples were pressed at 566 kg cm^{-2} for 1 min into thin self-supporting wafers. The wafers were fixed in a movable sample holder inside a chamber which was connected to an oven at the upper end and to an IR quartz cell, equipped with CaF_2 windows, at the bottom. This construction allowed IR measurements subsequently after vacuum and/or thermal treatments (inside the oven) without exposing the sample to air.

The wafers were first treated under vacuum at 673 K for 4 h to remove water and other adsorbed species. The FT-IR transmission spectra were recorded in the 399–4000 cm^{-1} range at 4 cm^{-1} resolution. Spectra of the empty cell under vacuum were collected as the background.

Results

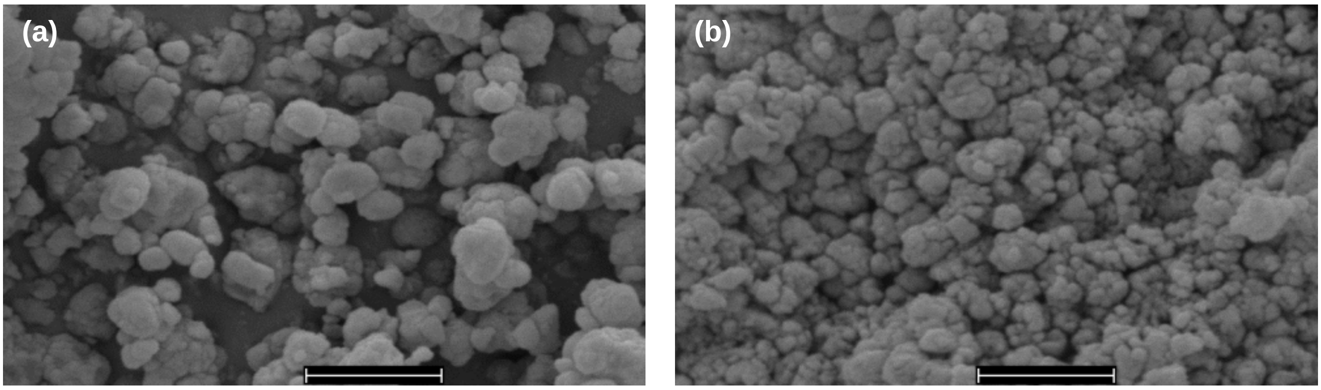

Figure D1. SEM micrographs of H-ZSM-5 (a) and *meso*H-SZM-5 (b). Scale bars correspond to 2 μm.

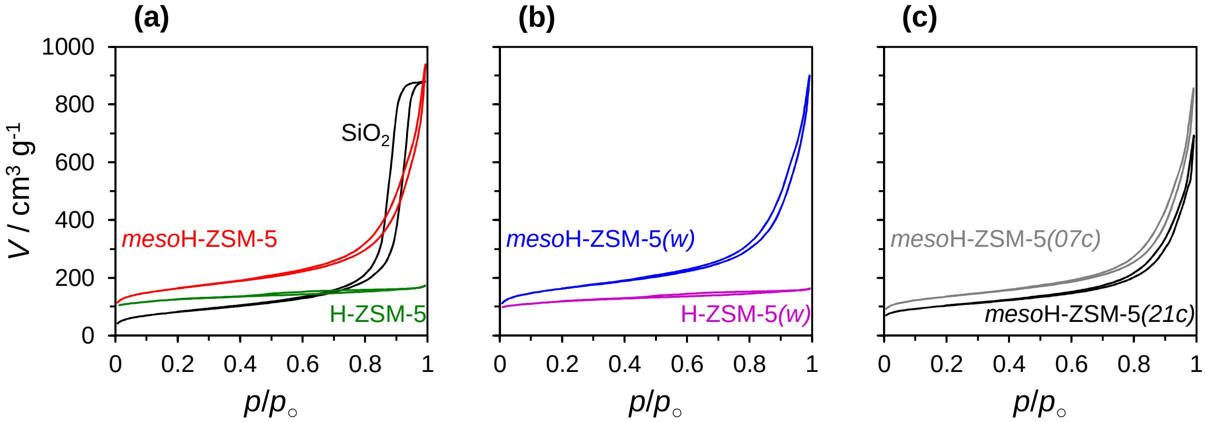

Figure D2. N_2 physisorption isotherms of SiO_2 and the zeolites (a), acid washed zeolites (b), and carbon deposited mesoporous zeolites (c) at 77 K.

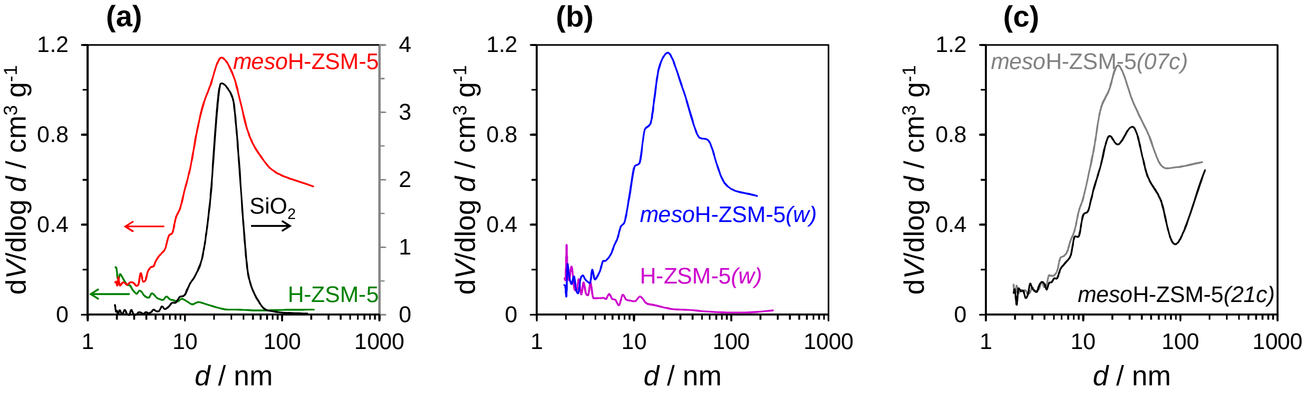

Figure D3. Pore size distribution of SiO_2 and the zeolites (a), acid washed zeolites (b), and carbon deposited mesoporous zeolites (c). The distribution was derived from the adsorption branch of N_2 physisorption isotherms at 77 K, employing the BJH method.

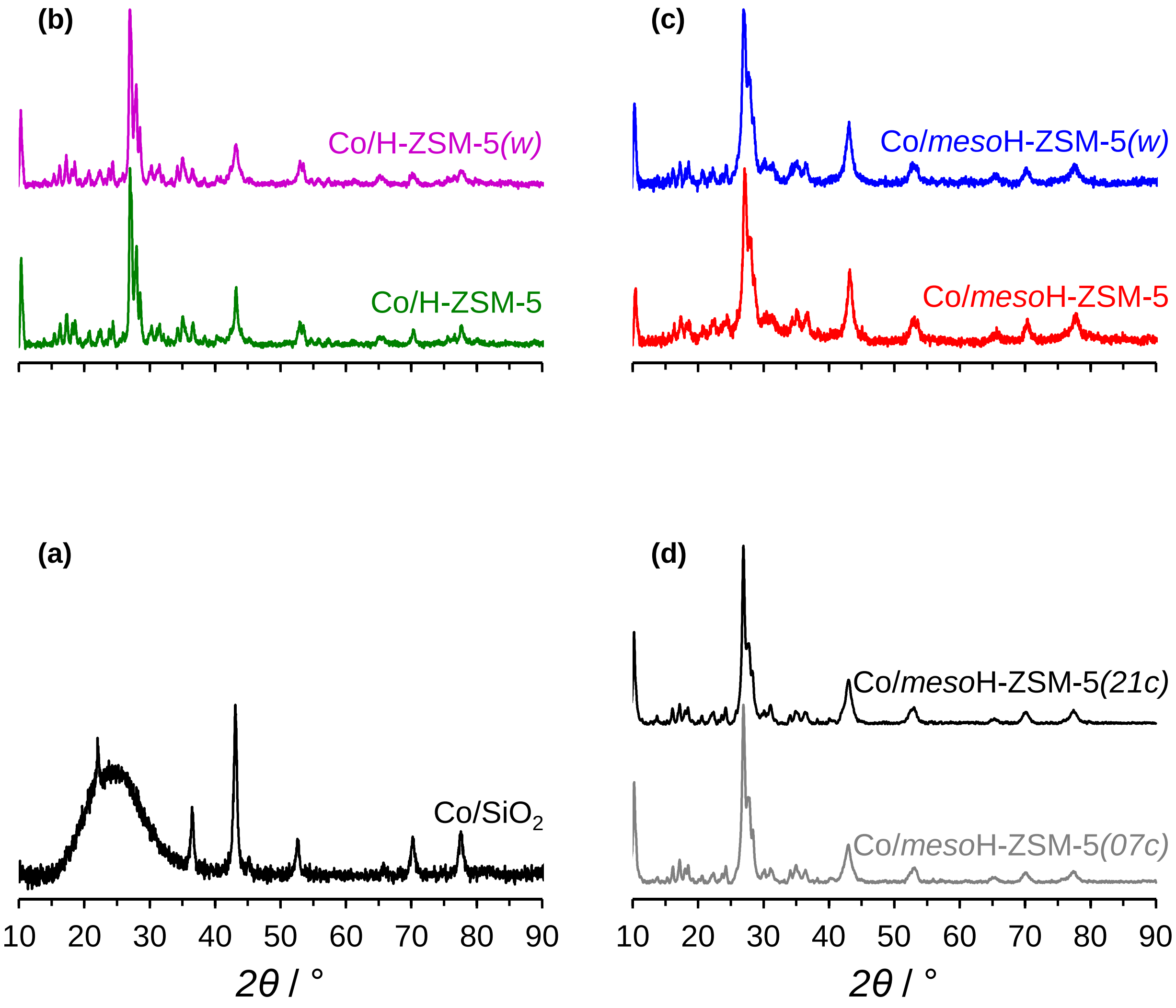

Figure D4. XRD patterns of Co-catalysts, supported on SiO_2 (a), microporous zeolites (b), mesoporous zeolites (c), and carbon deposited mesoporous zeolites (d).

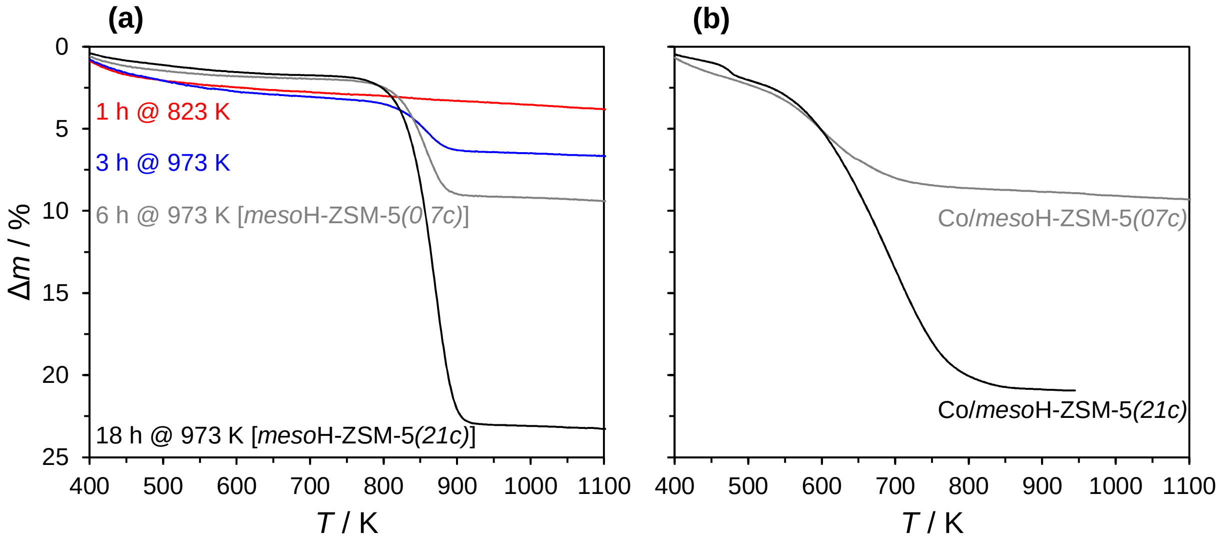

Figure D5. TGA patterns of *meso*H-ZSM-5 after carbon deposition at different conditions (a) and the prepared catalysts over two of the carbon deposited mesoporous zeolites (b). During the experiment, samples were heated under air flow with a heating rate of 5 K min^{-1} (a) or 1 K min^{-1} (b).

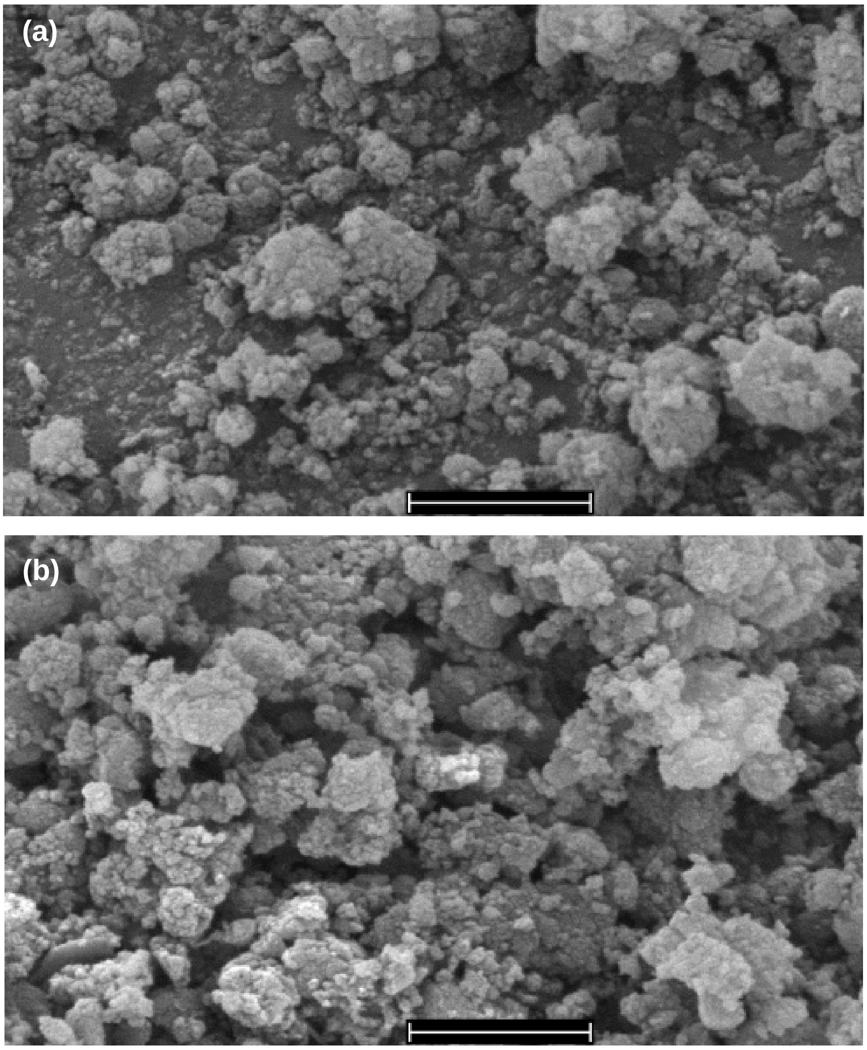

Figure D6. SEM micrographs of *meso*H-ZSM-5*(07c)* (a) and *meso*H-ZSM-5*(21c)* (b). Scale bars correspond to 2 μm.

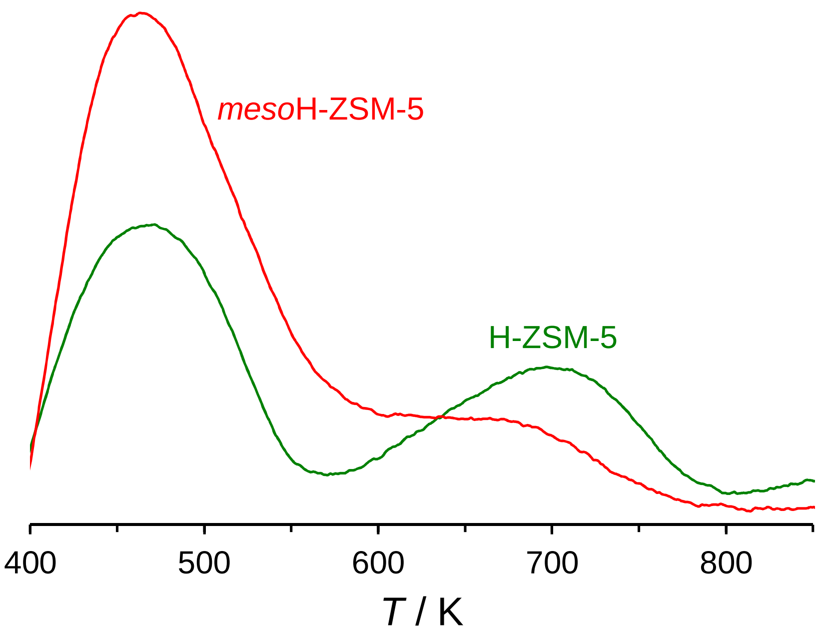

Figure D7. NH_3-TPD profiles (10 K min^{-1}) of H-ZSM-5 and *meso*H-ZSM-5. NH_3 was adsorbed at 373 K.

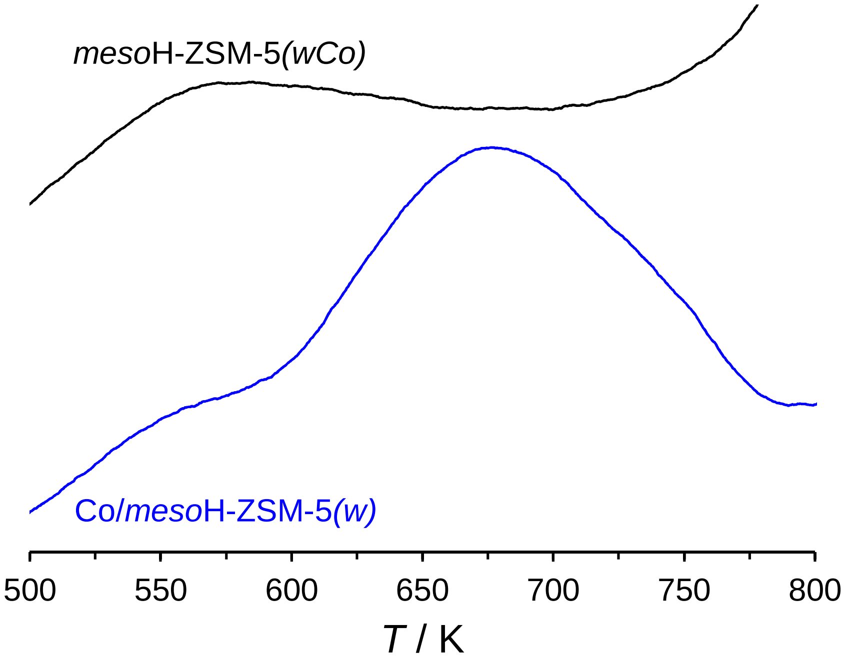

Figure D8. NH_3-TPD profiles (10 K min^{-1}) of Co/*meso*H-ZSM-5*(w)* and *meso*H-ZSM-5*(wCo)*. NH_3 was adsorbed at 473 K.

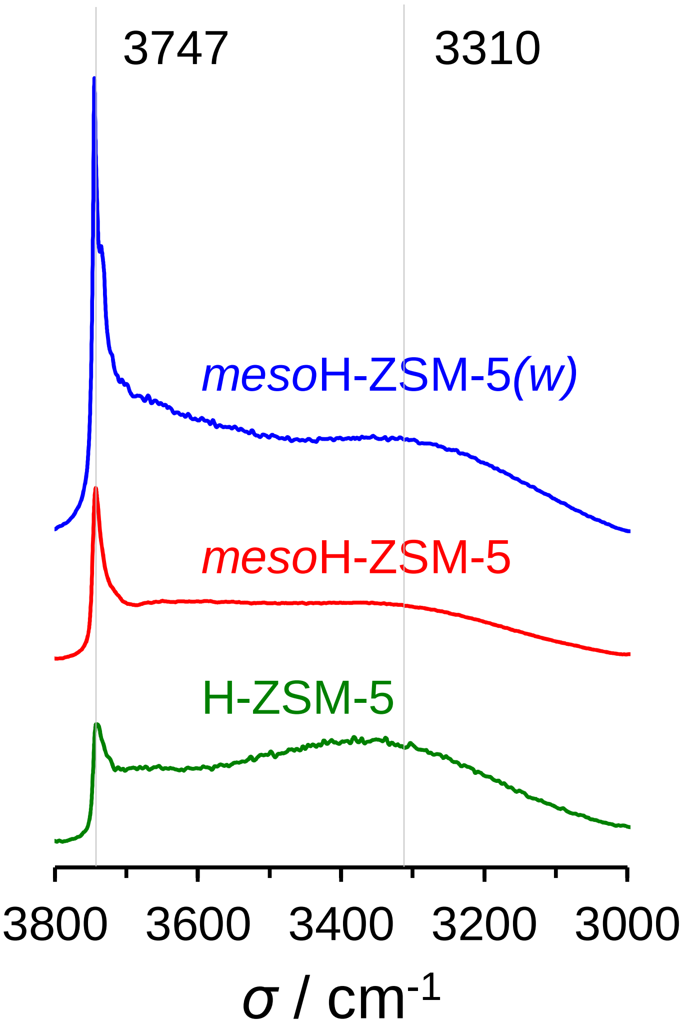

Figure D9. IR spectra of the zeolites in the OH-stretching region.

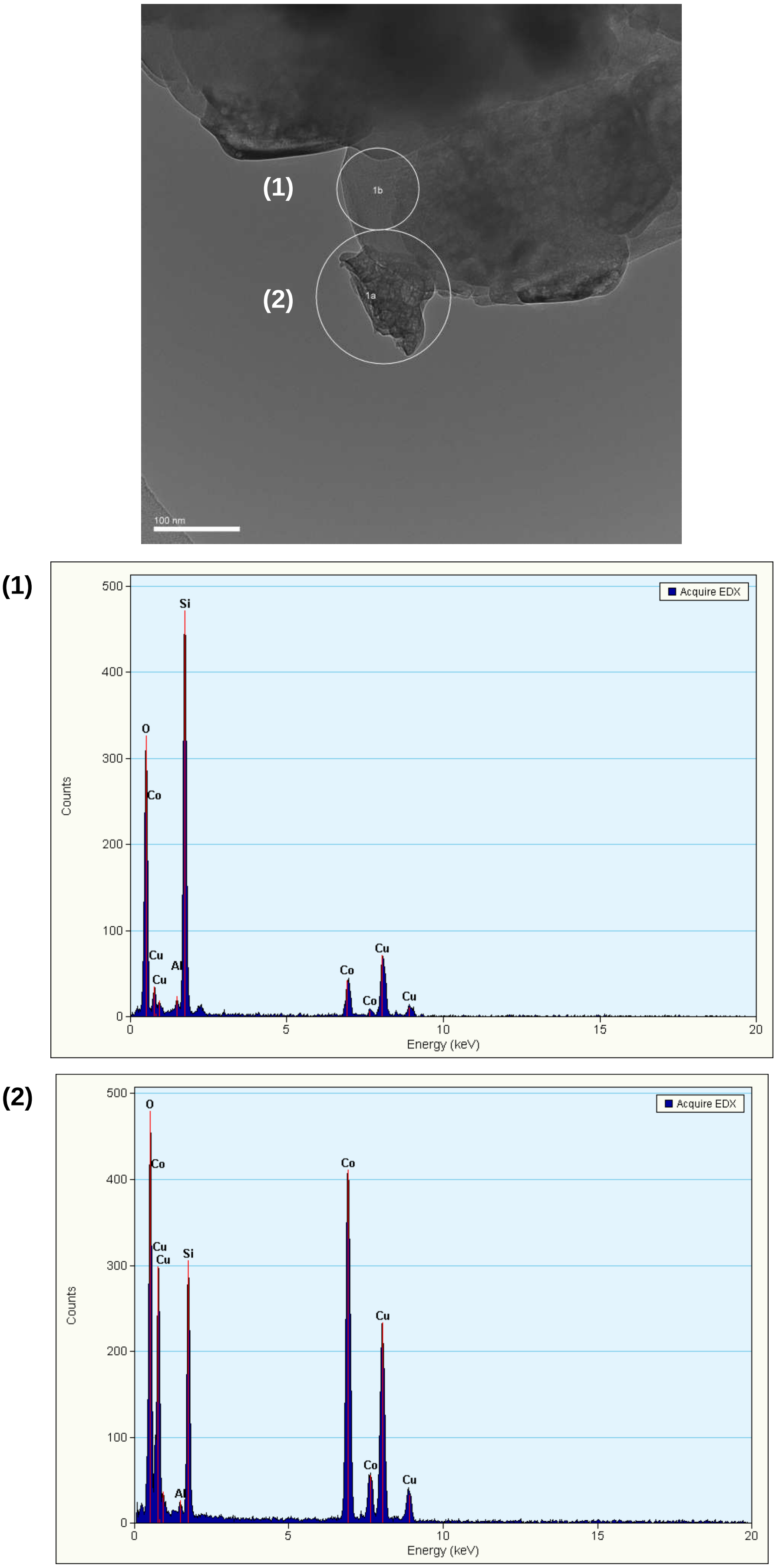

Figure D10. Energy dispersive X-ray spectroscopy (EDX) of Co/H-ZSM-5 (associated with Figure 3a/ Chapter 5)).

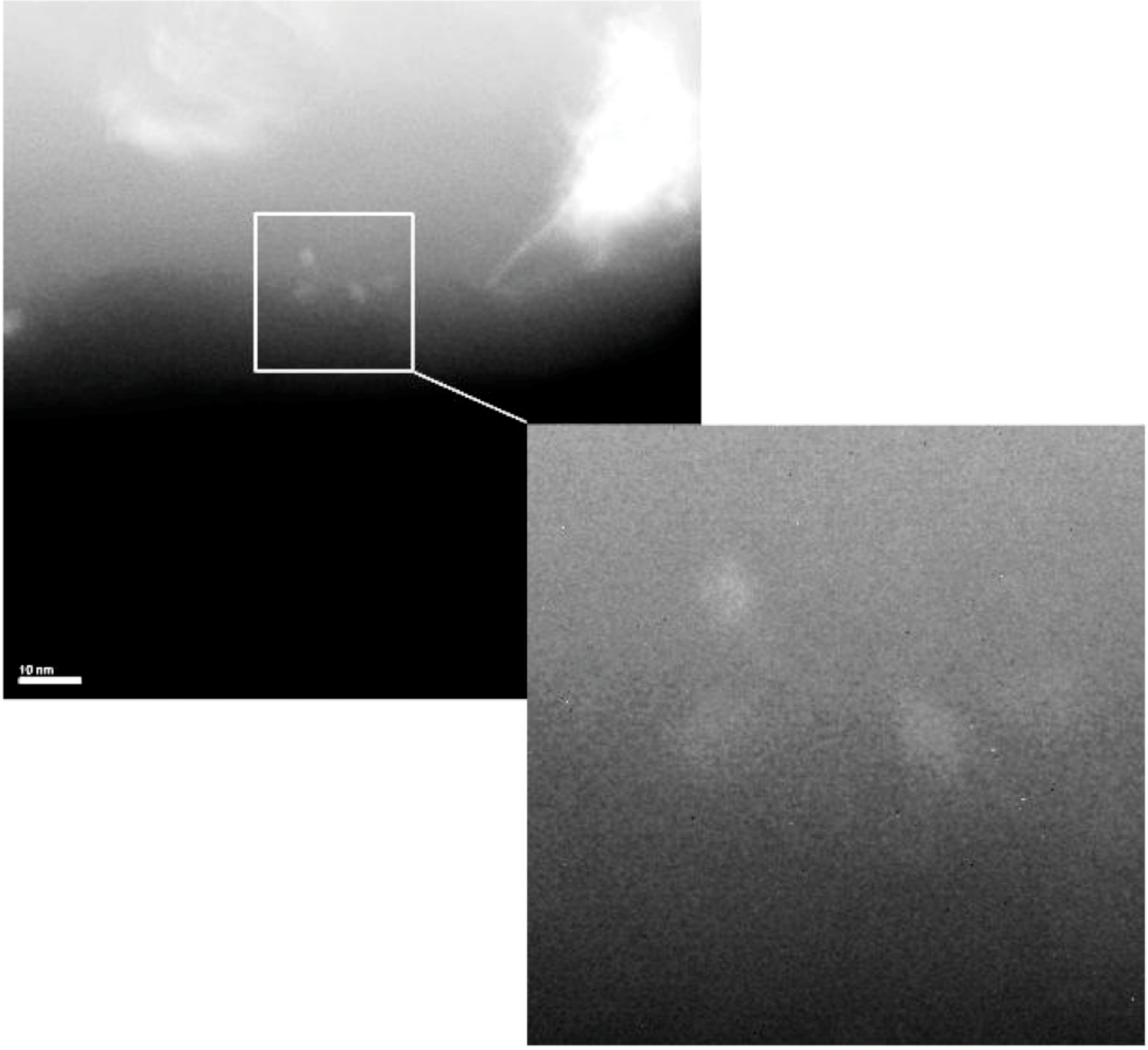

Figure D11. Dark-field TEM image of Co/H-ZSM-5 (associated with Figure 3c/Chapter 5). Scale bar corresponds to 10 nm. Square shows *ca.* 2 nm Co oxide particles.

Appendix E

Insights into the catalytic performance of mesoporous H-ZSM-5-supported cobalt in Fischer-Tropsch synthesis

Presentation of X-ray diffraction patterns and additional catalyst performance data, associated with Chapter 6.

Experimental

Materials

Amorphous SiO_2 (CARiACT Q-10) with surface area and pore volume of 293 m^2 g^{-1} and 1.35 cm^3 g^{-1}, respectively, was provided by Fuji Silysia Chemical Ltd. ZSM-5 zeolite in ammonium form with nominal Si/Al ratio of 40 was purchased from Zeolyst (CBV 8014) and calcined at 823 K for 5 h to obtain H-ZSM-5. 1 M tetrapropylammonium hydroxide (TPAOH), 70 wt% nitric acid (HNO_3), 1.5 wt% ruthenium(III) nitrosyl nitrate ($Ru(NO)(NO_3)_x(OH)_y$), 35 wt% zirconyl nitrate ($ZrO(NO_3)_2$) solutions, and Cobalt(II) nitrate hexahydrate ($Co(NO_3)_2$•$6H_2O$) salt were purchased from Sigma-Aldrich. All chemicals were used without any further purification steps.

Support preparation and catalyst synthesis

Mesoporous H-ZSM-5 was prepared by subsequent base and acid treatments. Desilication was carried out in 1 M TPAOH aqueous solution in a capped vessel ($\text{volume}_{\text{base solution}}/\text{weight}_{\text{zeolite}}$ = 8.0 cm^3 g^{-1}) and under stirring at 343 K for 1 h in an oil bath. This treatment was followed by immediate quenching in a water-ice bath and centrifugation to separate the zeolite powder from the solution. The residue of the desilicating agent was removed from the zeolite crystallites by subsequent redispersion in deionized water and centrifugation cycles until neutral pH was reached. The samples were then kept overnight at 333 K followed by drying at 393 K for 12 h and calcination at 823 K for 5 h. Subsequent to the heat treatments, mesoporous H-ZSM-5 was acid treated in 1 M HNO_3 aqueous solution ($\text{volume}_{\text{acid solution}}/\text{weight}_{\text{zeolite}}$ = 28.6 cm^3 g^{-1}) at 343 K for 2 h under stirring in an oil bath. After quenching, samples were thoroughly washed with deionized water, dried, and calcined the same as after the above-mentioned desilication procedure. The mesoporous H-ZSM-5 before acid-treatment is denoted as '*meso*H-ZSM-5*(o)*' and the acid-washed zeolite is denoted as '*meso*H-ZSM-5'.

FTS catalysts were prepared by incipient wetness impregnation. All the supports were dried overnight at 393 K before impregnation. A fraction of *meso*H-ZSM-5 was loaded with *ca.* 5 wt% Zr using a $ZrO(NO_3)_2$ solution. This sample was then kept overnight in a desiccator at room temperature, dried at 393 K for 12 h, and calcined at 823 K for 5 h ('ZrO_2/*meso*H-ZSM-5'). Amorphous SiO_2, *meso*H-ZSM-5*(o)*, *meso*H-ZSM-5, and ZrO_2/*meso*H-ZSM-5 were used as carriers and loaded with *ca.* 20 wt% (or 10 wt% in one case) of Co, employing aqueous $Co(NO_3)_2$•$6H_2O$ solutions as precursors. To include Ru in the catalyst composition, ruthenium nitrosyl nitrate was added to the precursor solution and co-impregnated with Co to obtain a Ru loading of 0.3 wt%. After impregnation, samples were dried in desiccator and 393 K as explained above. Subsequently, the catalysts were calcined at 673 K for 2h. A heating rate of 2 K min^{-1} and static air conditions were applied for all the above-mentioned drying and calcination steps.

Characterization

The XRD patterns were recorded in Bragg-Brentano geometry in a Bruker D8 Advance diffractometer equipped with a LynxEye position sensitive detector. Measurements were performed at room temperature, using monochromatic Co Kα (λ = 1.788970 Å) radiation in the 2θ range from 5° to 90°. All patterns were background-subtracted to eliminate the contribution of air scatter and possible fluorescence radiation.

Catalyst performance experiments (Fischer–Tropsch synthesis)

Fischer-Tropsch synthesis (FTS) experiments were performed on the six-flow fixed-bed microreactor setup described in Chapter 2. For all experiments, 0.250 g of fresh catalyst (100–212 μm) was diluted with SiC of similar size to attain a constant bed volume of ca. 1.3 cm^3. Catalysts were activated *in situ* prior to FTS reaction by H_2, at 773 K for 13 h at atmospheric pressure followed by cooling to 453 K under H_2 flow. After increasing the pressure to the process value (15 bar total pressure), CO was gradually introduced to the feed stream at 453 K in order to reach its final concentration (H_2/CO = 1 or 2) in 1 h. Subsequently, the reactor was heated to the process temperature (513 K). A rate of 2 K min^{-1} was applied for all the heating/cooling steps.

During FTS experiments, heavy hydrocarbons (wax) were collected by gas/liquid separators at 448 K and reaction pressure. After expansion of the product flow to atmospheric pressure by back pressure controllers, lighter hydrocarbons and water were collected in cold traps at *ca.* 278 K. After separation from water, these liquid hydrocarbons as well as the wax were weighted, dissolved in CS_2, and analyzed offline by a simulated distillation (SimDis) GC (Hewlett Packard 5890, Series II) equipped with an FID and HP-1 column (7.5 m × 0.53 mm, film thickness 2.65 μm), using He as carrier gas. During the analysis, the oven temperature was ramped from 308 to 623 K (14 K min^{-1}) and kept at the final temperature for 5 min. N_2, CO, and CO_2 as well as light hydrocarbons in the gas phase were analyzed online by a Compact GC (Interscience), equipped with three columns and detectors in parallel, applying He as carrier gas. In the first column (Carboxen 1010, 10 m × 0.32 mm), N_2, CO, CH_4, and CO_2 were separated at 333 K and analyzed by TCD. In the second column (Al_2O_3/KCl, 10 m × 0.32 mm) and FID detection, separation between all C1–C4 components was achieved at 434 K. In the third column (RTx-1 0.5μm, 15 m × 0.32 mm), C5–C10 hydrocarbons were separated at 353 K and analyzed by FID.

Results

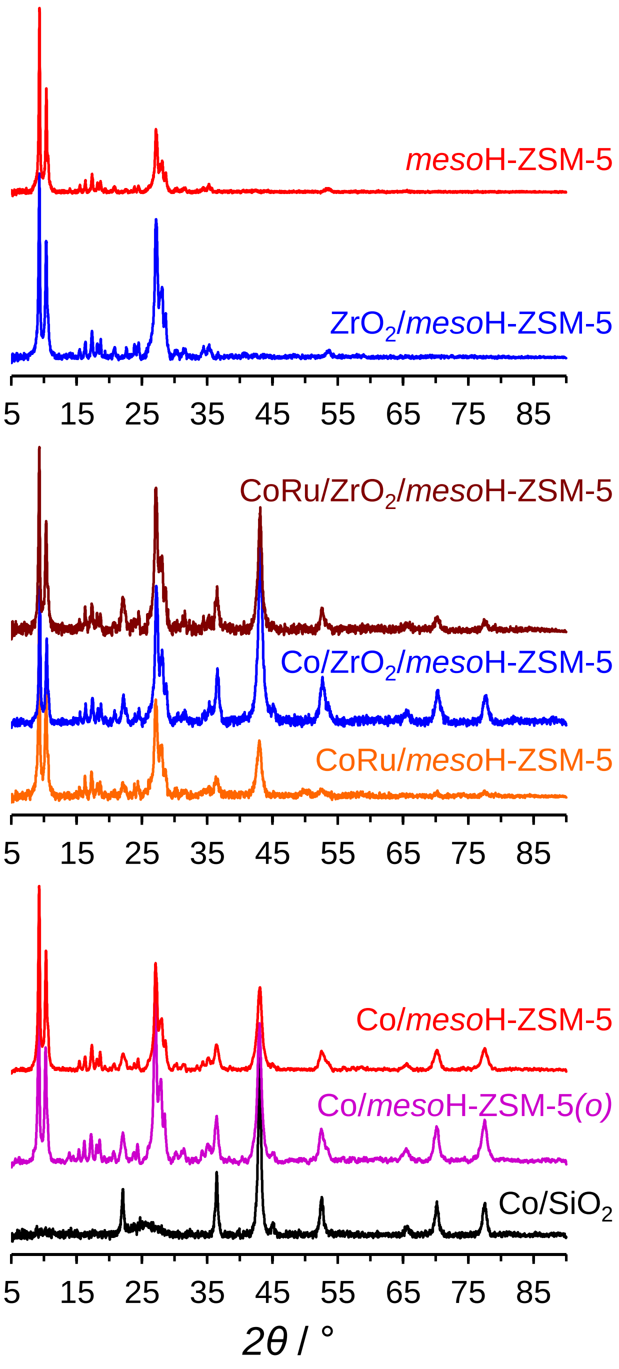

Figure E1. XRD patterns of the fresh FTS catalysts and supports.

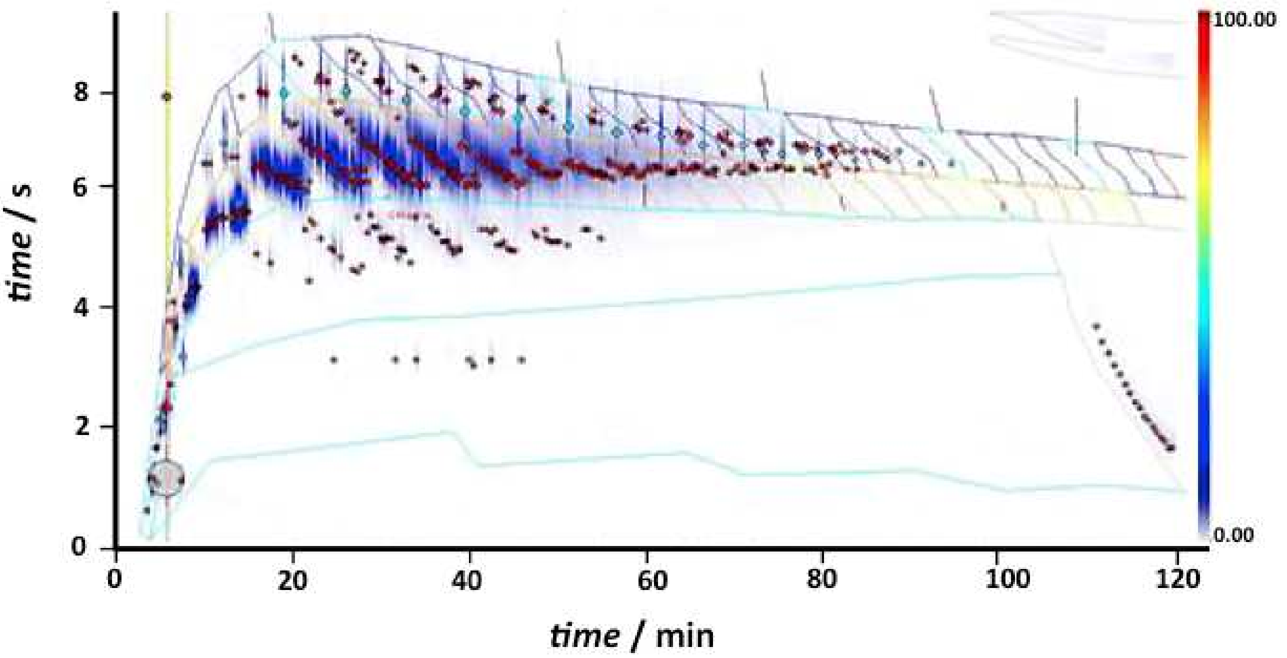

Figure E2. 2D chromatogram of liquid hydrocarbons, produced over Co/*meso*H-ZSM-5 (associated with Figure 9/Chapter 6). Liquid products were collected after 140 on-stream at 513 K, 15 bar total pressure, feed composition $H_2/CO = 1$, and *GHSV* = 12 m^3_{STP} kg^{-1}_{cat} h^{-1}.

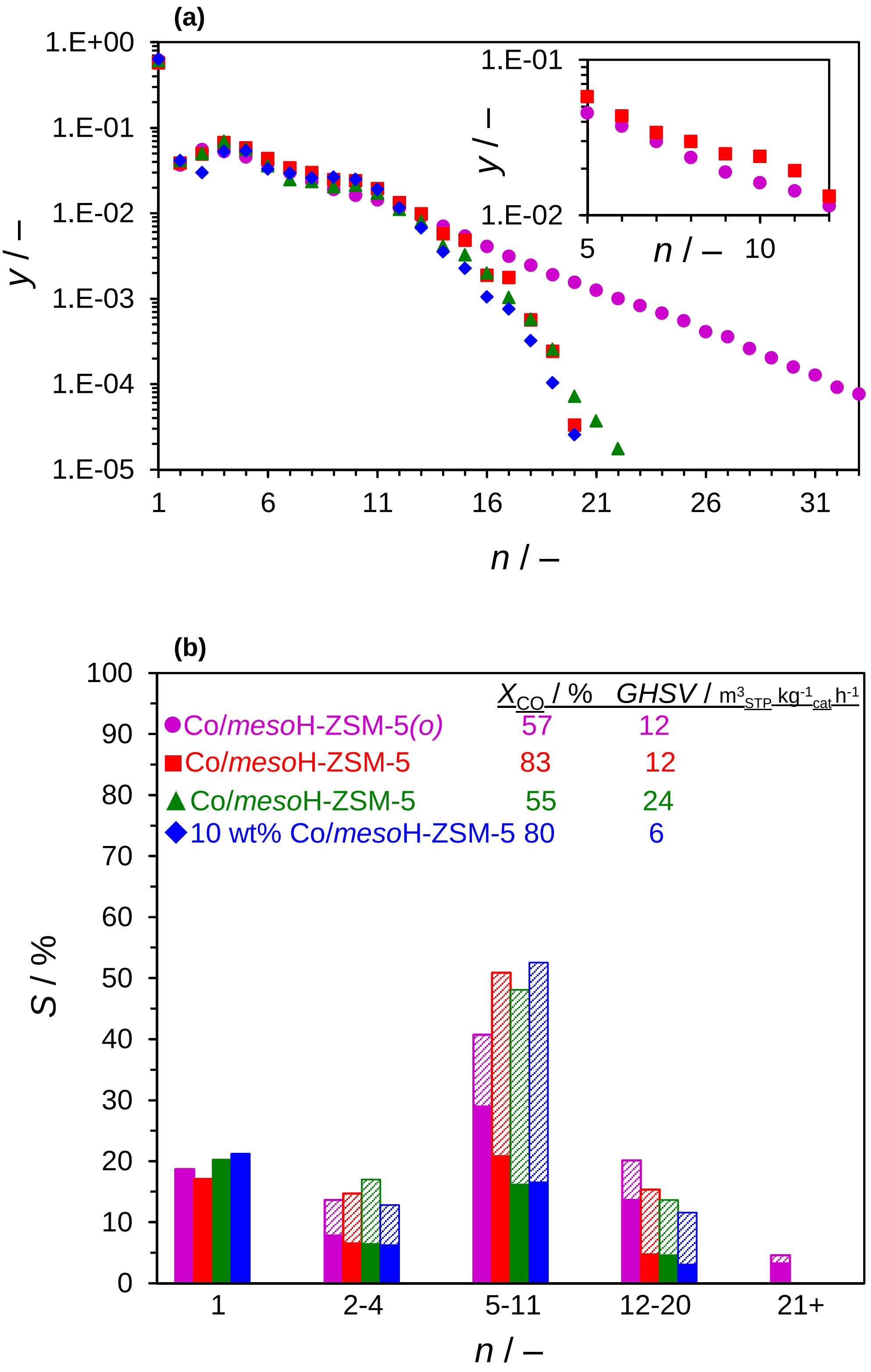

Figure E3. Fractional molar composition of FTS product mixtures (a) and carbon selectivity of FTS products (b) after 25 h on-stream at 513 K, 15 bar total pressure, and feed composition H_2/CO = 2. In each carbon number group from left to right: Co/*meso*H-ZSM-5*(o)*, Co/*meso*H-ZSM-5, Co/*meso*H-ZSM-5, and 10 wt% Co/*meso*H-ZSM-5. ■: *n*-paraffins; ▨: sum of isoparaffins and olefins. Co loadings are 20 wt%, unless indicated otherwise.

Appendix F

Effect of zeolite structure in hierarchical zeolite-supported cobalt-catalysts for the direct conversion of biosyngas into liquid fuels

Presentation of additional N_2 physisorption data, elemental analysis, X-ray diffraction patterns, and temperature-programmed reduction by H_2 profiles, associated with Chapter 7.

Experimental

Characterization

N_2 physisorption was performed in an Autosorb-6B unit (Quantachrome Instruments) at liquid nitrogen temperature (77 K). Prior to the experiment, *ca.* 0.1 g of the samples were degassed overnight in an Autosorb Degasser unit (Quantachrome Instruments) under vacuum at 623 K.

Elemental analysis was performed with PerkinElmer Optima instruments. After sample dilution, analysis was done by inductively coupled plasma optical emission spectrometry (ICP-OES).

The X-ray diffraction (XRD) patterns were recorded in a Bruker D8 Advance diffractometer equipped with a Vantec position sensitive detector. Measurements were performed at room temperature, using monochromatic Co Kα radiation in the 2θ range from 5° to 90°. The samples were placed on a Si substrate and rotated during measurements. All patterns were background-subtracted to eliminate the contribution of air scatter and possible fluorescence radiation.

Temperature-programmed reduction by H_2 (TPR(H_2)) was performed on a homemade equipment. *Ca.* 0.1 g of Co containing samples were mounted in a temperature controlled reactor where 27 cm^3_{STP} min^{-1} flow of 7.4% H_2 in Ar was fed over the samples. The reactor temperature was then ramped from room temperature to 1173 K with a heating rate of 5 K min^{-1} and the H_2 consumption was monitored by a TCD. Water was removed by a Permapure membrane dryer. Calibration was performed with CuO.

Results

Table F1 Textural and chemical properties of the supports and catalysts.

Support/Catalyst	S / m^2 g^{-1}		V / cm^3 g^{-1}			Co	
	total[a]	meso[b]	total[c]	micro[d]	meso[e]	wt%[f]	d_{Co}[g] / nm
SiO_2	293	248	1.35	0.02	1.34	n.a.[h]	n.a.
Co/SiO_2	199	180	0.89	0.01	0.88	18.6	16
H-ZSM-5	460	52	0.26	0.18	0.08	n.a.	n.a.
*meso*H-ZSM-5	691	470	0.67	0.09	0.58	n.a.	n.a.
Co/*meso*H-ZSM-5	509	311	0.50	0.08	0.41	23.8	10
H-ITQ-2	822	604	0.93	0.10	0.84	n.a.	n.a.
Co/H-ITQ-2	518	364	0.53	0.07	0.46	16.2	14
H-USY	882	91	0.51	0.34	0.18	n.a.	n.a.
*meso*H-USY	757	324	0.63	0.18	0.44	n.a.	n.a.
Co/*meso*H-USY	569	222	0.44	0.15	0.30	18.4	13

[a] BET surface area; [b] Mesopore surface area obtained from the *t*-plot applied to the N_2 isotherm; [c] Total pore volume; [d] Micropore volume obtained from the *t*-plot applied to the N_2 isotherm; [e] Mesopore volume calculated as $V_{meso} = V_{total} - V_{micro}$; [f] Obtained from ICP-OES; [g] Co crystallite size calculated from $d(Co^0) = 0.75d(Co_3O_4)$, where $d(Co_3O_4)$ is derived from XRD, applying the Scherrer equation; [h] Not applicable.

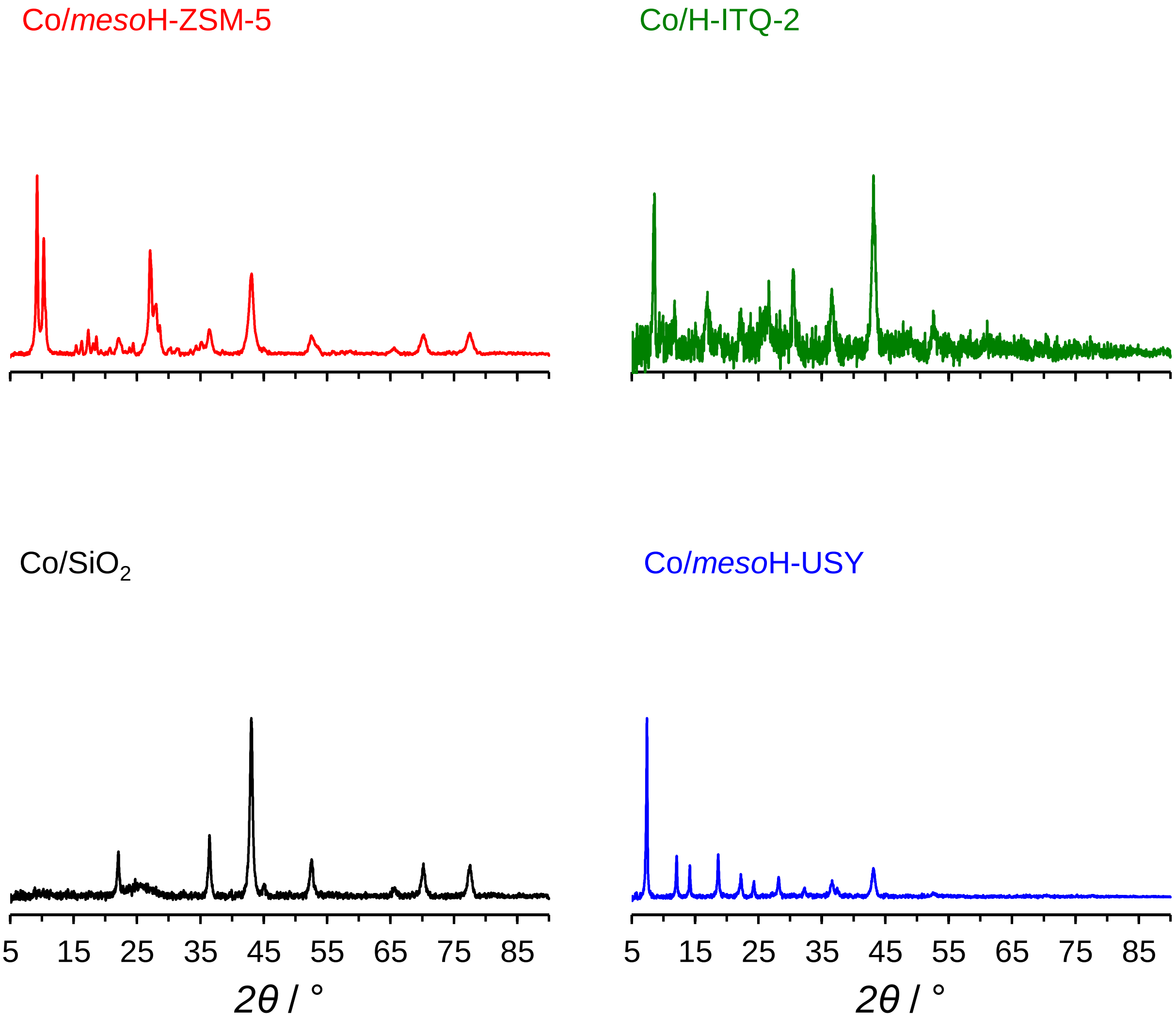

Figure F1. XRD patterns of Co-catalysts.

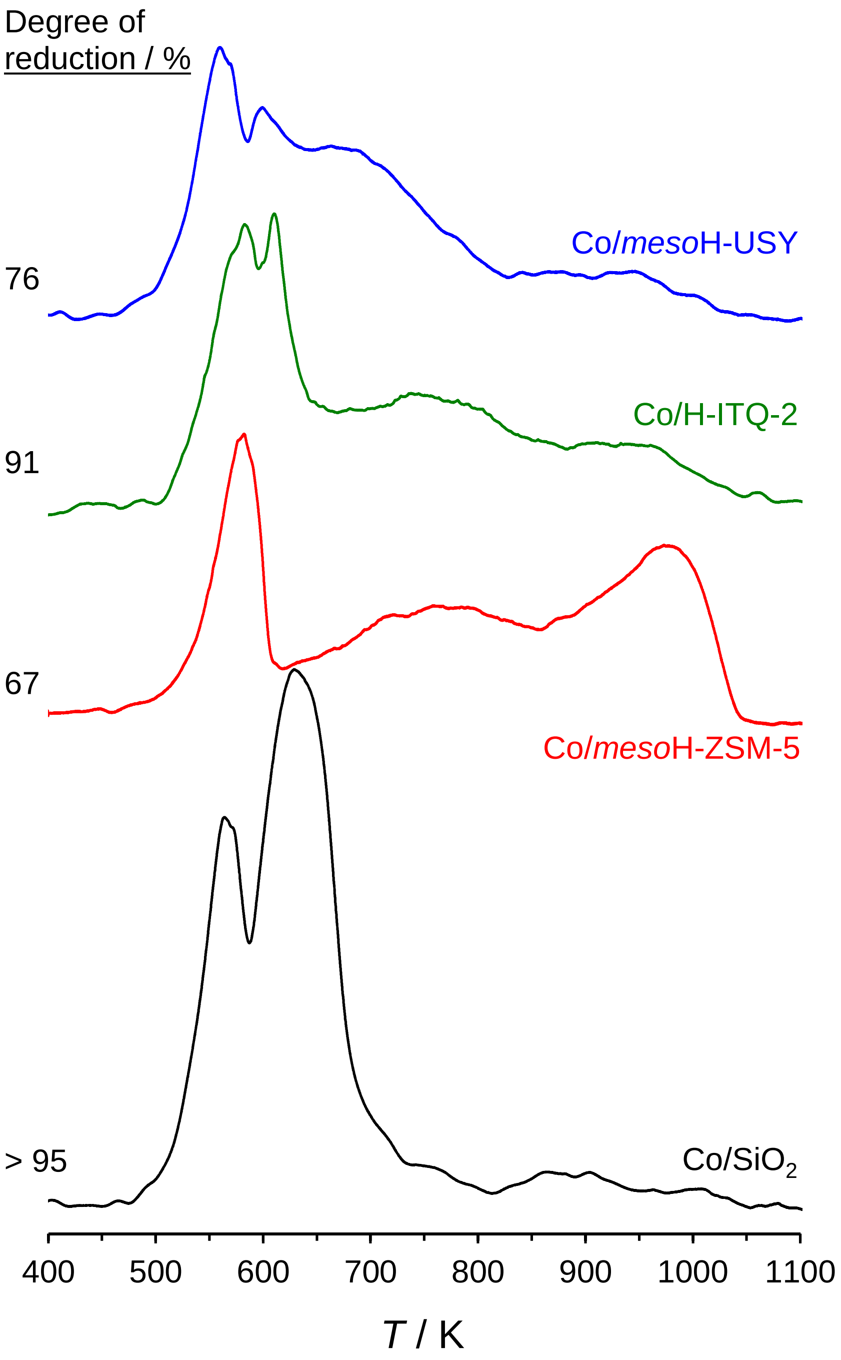

Figure F2. TPR(H_2) profiles (5 K min^{-1}) of Co-catalysts. Indicated numbers are the degree of reduction, associated with each profile, assuming H_2 consumption for reduction of Co_2O_3 to Co.

Samenvatting

Het ontwerp en de ontwikkeling van katalysatorformuleringen voor de maximalisering van de directe productie van vloeibare brandstoffen door het combineren van Fischer-Tropsch synthese (FTS) en het kraken en isomeriseren van koolwaterstoffen in één katalysator deeltje (bifunctionele FTS katalysator) is onderzocht in deze thesis.

Om dit doel te bereiken, moest naast de FTS functionaliteit een tweede functionaliteit worden toegevoegd aan de katalysator formulering, om zo de limitatie van de klassieke Anderson-Schulz-Flory (ASF) verdeling van FTS producten te doorbreken. Omdat het omzetten van de FTS koolwaterstoffen voornamelijk is gebaseerd op zuur-gekatalyseerde reacties, zijn zeolieten potentiële kandidaten voor deze aanpak. In dit verband benadrukt recente literatuur het gebruik van H-ZSM-5 om de volgende redenen: (1) het is een van de weinige zeolieten die op industriële schaal wordt geproduceerd en toegepast wordt voor zuur-gekatalyseerde koolwaterstof conversie reacties; (2) door zijn smalle kanaal-type structuur en goed verdeelde zure actieve plaatsen, bezit het een relatieve stabiele katalytische werking, in het bijzonder onder de lage temperatuur Fischer-Tropsch procescondities; en (3) naast het zuur-gekatalyseerd kraken, heeft het een redelijke isomerisatie en oligomerisatie activiteit op lage temperaturen, wat essentieel is om het octaangetal te verhogen in het geval van de benzine fractie en de koude stromingseigenschappen te verbeteren voor diesel (Hoofdstuk 1).

Alle FTS experimenten beschrieven in dit proefschrift zijn uitgevoerd op apparatuur die ontworpen en gebouwd is op de TU Delften is beschreven in hoofdstuk 2. De experimentele opbouw is gebaseerd op een “six-flow microreactor” concept, zes parallelle gepakt bed microreactoren, dat zowel een verhoogde experimentele doorzet als precisie biedt. Laatstgenoemde is toe te schrijven aan de gelijke operationele condities (in termen van procestemperatuur, aanvoersamenstelling, apparatuursomstandigheden, etc.) waaronder de zes parallelle katalysatoren worden getest. De voorwaarde is dat alle reactoren (stromen) zich hetzelfde zouden moeten gedragen, m.a.w. dat ze gelijke resultaten leveren tijdens het gebruik van dezelfde katalysator. Het functioneren van deze apparatuur bevestigt dat het inderdaad mogelijk is om reproduceerbare activiteits- en selectiviteitsdata te verkrijgen binnen een acceptabele experimentele fout (hoofdstuk 2). Het opnemen van aparte massadebiet- en drukregelaars samen met productscheiding in iedere stroom maakt het mogelijk om reacties uit te voeren met hoge productie van vloeistoffracties (zoals in conventionele enkelstroom uitvoeringen). Dit is cruciaal voor een complete kwantificering van FTS product samenstellingen en betekent tevens ook het voordeel over apparatuur met meer dan 10 parallelle reactoren waar om instrumentele redenen dit leidt tot verhoogd installatievolume, kosten en operationele complexiteit. Om die reden **combineert een zes-stroom gepakt bed microreactor de voordelen van ’high-throughput’ apparatuur en conventionele FTS laboratoriumschaal opstellingen** (hoofdstuk 2).

In hoofdstuk 3 is het combineren van de kobalt (Co) actieve fase en zure functionaliteit van H-ZSM-5 in FTS onderzocht in twee verschillende katalysator configuraties: (*i*) H-ZSM-5 als katalytische coating op Co en (*ii*) H-ZSM-5 als katalytische drager voor Co. Bolvormige Co/SiO_2 katalysator is gekozen als conventioneel FTS katalysator vergelijkingsmateriaal en is tevens gebruikt als precursor om de H-ZSM-5 gecoate Co-katalysator te synthetiseren.

In het eerste geval zijn verschillende silicalite-1 en H-ZSM-5 gecoate referentiemonsters bereid door de Co/SiO_2 te onderwerpen aan een directe hydrothermale procedure (allernieuwste methode om zeoliet coatings te produceren). Het silica in de Co/SiO_2 katalysator wordt omgezet in de zeoliet wanneer het wordt blootgesteld aan de hydrothermale synthesecondities terwijl de originele vorm van de drager bewaard blijft na de omzetting. Door deze synthesewijze worden Co_3O_4 agglomeraten bedekt met een H-ZSM-5 coating op nanometerschaal. De resulterende bifunctionele katalysator verlaagt de productie van FTS was (C_{21+}) aanzienlijk in vergelijking met Co/SiO_2. Echter, het membraaneffect van de coating resulteert in massatransportlimitering die de productiviteit verlaagt. In de afwezigheid van de zuurfunctionaliteit zorgt de afzetting van ‘coke’ voor deactivering van de silicalite-1 gecoate referentie katalysator. De H-ZSM-5 gecoate Co-katalysator vertoont lagere CO conversieniveaus dan de conventionele Co/SiO_2 katalysator vanwege de membraancoating. Deze verlaagde productiviteit en blootstelling van de Co kristallieten aan de hydrothermale omstandigheden kunnen worden beschouwd als de grootste nadelen van deze methode.

Aan de andere kant **demonstreert de systematische vergelijking van katalytische werking tussen fysisch gemengde gecoate katalysator en niet-zure gecoate katalysatoren dat de directe nabijheid tussen de FTS- en de zure actieve plaatsen essentieel is voor het verbeteren van de bifunctionaliteit van de katalysator om zodoende de selectiviteit naar vloeibare producten te verhogen en de productie van lange koolwaterstoffen te elimineren** (hoofdstuk 3). Dit contact kan worden gemaximaliseerd wanneer Co direct wordt aangebracht op het zeoliet volgens configuratie (*ii*). Omdat het Co beter bereikbaar is in deze configuratie, kunnen transportlimitaties ten gevolge van het membraaneffect van een zeolietcoating worden geëlimineerd terwijl de belangrijke directe nabijheid van de twee functionaliteiten wordt behouden.

Om te compenseren voor de relatief lage intrinsieke activiteit van FTS katalysatoren en om de productiviteit te verhogen, zijn hoge metaalladingen vereist in FTS katalysator formuleringen. Over het algemeen zijn microporeuze zeolieten vrij van mesoporeus oppervlak, essentieel voor een optimale dispersie van Co deeltjes met hoge metaallading. Daarentegen is de vorming van metaalclusters in de microporiën ongewenst, aangezien Co deeltjes kleiner dan 6 nm niet optimaal fungeren als FTS katalysatoren in termen van activiteit en selectiviteit. Op grond daarvan is mesoporeus H-ZSM-5 (‘*meso*H-ZSM-5’) bestudeerd als drager voor Co-gebaseerde FTS katalysatoren in hoofdstukken 4 tot en met 7.

Syntheseoptimalisatie van *meso*H-ZSM-5 is uitgevoerd door demetallisering via opeenvolgende base- en zuurbehandelingen. NaOH (basisch, anorganisch) en tetrapropylammonium hydroxide (TPAOH, organisch) basen werden gebruikt als desilicatiemiddel. Onder gelijke behandelingscondities resulteerde het gebruik van NaOH voor een hogere desilicatie dan TPAOH, en werden mesostructuren gecreëerd met poriegroottes en –volumes gelijk aan de amorfe SiO_2 drager. TPAOH desilicatie verloopt op een meer gecontroleerde manier en leidt tot hogere mesoporositeit, wat duidt op en hogere mate van hiërarchie van grote holtes verbonden door kleinere mesoporiën. Bovendien geniet TPAOH de voorkeur over NaOH om de reden dat Na^+ een bekend vergif is voor Co-gebaseerde FTS katalysatoren en dat minieme hoeveelheden resulteren een lagere FTS activiteit dan de monsters behandeld met organische basen (hoofdstuk 4).

De achtereenvolgende zuurbehandeling met HNO_3 verwijdert het buiten het raamwerk geproduceerde aluminium gevormd door de zeolietdesilicatie, en de behandeling bevordert de FTS activiteit. Tevens herstelt de zuurbehandeling de Brønstedzuurgraad van *meso*H-ZSM-5 (hoofdstuk 5).

Het grote mesoporeuze oppervlak van *meso*H-ZSM-5 is gunstig voor de metaaldispersie bij hoge Co-belading. **De Co/*meso*H-ZSM-5 katalysator is een vele malen actievere FTS katalysator dan de Co/H-ZSM-5 en de conventionele Co/SiO_2. Daarnaast is de operationele stabiliteit van de Co/*meso*H-ZSM-5 vergelijkbaar aan de Co/SiO_2 met betrekking tot CO conversie gedurende 140 uur FTS operatie.** In vergelijking met Co/H-ZSM-5 verhogen de verbeterde transporteigenschappen van *meso*H-ZSM-5 de selectiviteit van de gedragen Co-katalysator naar de vloeibare koolwaterstoffen en verlagen die naar methaan. **De hoge selectiviteit naar vloeibare koolwaterstoffen van H-ZSM-5-gedragen Co-katalysatoren is zichtbaar als een scherpe scheidslijn in de molaire productdistributie boven C_{11} ten opzichte van de ASF-verdeling van conventionele katalysatoren zoals Co/SiO_2. Metingen na 140 uur bedrijf tonen aan dat Co/*meso*H-ZSM-5 circa driemaal selectiever is naar de C_5-C_{11} fractie dan Co/SiO_2, en daarbij tevens een groot deel aan onverzadigde koolwaterstoffen naast α-alkenen produceert. Evenzo wordt de wasproductie significant onderdrukt over de zeolietkatalysator** (513 K, 15 bar totaal druk, aanvoersamenstelling $H_2/CO = 1$, en de $GHSV = 12\ m^3_{STP}\ kg^{-1}_{cat}\ h^{-1}$) (hoofdstukken 5 en 6).

De herkomst van de methaanselectiviteit over zeoliet-gedragen Co-katalysatoren is ook onderzocht. *meso*H-ZSM-5 is gebruikt als drager voor een serie van Co-gebaseerde FTS katalysatoren waaraan verschillende beladingen van ZrO_2 en/of Ru zijn toegevoegd als promotors. Door middel van geavanceerde katalysator karakteriseringstechnieken (inclusief *quasi in situ* donkerveld transmissie-elektronenmicroscopie, synchrotron-gebaseerde röntgenstraling absorptie-spectroscopie, nl. EXAFS en

XANES, etc.) naast een gedetailleerde katalysator prestatiebepaling is een relatie bepaald tussen de structurele kenmerken van de zeoliet-gedragen Co en activiteit en selectiviteit in FTS. De toevoeging van ZrO_2 of Ru verhoogt de Co-reduceerbaarheid aanzienlijk tijdens activering bij 773 K en verbetert de FTS activiteit gedurende de eerste 80 uur van operatie, waarna de activiteit geleidelijk terugkeert naar het niveau van de katalysator zonder promotor. De katalysatorpromotie heeft geen significante invloed op de productselectiviteit (hoofdstuk 6). **De methaanselectiviteit van de zeoliet-gedragen Co-katalysatoren wordt toegeschreven aan de belangrijkste zijreacties, directe CO-hydrogenering en koolwaterstofhydrogenolyse, over coordinatief onverzadigde Co-plaatsen die worden gestabiliseerd door sterke metaal-zeolietinteracties** (hoofdstuk 5 en 6).

Daarbij zijn naast *meso*H-ZSM-5 meerdere zeoliettopologieën onderzocht als FTS katalysatordrager: gedelamineerd MWW (H-ITQ-2) en mesoporeus FAU (hoofdstuk 7). Alle zeolietdragers werden zorgvuldig gekarakteriseerd op het aantal en sterkte van de zure sites met temperatuur-geprogrammeerde NH_3-desorptie en pyridineadsorptie. Om de rol van zuurgekatalyseerde reacties in de veranderde productverdeling te onderzoeken, inclusief hydro-kraken en isomerisatie, zijn zuur-gekatalyseerde model reacties van normaal hexaan en 1-hexeen uitgevoerd. **De zuurdichtheid en –sterkte van de zeoliet zijn essentiële parameters om de FTS productselectiviteit naar vloeibare koolwaterstoffen te sturen. Alleen de sterke zure sites, welke actief zijn voor het hydro-kraken in het operationele temperatuurgebied van Co-gebaseerde FTS katalysatoren, resulteren in afwijkingen van de conventionele ASF productdistributie** (hoofdstuk 7). Het met opzet gedeeltelijk deactiveren van de Brønsted zure sites in *meso*H-ZSM-5 door middel van koolstof deeltjes gedurende de katalysatorsynthese vermindert de *iso*- tot *n*-alkaan verhouding en de selectiviteit naar de benzinefractie, wat des te meer de bovengenoemde rol van zuurgekatalyseerde reacties in het sturen van de productselectiviteit bevestigt (hoofdstuk 5). **Wanneer de zure sites zich dicht nabij FTS-sites bevinden op nanometerschaal, dan is het mogelijk dat de primaire FTS producten zoals α-alkenen gekraakt of geïsomeriseerd worden voordat ze worden gehydrogeneerd. In feite ligt de 1-hexeen conversie aanmerkelijk hoger dan de die van *n*-hexaan over *meso*H-ZSM-5** (hoofdstuk 6). Het klassieke mechanisme van deze zuurgekatalyseerde reacties verhoogt de vertakkingsgraad van de koolwaterstoffen door de herstructurering van een secundair carbocation naar een geprotoneerd dialkylcyclopropaan. Omdat FTS grotendeels lineaire α-alkenen produceert, worden er ook aanzienlijke hoeveelheden van andere onverzadigde koolwaterstoffen gevormd op de zure sites.

Onze resultaten demonsteren in alle opzichten dat het gebruik van mesoporeuze zeolieten als FTS-dragers veelbelovend is voor de directe synthese van vloeibare brandstoffen vanuit synthesegas. De uitdaging die ons rest is de verbeterde controle over de productselectiviteit van deze bifunctionele katalysatoren. In dit opzicht is het essentieel om de bovengenoemde oorzaken van de methaanproductie op de zeoliet-gedragen Co-katalysatoren aan te pakken. Bovendien is het vereist om een beter onderscheid te maken tussen en om te definiëren wat het aandeel is van ‘het metaal’ en ‘de zeoliet/zuurgraad’ functionaliteiten in het productspectrum van deze katalysatoren. Alhoewel dit begrip in open literatuur wordt genegeerd of gebrekkig wordt beschreven, is het van ongekend belang voor verdere katalysatoroptimalisatie betreffende het productspectrum en praktische toepassing. Van essentieel belang voor een beter begrip van bifunctionele FTS systemen zijn gedetailleerde zuur-gekatalyserde koolwaterstof conversiestudies onder relevante FTS procescondities, in combinatie met referentie-experimenten en uitgebreid kinetisch onderzoek. Ten slotte is de stabiliteit van de katalysatoren op lange termijn grotendeels onverkend.

Onlangs is een nieuwe promovendus in de Catalysis Engineering sectie van de Technische Universiteit Delft begonnen aan vervolgonderzoek op dit onderwerp.

About the author

Sina Sartipi was born on twenty-first of September, 1981 in Tehran, Iran. After obtaining his high school diploma in mathematics and physics, he continued his studies in chemical engineering at the University of Tehran, Iran. He received both the bachelor and master of science from the same university. In 2007 he was introduced to the field of heterogeneous catalysis during his MSc thesis, entitled “Investigation of the effects of precious metal nanoparticles on the performance of perovskite catalytic converters”.

Sina Sartipi moved to the Netherlands in 2009 to do a PhD in chemical engineering at the Catalysis Engineering section of Delft University of Technology (Faculty of Applied Sciences, Department of Chemical Engineering). His PhD research, described in this thesis, was supervised by Prof.dr. Freek Kapteijn and Dr. Jorge Gascon. This work was part of the Smart Mix CatchBio program in the Netherlands.

Currently, Sina Sartipi is a postdoctoral researcher at Delft University of Technology. The highlighted research topics that he is involved in include heterogenization of hydroformylation catalysts, utilization of metal organic frameworks (MOFs) for heterogeneous catalysis, and development of Fischer-Tropsch synthesis catalysts. He has (daily) supervised three MSc and two BSc projects, two undergraduate and one guest PhD students, and contributed to the tutorial training of the chemical engineering undergraduate course “Process technology II” (chaired by Prof.dr. Freek Kapteijn). He is the first and corresponding author of eight (co-author of nine) peer reviewed articles, including two journal covers.

List of publications

Articles in journals

- **S. Sartipi**, M. Makkee, F. Kapteijn, Jorge Gascon, "*Catalysis Engineering of bifunctional solids for the one-step synthesis of liquid fuels from syngas-A review*", Catal. Sci. Technol. (**2014**) In Press. DOI: 10.1039/c3cy01021j
- **S. Sartipi**, M. Alberts, V.P. Santos, M. Nasalevich, J. Gascon, F. Kapteijn, "*Insights into the Catalytic Performance of Mesoporous H-ZSM-5-Supported Cobalt in Fischer–Tropsch Synthesis*", ChemCatChem 6 (**2014**) 142-151. DOI: 10.1002/cctc.201300635 [Journal Cover]
- **S. Sartipi**, H. Jansma, D. Bosma, B. Boshuizen, M. Makkee, J. Gascon, F. Kapteijn, "*Six-flow operations for catalyst development in Fischer-Tropsch synthesis: Bridging the gap between high-throughput experimentation and extensive product evaluation*", Rev. Sci. Instrum. 84 (**2013**) 124101. DOI: 10.1063/1.4834895
- **S. Sartipi**, K. Parashar, M.J. Valero-Romero, V.P. Santos, B. van der Linden, M. Makkee, F. Kapteijn, J. Gascon, "*Hierarchical H-ZSM-5-supported cobalt for the direct synthesis of gasoline-range hydrocarbons from syngas: Advantages, limitations, and mechanistic insight*", J. Catal. 305 (**2013**) 179-190. DOI: 10.1016/j.jcat.2013.05.012
- **S. Sartipi**, M. Alberts, M.J. Meijerink, T.C. Keller, J. Pérez-Ramírez, J. Gascon, F. Kapteijn, "*Towards Liquid Fuels from Biosyngas: Effect of Zeolite Structure in Hierarchical-Zeolite-Supported Cobalt Catalysts*", ChemSusChem 6 (**2013**) 1646-1650. DOI: 10.1002/cssc.201300339
- **S. Sartipi**, J.E. van Dijk, J. Gascon, F. Kapteijn, "*Towards bifunctional catalysts for the direct conversion of syngas to gasoline range hydrocarbons: H-ZSM-5 coated Co versus H-ZSM-5 supported Co*", Appl. Catal. A-Gen. 456 (**2013**) 11-22. DOI: 10.1016/j.apcata.2013.02.012
- **S. Sartipi**, K. Parashar, M. Makkee, J. Gascon, F. Kapteijn, "*Breaking the Fischer-Tropsch synthesis selectivity: Direct conversion of syngas to gasoline over hierarchical Co/H-ZSM-5 catalysts*", Catal. Sci. Technol. 3 (**2013**) 572-575. DOI: 10.1039/c2cy20744c [Journal Front Cover]
- S. Khajavi, **S. Sartipi**, J. Gascon, J.C. Jansen, F. Kapteijn, "*Thermostability of hydroxy sodalite in view of membrane applications*", Microporous Mesoporous Mat. 132 (**2010**) 510-517. DOI: 10.1016/j.micromeso.2010.03.035

- **S. Sartipi**, A.A. Khodadadi, Y. Mortazavi, "*Pd-doped $LaCoO_3$ regenerative catalyst for automotive emissions control*", Appl. Catal. B-Environ. 83 (**2008**) 214-220. DOI: 10.1016/j.apcatb.2008.02.014

Oral presentations

- *Hierarchical zeolite supported cobalt for the direct production of liquid fuels from syngas: effect of zeolite structure*, Sina Sartipi, Freek Kapteijn, and Jorge Gascon/Sina Sartipi, 2013 American Institute of Chemical Engineers Annual Meeting (2013 AIChE), San Francisco-California-USA, 3–8 November 2013.
- *Towards Tailor Made, Multi-Functional, Fischer-Tropsch Catalysts*, Jorge Gascon, Sina Sartipi, Vera P. Santos, Michiel Makkee, and Freek Kapteijn/Jorge Gascon, XIVth Netherlands Catalysis and Chemistry Conference (NCCC XIV), Noordwijkerhout-The Netherlands, 11–13 March 2013.
- *In Situ Valorisation of Biomass: "From BioSynGas to liquid fuel"*, Sina Sartipi, Jorge Gascon, and Freek Kapteijn/Sina Sartipi, CatchBio Progress Meeting (CPM) 2013, Nunspeet-The Netherlands, 23–24 January 2013.
- *Engineering bi-functional catalysts for the direct synthesis of fuels from bio-syngas*, Jorge Gascon, Sina Sartipi, Michiel Makkee, and Freek Kapteijn/Jorge Gascon, TMFB (Tailor-Made Fuels from Biomass) and CatchBio Joint Symposium, Aachen-Germany, 20 September 2012.
- *Bifunctional Core-Shell Catalysts: "Towards direct gasoline production in Fischer-Tropsch Synthesis"*, Sina Sartipi, Johannes E. van Dijk, Jorge Gascon, and Freek Kapteijn/Sina Sartipi, XIIIth Netherlands Catalysis and Chemistry Conference (NCCC XIII), Noordwijkerhout-The Netherlands, 5–7 March 2012.
- *In Situ Valorisation of Biomass: "From BioSynGas to liquid fuel"*, Sina Sartipi, Johannes E. van Dijk, Kshitij Parashar, Jorge Gascon, and Freek Kapteijn/Sina Sartipi, CatchBio Progress Meeting (CPM) 2012, Nunspeet-The Netherlands, 25–26 January 2012.
- *In Situ Valorisation of Biomass: "From BioSynGas to liquid fuel"*, Sina Sartipi, Jorge Gascon, and Freek Kapteijn/Sina Sartipi, CatchBio Progress Meeting (CPM) 2011, Nunspeet-The Netherlands, 26–27 January 2011.
- *In Situ Valorisation of Biomass: "From BioSynGas to liquid fuel"*, Sina Sartipi, Jorge Gascon, and Freek Kapteijn/Sina Sartipi, CatchBio Progress Meeting (CPM) 2010, Nunspeet-The Netherlands, 27–28 January 2010.

Poster presentations

- *Bifunctional catalysts for direct production of liquid fuels from syngas,* Sina Sartipi, Jorge Gascon, and Freek Kapteijn/Sina Sartipi, XVth Netherlands Catalysis and Chemistry Conference (NCCC XV), Noordwijkerhout-The Netherlands, 10–12 March 2014.
- *Bifunctional catalysts for the direct production of liquid fuels from syngas,* Sina Sartipi, Jorge Gascon, and Freek Kapteijn/Sina Sartipi, 1st Annual Event of the Process Technology Institute (1st DPTI), Den Haag-The Netherlands, 14 November 2013.
- *Modification of zeolite crystallites for cobalt-based catalyst applications in bifunctional Fischer-Tropsch Synthesis,* Sina Sartipi, Jorge Gascon, and Freek Kapteijn/Freek Kapteijn, 17th International Zeolite Conference (IZC 17th), Moscow-Russia, 7–12 July 2013.
- *In Situ Valorisation of Biomass: "From BioSynGas to liquid fuel"*, Sina Sartipi, Jorge Gascon, and Freek Kapteijn/Sina Sartipi, CatchBio Progress Meeting (CPM) 2013, Nunspeet-The Netherlands, 23–24 January 2013.
- *Bifunctional catalysts for the direct conversion of syngas to gasoline range hydrocarbons: "Co/H-ZSM-5 versus H-ZSM-5/Co"*, Sina Sartipi, Johannes E. van Dijk, Kshitij Parashar, Jorge Gascon, and Freek Kapteijn/Jorge Gascon, International Program Committee meeting of the TU Delft Process Technology Institute, Delft-The Netherlands, 27 November 2012.
- *Bifunctional Catalysts for the Direct Conversion of Syngas to Gasoline Range Hydrocarbons,* Sina Sartipi, Johannes E. van Dijk, Kshitij Parashar, Jorge Gascon, and Freek Kapteijn/Sina Sartipi, International Symposium on Zeolites and MicroPorous Crystals (ZMPC2012), Hiroshima-Japan, 28 July–1 August 2012.
- *Bifunctional catalysts for the direct conversion of syngas to gasoline range hydrocarbons,* Sina Sartipi, Johannes E. van Dijk, Kshitij Parashar, Jorge Gascon, and Freek Kapteijn/Sina Sartipi, International Symposium on Alternative Clean Synthetic Fuels (SynFuel 2012), Munich-Germany, 29–30 June 2012.
- *Cobalt Supported on Hierarchical Zeolites: "Bifunctional catalyst for FTS product selectivity control"*, Kshitij Parashar, Sina Sartipi, Jorge Gascon, and Freek Kapteijn/María José Valero-Romero, TG (Technologisch Gezelschap) Symposium, Smart Materials: Smart outside, Chemistry inside, Delft-The Netherlands, 26 April 2012.
- *Cobalt Supported on Hierarchical Zeolites: "Bifunctional catalyst for FTS product selectivity control"*, Kshitij Parashar, Sina Sartipi, Jorge Gascon, and Freek Kapteijn/Kshitij Parashar, XIIIth Netherlands Catalysis and Chemistry Conference (NCCC XIII), Noordwijkerhout-The Netherlands, 5–7 March 2012.

- *In Situ Valorisation of Biomass: “From BioSynGas to liquid fuel”*, Sina Sartipi, Johannes E. van Dijk, Kshitij Parashar, Jorge Gascon, and Freek Kapteijn/Sina Sartipi, CatchBio Progress Meeting (CPM) 2012, Nunspeet-The Netherlands, 25–26 January 2012.
- *In Situ Valorisation of Biomass: “From BioSynGas to liquid fuel”*, Sina Sartipi, Jorge Gascon, and Freek Kapteijn, OSPT Miniposter booklet 2011.
- *In Situ Valorisation of Biomass: “From BioSynGas to liquid fuel”*, Sina Sartipi, Johannes. E. van Dijk, Jorge Gascon, and Freek Kapteijn/Sina Sartipi, CatchBio Mid-Term Review 2011, Urmond-The Netherlands, 28 September 2011.
- *Synthesis of bifunctional core-shell catalysts: “An approach for GTL process intensification”*, Sina Sartipi, Jorge Gascon, and Freek Kapteijn/Sina Sartipi, 10th International Conference on Catalysis in Membrane Reactors (ICCMR 10), Saint-Petersburg-Russia, 20–24 June 2011.
- *In Situ Valorisation of Biomass: “From BioSynGas to liquid fuel”*, Sina Sartipi, Jorge Gascon, and Freek Kapteijn/Sina Sartipi, CatchBio Progress Meeting (CPM) 2011, Nunspeet-The Netherlands, 26–27 January 2011.
- *In Situ Valorisation of Biomass: “From BioSynGas to liquid fuel”*, Sina Sartipi, Jorge Gascon, and Freek Kapteijn, OSPT Miniposter booklet 2010.
- *In Situ Valorisation of Biomass: “From BioSynGas to liquid fuel”*, Sina Sartipi, Jorge Gascon, and Freek Kapteijn/Sina Sartipi, CatchBio Progress Meeting (CPM) 2010, Nunspeet-The Netherlands, 27–28 January 2010.

Acknowledgments

The committee members of my PhD defense, including Prof. Ye Wang (Xiamen University), Prof.dr. Javier Pérez-Ramírez (ETH Zürich), Prof.dr.ir. Krijn P. de Jong (Utrecht University), Dr. Herman P.C.E. Kuipers (Shell Global Solutions International B.V.), Prof.dr.ir. M. Makkee (Politecnico di Torino/Delft University of Technology), and Prof.dr.ir. Herman van Bekkum (Delft University of Technology) are acknowledged for accepting our invitation and for reviewing this work.

Doing a PhD is very much like a trip. A trip that makes the PhD student not only educated, but also wiser, more experienced, and stronger. For me this journey started with an e-mail from Prof.dr. Freek Kapteijn, disclosing: “our congratulations! … we selected you as best candidate for a PhD position in our group on a project within the framework of the 'CatchBio' programme in The Netherlands”. Freek, I kept that e-mail since your response was life changing. I am very grateful for giving me the opportunity to become a member of the Catalysis Engineering research group at Delft University of Technology.

As a traveler needs to identify his path, one of the most challenging parts of a PhD program is to define a plan and structure ones way through it. Dr. Jorge Gascon, your supervision shed light on the road and showed me the way to face this challenge. I am thankful for all your help and support. I enjoyed the research we did during the past five years a lot. I would also like to thank Prof.dr.ir. Michiel Makkee for his regular guidance and advice, and Dr. Patricia Kooyman for transmission electron microscopy imaging.

I acknowledge the work of Harrie Jansma, Duco Bosma, and Bart Boshuizen regarding the “six-flow fixed-bed microreactor Fischer-Tropsch synthesis” setup construction. I also thank Bart van den Linden, Kevin Mouthaan, and Willy Rook for their continuous technical support, and Els Arkesteijn for her assistance.

The user committee members of the CatchBio project 053.70.005, especially Dr. Colin J. Schaverien (Shell Global Solutions International B.V.), Dr. Robert Terörde (BASF), and Dr. Jan Kees van der Waal (Avantium Technologies) are acknowledged for the fruitful discussions and their input to this project.

I acknowledge Prof.dr. Javier Pérez-Ramírez for his co-authorship in one of the journal publications (*ChemSusChem 6 (2013) 1646*) and Prof.dr. Avelino Corma for providing the H-ITQ-2 sample. Dr. Eelco Vogt (Albemarle Catalysts Company B.V.) and Dr. Johan Heiszwolf are thanked for giving us the opportunity to use the facilities at Albemarle Catalysts Company B.V. to prepare one of our samples.

There were many colleagues and friends that accompanied me through this journey. I gained a great deal of experience from the MSc/BSc projects I supervised. For that I would like to thank all my very good (former) students, including Erik van Dijk, Kshitij Parashar, Margje Alberts, and Mark J. Meijerink. María José Valero-Romero, I am very glad that you decided to do a research stay at Delft University of Technology, assisting this project. Thank you for the energy you put in this work. Special thanks to my colleagues at the Catalysis Engineering section, Dr. Vera Santos and Maxim Nasalevich for their scientific collaborations. I gratefully acknowledge Tim Wezendonk for translating the summary section of this book (Samenvatting) and Dr.ir. Rob J. Berger for translating the Propositions (Stellingen) to Dutch.

In addition to the scientific and professional experiences I gained during the PhD period, those of relationships were the most precious! Canan Gücüyener, Vera Santos, Jana Juan-Alcañiz, Pablo Serra-Crespo, Enrique Ramos Fernandez, Alberto Martínez Joaristi, Maxim Nasalevich, Irina Prokopyeva, Emmanuel Skupien, Tania Ródenas-Torralba, Hakeem Abrar Ahmad, Martijn de Lange, Elena García Pérez, Søren Vendelbo, and all other colleagues in the Catalysis Engineering section, it was/is a pleasure working with you and having you as friends, Thank you for everything… Especial thanks to Canan and Jana, the paranymphs of my PhD defense ceremony.

I would like to express my respect to Dr. Abbas-ali Khodadadi (University of Tehran) and Dr. Yadollah Mortazavib (University of Tehran) by whom I was introduced to the field of heterogeneous catalysis during my MSc thesis.

The last but not least, I would like express my appreciations and respect to my family that are thoroughly ‘the stars of my life’: my mother (Dr. Azadeh Nazari), father (Ir. Mehdi Sartipi), sister (Yasamin Sartipi), wife (Pegah Mohtadi Tabrizi), grandmother (Foroozan Rastan), and aunt (Dr. Niloofar Nazari). *Maman*, *baba*, and Madi, I owe my wellbeing to you and will always do… My achievements, if any, will always be yours and words are not capable to describe how I am grateful for that. Pegah, *azizam*, thank you for all the love you bought to my life. You have always been there for me through this period. I am grateful for that and will do my best in the life we are sharing together. Yasi, thank you for your care, I wish you all the best. *Khaleh*, I am grateful for all your supports during the past five years that I moved to the Netherlands. Your continuous help means a lot to me, knowing that things could have been much more challenging without the presence of you and my cousins (Ayeh Zarrinkhameh and Iman Zarrinkhameh).